FEUP Universidade do Porto
Faculdade de Engenharia

UNCERTAINTY QUANTIFICATION IN OPERATIONAL MODAL ANALYSIS AND CONTINUOUS MONITORING OF SPECIAL STRUCTURES

Sandro Diord Rescinho Amador

A dissertation presented to the Faculty of Engineering of University of Porto
for the degree of Doctor in Civil Engineering.
Supervisors: Álvaro Cunha (Full Professor); Elsa Caetano (Associate Professor).

ABSTRACT

This thesis addresses three key issues of a real-life vibration-based structural health monitoring system. The first is related to the estimation of the modal parameters of the monitored structures from output-only data together with their confidence intervals. Since the source of vibration of the monitored structures are mostly the unmeasurable ambient excitations, all estimates from the output responses are contaminated with disturbances of statistical nature which are, in turn, disseminated to the identified modal parameters. Hence the need to consider not only the modal parameter estimates, but also their uncertainties in damage assessment. Therefore, apart from discussing the strategies and techniques employed to automatically track the dynamic properties of the monitored structures, the techniques used to estimate the confidence bounds are also addressed and two approaches are proposed to estimate these uncertainties in the present work.

The second key issue involves the automation of the modal parameter estimation. In fact, a successful assessment of the health condition based on modal properties is only feasible if these parameters are automatically extracted from the vibration raw data acquired over the course of a continuous monitoring. Given the huge amount of datasets acquired over time, such task is required to be performed by automated applications which are capable of tracking, amongst other useful information, the modal parameters from these data. Once they are initially configured, it is expected that such applications are capable of extracting this information with no further intervention.

Finally, the third key issue concerns the detection of damage under varying environmental conditions. In real-life applications structures are subjected to changes in such conditions (e.g., temperature, humidity, wind, traffic, etc.). Therefore, if the modal parameter estimates are intended to be used as damage indicators, the variations induced by these conditions must be taken into account, otherwise they may mask the changes caused by structural damage. If these variations are not accounted, false-positive or negative damage diagnosis may occur and, therefore, vibration-based health monitoring becomes inefficient. In these conditions, environmental models can be applied to such properties, so that they can be used to diagnose damage. In order to discuss the application of such models from a practical point of view, a thorough analysis of data from a continuous monitoring of a football stadium suspension roof is presented. The result of this analysis indicates that a slight structural change has occurred in the roof structure.

RESUMO

Esta tese aborda três questões-chave de um sistema real de monitorização da condição estrutural baseado nas respostas em vibração. A primeira está relacionada com a estimativa dos parâmetros modais das estruturas monitoradas a partir somente dos dados de resposta, juntamente com seus intervalos de confiança. Uma vez que as fontes de vibração das estruturas monitorizadas são principalmente as excitações ambientais imensuráveis, esses dados de resposta são contaminados com distúrbios de natureza estatística, que são, por sua vez, disseminados para os parâmetros modais identificados. Daí a necessidade de se considerar não apenas as estimativas dos parâmetros modais, mas também as suas incertezas na avaliação de danos. Portanto, para além de discutir as estratégias e técnicas aplicadas para identificar automaticamente as propriedades dinâmicas das estruturas monitorizadas, as técnicas usadas para estimar os intervalos de confiança são também analisadas e são propostas duas abordagens para estimar estas incertezas no presente trabalho.

A segunda questão envolve a automação da estimação de parâmetros modais. Na verdade, a avaliação da condição estrutural com base nesses parâmetros só é realizável se eles forem automaticamente extraídos dos dados de vibração adquiridos ao longo da monitorização contínua. Dado a grande volume de dados adquiridos ao longo do tempo, tal tarefa deve ser realizada por aplicações automatizadas que sejam capazes de extrair tais parâmetros, entre outras informações úteis relativamente a condição estrutural das estruturas monitorizadas. Uma vez configurados inicialmente, espera-se que tais aplicações sejam capazes de extrair estas informações sem nenhuma intervenção adicional.

Finalmente, a terceira questão diz respeito à deteção de danos em condições ambientais variáveis. Uma vez que as estruturas reais estão sujeitas ás acções ambientais (como, por exemplo, temperatura, umidade, vento, tráfego, etc.), as variações induzidas por essas acções devem ser consideradas se as estimativas dos parâmetros modais forem utilizadas como indicadores de dano, caso contrário, elas podem mascarar as alterações estruturais causadas por danos. Se essas variações não forem contabilizadas, o diagnóstico de dano falso-positivo ou negativo pode ocorrer e, portanto, a avaliação da condição estrutural com base nos dados de vibração torna-se ineficiente. Nessas condições, modelos ambientais podem ser aplicados às estimativas de parâmetros modais de modo a que eles possam ser utilizados para diagnosticar danos. De modo a discutir a aplicação desses modelos ambientais de forma prática, a análise completa dos dados de monitorização contínua da cobertura suspensa de um estádio de futebol é apresentada. O resultado dessa análise indica que uma leve alteração permanente no comportamento estrutural da cobertura ocorreu.

RÉSUMÉ

Cette thèse porte sur trois questions clés d'un système de surveillance de santé structurale basée sur les vibrations de la vie réelle. La première est liée à l'estimation des paramètres modaux des structures contrôlées à partir des données de sortie uniquement avec leurs intervalles de confiance. Depuis la source de vibration des structures contrôlées sont pour la plupart les excitations ambiantes non mesurables, toutes les estimations des réponses de sortie sont contaminés par des perturbations de nature statistique, à leur tour, diffusés aux paramètres modaux identifiés. D'où la nécessité de tenir compte non seulement de l'estimation des paramètres modaux, mais aussi des incertitudes dans l'évaluation des dommages. Par conséquent, en dehors de discuter des stratégies et des techniques utilisées pour suivre automatiquement les propriétés dynamiques des structures contrôlées, les techniques utilisées pour estimer les limites de confiance sont également abordées et deux approches sont proposées pour estimer ces incertitudes dans le présent ouvrage.

La deuxième question clé consiste à l'automatisation estimation des paramètres modaux. En fait, une évaluation positive de l'état de santé basé sur les propriétés modales est seulement possible si ces paramètres sont automatiquement extraits des données brutes de vibration acquis au cours d'un contrôle continu. Compte tenu de l'énorme quantité de jeux de données acquises au fil du temps, cette tâche doit être effectuée par des applications automatisées qui sont capables de suivi, entre autres informations utiles, les paramètres modaux de ces données. Une fois qu'ils sont initialement configurés, il est prévu que de telles applications soient capables d'extraire ces informations sans autre intervention.

Enfin, la troisième question clé concerne la détection des dommages dans diverses conditions environnementales. Les structures réelles sont soumises à des évolutions de telles conditions en (température, humidité, vent, trafic, etc.). Par conséquent, si les estimations des paramètres modaux sont destinés à être utilisés comme indicateurs de dommages, les variations induites par ces conditions doivent être prises en compte, sinon ils peuvent masquer les changements causés par des dommages structurels. Si ces variations ne sont pas comptabilisés, faux-positif ou négatif dommages diagnostic peut se produire et, par conséquent, la surveillance de la santé sur la base des vibrations devient inefficace. Dans ces conditions, les modèles de l'environnement peuvent être appliquées à ces propriétés, de sorte qu'ils puissent être utilisés pour diagnostiquer des dommages. Afin de discuter de l'application de ces modèles à partir d'un point de vue pratique, une analyse approfondie des données d'une surveillance continue d'un toit de suspension de stade de football est présentée. Le résultat de cette analyse indique qu'une légère modification de structure est produite dans la structure du toit.

AKNOWLEDGEMENTS

To all who have helped me during my Ph.D. research, in particular, to Professors Álvaro Cunha and Elsa Caetano for providing the necessary resources for the development of this work. A special thanks to FCT and FEUP for providing the grants that supported my Ph.D. research, to Filipe Magalhães for his help with the ambient vibration test as well as with the continuous dynamic monitoring of the Braga Sports Stadium suspension roof, and to Nuno Martins for the analysis of the wind data, whose results are presented in this thesis. My sincere thanks also goes to:

- Professor Rui Calçada, from FEUP, for supporting and encouraging me to participate in the summer course held at Bauhaus University, in Weimar, Germany, in 2011, as well as for the interesting discussions about high speed railway bridges;
- Professor Volkmar Zabel, from Bauhaus University, for giving me insights on model updating, as well as for his invitation to collaborate with his research group in Weimar.
- Doctor Christof Devriendt and Professor Patrick Guillaume, from Vrije Universiteit (Brussels), for their hospitality and the interesting discussions about frequency-domain identification techniques during my stay in Brussels by the time of the ISMA Conference held in Leuven, in 2012, and for the invitation to cooperate with their research team in Brussels. Although it was not possible to achieve this cooperation, I was very grateful and honoured with such an invitation.
- Ana Matos, from FEUP, for helping me with the academic services.

I also thank my new friends from Porto, without whom it would not have been possible to surpass the difficulties and limitations I came across along this Ph.D. journey. I would like to express my gratitude to the members of the jury, in particular, to the president of the jury Rui Manuel Carvalho Marques and to Carlos Manuel Ramos Moutinho, both from FEUP, and to the external members Carlos Alberto da Silva Rebelo, from University of Coimbra, and Carlos Manuel José Luis Ferreira da Silva Ramos, from University of Minho.

Finally, I want to express my deepest gratitude to my family for the motivation and support provided during the last year of my research. Without this support it would not have been possible to carry out all the theoretical developments related with the Maximum Likelihood Estimators presented in this thesis.

NOMENCLATURE

Abbreviatures

AVT	**A**mbient **V**ibration **T**est
DFT	**D**iscrete **F**ourier **T**ransform
DOF	**D**egrees **O**f **F**reedom
EMA	**E**xperimental **M**odal **A**nalysis
FDD	**F**requecy **D**omain **D**ecomposition
FE	**F**inite **E**lement
GUI	**G**raphical **U**ser **I**nterface
LMFD	**L**eft **M**atrix **F**raction **D**escription
LSCF	**L**east **S**quares **C**omplex **F**requency-domain
LSFD	**L**east **S**quares **F**requency-**D**omain
LS	**L**east **S**quares
MFD	**M**atrix **F**raction **D**escription
MIMO	**M**ultiple **I**nputs **M**ultiple **O**utputs
MISO	**M**ultiple **I**nputs **S**ingle **O**utput
MLE-CDM	**M**aximum **L**ikelihood **E**stimator in **C**ommon **D**enominator **M**odel formulation
MLE-MM	single reference **MLE** in (pole-residue) **M**odal **M**odel formulation
MLE	**M**aximum **L**ikelihood **E**stimator
ML	**M**aximum **L**ikelihood
MPE	**M**odal **P**arameter **E**stimation
NLS	**N**on-linear **L**east-**S**quares
OMA	**O**perational **M**odal **A**nalysis
PCA	**P**rincipal **C**omponent **A**nalysis
pLSCE	**p**oly-reference **L**east **S**quares **C**omplex **E**xponential
pLSCF	**p**oly-reference **L**east-**S**quares **C**omplex **F**requency
pMLE-MM	**p**oly-reference **M**aximum **L**ikelihood **E**stimator in **M**odal **M**odel formulation
PoGER	**Po**st **G**lobal **E**stimation **R**e-scaling
PoSER	**P**ost **S**eparate **E**stimation **R**e-scaling
PP	**P**ick **P**icking
PreGER	**Pre** **G**lobal **E**stimation **R**e-scaling
PSD	**P**ower **S**pectra **D**ensity
RMFD	**R**ight **M**atrix **F**raction **D**escription

RMS	**R**oot **M**ean **S**quare
SHM	**S**tructural **H**ealth **M**onitoring
SIMO	**S**ingle **I**nput **M**ultiple **O**utputs
SISO	**S**ingle **I**nput **S**ingle **O**utput
SSI-COV	**COV**ariance-driven **S**tochastic **S**ubspace **I**dentification
SSI-DATA	**DATA**-driven **S**tochastic **S**ubspace **I**dentification
SSI	**S**tochastic **S**ystem **I**dentification
SVD	**S**igular **V**alue **D**ecomposition
ZOH	**Z**ero **O**rder **H**old

Operators

$(\bullet)^{\dagger}$	Moore-Penrose pseudo-inverse of a matrix
$(\bullet)^{H}$	Complex conjugate transpose (Hermitian) of a matrix
$(\bullet)^{T}$	Transpose
$(\hat{\bullet})$	Estimated quantity
$\lvert\bullet\rvert$	Absolute value of a complex number
$\lVert\bullet\rVert$	Euclidian norm
$\mathscr{L}[\bullet]$	Laplace transform
$\otimes$	Kronecker product
$\mathrm{Re}(\bullet)$, $\mathrm{Im}(\bullet)$	Real and imaginary part of a complex number
$\mathbf{E}[\bullet]$	Expected value operator
$\mathrm{Cov}(\bullet)$	Covariance operator
$\mathrm{Var}(\bullet)$	Variance operator
$\mathrm{vec}(\bullet)$	Column stacking operator
$(\bullet)_D$	Diagonal operator
$(\bullet)^{*}$	Complex conjugate

Symbols

$[Res]_i$	Modal residue matrix of mode i
α_i	Denominator scalar polynomial coefficients of the common denominator model at model order i
β_i	Numerator matrix polynomial coefficients of common denominator model at model order i
Δt	Sampling period
Δ_e	Vector containing the contributions of the predicted errors to each measured

	output
$\Delta_e^{(o)}$	Contribution of the predicted error to output o
$\Delta_{\hat{y}_m}$	Vector containing the contributions of mode m to each measured output
$\delta_{\hat{y}_m}$	Total contribution of mode m to the measured outputs
$\Delta_{\hat{y}_m}^{(o)}$	Contribution of mode m to output o
$\Delta_{\hat{y}}$	Vector containing the contributions of the identified modes to each measured output
$\Delta_{\hat{y}}^{(o)}$	Contribution of the identified modes to output o
δ_{pq}	Kronecker delta
ε, ν	Rayleigh damping constants $C_1 = \varepsilon K + \nu M$
η	Exponential window function
Γ	Diagonal matrix having $2\xi_{n_i}\omega_{n_i}$ as elements
γ	Coherence function at frequency line f
Γ_i^{ref}	Reduced reversed stochastic controllability matrix of order i
$\hat{S}_{yy}^{+}(\omega)$	Half spectra matrix
$\hat{X}_i$	Kalman filter state sequence
$\hat{y}_{k_m}$	Predicted output vector containing the response of the m^{th} mode
Λ	Diagonal matrix containing the eigenvalues of the **FE** model λ_i
Λ_c	Diagonal matrix containing the continuous-time eigenvalues λ_i, λ_i^*
Λ_d	Diagonal matrix containing the discrete-time eigenvalues μ_i, μ_i^*
λ_i	Continuous-time eigenvalue
$\mathscr{P}_i^{\text{ref}}$	Projection of the row space of the future outputs into the row space of the past references
μ_i	Discrete-time eigenvalue
Ω	Diagonal matrix containing the circular eigenfrequencies ω_{n_i} [rad/s]
ω	Circular frequency [rad/s]
ω_{n_i}	Circular eigenfrequency [rad/s]
Φ	Real eigenvector matrix of the **FE** model (proportional damping)
Ψ	Complex eigenvector matrix of the state-space model
ψ_i	Complex eigenvector of the state-space model
Σ	State covariance matrix
σ_x	Standard deviation of variable x
Σ_Y	Covariance of the outputs
CL	Center line of the control chart
$\mathbf{d}(\alpha, \omega)$	Denominator scalar polynomial
$\mathbf{D}(\Theta, \omega)$	Denominator polynomial in matrix form

LCL	Lower control limit of the control chart
$\mathbf{N}(\beta,\omega)$	Numerator polynomial in matrix form
UCL	Upper control limit of the control chart
Θ	Complex eigenvector matrix of the **FE** model (non-proportional damping)
θ_i	Complex eigenvector of the **FE** model (non-proportional damping)
Υ	Principal component transformation matrix
$\varepsilon(\Theta,\omega)$	Residual errors from a preliminary **LS** estimation
$\Omega(\omega)$	Polynomial basins in Laplace domain ($\Omega(\omega)=s$) or in Z-domain ($\Omega(\omega)=\mathrm{z}$)
φ_i	Real eigenvector of the **FE** model (proportional damping)
Θ	Model parameter vector
ξ_{n_i}	Modal damping ratio
$\{1\}_{N_o}$	Column vector with N_o components, all equal to one
a, b, c	Denominator scalar coefficients of the enhanced lower and upper residual model
A, B, C, D	Discrete-time state-space model
A_c, B_c, C_c, D_c	Continuous-time state-space model
a_i, b_i	"Modal a" and "modal b" coefficients
AR, BR, CR	Numerator matrix coefficients of the enhanced lower and upper residual model
C_a, C_b, C_d	Output location matrices for acceleration, velocity and displacement
$d(\omega)$	Denominator scalar of the enhanced lower and upper residual model
E	Matrix or vector containing the residual errors
$f(t)$	Excitation force vector at time t (**FE** model)
F_1	Input location matrix (**FE** model)
f_{n_i}	Eigenfrequency [Hz]
$F_{n_p,n_p-m}(\alpha)$	α percentage point of the F-distribution with m and n_p-m **DOF**s
G	"Next state-output" covariance matrix
G^{ref}	Reduced "next state - output" covariance matrix
G_m	Discrete-time stochastic modal participation matrix
$g_{d_i}^T$	Discrete-time stochastic modal participation vector (row of G_m^T)
g_i	Continuous-time operational factor vector (row of G_{cm}^T)
$H(\omega)$	**FRF** matrix
$H(s)$	Transfer function matrix in Laplace-domain
H^{ref}	Output data block Hankel matrix
H_1, H_2	H_1 and H_2 **FRF** estimators
J	Jacobian matrix

j	Imaginary unit $j = \sqrt{-1}$
K	Kalman gain
k	Discrete time instant $t = k\Delta t$, $k \in \mathbb{N}$
L	Continuous-time modal input matrix (modal participation matrix) $L^T = \Psi^{-1} B_c$
L_d	Discrete-time modal input matrix (modal participation matrix) $L_d^T = \Psi^{-1} B$
$l_{d_i}^T$	Discrete-time modal participation vector (row of L_d^T)
l_i^T	Continuous-time modal participation vector (row of L^T)
$l_{Log-ML-CDM}$	Logarithmic cost function of the "log-like" **MLE-CDM**
$l_{Log-pML-MM}$	Logarithmic cost function of the "log-like" **pMLE-MM**
l_{ML-MM}	Cost function of the **MLE-MM**
l_{pML-MM}	Cost function of the **pMLE-MM**
L_s	Selection matrix that selects the references from the outputs
LR, UR	Lower and upper residuals
M, C_1, K	Mass, damping and stiffness matrix (**FE** model)
$m\gamma_o^2$	Multiple coherence function
m_i, k_i	Modal mass and modal stiffness
n	State-space model order $n = 2N_m$
$N(\omega)$	Numerator matrix of the enhanced lower and upper residual model
n_a, n_b	Auto-regressive and exogeneous order
N_i	Number of inputs
N_k	Number of time samples
n_k	Time delay between input and output
N_m	Number of **DOF**s (**FE** model)
N_o	Number of outputs
N_{ref}	Number of reference sensors
O_i	Observability matrix of order i
P	Forward state covariance matrix
Q, R	Factors from a QR factorization
Q, R, S	Process and measurement noise covariance matrices
$q(t)$, $\dot{q}(t)$, $\ddot{q}(t)$	Displacement, velocity and acceleration vector at time t (**FE** model)
q_k, $\dot{q}_k$	Displacement and velocity vector at discrete time instant k (**FE** model)
$q_m(t)$	Modal displacement vector
R_e	Covariance matrix of the innovations e_k
R_i	Output covariance matrix at time lag i
R_{uu}	Input covariance matrix in case of white noise inputs
$S_{uu}(\omega)$	Spectra matrix of the inputs

$S_{uy}(\omega)$	Input-output Spectra matrix
$S_{yu}(\omega)$	Output-input spectra matrix
$S_{yy}(\omega)$	Spectra matrix of the outputs
T	Similarity transformation
t	Continuous time variable
T^2	T^2-statistic
$t_{N_k-n_p,\alpha/2}$	Upper $100(\alpha/2)$ percentile of a t-distribution with $N_k - n_p$ **DOF**s
U, S, V	**SVD** factors
U, W	Auxiliary matrices for the derivation of the state-space model from the **FE** model
$U(s)$	Input in the Laplace-domain
$u(t)$	Input at time t
u_k	Input at time instant k
V	Continuous-time modal output matrix $V = C_c\Psi$
V_d	Discrete-time modal output matrix $V_d = C_d\Psi$
v_k	Measurement noise at time instant k
v_{d_i}	Discrete-time mode shape vector
v_i	Continuous-time mode shape vector
w_k	Process noise vector at time instant k
W_γ	Window function
X	Principal component score matrix
$X(s)$	State in the Laplace domain
$x(t)$	State at time t
x_k	State at time instant k
$x_m(t)$	Modal state at time t $(x(t) = \Psi x_m(t))$
$x_m^{(i)}(t)$	i^{th} Component of the modal state $x_m(t)$
$x_{m_k}^{(i)}$	i^{th} Component of the modal state x_{m_k}
Y	Matrix containing the sampled outputs
$Y(s)$	Output in the Laplace domain
$y(t)$	Output at time t
$y_i(t)$	Contribution of mode i to the output at time t
y_k	Output at time instant k
y_k^{ref}	Reference output at time instant k
y_{k_i}	Contribution of mode i to the output at time instant k
Z	Matrix containing the sampled predictors
$Z(s)$	Dynamical stiffness in Laplace-domain

CONTENTS

Chapter 1

INTRODUCTION

This first chapter presents the general aspects, such as, research context, motivation and main objectives of the of the present thesis. The chapter is intended to provide a general overview of the activities developed in context of the present research, as well as a brief description of the following chapters. The main subjects addressed in the framework of the thesis - modal identification with uncertainty quantification, automated dynamic monitoring and damage detection with emphasis on vibration-based methods - are discussed in Section 1.1. In Section 1.2, the main contributions of this thesis are highlighted and in Section 1.3, the organization of the text is finally presented.

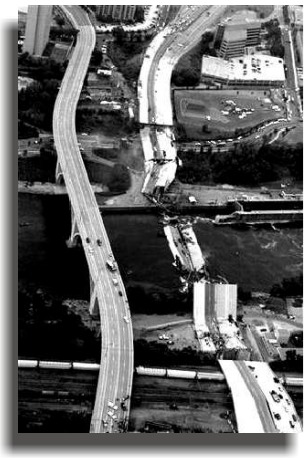

1.1. Research Context

In recent years, an increasing interest on **S**tructural **H**ealth **M**onitoring (**SHM**) in the domain of structural and civil engineering has been observed. The growth of interest on this scientific domain is explained, amongst other reasons, by the broad range of possible applications in structural engineering, as well as by the necessity to stablish a reliable approach to assess the health condition of the civil engineering structures which are subjected to varying operational and environmental conditions over the time. The development of numerical methods of structural analysis allied to the improvements on the processing capacity of the digital computers over the last decades lead to the development of more precise tools and techniques of structural analysis, allowing engineers to simulate more accurately the static and dynamic behaviour of these structures. These improvements, in turn, lead to construction of civil structures with more audacious and complex architectural and structural designs.

It turns out that, given the difficulties of modelling the environmental and operational actions, as well as the damage induced effects, the behaviour of these structures under operational conditions is not easy to predict. Several examples of structures that collapsed or suffered from serviceability problems are eventually found in literature. Perhaps, one of the most notorious cases of structural failures is the collapse of the *Tacoma Narrows* suspension bridge shown in Fig. 1.1a. Constructed to link Tacoma and Gig Harbor, Washington, USA, and inaugurated in July, 1940, this bridge collapsed four months later due to flutter of the bridge deck. Recently, another structural accident that has drawn the attention of civil engineering community due to its catastrophic dimensions was the collapse of *"9340"* Bridge (also known as *"I-35W"* Bridge) (Fig. 1.1b).

(a) (b) (c)

Fig. 1.1 – Examples of structures subjected dynamic actions: *"Tacoma Narrows"* Bridge, Washington, USA, opened to public in July, 1940, and collapsed 4 months later (a), central span of the *"Rio-Niteroi"* Bridge, Rio de Janeiro, Brazil (b), and *"9340"* Bridge (also known as *"I-35W"* Bridge), Minneapolis, Minnesota, EUA, collapsed in 2007 (c).

Constructed over Mississippi River, in Minneapolis, Minnesota, USA, the structure was opened to traffic in 1967 and collapsed in 2007 in the middle of rush hour. Subsequent investigations

pointed to design flaws, fatigue and increase of the dead load over the years, as the main causes of the collapse (NTSB, 2008). Apart the from the serious accidents, several cases of abnormal behaviour compromising the comfort and serviceability of civil structures due to excessive vibrations are eventually reported. As an example, Fig. 1.1c shows the central span of the *"Rio-Niteroi"* Bridge, in Rio de Janeiro, Brazil. The occurrences of wind gusts with speeds not much higher than 55 km/h were enough for the authorities to interrupt traffic on the bridge due to the high oscillations of the central span that, in more extreme environmental conditions, came to reach 0.6 m (Battista and Pfeil, 2000).

In this context, vibration-based **SHM** has been increasingly used as a reliable tool, amongst other purposes, to reduce the risk of structural failure and prevent improper serviceability of civil engineering structures. One of main advantages of the vibration-based **SHM** with regard to the other health assessment techniques is the fact that it consists of a non-destructive and global approach. The idea behind this technique is that both local and global damage events can change the overall stiffness of the structures and the damage induced changes are, in turn, reflected in the global dynamic properties of the structure. Therefore, the variation of these properties over time can be used as indicators of the structural health condition of the monitored structures.

Thanks to its non-destructive characteristic, vibration-based **SHM** been widely applied in civil engineering to assess the structural performance under environmental conditions and detect damage over the time. In addition to all the aforementioned applications, there are several other circumstances in which vibration-based **SHM** may be required, as, for instance (Ross and Matthews, 1995):

(i) monitoring of the modifications to an existing structure;

(ii) monitoring the structures affected by external works;

(iii) monitoring during demolition;

(iv) monitoring of structures subject to long-term movement or degradation of materials;

(v) feedback loop to improve future design based on experience,

(vi) fatigue assessment;

(vii) novel systems of construction;

(viii) assessment of post-earthquake structural integrity;

(ix) decline in construction and growth in maintenance old structures; and

(x) the move towards performance-based design philosophy.

Apart from the broad range of applications, the benefits to be gained with the employment of

vibration-based monitoring systems to detect damage justifies the great interest demonstrated by the civil engineering community over the last years on this subject area. Furthermore, if a continuous vibration-based monitoring is employed, economic benefits can also be obtained with the reduction of the maintenance costs of the monitored structures, for example, by avoiding unnecessary inspection activities. The positive aspects related to vibration-based health monitoring allied to the encouraging results obtained with such approach have motivated several studies all over the world (Peeters, 2000; Döhler et al., 2014).

An extensive literature review about **SHM** is found in Ross and Matthews (1995), Doebling et al. (1996) and Sohn et al. (2004), and practical applications of long-term vibration-based **SHM** in the context of detect damage detection of civil structures are discussed, for instance, in Magalhães (2010), Hu et al. (2012) and Cunha et al. (2013). According to Rytter (1993), the damage state of a structure can be categorized in five levels according to the assessment needed to answer the following questions:

(1) Existence. Is there damage in the structure?

(2) Location. Where is the damage in the structure?

(3) Type. What kind of damage is present in the structure?

(4) Extent. How severe is the damage in the structure?

(5) Prognosis. What is remaining of life of the structure?

Practical applications of **SHM** have been reported worldwide. An emblematic example of continuously monitored structure is the *Tsing Ma* bridge, in Hong Kong, which was constructed in 1997 and came to be monitored by nearly 600 sensors (Fig. 1.2a) (Farrar et al., 1999). Another notorious example of monitored structure is the *Orensund* bridge, located between the cities of Copenhagen, Denmark and Malmo, Sweden (Fig. 1.2b) whose cables, deck and towers were continuously monitored by a total 22 tri-axial accelerometers. More recently, a vibration-based monitoring system was implemented in *Infante D. Henrique* bridge located between the cities of Vila Nova de Gaia and Porto, Portugal (Fig. 1.2c).

In operation since September, 2007, this dynamic monitoring system is basically composed by two digitizers and 12 force balance accelerometers, and is complemented by an independent static monitoring system that was installed in the bridge during its construction. This static monitoring system comprises strain gages, clinometers and temperature sensors embedded in the concrete. The measurements provided by the 8 temperature sensors of the static monitoring system, in combination with the data collected by means of the 12 force-balance accelerometers of the dynamic monitoring system, has allowed for the assessment of the influence of the environmental and operational conditions, as well as the structural health condition of the monitored

structure over the time (Magalhães, 2010).

Given the few amount of sensors generally used in continuous monitoring of civil engineering structures, damage assessment by means of the vibrational responses is normally based on level 1, which is suitable to detect the abnormal structural changes due to damage events and trigger further detailed investigations that may than demand higher levels of damage assessment. In the context of this thesis, only damage detection based on level is covered. The assessment of damage in the present work is basically carried out in two steps. In a first step, the modal parameters are identified within a reference time frame and subsequently used to stablish a statistical model for the monitored structure. Afterwards, based on this model, statistical hypothesis tests are carried out to judge whether the parameters identified out of the reference period can still be explained by the model derived with the reference parameters.

The main advantage of the method is that no new environmental model needs to be estimated as new data become available.

(a) (b) (c)

Fig. 1.2 – Examples of structures monitored by several sensors: *Tsing Ma* bridge, Hong Kong, constructed in 1997 (a), *Orisund* bridge located between the cities of Copenhagen, Denmark and Malmo, Sweden (b), and *Infante D. Henrique* Bridge, between the cities of Porto and Vila Nova de Gaia, Portugal (c).

Since the modal parameters are used as damage indicators, the output-only modal identification techniques play a fundamental role in vibration-based **SHM** and, therefore, they are extensively discussed in this thesis. In fact, damage detection based on the modal parameters is only feasible if accurate estimates of these parameters are tracked from the vibration responses acquired by the dynamic monitoring systems over the time. Thanks to the recent advances in **E**xperimental and **O**perational **M**odal **A**nalysis (**EMA** and **OMA**), more precise modal parameter estimates can be obtained, fact that contributed to the consolidation of the vibration-based monitoring as a reliable approach to detect damage. Amongst the main advances in the parametric modal identification techniques, are the development of stochastic subspace methods (Overchee and De-Moor, 1996; Peeters, 2000) in time-domain such as the **COV**ariance-driven **S**tochastic **S**ubspace **I**dentification (**SSI-COV**) and the **DATA**-driven **S**tochastic **S**ubspace **I**dentification

(**SSI-DATA**), as well as the frequency-domain methods **p**oly-reference **L**east-**S**quares **C**omplex **F**requency (**pLSCF**) (Guillaume et al., 2003; Peeters et al., 2007) and **M**aximum **L**ikelihood **E**stimator (**MLE**) (Schoukens and Pintelon, 1991; Guillaume, 1992; El-Kafafy, 2013).

Given the importance of the **M**odal **P**arameter **E**stimation (**MPE**) in the context of damage detection and **OMA**, this thesis also devotes an extensive discussion to the recent advances in input-output and output-only identification techniques, particularly to the **M**aximum **L**ikelihood (**ML**) based identification methods such as the **p**oly-reference **MLE** in **M**odal **M**odel formulation (**pMLE-MM**) and the **MLE** formulated in **C**ommon **D**enominator **M**odel (**MLE-CDM**), both used in **EMA** and **OMA** to track the modal parameters together with their uncertainties intervals.

1.2. Motivation, Main Objectives and Contributions of the Thesis

The challenges involved in the implementation of a robust vibration-based monitoring system to detect damage in civil structures, as well as the promising perspective of this approach are, amongst others reasons, the main motivations of the present work. One of the key steps to achieve this goal is the development of an automated monitoring application to process the acquired vibration raw data and extract conclusive results regarding the health condition of the monitored structures. Considerable efforts have been made towards the development of a robust, accurate, reliable and fully automated monitoring application. One of the most important tasks performed by such applications is the automated extraction of the modal properties from the vibration raw data continuously acquired over course of the monitoring period.

In this context, this thesis addresses three key issues of a real-life vibration-based continuous monitoring. The first is related to the estimation of the modal parameters of the monitored structures from output-only data together with their confidence intervals. Since the source of vibration of the monitored structures are mostly the unmeasurable ambient excitations, all estimates from the output responses are contaminated with disturbances of statistical nature which are, in turn, disseminated to the identified modal parameters. This disturbances occurs, amongst other reasons, due to finite data length, colored noise, non-stationary excitations, model order reduction or other operational influences. Hence the need to consider not only the modal parameter estimates, but also their quality in damage assessment of the monitored structures. Therefore, apart from discussing the strategies and techniques employed to automatically extract the dynamic properties, the techniques used to estimate the confidence bounds are also addressed and two approaches are proposed to estimate these uncertainties in the present work. This will be detailed elaborated in Chapter 3.

The second key issue involves the automation of the **MPE**. In fact, a successful assessment of

the health condition based on modal properties is only feasible if these parameters are automatically extracted from the vibration raw data acquired over the course of a continuous monitoring. Given the huge amount of datasets acquired over time, such task is required to be performed by automated applications capable of tracking, amongst other useful information, the modal parameters from these data. Once they are initially configured, it is expected that such applications are capable of extracting this information with no further intervention. In this work, an automated procedure to track the modal parameters from the vibration raw data is presented. This automated identification procedure is based on a new criteria to sort the physical modal parameters from the poles tracked by the **MPE** techniques discussed in Chapter 3 and is detailed described in Chapter 4.

Finally, the third key issue concerns the detection of damage under varying environmental conditions. In real-life applications structures are subjected to changes in such in conditions (e.g., temperature, humidity, wind, traffic, etc.). Therefore, if the modal parameter estimates are intended to be used as damage indicators, the variations induced by such conditions must be taken into account, otherwise they may mask the changes caused by structural damage. If such variations are not accounted in damage detection, false-positive or negative damage diagnosis may occur and, therefore, vibration-based health monitoring becomes inefficient or unreliable. In these conditions, environmental models can be applied to the estimated modal properties so that they can be used to diagnose damage. In this thesis, the techniques used to address this issue are also discussed in Chapter 4.

In synthesis, the original contributions of this work are the following:

- Some of the most widely used models of vibrating structure in **EMA** and **OMA** are reviewed in this thesis. From this review, it was shown the relations between the finite element models of structures that are excited by measured or unmeasured forces, and the models of vibrating structures commonly used in modal analysis: state-space model, modal model, left and right matrix fraction description models, and common-denominator model;
- Some of the most important state-of-the-art methods for the identification of deterministic and stochastic systems, are reviewed. The efficiency of these methods are discussed from a practical point of view by means of simulated and real-life examples;
- A novel non-linear parametric modal identification technique is proposed. This new approach consists of a single reference **MLE** formulated in (pole-residue) **M**odal **M**odel (**MLE-MM**). The efficiency of this novel identification method is assessed by means of a simulated **EMA** and the resulting estimates are compared to those identified with the

pMLE-MM;

- Derivation of an alternative in implementation of the **pMLE-MM**. One of the main advantage if this proposed approach with regard to its first implementation, is the possibility to estimate the confidence intervals for the modal parameter estimates without the need of explicit linearisation formulas;
- A novel strategy to estimate the confidence bounds on the modal parameters provided by the **SSI-DATA** and **SSI-COV** techniques. In such strategy, the modal parameters provided by both **SSI** methods are used as starting guess by the **pMLE-MM** in a second step of the identification process to: (1) estimate the confidence intervals of the estimated modal parameters and, optionally, (2) optimize these parameters in a non-linear least squares sense and provide the uncertainties of the optimized modal parameters;
- Development of a new algorithm to automatically interpret stabilization diagrams constructed with the parametric methods **SSI-DATA**, **SSI-COV** and **pLSCF**;
- Overview of the underlying theory of the methods commonly used to remove the influence of environmental and operational effects from the modal parameters with the aim of obtaining indicators of abnormal structural changes;
- Application of the combined **pLSCF-pMLE-MM**, **SSI-DATA-pMLE-MM** and **SSI-COV-pMLE-MM** to a multi-patch **OMA** aiming at tracking the modal parameters of a football stadium suspension roof, which was conducted in two steps. At first, the modal parameters together with their confidence intervals were tracked from each dataset to assess, on the one hand, the efficiency of these combined techniques and, on the other hand, the modes which were more exited by the environmental and operational conditions; and, finally, **MPE** with the combined **pLSCF-pMLE-MM** and **SSI-COV-pMLE-MM** using all datasets at once to yield the modal parameters with high spatial resolution for the mode shapes of vibration.
- Development of a dynamic monitoring software in Java® platform, called *VibMonitor*, that includes several subroutines developed to: (1) manage and pre-process the raw data files; (2) automatically track the modal parameters; (3) remove environmental and operational effects from the estimated modal parameters; and (4) automatically detect, resorting to control charts, structural changes in the monitored structures;
- Improvement of a **G**raphical **U**ser **I**nterface (**GUI**) for output-only modal analysis. Initially developed to estimate the modal parameters from a single dataset at time, this interface was extended to extract the modal parameters from multiple datasets at once by means of a single stabilization diagram;

- Development of a **GUI** Toolbox in Matlab® platform, called *VibMonitor Viewer*, which was developed in the framework of this thesis, amongst other purposes, to assist the analysts on handling and analysing the results obtained with the dynamic monitoring software *VibMonitor*.
- Finally, an extensive analysis of data from the continuous monitoring of tha Braga Stadium suspension roof is presented. This analysis is unique in that it combines data from a dynamic monitoring system and from a wind measurement system aiming at assessing the influence of the wind on the structural behaviour of the suspension roof. The analysis these data demonstrated that a slight permanent structural change in roof structure could successfully be detected under varying environmental conditions.

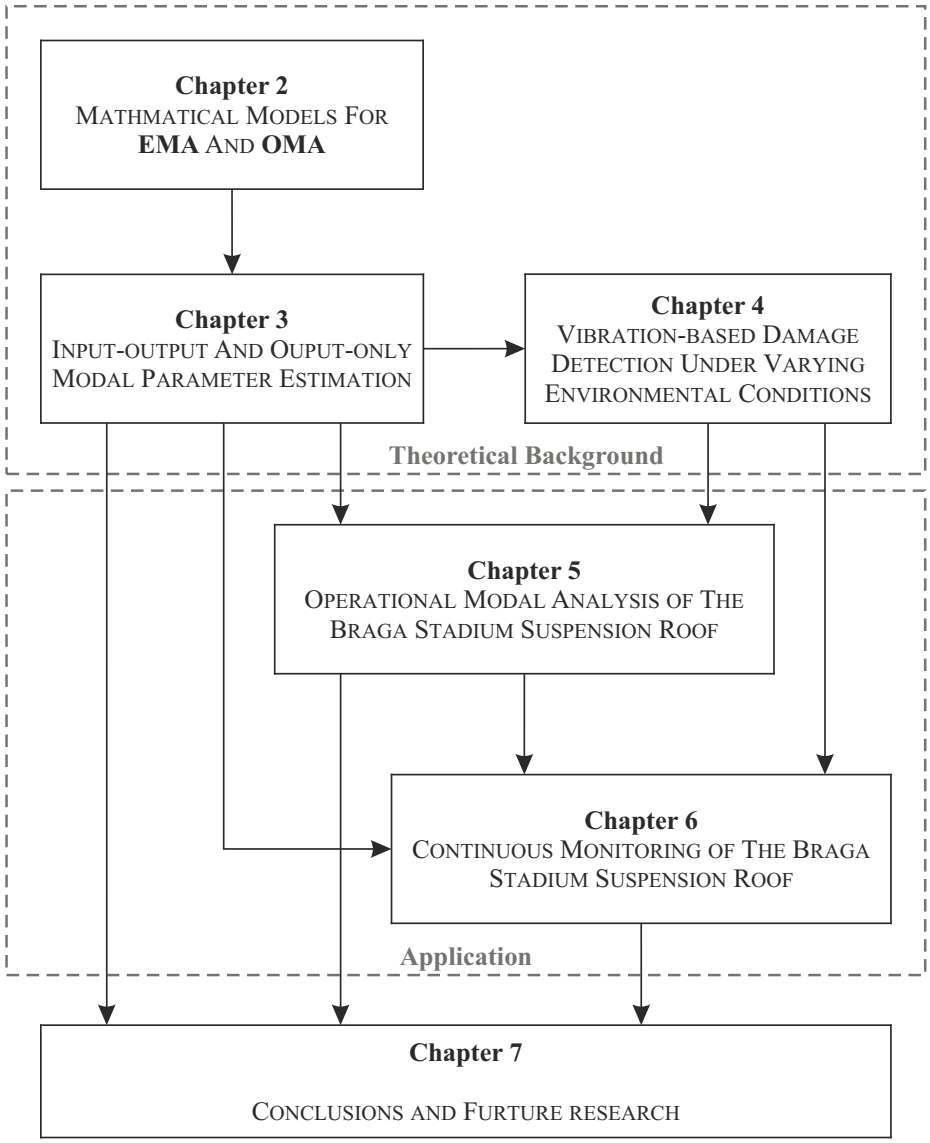

Fig. 1.3 – Organization of the text of the thesis. The first part addresses the theoretical background and second is devoted to the application of the theory to a real-life structure.

1.3. Organization of the Text

The organization of the chapters of this thesis is illustrated in Fig. 1.3 and a overview of each chapter is given in the following.

Chapter 1 introduces the thesis by contextualizing the research, highlighting the main contributions and illustrating the organization of the text.

Chapter 2 presents a review of the state-of-the-art of the mathematical models of vibrating structures. This chapter stablish connections between Finite Element Models of civil engineering, state-space models from electrical engineering and modal models developed in mechanical engineering. A simulation example is introduced that illustrates the application of the these models from a practical point of view.

Chapter 3 discusses the modal identification techniques used in the framework of this thesis. In this chapter, it is outlined the techniques and strategies implemented to track the modal properties together with their confidence intervals by means of the input-output and output-only identification techniques. Special emphasis is devoted in this chapter to the non-linear identification techniques based on frequency-domain maximum likelihood approach. To illustrate the application of theory from practical point of view, all methods are applied to simulated examples.

Chapter 4 addresses the three key issues involved in automated dynamic monitoring of civil structures under varying environmental and operational conditions: (1) the automated interpretation of stabilization diagrams to track the modal parameters together with their confidence intervals; (2) the statistical methods used to model and remove the environmental and operational effects from the estimated natural frequencies; and finally, (3) damage detection by making use of control charts.

Chapter 5 is essentially devoted to the application of the identification methods discussed in Chapter 3 to characterize the modal behaviour of a football Stadium Suspension Roof. This chapter is essentially divided into two parts. The first presents results of the modal analysis which was carried to assess the variation of the modal parameters, their corresponding uncertainty bounds, as well as the modal contributions over the different acquired datasets. Apart from this assessment, the first part also aims at demonstrating the efficiency of the combined methods **pLSCF-pMLE-MM**, **SSI-DATA-pMLE-MM** and **SSI-COV-pMLE-MM**, both on estimating the confidence intervals and on optimizing the modal parameters. The second part presents the results of the multi-patch **OMA** of the suspension roof. In this latest part, the combined techniques **pLSCF-pMLE-MM** and **SSI-COV-pMLE-MM** are applied to estimate the modal parameters of the roof structure with high spatial resolution for the mode shapes of

vibration.

Chapter 6 begins by describing the main characteristics of the two monitoring systems implemented to assess the influence of the environmental and operational conditions, as well as to detect damage in the roof structure. Next, an overview of the tools and applications developed to automatically track the modal properties of the suspension roof is also presented. Finally, the chapter ends by discussing the most relevant results acquired both monitoring systems.

Chapter 7 summarizes the main conclusions of this work and provides some suggestions for further research.

Chapter 2

MATHEMATICAL MODELS FOR EMA AND OMA

In this chapter, the models of vibrating structures suitable for **EMA** and **OMA** in time and frequency domain are discussed. The chapter is essentially divided into three parts: the first part addresses the time-domain models of vibrating structures; the second provides an overview of non-parametric pre-processing techniques commonly used in **EMA** and **OMA**; and finally, in the last part of the chapter, the frequency-domain model are discussed. Special attention is dedicated to the state space, common denominator and right fraction models as they are widely used in the framework of this thesis.

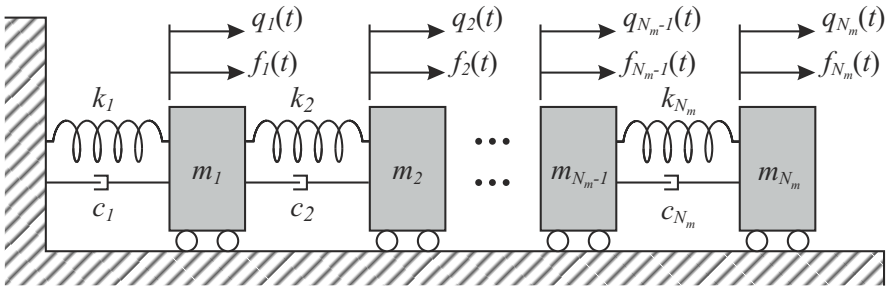

2.1. Introduction

Several mathematical models of vibrating structures are found in literature to describe the dynamic behaviour of structures. An interesting aspect about the these models is that they are based on three different approaches: the finite element model used to simulate the structural behaviour of civil engineering structures, the modal model originated in mechanical engineering, and the state-space models which is commonly used in electrical engineering. In fact, although these approaches address the vibration phenomenon from different point of views, it is verified that they are closely related among themselves. These models can be basically divided according to the domain of analysis (e.g. time and frequency-domain) and to the type of analysis, namely, **EMA** or **OMA**. Depending the relations they describe (e.g. analytical or experimental), they are also categorized either as continuous or discrete-time models.

In this chapter, some the main parametric mathematical models in time and frequency-domain used in **MPE** are discussed. The main purpose of the chapter is, on the one hand, to present an overview of the models used in modern modal analysis and, on the other hand, to introduce the notation used throughout the thesis.

2.2. Newton's Equation of Motion for Vibrating Structures

In general, for simplification purposes, real-life structures are assumed to be continuous and homogeneous elastic systems with an infinite number of **D**egrees **O**f **F**reedom (**DOF**) whose dynamic behaviour can be approximated by the models with multiple **DOF**s illustrated in Fig. 2.1. Theoretically, this approximation can be achieved by a system with finite **DOF**s, as many as necessary, to reach the desired accuracy.

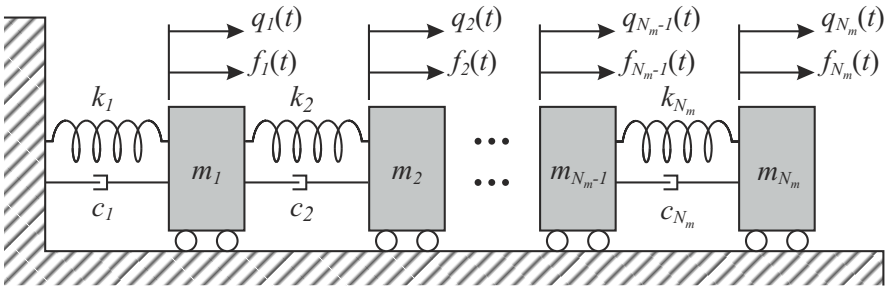

Fig. 2.1 – Mechanical system with multiple **DOF**s.

Normally, in practical applications (e.g. in civil and mechanical engineering), only a small subset of the structure's **DOF**s is necessary to characterize its dynamic behaviour. This characterization is performed by discretising the real structure into a representative mechanical system with N_m **DOF**s of Fig. 2.1 by means of the **F**inite **E**lement (**FE**) method so that the resulting system can the be described by the so-called Newton's equation of motion:

$$M\ddot{q}(t) + C_1\dot{q}(t) + Kq(t) = f(t) = F_1u(t) \tag{2.1}$$

where $f(t), q(t) \in \mathbb{R}^{N_m}$ are the input force and the output displacement vectors evaluated at time instant t, respectively; M, C_1 and $K \in \mathbb{R}^{N_m \times N_m}$ are, respectively, the mass, damping and stiffness matrices; $F_1 \in \mathbb{R}^{N_m \times N_i}$ is a mapping matrix with ones and zeros at appropriate positions to specify the **DOF**s at which the inputs are applied and $u(t) \in \mathbb{R}^{N_i}$ is a vector containing the N_i inputs. The derivation of the solution of Newton's equation of the motion (2.1) is classical and, therefore, can be found in several books as, for instance, Maia et al. (1998) and Ewins (1984). As the differential equation (2.1) is linear, its solution has the following form:

$$q(t) = q_h(t) + q_p(t) \tag{2.2}$$

with $q_p(t)$ denoting the particular or complementary solution and $q_h(t)$ the solution of the homogeneous form of eq. (2.1). The particular solution $q_p(t)$ depends on the force $f(t)$, and therefore, it is not possible to derive analytical solutions for eq. (2.1) for all input forces $f(t)$, nevertheless this equation can be analytically solved for few specific cases such as constant and harmonic forces. If the input forces are neglected, eq. (2.1) reduces to its homogeneous form which corresponds the so-called free vibration equation of motion. By solving this equation, important conclusions are drawn regarding the dynamic properties of the structures, specially if the specific cases of damping are taken into account as discussed in the following sections.

2.2.1. Undamped Vibration Models

In practice, it is known that real life structures dissipates energy when they vibrate and, therefore, the undamped models of vibrating structures are not considered realistic. Yet despite this fact, some important conclusions are drawn with regard to the general solution of the differential equation (2.1) if this damping hypothesis is considered. When damping is neglected, the homogeneous equation corresponding to (2.1) becomes:

$$M\ddot{q}(t) + Kq(t) = 0 \tag{2.3}$$

whose general solution is known to have the following form:

$$q(t) = \varphi e^{\lambda t} \tag{2.4}$$

with φ and λ denoting a displacement amplitude vector and a scalar constant, respectively.

Inserting eq. (2.4) into (2.3), the following eigenvalue problem is obtained:

$$(K+\lambda^2 M)\varphi = 0 \tag{2.5}$$

Adopting the non-trivial solution for eq. (2.5), $(-\lambda_i^2) \in \mathbb{R}$ and $\varphi_i \in \mathbb{R}^{N_m}$ ($\forall i = 1, 2, \cdots, N_m$) are found as any of the N_m real eigenvalues and eigenvectors, respectively. The eigenvalues $(-\lambda^2)$ can be expressed as:

$$\omega_{n_i}^2 = -\lambda_i^2 \quad \Leftrightarrow \quad \omega_{n_i} = j\lambda_i, \tag{2.6}$$

where $j = \sqrt{-1}$ denotes the imaginary unit and ω_{n_i} the eigenfrequency (in rad/s) corresponding to the i^{th} eigenvalue. The complete solution of the homogeneous differential equation (2.3) can be synthesized in matrix formulation, as:

$$\Omega^2 = \left[\backslash \omega_{n_i}^2 \backslash\right] = \begin{bmatrix} \omega_{n_1}^2 & 0 & \cdots & 0 \\ 0 & \omega_{n_2}^2 & \cdots & 0 \\ \vdots & \vdots & \ddots & \vdots \\ 0 & 0 & \cdots & \omega_{n_{N_m}}^2 \end{bmatrix} \in \mathbb{R}^{N_m \times N_m}, \quad \Phi = \begin{bmatrix} \varphi_1 & \varphi_2 & \cdots & \varphi_{N_m} \end{bmatrix} \in \mathbb{R}^{N_m \times N_m} \tag{2.7}$$

and the eigenvalue problem (2.5) can be reformulated in matrix notation, as:

$$(K+\Omega^2)\Phi = 0 \tag{2.8}$$

where Ω^2 and Φ are the matrices containing all the eigenvalues and eigenvectors corresponding to eq. (2.5). It is straightforward to prove that Φ is an orthogonal matrix and, by taking advantage of this particular property, the following relations are established (Maia et al., 1998):

$$\Phi^T M \Phi = \left[\backslash m_i \backslash\right], \quad \Phi^T K \Phi = \left[\backslash k_i \backslash\right] \tag{2.9}$$

$$\omega_{n_i} = \sqrt{\frac{k_i}{m_i}}$$

with $\left[\backslash m_i \backslash\right]$ and $\left[\backslash k_i \backslash\right]$ denoting the modal mass and the modal stiffness, respectively, and the operator $(\bullet)^T$ stands for the matrix transpose. A common practice in modal analysis is to modify

the scale of the eigenvectors Φ such that:

$$\Phi^T M \Phi = I_{N_m}, \quad \Phi^T K \Phi = \Omega^2 \tag{2.10}$$

where Φ is now a matrix containing the mass normalized eigenvectors in its columns and $I_{N_m} \in \mathbb{R}^{N_m \times N_m}$ is the identity matrix. It is worth noting that, in the context of modal analysis, the eigenvectors φ_i are physically interpreted as the deformed shapes associated to the vibration modes of the structure. Hence, these eigenvectors are commonly referenced as *mode shapes*. In the undamped case, in particular, as these eigenvectors are real, they are also referenced as *normal modal vectors*.

2.2.2. Proportional Damping Models

Since it is very difficult to quantify the distribution of the damping forces over system's **DOFs** in the same way as the mass and stiffness, it is not possible to stablish a closed formulation to computed the damping matrix C_1 in eq. (2.1). In order to overpass such difficulty, other simplified damping models can be developed to simulate the effects of these dissipative forces. These simplified damping models tend to privilege more the mathematical convenience than the physical representation. One of the main examples of these models is the proportional viscous damping, which assumes that the dissipative forces are distributed over the system's **DOFs** in the same way as the mass and stiffness. This hypothesis can be adopted to model the dynamic behaviour of most structures without significant loss of precision.

It considers that damping matrix is proportional to the stiffness or mass matrices, or is given as linear combination of the mass and stiffness matrices. In practice, a commonly used hypothesis in **FE** analysis to simulate and predict the dynamic behaviour of structural systems is known as the Rayleigh damping (Chopra, 1995). This hypothesis considers that the damping matrix C_1 in eq. (2.1) is given as a linear combination of the mass and stiffness matrices, as:

$$C_1 = \varepsilon K + \nu M \tag{2.11}$$

where ε and ν are two scalar constants that can be computed using the strategy found in Chopra (1995). The assumption proportional damping implies that Φ diagonalizes the damping matrix C_1 in the same way as the mass and stiffness matrices, as expressed in (2.9). Taking into account this assumption and the definition of modal damping ratio $\xi_{n_i} = c_i/2m_i\omega_{n_i}$, the following relations are easily derived:

$$\Phi^T C_1 \Phi = \left[\backslash c_i \backslash \right] = \left[\backslash 2\xi_{n_i} \omega_{n_i} m_i \backslash \right] = \Gamma \left[\backslash m_i \backslash \right] \tag{2.12}$$

with

$$\Gamma = \left[\backslash 2\xi_{n_i} \omega_{n_i} \backslash \right] \tag{2.13}$$

By Adopting the assumption of proportional damping, it is straightforward to derive a solution for the free vibration model associated to eq. (2.1) in the same basins as for the undamped case presented in Section 2.2.1. This derivation starts by solving the homogeneous form of eq. (2.1):

$$M\ddot{q}(t) + C_1 \dot{q}(t) + Kq(t) = 0 \tag{2.14}$$

Since eq. (2.14) is satisfied for each eigenvector and its corresponding eigenvalue, it can be rewritten as:

$$\left(\lambda_i^2 M + \lambda_i C_1 + K\right) \varphi_i = 0 \tag{2.15}$$

Pre-multiplying eq. (2.15) by φ_i^T, yields

$$\lambda_i^2 \varphi_i^T M \varphi_i + \lambda_i \varphi_i^T C_1 \varphi_i + \varphi_i^T K \varphi_i = 0 \tag{2.16}$$

Taking into account the orthogonality properties of the eigenvectors φ_i and the definition of proportional damping (2.12), eq. (2.16) becomes:

$$\lambda_i^2 m_i + \lambda_i c_i + k_i = 0 \tag{2.17}$$

whose corresponding solution is given by:

$$\lambda_i, \lambda_i^* = -\xi_{n_i} \omega_{n_i} \pm j\sqrt{1 - \xi_{n_i}^2}\,\omega_{n_i}, \quad i = 1, 2, \cdots, N_m \tag{2.18}$$

where the operator $(\bullet)^*$ denotes complex conjugate.

2.2.3. General Viscous Damping Models

In several cases where the damping is low as, for instance, in case of civil engineering structures, it is possible to consider the assumption of proportional damping discussed in Section 2.2.2 to

estimate the damping matrix and, therefore, to model the dynamic behaviour of these structural systems without a significant loss in accuracy. However, when dealing with highly damped systems or systems with localized dampers, another damping model needs to be considered. The first step towards the derivation of such model consists of solving the equation of motion (2.1), whose homogeneous solution has the following form:

$$q_h(t) = \theta e^{\lambda t} \tag{2.19}$$

The parameters λ and θ denote, in this context, a constant and vector of displacement amplitudes, respectively. A convenient way to solve the homogeneous differential equation (2.14) consists of rewriting such equation into a first order differential equation. By taking into account the trivial equation $\dot{q}(t) = \dot{q}(t)$, eq. (2.14) can be rewritten as:

$$U\dot{x}(t) + Wx(t) = 0 \tag{2.20}$$

with

$$x(t) = \begin{bmatrix} q(t) \\ \dot{q}(t) \end{bmatrix}, \quad U = \begin{bmatrix} C_1 & M \\ M & 0 \end{bmatrix} \quad W = \begin{bmatrix} K & 0 \\ 0 & -M \end{bmatrix} \tag{2.21}$$

where $x(t) \in \mathbb{R}^{n\times 1}$ is known as the *state vector* evaluated at time t, and $U \in \mathbb{R}^{n\times n}$ and $W \in \mathbb{R}^{n\times n}$ are symmetric matrices, with $n = 2N_m$. Since eq. (2.20) is a system of first order linear and homogeneous differential equations with constant matrix coefficients, the solution of such equation is given by the following expression:

$$x_h(t) = \psi e^{\lambda t} \tag{2.22}$$

Such expression is composed by a complex constant λ and a complex vector ψ which represents the possible solutions of the homogeneous equation (2.20). By substituting eq. (2.22) into (2.20), the following complex generalized eigenvalue problem is obtained:

$$(U\lambda + W)\psi = 0 \tag{2.23}$$

whose corresponding non-trivial solution is given by:

$$\psi_i = \begin{bmatrix} \theta_i \\ \theta_i \lambda_i \end{bmatrix}, \quad \psi_i^* = \begin{bmatrix} \theta_i^* \\ \theta_i^* \lambda_i^* \end{bmatrix} \tag{2.24}$$

where $\psi_i \in \mathbb{C}^{n\times 1}$ are the eigenvectors of the linear homogeneous equation (2.20), $\theta_i \in \mathbb{C}^{N_m \times 1}$ the eigenvectors related to the second order homogeneous equation (2.14) and λ_i the corresponding eigenvalues. Similarly to the proportional damping models, these eigenvalues are given by following expression:

$$\lambda_i, \lambda_i^* = -\xi_{n_i}\omega_{n_i} \pm j\sqrt{1-\xi_{n_i}^2}\omega_{n_i}, \quad i = 1, 2, \cdots, N_m. \tag{2.25}$$

All the n eigenvalue problems (2.23) can be formulated into matrix notation, as:

$$(U\Lambda + W)\Psi = 0 \tag{2.26}$$

with

$$\begin{aligned} \Lambda_c &= \begin{bmatrix} \Lambda & 0 \\ 0 & \Lambda^* \end{bmatrix}, \\ \Psi &= \begin{bmatrix} \psi_1 & \psi_2 & \cdots & \psi_{N_m} & \psi_1^* & \psi_2^* & \cdots & \psi_{N_m}^* \end{bmatrix} = \begin{bmatrix} \Theta & \Theta^* \\ \Theta\Lambda & \Theta^*\Lambda^* \end{bmatrix} \end{aligned} \tag{2.27}$$

$$\Lambda = \begin{bmatrix} \backslash \lambda_i \backslash \end{bmatrix}, \quad \Theta = \begin{bmatrix} \theta_1 & \theta_2 & \cdots & \theta_{N_m} \end{bmatrix} \tag{2.28}$$

Given the orthogonality property of Ψ, it is straightforward to prove that

$$\Psi U \Psi^T = \begin{bmatrix} \backslash a_i \backslash \end{bmatrix}, \quad \Psi W \Psi^T = \begin{bmatrix} \backslash b_i \backslash \end{bmatrix} \tag{2.29}$$

and also that

$$\Lambda_c = -\begin{bmatrix} \backslash b_i \backslash \end{bmatrix}^{-1} \begin{bmatrix} \backslash a_i \backslash \end{bmatrix} \tag{2.30}$$

where the diagonal matrices $\begin{bmatrix} \backslash a_i \backslash \end{bmatrix}$ and $\begin{bmatrix} \backslash b_i \backslash \end{bmatrix}$ are known, respectively, as the *modal matrix a* and *modal matrix b*.

Example 1
In order to present the theory from a practical point of view, an example is introduced to

illustrate the application of the models and techniques discussed throughout Chapters 2, 3 and 4. The example consists of a lattice tower structure constituted by two segments of equal height and by variable equilateral triangular sections. The lower section is scaled with regard to the upper one by a factor of 2. The finite element model of the tower structure is illustrated in Fig. 2.2.

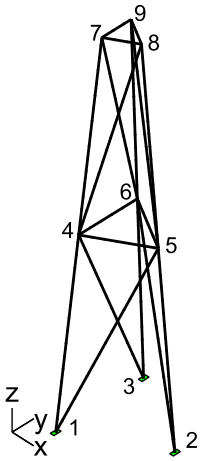

Fig. 2.2 – Finite element model of the tower example used in the simulated analysis.

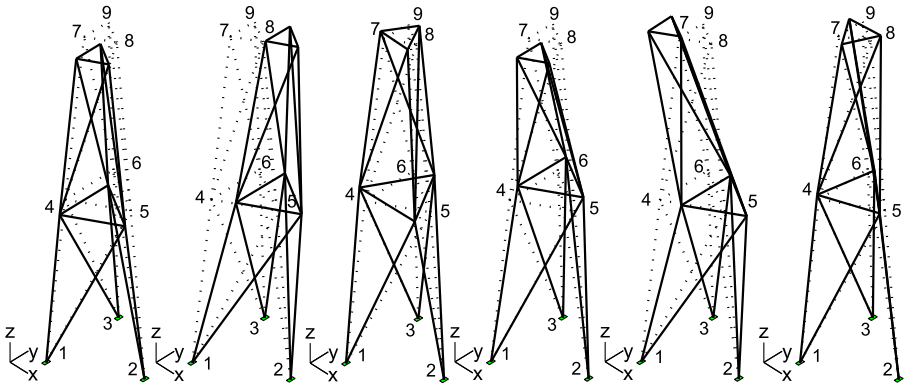

Fig. 2.3 – First six modes shapes of the tower structure: 1st bend mode in Y direction (BY1) (a), 1st bend mode in X direction (BX1) (b), 1st torsion mode (T1) (c), 2nd bend mode in Y direction (BY2) (d), 2st bend mode in X direction (BX2) (e) and 2nd torsion mode (T2) (f).

Tab. 2.1 – Modes of the **FE** model of the lattice structure.

Mode	Type	f_{n_i} (Hz)	ξ_{n_i} (%)
1	1st bending mode in Y direction (BY1)	1.2869	1.0
2	1st bending mode in X direction (BX1)	1.2937	1.0
3	1st torsional mode (T1)	2.2251	1.0
4	2nd bending mode in Y direction (BY2)	3.8713	1.0
5	2nd bending mode in X direction (BX2)	3.8932	1.0
6	2nd torsional mode (T2)	6.1745	1.0

This model is composed by beam elements with 6 **DOF**s per node. The nodes of the foundations are clamped and the others have 3 **DOF**s: two translations in x and y, and one rotation

around z-axis; and the remaining **DOF**s are set equal to zero. These settings result in a **FE** model with a total of $N_m = 18$ **DOF**s. The symmetry of the structure was slightly broken by defining different geometry and materials to the column elements in order to simulate the behaviour of tower-like structures, which normally present very close spaced of bending modes. Once the mass and stiffness matrices, M and K, of the simulated structure have been found, the eigenfrequencies $f_{n_i} = \omega_{n_i}/2\pi$ and the corresponding mode shapes φ_i are computed by solving the generalized eigenvalue problem (2.8).

The first 6 modal configurations and the corresponding modal parameters of the **FE** model of the lattice tower are presented in Fig. 2.3 and Tab. 2.1, respectively. The structural damping, on the other hand, is modelled as the special case of proportional damping (discussed in Section 2.2.2) by setting the damping coefficients of all modes equal to 1%.

2.3. Continuous-Time State-Space Models

As shown in Section 2.2.3, the solution of the homogeneous form of the equation of the motion (2.14) is easily derived when this equation is rewritten into a state equation. This approach is commonly used in control theory and can be extended to model other phenomena of different subject areas whose input-output relationship are synthesized by Fig. 2.4 and governed by first-order differential equations. In mechanical and civil engineering, in particular, the state-space models has also been used to model the dynamic behaviour of structural systems, amongst other phenomena. In fact, a state-space representation of the dynamic system with N_i inputs, $u_i(t)$, and N_o outputs, $y_o(t)$, illustrated in Fig. 2.4 comprises two sets of equations, namely, the so-called *state* and *observation* equations.

The derivation of such equations is rather classical and is found, for instance, in Maia et al. (1998), Peeters (2000) and Cauberghe (2004), and is also discussed in the following sections to introduce the notation used by the system identification techniques presented in Chapter 2.

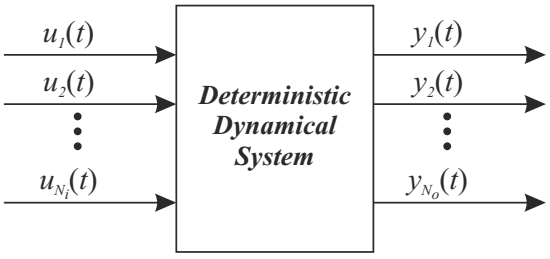

Fig. 2.4 – Deterministic dynamical system with N_i inputs, $u(t)$, and N_o outputs, $y(t)$.

2.3.1. The State Equation

The set of *state equations* is obtained by reformulating the second order differential equation (2.1) into a first order form. Considering the trivial relationship $\dot{q}(t) = \dot{q}(t)$, eq. (2.1) is easily reformulated as:

$$\begin{bmatrix} \dot{q}(t) \\ \ddot{q}(t) \end{bmatrix} = \begin{bmatrix} 0_{N_m} & I_{N_m} \\ -M^{-1}K & -M^{-1}C \end{bmatrix} \begin{bmatrix} q(t) \\ \dot{q}(t) \end{bmatrix} + \begin{bmatrix} 0_{N_m} \\ M^{-1}F_1 \end{bmatrix} u(t) \tag{2.31}$$

or, in a more synthetic form, as:

$$\dot{x}(t) = A_c x(t) + B_c u(t) \tag{2.32}$$

with

$$x(t) = \begin{bmatrix} \dot{q}(t) \\ \ddot{q}(t) \end{bmatrix} \in \mathbb{R}^{n\times 1}, \quad A_c = \begin{bmatrix} 0_{N_m} & I_{N_m} \\ -M^{-1}K & -M^{-1}C_1 \end{bmatrix} \in \mathbb{R}^{n\times n}, \quad B_c = \begin{bmatrix} 0_{N_m} \\ M^{-1}F_1 \end{bmatrix} \in \mathbb{R}^{n\times N_m} \tag{2.33}$$

where $A_c \in \mathbb{R}^{n\times n}$ is known as the *state matrix* and $B_c \in \mathbb{R}^{n\times n}$ as the *input matrix*. Comparing eq. (2.33) to (2.20), yields:

$$A_c = -U^{-1}W \tag{2.34}$$

Isolating matrices U and W in eqs. (2.29), and inserting them into eq. (2.34) leads to the following eigenvalue problem:

$$A_c\Psi = \Psi\Lambda_c \tag{2.35}$$

2.3.2. The Observation Equation

In practice, the number of **DOF**s measured in an experimental or operational modal analysis is limited by the amount sensors available, which is generally well bellow the structure's **DOF**s. Therefore, only the responses of a small subset of these **DOF**s are measured. Moreover, the output responses can be simultaneously measured at the same locations by displacement, velocity (laser vibrometer) and acceleration sensors. Therefore, another equation needs to be formulated in order to take into account these practical aspects. This equation is known as the *observation equation* and is expressed by:

$$y(t) = C_a\ddot{q}(t) + C_v\dot{q}(t) + C_d q(t) \tag{2.36}$$

where $y \in \mathbb{R}^{N_o\times 1}$ are the measured output responses; $C_a, C_v, C_d \in \mathbb{R}^{N_o\times N_m}$ are the output loca-

tion matrices for acceleration, velocity and displacement, respectively. The observation equation (2.36) can also be reformulated into a first order differential equation by using eq. (2.1) to eliminate $\ddot{q}(t)$ in combination with the definition of the *state vector* as in eq. (2.21). Such reformulation yields:

$$y(t) = C_c x(t) + D_c u(t) \tag{2.37}$$

with

$$C_c = \begin{bmatrix} C_d - C_a M^{-1} K & C_v - C_a M^{-1} C_1 \end{bmatrix} \tag{2.38}$$

and

$$D_c = C_a M^{-1} F_1 \tag{2.39}$$

where $C_c \in \mathbb{R}^{N_o \times n}$ and $D_c \in \mathbb{R}^{N_o \times N_i}$ are known as the *output matrix* and the *direct transmission matrix*, respectively.

2.3.3. The State-Space Equation

Combining the state equation (2.32) with the observation equation (2.37), yields:

$$\begin{aligned} \dot{x}(t) &= A_c x(t) + B_c u(t) \\ y(t) &= C_c x(t) + D_c u(t) \end{aligned} \tag{2.40}$$

which corresponds to the classical deterministic continuous-time estate-space model of a vibrating structure. Differently from the model represented by the equation of motion (2.1) whose order is defined by number of **DOF**s N_m, the order of the state-space models is given by the dimension of the state-vector $x(t)$ which is $n = 2N_m$. The advantages of the state-space models (2.40) with regard to the vibration model (2.1) include the possibility to compute the outputs $y(t)$ of the dynamic system due to the inputs $u(t)$, as well as to transform the scale of the state vector $x(t)$, such that

$$x(t) = T z(t) \tag{2.41}$$

where $T \in \mathbb{C}^{n \times n}$ is a non-singular complex square matrix. This operation is called *similarity transformation* and its application results in the following state-space model:

$$\begin{aligned} \dot{z}(t) &= A_s z(t) + B_s u(t) \\ y(t) &= C_s z(t) + D_s u(t) \end{aligned} \tag{2.42}$$

with

$$\begin{aligned} A_s &= T^{-1} A_c T \\ B_s &= T^{-1} B_c \\ C_s &= C_c T \\ D_s &= D_c \end{aligned} \tag{2.43}$$

An important property of the *similarity transformation* (2.41) is that, although the matrix coefficients A_s, B_s, C_s and D_s, and the state-vector $z(t)$ define another state-space model, the input-output relationships remains unchanged. It is also worth mentioning that, differently from the unscaled state vector $x(t)$, $z(t)$ has not the physical meaning of displacements and velocities.

2.3.4. Modal Parameters of a Continuous-Time State-Space Model

A special similarity transformation is obtained by substituting T by Ψ in eq. (2.42) and inserting the modal decomposition of A_c (2.35) in this equation. This similarity transformation yields the so-called *modal state-space model*, given as follows:

$$\begin{aligned} \dot{x}_m(t) &= \Lambda_c x_m(t) + L^T u(t) \\ y(t) &= V x_m(t) + D_c u(t) \end{aligned} \tag{2.44}$$

where $x_m(t) \in \mathbb{C}^{n\times 1}$ is the modal state vector. The matrices L^T and V are known as the modal input matrix and the modal output matrix, respectively, and are computed as:

$$\begin{aligned} L^T &= \Psi^{-1} B_c \\ V &= C_c \Psi \end{aligned} \tag{2.45}$$

These matrices are assumed to have, respectively, the following structures:

$$\begin{aligned} L^T &= \begin{bmatrix} l_1^T & l_2^T & \cdots & l_{N_m}^T \end{bmatrix} \\ V &= \begin{bmatrix} v_1 & v_2 & \cdots & v_{N_m} \end{bmatrix} \end{aligned} \tag{2.46}$$

with $l_i \in \mathbb{C}^{1\times N_i}$ denoting the modal participation vector and $v_i \in \mathbb{C}^{N_o\times 1}$ the observed mode shape vector, both corresponding to the i^{th} vibration mode. The matrices L^T, V and Λ_c correspond to

the modal parameters of the state-space models. From definitions of U, B_c and Ψ, (2.21), (2.33) and (2.27) and taking into account the orthogonality condition of U (2.29), the modal input matrix L^T can be written as:

$$L^T = \left[\backslash b_i \backslash\right]^{-1} \begin{bmatrix} \Theta^T \\ \Theta^H \end{bmatrix} \tag{2.47}$$

where the operator $(\bullet)^H$ denotes the complex conjugate transpose (Hermitian) of a matrix. The output matrix V, on the other hand, can also be expressed as a function of the complex eigenvector Θ. Inserting Ψ (2.27) and C_c (2.38) into the definition of V (2.45), the following relations obtained:

$$V = C_c\Psi = \begin{bmatrix} C_d - C_a M^{-1}K & C_v - C_a M^{-1}C_1 \end{bmatrix} \begin{bmatrix} \Theta & \Theta^* \\ \Theta\Lambda & \Theta^*\Lambda^* \end{bmatrix} \tag{2.48}$$

If the responses are measured either by displacement, velocity or acceleration sensors at a time, the matrix containing the observed mode shapes, V, is computed, respectively, as:

$$V = C_d \begin{pmatrix} \Theta & \Theta^* \end{pmatrix} \tag{2.49}$$

$$V = C_d \begin{pmatrix} \Theta\Lambda & \Theta^*\Lambda^* \end{pmatrix} \tag{2.50}$$

$$V = C_d \begin{pmatrix} \Theta\Lambda^2 & \Theta^*\Lambda^{*2} \end{pmatrix} \tag{2.51}$$

An important characteristic of the modal parameters L^T, V and Λ_c is that they are insensitive to changes of scale the state vector, which implies that, whatever the transformation matrix is chosen to apply the similarity transformation (2.41), the scales of these modal parameters are not affected (Peeters, 2000).

Modal Decomposition and Modal Responses

Due to the diagonal structure of the eigenvalue matrix Λ_c, the modal state-space model (2.44) can be reformulated such that the total response y_k can be split into contributions due to the modes. The following reformulation is only valid if the outputs are measured in acceleration. If such quantity is measured, the direct transmission matrix D_c can be written as:

$$D_c = C_c A_c^{-1} B_c \tag{2.52}$$

This expression is found by means of the definitions of the state-space matrices as in eqs. (2.33), (2.38) and (2.38). By inserting the eigenvalue decomposition of A_c (2.35) and eqs. (2.45) into (2.52), the following decomposition is obtained:

$$D_c = V \Lambda_c^{-1} L^T = \sum_{i=1}^{n} \frac{1}{\lambda_i} v_i l_i^T \tag{2.53}$$

By inserting the modal decomposition (2.53) into the modal state-space model (2.44), the output vector $y(t)$ can be written as a sum of the n modal contributions $y_i(t)$, as follows:

$$y(t) = \sum_{i=1}^{n} y_i(t) \tag{2.54}$$

where $y_i(t) \in \mathbb{R}^{n \times 1}$ is a vector containing the output response due to the i^{th} vibration mode and is computed by using the following order-one state-space model:

$$\begin{aligned} \dot{x}_m^{(i)}(t) &= \lambda_i x_m^{(i)}(t) + l_i^T u(t) \\ y_i(t) &= v_i x_m^{(i)}(t) + \frac{1}{\lambda_i} v_i l_i^T u(t) \end{aligned} \tag{2.55}$$

with the complex scalar $x_m^{(i)}(t)$ standing for the i^{th} component of the modal state vector $x_m(t)$.

Normal Mode State-Space Models

The normal mode state-space models are based on the proportional damping vibration models and are a particular case of the general viscous damping. As discussed in Section 2.2.2, the assumption of proportional damping implies in a mathematical simplification such that mode shapes are real or have at least a constant phase angle that can be rescaled to real ones. The transformation of the state-space model (2.40) into a normal mode form starts by applying the following similarity transformation:

$$x(t) = T_n z(t) \tag{2.56}$$

where the transformation matrix T_n is given by:

$$T_n = \begin{bmatrix} \Phi & 0 \\ 0 & \Phi \end{bmatrix} \tag{2.57}$$

and state-space vector $z(t)$ is given as a combination of the modal displacements and velocities:

$$z(t) = \begin{bmatrix} q_m(t) \\ \dot{q}_m(t) \end{bmatrix} \tag{2.58}$$

The parameter $q_m(t) = \Phi^T q(t) \in \mathbb{R}^{N_m \times 1}$ in eq. (2.58) is vector containing the modal displacements. By applying the similarity transformation (2.56), the following normal mode state-space model is obtained:

$$\begin{aligned} \dot{z}(t) &= A_n z(t) + B_n u(t) \\ y(t) &= C_n z(t) + D_n u(t). \end{aligned} \tag{2.59}$$

where the normal mode state-space matrices A_n, B_n, C_n and D_n are computed as follows:

$$\begin{aligned} A_n &= T_n^{-1} A_c T_n = \begin{bmatrix} 0 & I \\ -\Omega^2 & -\Gamma \end{bmatrix} & B_n &= T_n^{-1} \begin{pmatrix} 0 \\ \left[\backslash 1/m_i \backslash \right] \Phi^T F_1 \end{pmatrix} \\ C_n &= C_c T_n = \begin{pmatrix} C_d \Phi - C_a \Phi \Omega^2 & C_v \Phi - C_a \Phi \Gamma \end{pmatrix} & D_n &= D_c = C_a \Phi \left[\backslash 1/m_i \backslash \right] \Phi^T F_1 \end{aligned} \tag{2.60}$$

Model Reduction in Continuous Time

One of the main advantages of the normal mode state-space models is that they can be easily reduced by selecting only the first relevant modes. Assuming N_r as the number of relevant modes to be selected from the full model containing n vibration modes, a reduced model is obtained by evaluating matrices Ω, Γ, $\left[\backslash 1/m_i \backslash \right]$ and Φ, as follows:

$$\Omega_r = \left[\backslash \omega_{n_i}{}^2 \backslash \right], \quad \left[\Gamma_r = \backslash 2\xi_{n_i}\omega_{n_i} \backslash \right], \quad \left[\backslash 1/m_i \backslash \right], \quad \Phi_r = (\cdots \varphi_i \cdots), \quad i = 1, 2, \cdots, N_r$$

Once these matrices are computed, a reduced state-space model can be obtained by eliminating the non-relevant modes from the full model (2.44) (Peeters, 2000). The reduced state-space model is given by:

$$\begin{aligned} \dot{x}_r(t) &= \Lambda_{c_r} x_r(t) + L_r^T u(t) \\ y(t) &= V_r x_r(t) + D_{c_r} u(t). \end{aligned} \tag{2.61}$$

where Λ_{c_r}, V_r and L_r are matrices containing only the eigenvalues, observed mode shapes and the operational factors of the relevant modes, and D_{c_r} is the reduced direct transmission matrix, which is obtained by making use of the following modal decomposition:

$$D_{c_r} = V_r \Lambda_{c_r}^{-1} L_r^T \tag{2.62}$$

This expression follows from the elimination of the states corresponding to the non-relevant modes from the normal mode state-space models (2.59) and its derivation is detailed elaborated in Peeters (2000).

2.4. Discrete-Time State-Space Models

Although the continuous-time state-space models discussed in Section 2.36 can theoretically be used to model the dynamic behaviour of the structural systems, in practice, in experimental modal analysis, the input and output measurements are collected in discrete rather than in continuous time. Therefore, in order to address these practical aspects, the continuous state-space models (2.40) need to be reformulated in discrete time. Such reformulation can be derived by considering the **Z**ero **O**rder **H**old (**ZOH**) assumption, which means that the continuous time signal is piecewise constant over a certain fixed sampling period Δt. If this assumption is adopted, the continuous-time state-space equation can be solved at all discrete time instants $t = k\Delta t$ ($\forall k \in \mathbb{N}$ and $\forall t \in [t_k, t_{k+1}[$) and the following discrete state-space model is obtained:

$$\begin{aligned} x_{k+1} &= Ax_k + Bu_k \\ y_k &= Cx_k + Du_k. \end{aligned} \tag{2.63}$$

where $x_k = x(k\Delta t) = \left(q(k\Delta t)^T \ \dot{q}(k\Delta t)^T\right)^T = (q_k^T \ \dot{q}_k^T)^T$ is the *discrete-time state vector* containing the velocity and displacement vectors sampled in discrete-time, A the *discrete state matrix*, B the *discrete input matrix*, C the discrete output matrix, D the *direct transmission matrix*, and u_k and y_k are, respectively, the *discrete input vector* and the *discrete output vector*. The relations between the discrete state-space matrix coefficients A, C, B and D and their corresponding coefficients of the continuous-time state-space models are given by (Juang, 1996; Glad and Ljung, 2000):

$$A = e^{A_c \Delta t}, \quad B = \int_0^{\Delta t} e^{A_c \tau} d\tau, \quad B = (A - I) A_c^{-1} B_c, \quad C = C_c, \quad D = D_c \tag{2.64}$$

2.4.1. Modal Parameters of a Discrete-Time State-Space Model

The modal parameters of a discrete state-space model is derived from continuous-time state-space model. By inserting the eigenvalue decomposition of the continuous estate matrix A_c (2.35) into eq. (2.64) and expanding the matrix exponential function into a *Taylor* series, the following relations are obtained:

$$A = e^{A_c \Delta t} = e^{\Psi \Lambda_c \Psi^{-1} \Delta t} = \Psi \Lambda_d \Psi^{-1} \tag{2.65}$$

where Λ_d is the discrete eigenvalue matrix, which is given by:

$$\Lambda_d = \left[\backslash \mu_i \backslash \right] \tag{2.66}$$

with

$$\mu_i = e^{\lambda_i \Delta t} \;\Leftrightarrow\; \lambda_i = \frac{\ln(\mu_i)}{\Delta t} \tag{2.67}$$

Similarly to the continuous-time state-space models, the discrete modal participation matrix L_d^T and the discrete observed mode shapes V_d are computed as:

$$\begin{aligned} L_d^T &= \Psi^{-1} B \\ V_d &= C\Psi = C_c \Psi = V \end{aligned} \tag{2.68}$$

where L_d matrix is assumed to have a structure similar to that of L (2.46).

Modal Decomposition and Modal Responses

Similarly to the continuous-time state-space models, if the outputs are measured in acceleration, the modal decomposition of D is given as follows:

$$D = D_c = V \Lambda_c^{-1} L^T = V_d (\Lambda_d - I)^{-1} L_d^T = \sum_{i=1}^{n} \frac{1}{\mu_i - 1} v_{d_i} l_{d_i}^T \tag{2.69}$$

This expressions are found by using eqs. (2.64), (2.55), (2.45), (2.68) and (2.65). By making use of the modal decomposition of D matrix (2.69), the total output vector can be split into n modal contributions y_{k_i}. Similarly to the continuous-time state-space models, y_{k_i} is a vector

containing the output response due to the i^{th} vibration mode and is computed by using the following order-one discrete state-space model:

$$\begin{aligned} x_{m_{k+1}}^{(i)} &= \lambda_i x_{m_k}^{(i)} + l_{d_i}^T u_k \\ y_{k_i} &= v_{d_i} x_{m_k}^{(i)} + \frac{1}{\lambda_i} v_{d_i} l_{d_i}^T u_k \end{aligned} \tag{2.70}$$

where v_{d_i} is the i^{th} column of the observed mode shapes matrix V_d, $l_{d_i}^T$ the i^{th} row of the operational factor matrix L_d^T and the complex scalar $x_{m_k}^{(i)}$ stands for the i^{th} element of the modal state vector x_{m_k}.

Model Reduction in Discrete Time

A reduced model for the discrete-time state-space models can be obtained by following the same strategy applied for its continuous-time counterpart (see Section 2.3.3). By adopting a similar procedure, it is straightforward to derive the following reduced model:

$$\begin{aligned} \dot{x}_{k_r} &= \Lambda_{d_r} x_{k_r} + L_{d_r}^T u_k \\ y_k &= V_{d_r} x_{k_r} + D_r u_k. \end{aligned} \tag{2.71}$$

Similarly to the continuous-time state-space models, the reduced modal parameters Λ_{d_r}, V_{d_r} and L_{d_r} contain only the eigenvalues, observed mode shapes and the operational factors of the relevant modes. D_r is computed in a manner similar to that of eq. (2.62).

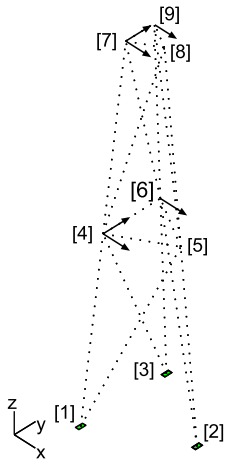

Fig. 2.5 – Sensors and measured directions.

Example 2

The **FE** model of the lattice tower illustrated in Fig. 2.2 and defined by the mass, stiffness and damping matrices M, K and C_1 is transformed into a normal mode state-space model discussed in Section 2.2.3. The structure is excited at all **DOF**s in both x and y-direction, independently, with white noise inputs. The simulated responses are measured in acceleration

at 6 **DOF**s as indicated in Fig. 2.5. By assuming that the two triangular sections behave as rigid diaphragms, the measured outputs are enough to yield the deformed configurations of the structure. The state matrices A_n, B_n, C_n and D_n can be computed using only the first six modes with eqs. (2.60). Assuming a sampling period of $\Delta t = 0.01$ s ($f_s = 100$ Hz) and **ZOH** on the inputs, these matrices are transformed into discrete state-space matrices A, B, C and D by means of eqs. (2.64). Once the discrete state-space matrices are computed, the modal contributions, y_{k_i}, can be computed using the one-order discrete state-space model (2.70). The output responses of the first 6 modes measured at node 4 in x-axis direction are shown in fig. 2.6.

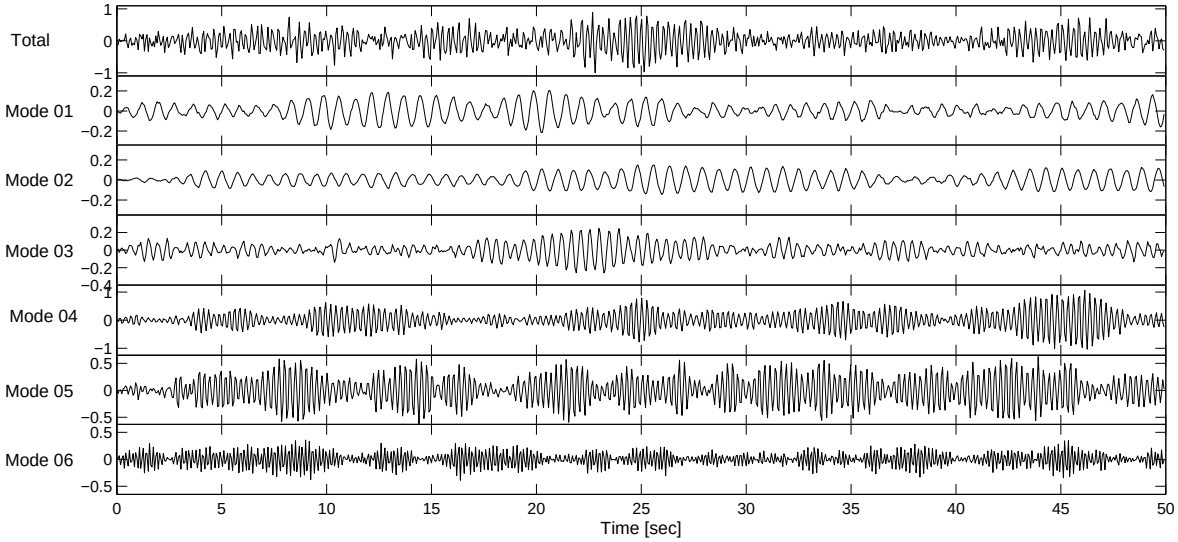

Fig. 2.6 – Modal responses with normalized amplitudes measured at node 4 in x-axis direction.

2.5. Stochastic State-Space Models

Up to now the state-space models discussed in the previous sections were addressed from a deterministic point of view, assuming that both inputs and outputs are measurable during the vibration tests and that the measured quantities are not affected by any disturbances. In practice, however, these measurements may be subjected to uncertainties due to noise and unmeasured inputs.

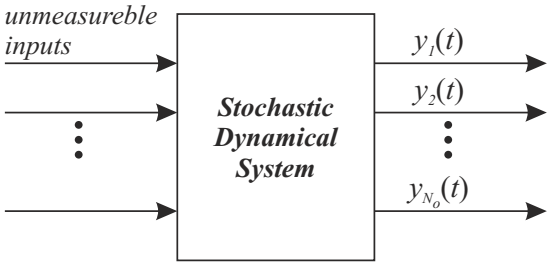

Fig. 2.7 – Stochastic dynamical system with unmeasurable inputs and N_o measurable outputs , $y(t)$.

Moreover, in some applications (e.g. in civil engineering) it is not possible to measure the input

forces, since the tested structures are excited by environmental and/or operational conditions such as wind, traffic or seismic actions. Under these circumstances, the knowledge of the deterministic inputs are replaced by stochastic processes and it is assumed that the inputs are realizations of these processes so that the dynamic systems excited by unmeasurable inputs illustrated in Fig. 2.7 can be modelled by the following discrete-time stochastic state-space models:

$$\begin{aligned} x_{k+1} &= Ax_k + w_k \\ y_k &= Cx_k + v_k \end{aligned} \tag{2.72}$$

The parameters $w_k \in \mathbb{R}^{n\times 1}$ and $v_k \in \mathbb{R}^{n\times 1}$ in eq. (2.72) are stochastic processes known as the *input noise process* and the *output noise process*, respectively. These noise sequences are assumed to have zero mean and covariance matrices:

$$\mathbf{E}[\begin{Bmatrix} w_p \\ v_p \end{Bmatrix} \begin{Bmatrix} w_q^T & v_q^T \end{Bmatrix}] = \begin{bmatrix} Q & S \\ S^T & R \end{bmatrix} \delta_{pq} \tag{2.73}$$

where $\mathbf{E}[\bullet]$ stands for the expected value operator, δ_{pq} is the Kronecker delta which equals the unit if $p = q$ and zero otherwise, and p and q are two arbitrary time instants.

2.5.1. Properties of the Stochastic State-Space Models

The stochastic state-space models (2.72) are assumed to be stationary with zero mean. The properties and definition of these models are briefly resumed as follows (Overchee and De-Moor, 1996; Peeters, 2000):

$$\mathbf{E}[x_k x_k^T] = \Sigma, \quad \mathbf{E}[x_k] = 0 \tag{2.74}$$

where Σ represents the state covariance independent of time k. Since the noise processes w_k and v_k are assumed to be zero mean and independent of the states x_k, the following properties are verified:

$$\mathbf{E}[x_k w_k^T] = 0, \quad \mathbf{E}[x_k v_k^T] = 0 \tag{2.75}$$

The output covariance matrices $R_i \in \mathbb{R}^{N_o \times N_o}$ are defined as:

$$R_i = \mathbf{E}[y_{k+i} y_k^T] \tag{2.76}$$

and the *next state - output covariance matrix* $G \in \mathbb{R}^{n \times N_o}$ as:

$$G = \mathbf{E}[x_{k+1} y_k^T] \tag{2.77}$$

Based on the previous definitions, the noise properties and on the assumption that the system is stationary, the following properties can be derived:

$$\begin{aligned} \Sigma &= A\Sigma A^T + Q \\ R_0 &= C\Sigma C^T + R \\ C &= A\Sigma C^T + S \end{aligned} \tag{2.78}$$

The output covariance matrix R_i can be computed from the measured data, once the state matrices A and C are found, as follows:

$$\begin{aligned} R_i &= CA^{i-1}G \\ R_{-i} &= G^T \left(A^{i-1}\right)^T C^T, \end{aligned} \quad i = 1, 2, \cdots \tag{2.79}$$

The stochastic model (2.72) is defined by the system matrices A, G, C and R_0. These matrices play a role to stochastic state-space models which is equivalent to that of the deterministic system matrices A, B, C and D to the deterministic state-space models discussed in Section 2.2.2. By inserting the eigenvalue decomposition of A (2.65) and the definition of V_d (2.68), eq. (2.79) can be reformulated as (Akaike, 1974; Peeters, 2000):

$$R_i = V_d \Lambda_d^{i-1} G_m, \quad i > 0 \tag{2.80}$$

with $G_m \in \mathbb{C}^{n \times N_o}$ known as the "*next modal state - output*" covariance matrix or *stochastic modal participation matrix*. This matrix plays a role in the output-only modal analysis which is equivalent to the modal participation matrix L_d^T in input-output modal analysis (Peeters, 2000). Moreover, similarly to L_d^T, G_m^T they are assumed to have the following structure:

$$G_m^T = \begin{bmatrix} g_{d_1}^T & g_{d_2}^T & \cdots & g_{d_{N_m}}^T \end{bmatrix}$$

where the vectors $g_{d_i} \in \mathbb{C}^{1 \times N_o}$ are the so-called *discrete-time stochastic modal participation vector* or *discrete-time operational factor vector*, which replace the modal participation factors l_{d_i}, in case of **OMA**.

2.5.2. Forward Innovation Model

The so-called forward innovation model is obtained by applying the steady-state Kalman filter to the stochastic state-space model (2.72). The Kalman filter is widely used in control theory and its main advantage is that it specifies how the states x_{k+1} are updated from x_k when a new observation y_k is obtained, without needing to reprocess the sequence of observations up to time k $(y_1, y_2, \cdots, y_k)$. Applying this filter to the state-space model (2.72), yields:

$$\begin{aligned} z_{k+1} &= Az_k + Ke_k \\ y_k &= Cz_k + e_k \end{aligned} \tag{2.81}$$

where $K \in \mathbb{R}^{n \times N_o}$ is the Kalman filter gain and $e_k \in \mathbb{R}^{N_o \times 1}$ is called innovations (or prediction errors) and consists of a zero mean white noise vector sequence, with covariance matrix:

$$\mathbf{E}[e_p e_q^T] = R_e \delta_{pq} \tag{2.82}$$

The forward innovation model (2.81) is defined by the system matrices A, K, C, R_e. These matrices are computed from the stochastic state-space system matrices A, G, C, R_0 which are, in turn, used to solve the so-called *discrete Riccati equation* (Arnold and Laub, 1984) for the positive definite solution P:

$$P = APA^T + (G - APC^T)(R_0 - CPC^T)^{-1}(G - APC^T)^T \tag{2.83}$$

where $P = \mathbf{E}[z_k z_k^T] \in \mathbb{R}^{n \times n}$ is the forward state covariance matrix. Once this matrix is found, the Kalman gain matrix is computed as:

$$K = (G - APC^T)(R_0 - CPC^T)^{-1} \tag{2.84}$$

and the covariance matrix of the innovations, R_e, as:

$$R_e = R_0 - CPC^T \tag{2.85}$$

2.6. Non-parametric Pre-processing for Frequency-Domain EMA

Since frequency-domain modal identification techniques use the estimated **FRF**s as primary data, the input and output signals acquired in time-domain need to be transformed into **FRF**s. This transformation starts by estimating the spectra of the acquired signals. One of the most

widely used methods to compute these spectra is the periodogram approach, also known as Welch's method (Mitra, 1998). The idea behind this approach is to split the measured time data sequence into N_b overlapping segments of equal length and, for each segment, apply the **D**iscrete **F**ourier **T**ransform (**DFT**) using a time window, w_k (e.g. Hanning, Hamming, ...), to minimize the leakage effects. Next, the **DFT**s $U_b(\omega)$ and $Y_b(\omega)$ of the inputs, $u_k^{(b)}$, and of the outputs, $y_k^{(b)}$, are computed for the b^{th} segment, respectively, by:

$$Y_b(\omega) = \sum_{k=0}^{N_s-1} w_k y_k^{(b)} e^{-j\omega k\Delta t} \tag{2.86}$$

$$U_b(\omega) = \sum_{n=0}^{N_s-1} w_k u_k^{(b)} e^{-j\omega k\Delta t} \tag{2.87}$$

where N_s is the number of sample points within each segment. The advantage of the Welch's method is the possibility to consider an overlapping between adjacent segments to estimate de **P**ower **S**pectra **D**ensities (**PSD**s). An overlapping in the range of 50% to 75% is commonly chosen in order to reduce the variance of the estimate. Once the **DFT**s of all segments are computed using eqs. (2.86) and (2.87), their corresponding auto and cross **PSD**s can be estimated using the following expressions:

$$\hat{S}_{yy}^{(b)}(\omega) = \frac{1}{\sum_{n=0}^{N_s-1} |w_n|} Y_b(\omega) Y_b^H(\omega_f) \tag{2.88}$$

$$\hat{S}_{uu}^{(b)}(\omega) = \frac{1}{\sum_{n=0}^{N_s-1} |w_n|} U_b(\omega) U_b^H(\omega) \tag{2.89}$$

$$\hat{S}_{yu}^{(b)}(\omega) = \frac{1}{\sum_{n=0}^{N_s-1} |w_n|} Y_b(\omega) U_b^H(\omega) \tag{2.90}$$

$$\hat{S}_{uy}^{(b)}(\omega) = \frac{1}{\sum_{n=0}^{N_s-1} |w_n|} U_b(\omega) Y_b^H(\omega) \tag{2.91}$$

with $\hat{S}_{yy}^{(b)}$ denoting the spectra matrix of the output responses, $\hat{S}_{uu}^{(b)}$ the spectra matrix of the input forces, $\hat{S}_{uy}^{(b)}$ the input-output matrix and $\hat{S}_{yu}^{(b)}$ the output-input spectra matrix. In a final step, the periodogram is estimated by computing the weighted periodogram of all segments and taking

the average:

$$\hat{S}_{yy}(\omega) = \frac{1}{N_b}\sum_{b=1}^{N_b}\hat{S}_{yy}^{(b)}(\omega) \tag{2.92}$$

$$\hat{S}_{uu}(\omega) = \frac{1}{N_b}\sum_{b=1}^{N_b}\hat{S}_{uu}^{(b)}(\omega) \tag{2.93}$$

$$\hat{S}_{yu}(\omega) = \frac{1}{N_b}\sum_{b=1}^{N_b}\hat{S}_{yy}^{(b)}(\omega) \tag{2.94}$$

$$\hat{S}_{uy}(\omega) = \frac{1}{N_b}\sum_{b=1}^{N_b}\hat{S}_{uu}^{(b)}(\omega) \tag{2.95}$$

Once the spectra matrices are estimated, the **FRF**s are computed by making use of one of the non-parametric **FRF** estimators. The most widely used estimator in **EMA** is the so-called H_1 **FRF** estimator. This estimator is formulated based on the assumption that the inputs are noise free and only the output measurements are affected by errors. This **FRF** estimator is given as:

$$H_1 = \hat{S}_{yu}\hat{S}_{uu}^{-1} \tag{2.96}$$

Another frequently used estimator in **EMA** is the H_2 **FRF** estimator. Unlike the H_1, this estimator assumes that the errors are only present in the inputs and the outputs are noise free. The H_2 **FRF** estimator is computed by:

$$H_2 = \hat{S}_{yy}\hat{S}_{uy}^{-1} \tag{2.97}$$

Apart from H_1 and H_2, there exist other estimators, as for instance, the H_v **FRF** estimator. The H_v **FRF** estimator assumes that: (i) the noise exists in the measured inputs and outputs; (ii) the noise in the inputs is uncorrelated with the noise in the outputs; and (iii) the noise in both types of signal is of equal amplitude (El-Kafafy, 2013). Detailed description and discussion about **FRF** estimators are found, for instance, in Rocklin and Vold (1985); Pintelon and Schoukens (2001); Verboven (2002) and El-Kafafy (2013). Apart from the **FRF** estimates, the noise information is also taken into account by some frequency-domain identification techniques. The noise in the H_1 and H_2 estimators is given by the variance $\hat{\sigma}_H^2(\omega_f)$ at each frequency line of the **FRF**. In case of **S**ingle **I**nput **S**ingle **O**utput (**SISO**) and **S**ingle **I**nput **M**ultiple **O**utputs (**SIMO**)

systems, the variance of the H_1 **FRF** estimator can be estimated by:

$$\hat{\sigma}^2_{H_{oi}} = \frac{1}{N_b}\left(\frac{1-\gamma^2_{oi}}{\gamma^2_{oi}}\right)|H_{oi}|^2 \tag{2.98}$$

where γ^2_{oi} is the coherence function, which is given as:

$$\gamma^2(\omega_f) = \frac{\left|\hat{S}_{uy}(\omega_f)\right|^2}{\hat{S}_{yy}(\omega_f)\hat{S}_{uu}(\omega_f)} \leq 1 \tag{2.99}$$

This function is commonly used in **EMA** to indicate how the output is correlated with the input. The closer to the unity this function is, the more the outputs are influenced by the inputs. On the other hand, the closer to zero it is, the more the outputs are contaminated by noise. In case of **MISO** and **MIMO** systems with uncorrelated outputs, the covariance matrix of the o^{th} row of the **FRF** matrix is given by:

$$\text{Cov}\left(H_o(\omega_f)\right) = \frac{1}{N_s}\left(1 - m\gamma^2_o(\omega_f)\right)\hat{S}_{y_o y_o}\hat{S}^{-1}_{uu} \tag{2.100}$$

where the subscript y_o denotes the **DFT** spectrum of a single measured output and $m\gamma^2_o(\omega_f)$ the multiple coherence function that indicates the coherence between each output and all the inputs, and is computed as:

$$m\gamma^2_o(\omega_f) = \frac{\hat{S}_{y_o u}\hat{S}^{-1}_{uu}\hat{S}_{uy_o}}{\hat{S}_{y_o y_o}} \tag{2.101}$$

Example 3

The exact **FRF** of the lattice tower structure illustrated in Fig. 2.2 is compared to the $H1$ **FRF** estimate. The inputs u_k and the outputs y_k sampled at 100 Hz are used to estimate the **FRF** matrix. A white noise was added to each output independently, with a noise-to-signal ratio (N/S) of 10%. The function `awgn` of MATLAB's Communication Toolbox (MathWorks, 2010) allows for adding noise to a signal with a specified N/S ratio. The input and noisy output sequences were filtered with an eight-order Chebyshev type I lowpass filter with a cutoff frequency of 10 Hz, and the resulting data of both sequences were resampled at a lower rate of 25 Hz.

These filtering and resampling procedures correspond to the application of the `decimate` command of MATLAB's Signal Processing Toolbox. Afterwards, the **FRF** matrix was estimated using the $H1$ **FRF** estimator discussed in Section 2.6. The estimated **FRF** matrix and its corresponding standard deviation were computed by evaluating eqs. (2.96) and (2.100), respectively, for each frequency line f ($\omega = 2\pi f$). A typical element of the estimated **FRF** matrix $\hat{H}(\omega)$ together with its standard deviation and the corresponding exact **FRF** are shown in Fig. 2.8.

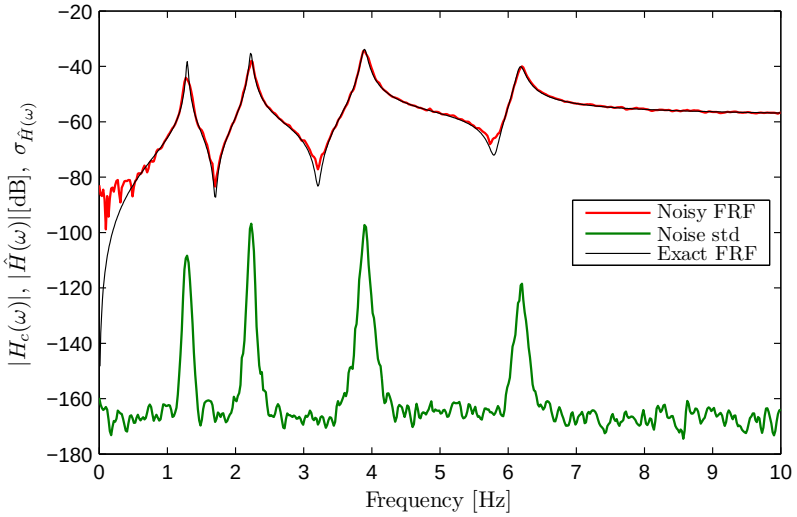

Fig. 2.8 – Exact and estimated elements $(1,1)$ of the **FRF** matrices $H_c(\omega)$ and $\hat{H}(\omega)$ together with the estimated standard deviation. This element corresponds to the **FRF** between the input at node 4 (x-axis direction) and the output at the same **DOF**. Absolute values of the exact (black line) and estimated (red line) **FRF** with $H1$ estimator, and the standard deviation estimates (green line).

2.7. Non-parametric Pre-processing for Time and Frequency-Domain OMA

Apart from the periodogram, other methods exist to estimate the power and cross spectra from the output responses measured in **OMA**. One of the most commonly used approaches is known as the correlogram approach (Mitra, 1998) and consists of an indirect non-parametric technique which estimates the spectra matrix by using the correlations of the output responses. These correlations are defined as:

$$R_i = \mathbf{E}[y_{i+k}(y_i)^T] \tag{2.102}$$

Assuming that the output responses correspond to a ergodic stochastic processes[1], the definition (2.102) becomes:

$$R_i = \lim_{N_k \to \infty} \frac{1}{N_k} \sum_{k=0}^{N_k-1} y_{i+k} y_i^T \tag{2.103}$$

with N_k standing for the number of measured output data samples. In practice, when a vibration test is performed, only a limited amount of outputs are sampled. If a sufficiently large number of data samples is acquired, the correlations can be estimated by simply dropping the limit and eq. (2.102) becomes:

[1] In a ergodic stochastic process the average over an infinite number of processes (i. e. the expected value of a time sample) can be replaced by the average over one infinitely long record of the process

$$\hat{R}_i = \frac{1}{N_k} \sum_{k=0}^{N_k-1} y_{i+k} y_i^T \tag{2.104}$$

Aiming at enhancing the performance of the computation of the modal parameters estimates by the system identification techniques, the covariances $\hat{R}_i$ can be replaced by the reference covariances $\hat{R}_i^{\text{ref}}$, which consists of the covariances between all outputs and only a subset of these outputs. This reduced covariance matrix is defined by:

$$R_i^{\text{ref}} = \mathbf{E}[y_{i+k}(y_i^{\text{ref}})^T] = \lim_{N_k \to \infty} \frac{1}{N_k} \sum_{k=0}^{N_k-1} y_{i+k}(y_i^{\text{ref}})^T \tag{2.105}$$

and estimated by:

$$\hat{R}_i^{\text{ref}} = \frac{1}{N_k} \sum_{k=0}^{N_k-1} y_{i+k} \left(y_i^{\text{ref}}\right)^T \tag{2.106}$$

where $y^{\text{ref}} \in \mathbb{R}^{N_{\text{ref}} \times 1}$ is a vector containing only the responses of the well-chosen reference sensors, with N_{ref} denoting the number of sensors chosen as references. By Assuming the definition of the reference outputs y^{ref}, the output vector y_k can be arranged such that:

$$y_k = \begin{bmatrix} y_k^{\text{ref}} \\ y_k^{\tilde{}\text{ref}} \end{bmatrix}, \quad y_k^{\text{ref}} = L_s y_k \tag{2.107}$$

with $y_k^{\tilde{}\text{ref}} \in \mathbb{R}^{(N_o - N_{\text{ref}}) \times 1}$ denoting a vector containing the responses measured by the non-reference sensors and $L_s \in \mathbb{R}^{N_{\text{ref}} \times N_o}$ a selection matrix containing zeros and ones conveniently positioned so that the reference outputs y_k^{ref} can be extracted from the responses y_k. By making use of the definition of the reference sensors, the covariance matrix can, alternatively, be computed by selecting the reference columns of the full covariance matrices R_i, as follows:

$$R_i^{\text{ref}} = R_i L_s^T \tag{2.108}$$

The definition of the reference sensors can be extended to define the reduced "*next state - output*" covariance matrix G^{ref}:

$$G^{\text{ref}} = \mathbf{E}[x_{i+k}(y_i^{\text{ref}})^T] = G L_s^T \in \mathbb{R}^{n \times N_{\text{ref}}} \tag{2.109}$$

as well as to define the factorization properties for the reduced covariance matrix in an analogue

manner as for the full covariance matrix (2.79):

$$\begin{aligned} R_i^{\text{ref}} &= R_i L_s^T = CA^{i-1}G^{\text{ref}} \\ R_{-i}^{\text{ref}} &= L_s R_i = \left(G^{\text{ref}}\right)^T \left(A^{i-1}\right)^T C^T, \end{aligned} \quad i = 1, 2, \cdots \tag{2.110}$$

Once the covariances are estimated, the weighted correlogram can be computed as the **DFT** of the weighted estimated correlation sequence (2.104):

$$\hat{S}_{yy}(\omega) = \sum_{k=-L}^{L} \eta_k \hat{R}_k^{\text{ref}} e^{-j\omega k\Delta t} \tag{2.111}$$

where L is the maximum number of time lags at which the correlations are estimated and η a window function. In other to avoid the greater statistical variance associated with the higher lags of the correlation estimates, L is typically much smaller than the number of data samples. In modal analysis context, it suffices to compute the so-called *half spectra* matrix, denoted by $\hat{S}_{yy}^{+}(\omega)$, which is obtained by using only the correlations having a positive time lags in eq. (2.111):

$$\hat{S}_{yy}^{+}(\omega) = \frac{\eta_0 \hat{R}_0^{\text{ref}}}{2} + \sum_{k=1}^{L} \eta_k \hat{R}_k^{\text{ref}} e^{-j\omega k\Delta t} \tag{2.112}$$

The parameters η in eq. (2.112) stands for the exponential window function which is computed by:

$$\eta_k = e^{-\beta k\Delta t} \tag{2.113}$$

where β is the exponential window constant used to reduce the noise, as well as the leakage effects. One of the advantages of the correlogram approach with regard to the periodogram is the possibility to remove the damping due to the time window function used (e.g. exponential window). The additional damping of the exponential window is removed once the system poles are estimated by using the following expression:

$$\lambda_{\text{corrected}} = \lambda_{\text{estimated}} + \beta \tag{2.114}$$

where $\lambda_{\text{estimated}}$ and $\lambda_{\text{corrected}}$ are, respectively, the poles estimated by using a parametric **MPE** technique and the corrected poles obtained after the removal of the additional damping due to the exponential window.

2.7.1. Derivation of the Noise Information

Unlike in **EMA**, the noise information is not available in **OMA**. Therefore, this information is derived by estimating the variance of the output **PSD**s (Parloo et al., 2001). In case of stationary operational conditions, the variance of the noise can be estimated by dividing the data sequence of N_k samples into N_b non-overlapping segments of N_s samples each, such that $N_b N_s \leq N$. If, for each segment s ($s = 1, 2 \cdots, N_b$) the spectra $\hat{S}_{yy}^{+(s)}(\omega)$ are computed, then the mean spectra can be estimated as:

$$\hat{S}_{yy}^{+}(\omega) = \frac{1}{N_b} \sum_{s=1}^{N_s} \hat{S}_{yy}^{+(s)}(\omega) \tag{2.115}$$

and the corresponding variance as (Guillaume et al., 1999; Parloo et al., 2001):

$$\hat{\sigma}^2_{S_{yy}^{+}(\omega)} = \frac{1}{N_b} \left(\frac{1}{N_b} \sum_{s=1}^{N_s} \left| \hat{S}_{yy}^{+(s)}(\omega) \right|^2 - \left| \hat{S}_{yy}^{+}(\omega) \right|^2 \right) \tag{2.116}$$

It turns out that, in real-life **OMA**, the vibration tests are performed on the structures subjected to non-stationary excitations forces (e.g. traffic, wind and seismic activities). Therefore, the employment of eq. (2.116) in such conditions can lead to an overestimation of the variance (Parloo et al., 2001) and, in turn, to an overestimation of the uncertainties on the modal parameter estimates. Under these circumstances, another approach can be used to estimate the variance the **PSD**s. This approach consists of estimating the variance of the **PSD**s by means of the square absolute of residual errors from a preliminary **L**east **S**quares (**LS**) estimation. This is accomplished by smoothing the these residual errors by making use of a frequency window W_γ. Assuming that the variance $\hat{\sigma}^2_{S_{yy}^{+}}$ is almost constant over the interval $\omega_{f-\Delta k} < \omega < \omega_{f+\Delta k}$, an estimate for this variance can be obtained from the following weighted average:

$$\hat{\sigma}^2_{S_{yy}^{+}(\omega_k)} = \frac{\sum_{k=f-\Delta k}^{f+\Delta k} W_\gamma(\omega_k - \omega_f) |\varepsilon(\Theta, \omega_k)|^2}{\sum_{k=f-\Delta k}^{f+\Delta k} W_\gamma(\omega_k - \omega_f)} \tag{2.117}$$

with

$$\varepsilon(\Theta, \omega_k) = S_{yy}^{+}(\Theta, \omega_k) - \hat{S}_{yy}^{+}(\omega_k) \tag{2.118}$$

where $S_{yy}^{+}(\Theta, \omega_k)$ is the parametric model synthesized after the preliminary **LS** estimation of the parameters Θ and W_γ a window function (e.g. Hanning or Hamming windows) centered around zero that slides along the frequency samples of the residual errors and is dependent of the shape parameter γ. If a Hanning window is used to smooth the residual errors, the parameter γ defines the number of frequency lines within the window. The optimum value

for this parameter depends on the number of frequency lines N_f of the spectra. A practical procedure to determine this parameter is discussed in (Ljung, 1999). This procedure consists of initially setting $\gamma = N_f/20$, and then compute and plot the corresponding estimate for various values of decreasing γ. By inspecting the differences among obtained the plots, one is able to identify the optimum value for γ.

Example 4
The non-parametric estimates of the output covariances R_i and the half spectra matrix $S_{yy}^{+}(\omega)$ of the lattice tower illustrated in Fig. 2.2 are computed from noisy contaminated outputs used to estimate the **FRF** matrix and its variance in **Example 3**. The computation of R_i and $S_{yy}^{+}(\omega)$ is accomplished by evaluating expressions (2.106) and (2.112), respectively.

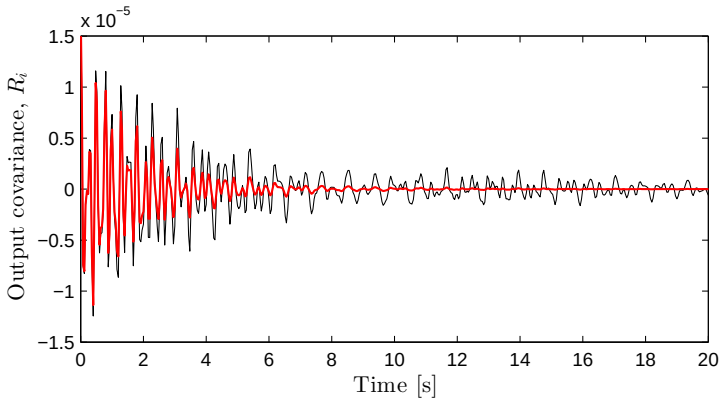

Fig. 2.9 – Element $(1,1)$ of the output covariance matrix, R_i, which corresponds to the auto covariance of the output response measured at node 4 (x-direction): covariance estimate before (black line) and after the application of the exponential window (red line).

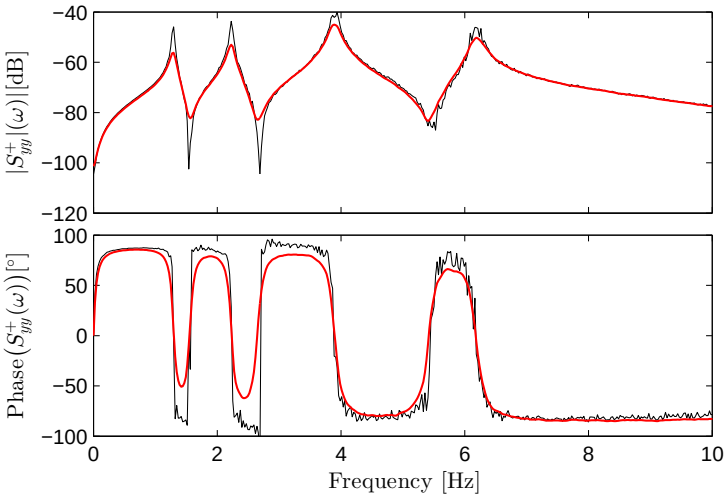

Fig. 2.10 – Element $(1,1)$ of the half spectra matrix, $\hat{S}_{yy}^{+}(\omega)$, which corresponds to the auto spectrum of the output response measured at node 4 (x-direction): absolute value (top) and the phase angle (bottom) before (black line) and after (red line) the application of the exponential window.

The output covariances are computed for 1024 time lags, whereas the half spectra are estimated for 512 frequency lines f ($\omega = 2\pi f$) in the range of 0-10 Hz. In order to minimize the leakage effects and the influence of the higher time lags, an exponential window function with a decay rate of 99.99% was applied to the output covariances. Typical elements of the noisy output covariances and spectra matrices are shown in Figs. 2.9 and 2.10, respectively. From these figures, it is obvious the influence of the exponential window.

2.8. Continuous-Time Frequency-Domain State-Space Models

In previous sections the vibration phenomenon was addressed by using the time-domain state-space models and it was shown how these models are related among themselves. In the following sections, the frequency-domain models are presented, and their applicability is discussed in the context of **EMA** and **OMA**. It is well known that the frequency-domain models allows for a better physical interpretation of the modal behaviour of vibrating structures with regard to the time-domain models, hence their importance in the context of modal analysis. Moreover, another advantage of the frequency-domain models with respect to their time-domain counterparts is the possibility to assess the modal parameters of the tested structures suited within a certain frequency band of interest.

Rather than the Impulsive Response Function or covariances modelled by the time-domain models, the **FRF** or the spectrum are the primary data to be modelled by the frequency-domain Models. Similarly to state-space models in time-domain, these frequency domain-models can also be formulated in a state-space basins. The derivation of such formulation starts by applying the Laplace transform $\mathscr{L}[\bullet]$ to the state-space model (2.40). Assuming zero initial conditions, the Laplace transform of such equation reads:

$$\begin{aligned} sX(s) &= A_c X(s) + B_c U(s) \\ Y(s) &= C_c X(s) + D_c U(s) \end{aligned} \tag{2.119}$$

in which

$$X(s) = \begin{bmatrix} Y(s) \\ sY(s) \end{bmatrix} \tag{2.120}$$

with $U(s)$ and $Y(s)$ are the Laplace transforms of the applied force $u(t)$ and the displacement $y(t)$, respectively, and s is the Laplace variable. By eliminating the states $Y(s)$ in eq. (2.119), yields:

$$Y(s) = H(s)U(s) \tag{2.121}$$

with $H(s) \in \mathbb{C}^{N_o \times N_i}$ denoting the transfer function between the outputs and inputs. It is straightforward to prove that this transfer function is related to the state spaces matrices, A_c, B_c, C_c and

D_c by means of the following expression:

$$H(s) = C_c(sI - A_c)B_c + D_c \tag{2.122}$$

If the Laplace variable is $s = j\omega$, eq. (2.122) is redefined as:

$$H(\omega) = C_c(j\omega I - A_c)B_c + D_c \tag{2.123}$$

where $H(\omega)$ is the so-called **FRF** matrix and ω can be any frequency of interest. In fact, the **FRF** is considered a particular case of the transfer function in which the tested structures corresponds to time-invariant systems and, therefore, the Laplace variable assumes pure imaginary values. By inserting the eigenvalue decomposition of A_c (2.35), and the definitions of the participation of factors L^T and observed mode shapes V (2.45) into eq. (2.123), the following expression is obtained:

$$H(\omega) = V(j\omega I - \Lambda_c)^{-1}L^T + D_c \tag{2.124}$$

In Peeters (2000) this equation is reformulated in terms of the modal parameters of the original **FE** model according to the type of the measured outputs (i.e. displacement, velocity and acceleration).

2.8.1. Output-only Frequency-Domain State-Space Model

It can be proven that spectra $S_{uu}(\omega)$ and $S_{yy}(\omega)$ corresponding, respectively, to the inputs $u(t)$ and outputs $y(t)$ are related to each other, as well as to the transfer function $H_c(\omega)$ defined in eq. (2.121) by means of the following expression (Ljung, 1999):

$$S_{yy}(\omega) = H(\omega)S_{uu}(\omega)H^H(\omega) \tag{2.125}$$

In case of **OMA**, the unmeasured inputs are replaced by white noise sequences whose corresponding spectrum R_{uu} is assumed to be constant and independent of the frequency ω. By considering this assumption, the expression for the output spectra (2.125) can be rewritten as:

$$S_{yy}(\omega) = H(\omega)R_{uu}H^H(\omega) \tag{2.126}$$

The modal form of the output spectra is obtained by inserting the modal decomposition of the transfer function (2.124) into eq. (2.126), yielding:

$$S_{yy}(\omega) = \left(V(j\omega I - \Lambda_c)^{-1}L^T + D_c\right) R_{uu} \left(D_c^T - L(j\omega I + \Lambda_c)^{-1}V^T\right) \tag{2.127}$$

Example 5
At this point another example is introduced to illustrate the application of the frequency-domain state-space models. The **FRF** and output spectra matrices of the lattice tower illustrated in Fig. 2.2 are computed by evaluating eqs. (2.123) and (2.126), respectively, in the range of 0-10 Hz for each frequency line f ($\omega = 2\pi f$). Typical elements of the **FRF** and output spectra matrices are shown in Figs. 2.11 and 2.12, respectively.

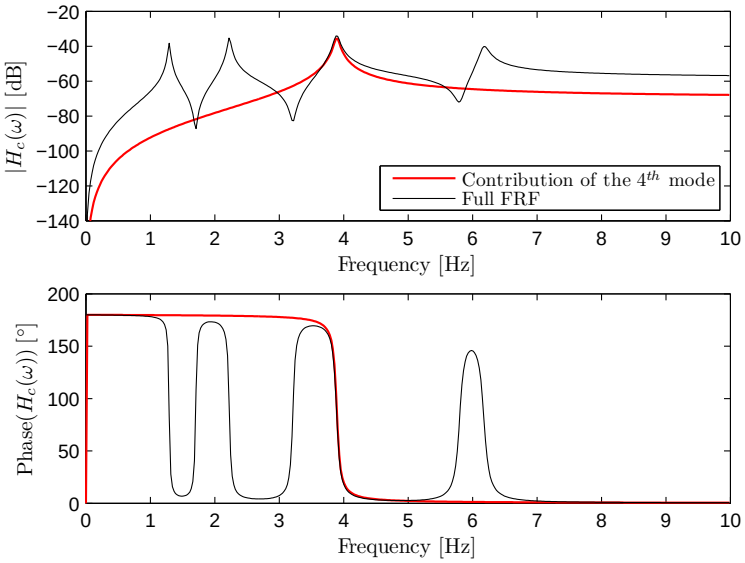

Fig. 2.11 – Element $(1,1)$ of $H(\omega)$, which corresponds to **FRF** between the input at node 4 (x-axis direction) and the output at the same **DOF**: absolute value of the **FRF** (top) and the phase angle (bottom). The black line represents the full **FRF** and the red line the contribution of the 4^{th} mode to the **FRF**.

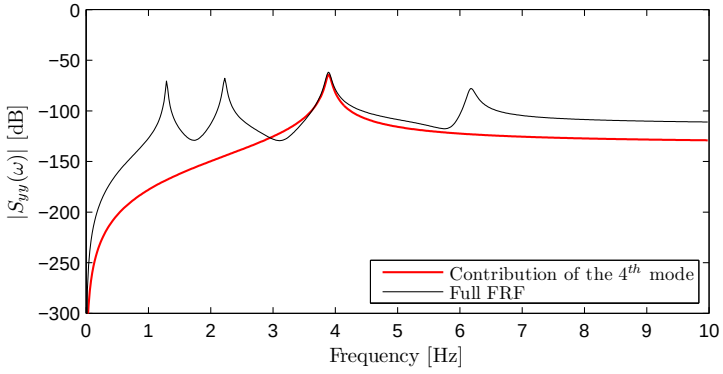

Fig. 2.12 – Absolute value of the element $(1,1)$ of the output spectra matrix $S_{yy}(\omega)$ which corresponds to the auto spectrum of the output response measured at node 4 (x-axis direction). The black line is the full spectrum and the red line represents the contribution of the 4^{th} mode to the spectrum.

2.9. The Modal Model

The modal model is one the most well-known models in frequency-domain. The advantages of this model include the possibility to characterize the modal behaviour of the tested structure

in terms of its modal parameters (i.e. poles, mode shapes and participation factors). The main disadvantage of this model, however, is that it is highly non-linear in the parameters and, therefore, most identification techniques can not be applied directly to estimate the modal parameters. This model is formulated by applying the Laplace transform to the equation of motion (2.1) and assuming zero initial conditions:

$$Z(s)Q(s) = U(s) \tag{2.128}$$

with $Z(s) = Ms^2 + C_1 s + K$ denoting the dynamical stiffness. Isolating $Q(s)$ in eq. (2.128), yields:

$$Q(s) = H(s)U(s) \tag{2.129}$$

where $H(s) = Z^{-1}(s) \in \mathbb{C}^{N_o \times N_i}$ is the transfer function matrix. Similarly to the continuous-time frequency-domain state-space models, this transfer function can be redefined as the following **FRF** matrix (Maia et al., 1998; Hu et al., 2012):

$$H(\omega) = V\left[j\omega I - \Lambda\right]^{-1} L^T + V^*\left[j\omega I - \Lambda^*\right]^{-1} L^H \tag{2.130}$$

and then reformulated in its partial fraction form:

$$H(\omega) = \sum_{i=1}^{N_m} \frac{v_i l_i^T}{j\omega - \lambda_i} + \frac{v_i^* l_i^H}{j\omega - \lambda_i^*} \tag{2.131}$$

One of the main advantages of the models in frequency-domain is the possibility to assess only the modal parameters suited within a certain frequency band of interest. In this case, the influence of out-of-band modes suited bellow and above this band are treated as lower and upper residuals. Assuming, for instance, that an **EMA** test is performed and that the output responses are measured in acceleration, the transfer function matrix $H(\omega)$ is given by:

$$H(\omega) = \sum_{i=1}^{N_m} \frac{v_i l_i^T}{j\omega - \lambda_i} + \frac{v_i^* l_i^H}{j\omega - \lambda_i^*} + [LR] + (j\omega)^2[UR] \tag{2.132}$$

where $LR, UR \in \mathbb{R}^{N_o \times N_i}$ are, respectively, the lower and upper residual terms added to eq. (2.131) to model the influence of the out-of-band modes in the considered frequency band. These residuals are defined according to the output quantity measured which can be either displacement, velocity or acceleration, and to the type of analysis performed, namely, **EMA** or **OMA**, as presented in Tab. 2.2 (Peeters et al., 2007).

The drawback of the lower and upper residual model as in eq. (2.132) is that it is not very

Tab. 2.2 – Lower and upper residuals (Peeters et al., 2007).

Measured Quantity	FRFs (EMA)		Full Spectra (OMA)		Half Spectra (OMA)	
	LR	UR	LR	UR	LR	UR
Displacement	$\frac{LR}{(j\omega)^2}$	UR	$\frac{LR}{(j\omega)^4}$	UR	$\frac{LR}{j\omega}$	$(j\omega)UR$
Velocity	$\frac{LR}{j\omega}$	$j\omega UR$	$\frac{LR}{(j\omega)^2}$	$(j\omega)^2 UR$	$\frac{LR}{j\omega}$	$(j\omega)UR$
Acceleration	LR	$(j\omega)^2 UR$	LR	$(j\omega)^4 UR$	$\frac{LR}{j\omega}$	$(j\omega)UR$

efficient on modelling the influence of the out-of-band modes which are suited very close to the band of interest (El-Kafafy, 2013). In Fladung (2012), it is shown that if the in-band and out-of-band modes are separated by a factor lower then ten, the influence of the lower and upper modes can no longer be efficiently approximated by the residual model (2.132). Moreover, it is verified that this situation is rather common in real life **EMA** and **OMA**. In such circumstances, another variant of the residual model with enhanced terms proposed by El-Kafafy (2013) can be used to minimize the influence of these modes on the band of interest and improve the accuracy of the estimates. This modal model with enhanced lower and upper residuals is given by:

$$H(\omega) = \sum_{i=1}^{N_m} \frac{v_i l_i^T}{j\omega - \lambda_i} + \frac{v_i^* l_i^H}{j\omega - \lambda_i^*} + \frac{N(\omega)}{d(\omega)} \tag{2.133}$$

with $N(\omega) \in \mathbb{C}^{N_o \times N_i}$ denoting the numerator matrix and $d(\omega) \in \mathbb{C}$ the denominator scalar of the new residual model given, respectively, by:

$$N(\omega) = [AR] + j\omega\,[BR] + (j\omega)^2\,[CR], \quad d(\omega) = a + j\omega b + (j\omega)^2 c \tag{2.134}$$

where $AR, BR, CR \in \mathbb{C}^{N_o \times N_i}$ are the numerator matrix coefficients, and $a, b, c \in \mathbb{C}$ the denominator scalar coefficients of the new upper and lower residual model (2.133). The denominator coefficients are defined in Tab. 2.3 according to the output response measured, as well as to the type of analysis performed (El-Kafafy, 2013).

Tab. 2.3 – Definition of the denominator coefficients of the enhanced lower and upper residual model (2.134) according to the type of the measured output and to the analysis performed.

Measured Quantity	FRFs (EMA)			Half Spectra (OMA)		
	a	b	c	a	b	c
Displacement	0	0	1	0	1	0
Velocity	0	1	0	0	1	0
Acceleration	1	0	0	0	1	0

2.9.1. Output-only Modal Model

As the inputs are unmeasurable in frequency-domain **OMA**, the only available information is the measured outputs. In this case, the inputs are assumed to be white noise sequences with a constant spectrum and the full output spectrum matrix $S_{yy}(\omega)$ is reformulated according to eq. (2.126). Under the white noise input assumption, it can be proven that the modal decomposition of the spectra matrix, S_{yy}, is obtained by inserting eq. (2.131) into eq. (2.126) and converting the resulting equation to the partial fraction form (Hermans and Van-Der-Auweraer, 1999; Peeters et al., 2007):

$$S_{yy}(\omega) = \sum_{i=1}^{N_m} \frac{v_i g_i^T}{j\omega - \lambda_i} + \frac{v_i^* g_i^H}{j\omega - \lambda_i^*} + \frac{g_i v_i^T}{-j\omega - \lambda_i} + \frac{g_i^* v_i^H}{-j\omega - \lambda_i^*} \tag{2.135}$$

where g_i stands for the *continuous-time stochastic modal participation vector* or the *operational reference factor vector*. This vector plays the same role in the continuous-time stochastic state-space model as the vector g_{d_i} in the discrete-time stochastic state-space model. Differently from the modal participation factor vectors l_i, physical interpretation of vectors g_{d_i} is less obvious as they are a function of all modal parameters of the system and the constant input spectra matrix R_{uu}. It can be shown that, in case of displacement measurements, the relation between this vector and the model parameters of the continuous-time state-space models is given by (Peeters, 2000):

$$g_i = l_i^T R_{uu} L \left(-\Lambda_c - \lambda_i I\right)^{-1} V^T \tag{2.136}$$

In practice, in the context of **OMA**, the modal parameters are usually identified by the frequency-domain estimators using the so-called half spectra rather then the full spectra model defined by eq. (2.135). The half spectra model, denoted by $S_{yy}^+(\omega)$, consists of the first two terms in the right hand side of eq. (2.135):

$$S_{yy}^+(\omega) = \sum_{i=1}^{N_m} \frac{v_i g_i^T}{j\omega - \lambda_i} + \frac{v_i^* g_i^H}{j\omega - \lambda_i^*} \tag{2.137}$$

It can be proven that the relation between the half spectra (2.137) and the full spectra (2.135) is given as follows (Cauberghe, 2004):

$$S_{yy}(\omega) = S_{yy}^+(\omega) + \left(S_{yy}^+(\omega)\right)^H \tag{2.138}$$

Similarly to the case of input-output modal analysis, if one is interested to assess only the vibration modes suited within a certain frequency band of interest, the influence of the out-of-band modes can be modelled by making use of the upper and lower residual models. Assuming, for instance, that the output responses are measured in acceleration, the frequency band of interest can be modelled by:

$$S_{yy}^{+}(\omega) = \sum_{i=1}^{N_m} \frac{v_i g_i^T}{j\omega - \lambda_i} + \frac{v_i^* g_i^H}{j\omega - \lambda_i^*} + \frac{[LR]}{j\omega} + j\omega[UR] \tag{2.139}$$

or by:

$$S_{yy}^{+}(\omega) = \sum_{i=1}^{N_m} \frac{v_i g_i^T}{j\omega - \lambda_i} + \frac{v_i^* g_i^H}{j\omega - \lambda_i^*} + \frac{N(\omega)}{d(\omega)} \tag{2.140}$$

It should be noted that the parameters of the residuals models in eqs. (2.139) and (2.140) are defined in Tabs. 2.2 and 2.3, respectively, according to the output quantity measured.

2.10. Common Denominator Model

The Common Denominator is a rather classical frequency-domain model largely used in modal analysis. This model is obtained by factorizing the modal model defined as in eq. (2.131) into a rational fraction of two polynomials, as:

$$H(\Theta, \omega) = \frac{\mathbf{N}(\beta, \omega)}{\mathbf{d}(\alpha, \omega)} \tag{2.141}$$

where the numerator $\mathbf{N}(\beta, \omega)$ and the denominator $\mathbf{d}(\alpha, \omega)$ are given, respectively, by:

$$\mathbf{N}_{oi}(\beta, \omega) = \sum_{r=0}^{n} \beta_{oi_r} \Omega_r(\omega), \quad \mathbf{d}(\alpha, \omega) = \sum_{r=0}^{n} \alpha_r \Omega_r(\omega) \tag{2.142}$$

with

$$\Theta = \begin{bmatrix} \beta_{11} \\ \vdots \\ \beta_{N_o N_i} \\ \alpha \end{bmatrix}, \quad \beta_{oi} = \begin{bmatrix} \beta_{oi_0} \\ \vdots \\ \beta_{oi_n} \end{bmatrix}, \quad \alpha = \begin{bmatrix} \alpha_0 \\ \vdots \\ \alpha_n \end{bmatrix}, \quad \Omega_r(\omega) = \Omega(\omega)^r, \quad r = 0, 1, \cdots, n \tag{2.143}$$

The polynomial basins $\Omega(\omega)$ in eqs. (2.142) can be evaluated in Laplace domain ($\Omega(\omega) = s$), for continuous-time models, or in z-domain $\left(\Omega(\omega) = e^{-j\omega\Delta t}\right)$, for discrete-time models. The relation between output o and input i is such that the denominator polynomial is common for all input-output relations. The relation between the modal model and the common-denominator model is obtained by considering the **FRF** between output o and input i, as follows:

$$H_{oi}(s) = \sum_{r=1}^{N_m} \frac{v_{r_o} l_{r_i}}{s-\lambda_r} + \frac{v_{r_o}^* l_{r_i}^*}{s-\lambda_r^*} = \sum_{r=1}^{N_m} \frac{[Res]_{r_{oi}}}{s-\lambda_r} + \frac{[Res]_{r_{oi}}^*}{s-\lambda_r^*} = \frac{\mathbf{N}_{oi}(\beta_{oi},\omega)}{\mathbf{d}(\alpha,\omega)} \tag{2.144}$$

with

$$[Res]_r = v_r l_r^T \in \mathbb{C}^{N_o \times N_i} \tag{2.145}$$

The modal model form of the second expression in eqs. (2.144) is also known as the pole-residue model. It is clear from eq. (2.141) that the roots of the denominator polynomial $\mathbf{d}(\alpha,\omega)$ corresponds to the system poles. The residuals $[Res]_r$, on the other hand, can be computed either in a least squares sense by the so-called **L**east **S**quares **F**requency-Domain (**LSFD**) estimator (see Appendix A.3) or from the numerator matrix by means of the following expression (Pintelon et al., 2007):

$$[Res]_{r_{oi}} = \lim_{\Omega(\omega_k)\to \mathrm{z}_r} (\Omega(\omega_k) - \mathrm{z}_r) H_{oi}(\Omega(\omega_k), \Theta) = \frac{\mathrm{z}_r \mathbf{N}_{oi}(\mathrm{z}_r^{-1}, \beta_{oi})}{\prod_{m\neq r}(1-\mathrm{z}_m^{-1} z_r)} \tag{2.146}$$

where z_r is the pole that corresponds to the evaluated modal residual $[Res]_r$ and z_m represents all the estimated poles which are different from z_r. In eq. (2.146), it is considered that the **FRF**s are evaluated in z-domain $\left(\Omega(\omega_k) = e^{-j\omega_k\Delta t}\right)$ and that a parameter constraint is applied by imposing $\alpha_0 = 1$. The estimation of the modal residues, $[Res]_r$, by means of the **LSFD** estimator is performed by using the pole-residue model with lower and upper residual terms. In case of displacement outputs, this model is given by:

$$H(\omega) = \sum_{r=1}^{N_m} \frac{[Res]_r}{j\omega-\lambda_r} + \frac{[Res]_r^*}{j\omega-\lambda_r^*} + [LR] + (j\omega)^2[UR] \tag{2.147}$$

Alternatively, this estimation can be carried out by making using of the pole residue model with enhanced lower and upper residual model:

$$H(\omega) = \sum_{r=1}^{N_m} \frac{[Res]_r}{j\omega-\lambda_r} + \frac{[Res]_r^*}{j\omega-\lambda_r^*} + \frac{N(\omega)}{d(\omega)} \tag{2.148}$$

The parameters of the residual models (2.147) and (2.148) are defined according to the measured output quantities in Tabs. 2.2 and 2.3, respectively. Once these residual matrices are calculated, the mode shapes and participation factors are computed by applying the **S**ingular **V**alue **D**ecomposition (**SVD**) to eq. (2.145) (Verboven, 2002; Cauberghe, 2004):

$$[Res]_r = USV = \begin{bmatrix} U_1 & U_2 \end{bmatrix} \begin{bmatrix} S_1 & 0 \\ 0 & 0 \end{bmatrix} \begin{bmatrix} V_1^T \\ V_2^T \end{bmatrix} = U_1 S_1 V_1 \tag{2.149}$$

Assuming that $[Res]_r$ is a rank-one matrix (i.e. with only one singular value different from zero) then U_1 represents the mode shape vector v_r and V_1 the modal participation factor vector l_r, whereas the singular value S_1 is used to scale these modal vectors.

2.11. Matrix Fraction Description Models

Another frequency-domain model widely used in **EMA** and **OMA** is the so-called **M**atrix **F**raction **D**escription (**MFD**) model. This model consist of a ratio between two matrix polynomials (Kailath, 1980). Two variants of this model can be used to describe the modal behaviour of vibrating structures in frequency domain, namely, the **R**ight and **L**eft **MFD** (**RMFD** and **LMFD**) models. The main advantage of theses models with regard to the common de denominator model is the possibility to perform what is known as *poly-reference* identification, which means that multiple **FRF**s can be simultaneously taken into account during the parametric **MPE**. Therefore, compared to the common denominator, the identification with the **MFD** models provides more accurate parametric estimates of very close spaced modes (Guillaume et al., 2003). The main disadvantage of the **MFD** models, however, is that the parametric **MPE** is generally more time-consuming than with the common denominator model.

2.11.1. Right Matrix Fraction Description Models

The **RMFD** considers the input-output measurements of the reference **DOF**s in the parametric estimation and can be considered as a poly-reference variant of the common denominator model. In fact, in case of **SIMO** systems, the **RMFD** model reduces to the common denominator model. This verified by comparing eq. (2.141) to the definition of the **RMFD** model given by:

$$H(\Theta, \omega) = \mathbf{N}(\Theta, \omega)\mathbf{D}(\Theta, \omega)^{-1} \tag{2.150}$$

where

$$\mathbf{N}(\Theta,\omega)=\sum_{r=0}^{n}\Omega_r(\omega)\beta_r \tag{2.151}$$

denotes the numerator matrix and

$$\mathbf{D}(\Theta,\omega)=\sum_{r=0}^{n}\Omega_r(\omega)\alpha_r \tag{2.152}$$

the denominator matrix polynomial, which is independent of the output o. The polynomial coefficients $\beta_r\in\mathbb{C}^{N_o\times N_i}$ and $\alpha_r\in\mathbb{C}^{N_i\times N_i}$ are the parameters to be estimated. In eq. (2.150) the o^{th} row the modelled **FRF**s matrix is given by:

$$H_o(\Theta,\omega)=\sum_{r=0}^{n}\Omega_r(\omega)\beta_{or}\left(\sum_{r=0}^{n}\Omega_r(\omega)\alpha_r\right)^{-1},\quad o=1,2,\cdots,N_o \tag{2.153}$$

with

$$\Theta=\begin{bmatrix}\beta_1\\ \vdots\\ \beta_{N_o}\\ \alpha\end{bmatrix},\quad \beta_o=\begin{bmatrix}\beta_{o0}\\ \vdots\\ \beta_{on}\end{bmatrix},\quad \alpha=\begin{bmatrix}\alpha_0\\ \vdots\\ \alpha_n\end{bmatrix} \tag{2.154}$$

The computation of the modal parameters with the **RMFD** models are performed in two steps. The poles and modal participation factors are computed in a first step from the denominator polynomial coefficients by reformulating $\mathbf{D}(\Theta,\omega)=0$ into a generalized eigenvalue problem. These parameters are than given as the resulting nN_i eigenvalues and eigenvectors, respectively. Once the poles and modal participation factors are computed, the mode shapes are obtained in second step of the identification process from the numerator polynomial coefficients or in a linear least squares sense by means of the **LSFD** estimator (see APPENDIX A.1).

2.11.2. Left Matrix Fraction Description Models

Unlike the **RMFD** model which considers the input-output measurements of the reference **DOFs**, the **LMFD** considers the input-output measurements of all **DOF**s simultaneously. The parametrization of the **FRF** matrix with **LMFD** models is given as follows:

$$H(\Theta,\omega)=\mathbf{D}(\Theta,\omega)^{-1}\mathbf{N}(\Theta,\omega) \tag{2.155}$$

with

$$\begin{aligned}\mathbf{N}(\Theta,\omega) &= \sum_{r=0}^{n} \Omega_r(\omega)\beta_r \in \mathbb{C}^{N_o\times N_i}, \quad \beta_r \in \mathbb{R}^{N_o\times N_i} \\ \mathbf{D}(\Theta,\omega) &= \sum_{r=0}^{n} \Omega_r(\omega)\alpha_r \in \mathbb{C}^{N_o\times N_o}, \quad \alpha_r \in \mathbb{R}^{N_o\times N_o}\end{aligned} \tag{2.156}$$

The computation of the modal parameters with the **LMFD** is performed by following the same strategy used by the **RMFD** model. The poles and mode shapes are computed in a first step from the denominator matrix polynomial by reformulating $\mathbf{D}(\Theta,\omega)=0$ into a generalized eigenvalue problem. These parameters are than given as the resulting nN_o eigenvalues and eigenvectors, respectively. Once the poles and their corresponding mode shapes are found, the modal participation factors can be obtained from the numerator polynomial coefficients or in a linear least squares sense by means of the **LSFD** algorithm (see APPENDIX A.2). It is worth noting that, similarly as in **EMA**, the modal parameters can be also estimated in **OMA** by using the **MFD** and common denominator models. As the half spectra are parametrized in exactly the same way as the **FRF**s, the output-only **MPE** with these models is accomplished by simply replacing the measured **FRF**s by the estimated half spectra (Peeters et al., 2007).

2.12. Conclusions and Remarks

In this chapter, some of the models of vibrating structure most widely used in **EMA** and **OMA** were discussed, and their main advantages and disadvantages were occasionally highlighted. An interesting aspect about these models is that, although they address the vibration phenomenon differently, it is verified that they closely related among themselves. Apart from the models addressed in this chapter, other models are found in literature, such as the **I**mpulse **R**esponse **F**unction (**IRF**). This model plays an important row in classical **EMA** and is detailed described, for instance, in Ewins (1984) and Maia et al. (1998). Other model commonly used in **OMA** is the **A**uto-Regressive **M**oving **A**verage (**ARMA**). This model is also considered very important in the context of **OMA** and is discussed, for instance, in Akaike (1974), Andersen (1997), Ljung (1999) and Peeters (2000).

Chapter 3

INPUT-OUTPUT AND OUTPUT-ONLY MPE

In this chapter, the state-of-the art of techniques used to identify the parametric models of vibrating structures presented in Chapter 2 are reviewed. This review is basically divided into two parts: the first addresses the time and the second part the frequency-domain identification techniques. In the context of frequency-domain identification techniques, apart from the review of the **EMA** and **OMA** estimators, it is also proposed two approaches: the first consist of a new (single-reference) **MLE** formulated in pole-residual modal model which can be used to estimate the modal parameters and their uncertainties; and the second corresponds to an alternative implementation of the poly-reference **MLE** formulated in modal model. Finally, at end of the chapter, the merging strategies suitable for multi-dataset **OMA** are also briefly reviewed.

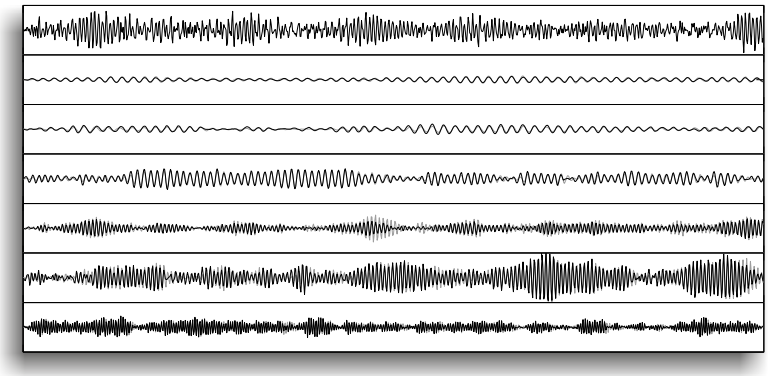

3.1. Introduction

Over the last years a lot of efforts have been done to improve the precision of the **MPE** in **EMA** and **OMA**. These efforts are reflected on the development of more precise and robust parametric and non-parametric estimators, which represent a second generation of identification techniques. Differently from the earliest generation which addresses the identification problem using **SISO**, **SIMO** and **MISO** systems, the latest identification techniques are also suitable to identify **MIMO** systems. According to the way they address the identification problem, these techniques can be split into two different categories, i.e, the parametric and non-parametric techniques. Amongst the non-parametric methods, a significant advance took place, particularly with the development of the **F**requecy **D**omain **D**ecomposition (**FDD**) method (Brincker et al., 2000, 2001), which is considered as a **SVD** extension of the classical **P**ick **P**icking (**PP**) method (Bendat and Piersol, 1993) and has been widely used in **OMA**.

With regard to the parametric methods, the advances verified over the last years are even more significant. Interesting discussion about the state-of-the-art of **EMA** and **OMA** identification techniques are found, for instance, in (Andersen, 1997; Peeters, 2000; Cauberghe et al., 2004) and in citations therein. Although not addressed in the framework this thesis, recent advances also took place among the **O**perational **M**odal **A**nalysis with e**X**ogenous inputs (**OMAX**) identification methods (Guillaume et al., 2006; Reynders, 2009). As this thesis is mainly focused on dynamic monitoring of civil engineering structures under environmental conditions, the **OMA** identification methods are covered in more detail. Therefore, some of the state-of-the-art **OMA** identification techniques are discussed in this Chapter, namely, the **pLSCF** (Guillaume et al., 2003) method formulated in frequency-domain and the time-domain **S**tochastic **S**ystem **I**dentification (**SSI**) techniques developed to estimate the modal parameters of output-only systems (Peeters, 2000; Overchee and De-Moor, 1996).

Initially formulated for input-output systems and also known by its commercial name Poly-MAX (Peeters et al., 2004c), the **pLSCF** method was afterwards extended to output-only systems (Peeters et al., 2007). In fact, this technique can be considered as poly-reference variant of the **L**east **S**quares **C**omplex **F**requency-domain (**LSCF**) method (Guillaume and Schoukens, 1998). One of the main features of the **pLSCF** method is the possibility to create clear and precise stabilization diagrams, allowing for distinguishing between close spaced modes. Another advantage of the identification with the **pLSCF** method is that the physical poles tend to stabilize faster over the identified model orders when compared to other **MPE** techniques, as, for instance, the **LSCF** and the **p**oly-reference **L**east **S**quares **C**omplex **E**xponential (**pLSCE**) (also known as **LSCE**-Prony) (Maia et al., 1998). More recently, significant improvements on the non-linear estimators like the **M**aximum **L**ikelihood (**ML**) **E**stimator (**MLE**) were also

verified.

Initially, problems such as convergence not being guaranteed, convergence to local minima, sensitivity to starting values and a high computational load were eventually related to these estimators. However, it seems that these drawbacks are overcome and the **MLE** has finally proven to be a robust method to estimate the modal parameters from noisy data (El-Kafafy et al., 2012b). Originally intended to estimate the modal parameters from **FRF**s using the common denominator model (Guillaume, 1992), the method was also extended to use spectra as primary data, so that it could also be used to estimate the modal parameters of output-only systems (Hermans et al., 1998; Guillaume et al., 1999). Afterwards, the **MLE** was also formulated to estimate the invariants of the modal model (El-Kafafy et al., 2013; El-Kafafy, 2013) and the uncertainty bounds on these estimates.

In this Chapter, apart from the review of some of the state-of-the-art modal identification techniques, two **ML**-based approaches are proposed. The first is intended to estimate the modal parameters and their corresponding confidence bounds, and consists of a single reference estimator formulated in pole-residue modal model; and the second corresponds to an alternative implementation of the **p**oly-reference **MLE** formulated in **M**odal **M**odel (**pMLE-MM**). The main idea behind these approaches is to optimize the estimates provided by the **LSCF** and **pLSCF** estimators and yield their uncertainty intervals. Aiming at assessing the efficiency of the first approach, it was applied to a simulated **EMA** to optimize the modal parameters and estimate their confidence bounds. The second approach consists of an alternative implementation of the **pMLE-MM** which was originally proposed by El-Kafafy (2013).

3.2. Identification of Stochastic State-space Models

SSI techniques are examples of the recent advances in time-domain **OMA**. In this section, a brief description of the **DATA** and **COV**ariance-driven **SSI** (**SSI-DATA** and **SSI-COV**) methods are presented. These techniques have become very popular among engineering community due to their robustness and precision verified even when dealing with nosy data. Further details about the background theory as well as the implementation of such techniques are found, for instance, in Overchee and De-Moor (1996) and Peeters (2000). In these methods, as the only available information are the outputs, its assumed that the systems (i.e. the tested structures) are excited by white noise processes and that the outputs are realization of these processes.

*3.2.1. The **SSI-COV** Method*

The **SSI-COV** technique identifies the stochastic state-space models described in Section 2.5 using the covariance of the reference output responses acquired in the vibration tests. The

identification with this technique starts by computing a Toeplitz matrix[1] of these covariances:

$$T_{1|i} = \begin{bmatrix} R_i^{\text{ref}} & R_{i-1}^{\text{ref}} & \cdots & R_1^{\text{ref}} \\ R_{i+1}^{\text{ref}} & R_i^{\text{ref}} & \cdots & R_2^{\text{ref}} \\ \vdots & \vdots & \ddots & \vdots \\ R_{2i-1}^{\text{ref}} & R_{2i-2}^{\text{ref}} & \cdots & R_i^{\text{ref}} \end{bmatrix} \tag{3.1}$$

By using the concepts of controllability and observability (Overchee and De-Moor, 1996; Sontag, 1998; Ljung, 1999) from control theory, the following matrices are defined:

$$O_i = \begin{bmatrix} C \\ CA \\ \vdots \\ CA^{i-1} \end{bmatrix}, \quad \Gamma_i^{\text{ref}} = \begin{bmatrix} A^{i-1}G^{\text{ref}} & \cdots & AG^{\text{ref}} & G^{\text{ref}} \end{bmatrix} \tag{3.2}$$

where $O_i \in \mathbb{R}^{N_o i \times n}$ and $\Gamma_i^{\text{ref}} \in \mathbb{R}^{n \times N_{\text{ref}} i}$ are, respectively, the observability and controllability matrices. By inserting eq. (2.110) into (3.2), it is straightforward to prove that toeplitz matrix $T_{1|i}$ (3.1) can be factorized as:

$$T_{1|i} = O_i \Gamma_i^{\text{ref}} \tag{3.3}$$

The Toeplitz matrix $T_{1|i}$ in eq. (3.1) can be also factorized using the **SVD**, as:

$$T_{1|i} = USV = \begin{bmatrix} U_1 & U_2 \end{bmatrix} \begin{bmatrix} S_1 & 0 \\ 0 & 0 \end{bmatrix} \begin{bmatrix} V_1^T \\ V_2^T \end{bmatrix} = U_1 S_1 V_1 \tag{3.4}$$

where $U_1 \in \mathbb{R}^{N_o i \times N_o i}$ and $V_1 \in \mathbb{R}^{N_{\text{ref}} i \times N_{\text{ref}} i}$ are orthonormal matrices and $S_1 \in (\mathbb{R}^+)^{N_o i \times N_{\text{ref}} i}$ a diagonal matrix with the positive singular values in ascending order. Comparing eqs. (3.3) and (3.4), the observability and controllability matrices can be calculated, respectively, as:

$$\begin{aligned} \Gamma_i^{\text{ref}} &= U_1 S_1^{1/2} T \\ O_i &= T^{-1} S_1^{1/2} V_1^T \end{aligned} \tag{3.5}$$

where $T \in \mathbb{C}^{N_o i \times N_o i}$ is a non-singular transformation matrix. As stated in Section 2.3.3, the modal parameters of a state-space model are insensitive to the transformation matrix used in

[1] A Toeplitz matrix is a matrix that is constant along its main diagonal.

the application of the similarity transformation. Given this particular property, one can simply set $T = I$. Once this transformation matrix is defined, the identification of the stochastic state-space model (2.72) with **SSI-COV** becomes straightforward. By taking advantage of the shift structure of the observability and controllability matrices in eq. (3.3), the system matrices C and G^{ref} can be written in Matlab® notation, as:

$$\begin{aligned} C &= O_{i[1:N_o,:]} \\ G^{\text{ref}} &= \Gamma^{\text{ref}}_{i[:,N_{\text{ref}}(i-1)+1:N_{\text{ref}}i]} \end{aligned} \tag{3.6}$$

The state transition matrix A, on other hand, can be estimated in different ways, as discussed in Peeters (2000) and Overchee and De-Moor (1996). In the present work, it was adopted the approach proposed by Kung (1978), which calculates this matrix by taking advantage of the shift structure of the observability matrix. According to this approach, the state transition matrix is calculated as function of the two different partitions of the observability matrix:

$$A = O^{\dagger}_{i[1:N_o(i-1),:]} O_{i[N_o+1:N_o i,:]} \tag{3.7}$$

where $(\bullet)^{\dagger}$ denotes the Moore-Penrose pseudo-inverse of a matrix. Once the system matrices A, C and G^{ref} are identified by means of eqs. (3.6) and (3.7), the identification of the modal parameters is theoretically solved. The fourth system matrix R_0^{ref} is found as the zero-lag output covariance matrix (see eq. (2.110)). Because the discrete poles Λ_d and the observed mode shapes V are calculated by

$$\begin{aligned} A &= \Psi \Lambda_d \Psi^{-1} \\ V &= C\Psi \end{aligned} \tag{3.8}$$

it suffices to compute the state-space matrices A and C to estimate these parameters. Once these matrices are computed, the identification problem is solved and the eigenfrequencies are computed by means of eq. (2.67).

Example 6
The **FE** model of the lattice tower presented in Fig. 2.2 is again used to illustrate the application of the identification techniques discussed in this chapter. The noisy contaminated covariance matrix estimated in **Example 4** is used to compute the Toeplitz matrix according to eq. (3.1) with a number of time lags $i = 40$. Afterwards this matrix was used by the **SSI-COV** technique to the estimate the modal parameters of the tower structure. The stabilization diagram constructed by identifying state-space models with order n ranging from 2 to 50 is shown in Fig. 3.1a. The two zooms of Figs. 3.1b and 3.1c show that it is possible to identify the two pairs of close spaced modes around 1.29 and 3.9 Hz. The identification

results obtained with the **SSI-COV** technique are summarized in Tab. 3.5 located at the end of Section 3.5.3.

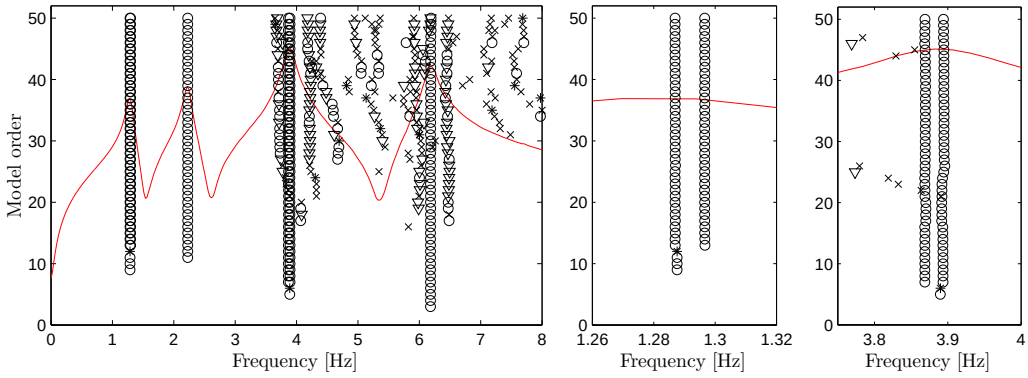

(a) (b) (c)

Fig. 3.1 – Stabilization diagram created with the **SSI-COV** technique by identifying models with order n ranging from 2 to 50 (a), and details of the two pairs of closed-spaced modes identified around 1.29 (b) and 3.87 Hz (b).

*3.2.2. The **SSI-DATA** Method*

Similarly to the **SSI-COV**, the **SSI-DATA** technique identifies the stochastic state-spaces models discussed in Section (2.5). The first implementations of the **SSI-DATA** algorithm are found, for instance, in Van Overschee and De Moor (1991, 1993). The original derivation of the **SSI-DATA** algorithm considered all the measured output responses as references. The idea of reducing the dimensions the of the system matrices by selecting just a subset of these responses as references was introduced by Peeters and De Roeck (1999a) and (1999b). One of the main advantages of the this identification method compared to its covariance-driven counterpart and to the frequency-domain estimators is that it identifies the modal parameters directly from the time series acquired in the vibration tests and, therefore, does not require any additional processing, neither to obtain the covariances nor the spectra matrices.

This particular characteristic, on its turn, implies in another advantage of the **SSI-DATA** with regard to the other **MPE** techniques, which is the possibility to decompose the measured outputs into modal responses. Detailed discussion and derivation of the **SSI-DATA** is found, for instance, in Overchee and De-Moor (1996), Ljung (1999) and Peeters (2000). Differently from the **SSI-COV**, which uses covariances as primary inputs, the **SSI-DATA** addresses the identification problem by projecting the row space of future outputs into the row space of past outputs. In fact, these projection plays the same role in the context of the identification with the **SSI-DATA** as the covariances with the **SSI-COV**. The idea behind this projection is to predict the future based on the useful information retained in the past. This projection is defined as:

$$\mathscr{P}_i^{\text{ref}} \equiv Y_f \Big/ Y_p^{\text{ref}} = Y_f (Y_p^{\text{ref}})^T (Y_p^{\text{ref}} (Y_p^{\text{ref}})^T)^\dagger Y_p^{\text{ref}} \tag{3.9}$$

where $Y_f \in \mathbb{R}^{N_o i \times N_k}$ and $Y_p^{\text{ref}} \in \mathbb{R}^{N_{\text{ref}} i \times N_k}$ are partitions of the block Hankel[2] matrix $H^{\text{ref}} \in \mathbb{R}^{(N_o+N_{\text{ref}})i \times N_k}$ defined as:

$$H^{\text{ref}} = \frac{1}{\sqrt{N_k}} \left[\begin{array}{cccc} y_0^{\text{ref}} & y_1^{\text{ref}} & \cdots & y_{N_k-1}^{\text{ref}} \\ y_1^{\text{ref}} & y_2^{\text{ref}} & \cdots & y_{N_k}^{\text{ref}} \\ \cdots & \cdots & \cdots & \cdots \\ y_{i-1}^{\text{ref}} & y_i^{\text{ref}} & \cdots & y_{i+N_k-2}^{\text{ref}} \\ \hline y_i & y_{i+1} & \cdots & y_{i+N_k-1} \\ y_{i+1} & y_{i+2} & \cdots & y_{i+N_k} \\ \cdots & \cdots & \cdots & \cdots \\ y_{2i-1} & y_{2i} & \cdots & y_{2i+N_k-2} \end{array}\right] = \left[\begin{array}{c} Y_{0|i-1}^{\text{ref}} \\ \hline Y_{i|2i-1} \end{array}\right] = \left[\begin{array}{c} Y_p^{\text{ref}} \\ \hline Y_f \end{array}\right] \begin{array}{l} \updownarrow \text{“past”} \\ \updownarrow \\ \updownarrow \text{“future”} \end{array} \tag{3.10}$$

It is worth noting that expression (3.9) is only a definition of the projection and, therefore, it is not intended to be used to calculate the projection $\mathscr{P}_i^{\text{ref}}$. Actually, this projection is calculated by applying the RQ factorization to the data Hankel matrix. Such factorization is given as follows:

$$H^{\text{ref}} = \left[\begin{array}{c} Y_p^{\text{ref}} \\ \hline Y_f \end{array}\right] = \left[\begin{array}{c} Y_{0|i}^{\text{ref}} \\ \hline Y_{i|i}^{\text{ref}} \\ \hline Y_{i+1|2i-1}^{-} \end{array}\right] = \left[\begin{array}{c} Y_p^{\text{ref}^+} \\ \hline Y_{i|i}^{\text{ref}} \\ \hline Y_f^{-} \end{array}\right] = RQ^T \tag{3.11}$$

where $Y_p^{\text{ref}^+}$, $Y_{i|i}^{\text{ref}}$ and Y_f^- are calculated by shifting the past and future outputs in the Hankel matrix by one block row; $Q \in \mathbb{R}^{N_k \times N_k}$ is an orthonormal matrix that satisfies $QQ^T = Q^T Q = I$ and $R \in \mathbb{R}^{(N_i+N_o)i \times N_k}$ a lower triangular matrix. These matrices can be expressed in terms of block rows and columns of the R and Q matrices, as follows:

$$H^{\text{ref}} = \begin{bmatrix} R_{11} & 0 & 0 & 0 \\ R_{21} & R_{22} & 0 & 0 \\ R_{31} & R_{32} & R_{33} & 0 \\ R_{41} & R_{42} & R_{43} & R_{44} \end{bmatrix} \begin{bmatrix} Q_1^T \\ Q_2^T \\ Q_3^T \\ Q_4^T \end{bmatrix} \tag{3.12}$$

From the definition (3.9) and the factorization (3.12), it is easy to derive the following orthogonal projections:

[2] In a Hankel matrix the elements suited in the anti-diagonal are constant.

$$\mathscr{P}_i^{\text{ref}} = \begin{bmatrix} R_{21} \\ R_{31} \\ R_{41} \end{bmatrix} Q_1^T, \quad \mathscr{P}_{i-1}^{\text{ref}} = \begin{bmatrix} R_{41} & R_{42} \end{bmatrix} \begin{bmatrix} Q_1^T \\ Q_2^T \end{bmatrix} \tag{3.13}$$

where $\mathscr{P}_{i-1}^{\text{ref}}$ is another projection which is calculated by shifting the past and future outputs in the Hankel matrix by one block row. Similar to the projection defined in eq. (3.9), this new projection is defined as:

$$\mathscr{P}_{i-1}^{\text{ref}} \equiv Y_f^- \Big/ Y_p^{\text{ref}+} \equiv Y_f^- (Y_p^{\text{ref}+})^T (Y_p^{\text{ref}+} (Y_p^{\text{ref}+})^T)^\dagger Y_p^{\text{ref}+} \tag{3.14}$$

From eq. (3.12), the partition $Y_{i|i}^{\text{ref}}$ can also be calculated as a function of the R and Q sub matrices:

$$Y_{i|i}^{\text{ref}} = \begin{bmatrix} R_{21} & R_{22} & 0 \\ R_{31} & R_{32} & R_{33} \end{bmatrix} \begin{bmatrix} Q_1^T \\ Q_2^T \\ Q_2^T \end{bmatrix} \tag{3.15}$$

Together with the projections $\mathscr{P}_i^{\text{ref}}$ and $\mathscr{P}_{i-1}^{\text{ref}}$, the partition $Y_{i|i}^{\text{ref}}$ will be also used to solve the identification problem with **SSI-DATA**.

Kalman Filter States

As discussed in Section 2.5.2, the Kalman filter provides an optimal prediction of the states x_k of a stochastic state-space model. These predictions, denoted as $\hat{x}_k$, are estimated by using the output measurements up to time instant $k-1$ $(y_0, y_1, \cdots, y_{k-1})$. If the initial state is $\hat{x}_0 = 0$, the corresponding covariance is given by $P_0 = \mathbf{E}[\hat{x}_0 \hat{x}_0^T]$ and the steady-state Kalman filter states $\hat{x}_k$ are estimated by the following recursive formula:

$$\begin{aligned} \hat{x}_k &= A\hat{x}_{k-1} + K_{k-1}(y_{k-1} - C\hat{x}_{k-1}) \\ K_{k-1} &= (G - AP_{k-1}C^T)(R_0 - CP_{k-1}C^T)^{-1} \\ P_k &= AP_{k-1}A^T + (G - AP_{k-1}C^T)(R_0 - CP_{k-1}C^T)^{-1}(G - AP_{k-1}C^T)^T \end{aligned} \tag{3.16}$$

where K_k is the Kalman filter gain and P_k the Kalman state covariance matrix. According to the main theorem of stochastic subspace identification, the projections $\mathscr{P}_i^{\text{ref}}$ can be factorized as (Overchee and De-Moor, 1996):

$$\mathscr{P}_i^{\text{ref}} = O_i \hat{X}_i = \begin{bmatrix} C \\ CA \\ \cdots \\ CA^{i-1} \end{bmatrix} \begin{bmatrix} \hat{x}_i & \hat{x}_{i+1} & \cdots & \hat{x}_{i+N_k-1} \end{bmatrix} \tag{3.17}$$

where $X_i \in \mathbb{R}^{n \times N}$ is The Kalman filter state sequence. The proof of the expression (3.17) is found in Overchee and De-Moor (1996). In eq. (3.16) it is considered that all the outputs are used as references. If only a subset of these responses are used as references, the following substitutions have to be made in eq. (3.16) (Peeters, 2000):

$$\begin{aligned} y_k &\rightarrow y_k^{\text{ref}} = L_s y_k \\ G &\rightarrow G L_s^T \\ C &\rightarrow L_s C \\ R_0 &\rightarrow R_0 L_s^T \end{aligned} \tag{3.18}$$

Applying the **SVD** to the projection matrix, $\mathscr{P}_i^{\text{ref}}$, and omitting the zero singular values and the corresponding singular vectors, yields:

$$\mathscr{P}_i^{\text{ref}} = U_1 S_1 V_1^T \tag{3.19}$$

where $U_1 \in \mathbb{R}^{N_o i \times n}$ and $V_1 \in \mathbb{R}^{N_{\text{ref}} i \times N_i i}$ are orthonormal matrices and $S_1 \in (\mathbb{R}^+)^{n \times n}$ a matrix containing the singular values in its main diagonal. The observability matrix and the Kalman filter state sequence are calculated by splitting the **SVD** in two parts:

$$\begin{aligned} O_i &= U_1 S_1^{1/2} T \\ \hat{X}_i &= O_i^{\dagger} \mathscr{P}_i^{\text{ref}} \end{aligned} \tag{3.20}$$

where the similarity transformation matrix can simply be defined as $T = I$. Once the projection $\mathscr{P}_i^{\text{ref}}$ is computed by means of eq. (3.13), the observability matrix O_i and the Kalman state sequence $\hat{X}_i$ can also be calculated using eqs. (3.20). The next step towards the solution of the identification problem consists of determining the system matrices A, G, C and R_0. The fist step to obtain these matrices is to factorize the projection $\mathscr{P}_{i-1}^{\text{ref}}$ defined in (3.14) into:

$$\mathscr{P}_{i-1}^{\text{ref}} = O_{i-1} \hat{X}_{i+1} \tag{3.21}$$

where observability matrix O_{i-1} is obtained by suppressing the last N_o rows of O_i:

$$O_{i-1} = O_{i[1:N_o(i-1),:]} \tag{3.22}$$

Since the projection $\mathscr{P}_{i-1}^{\text{ref}}$ is obtained using eq. (3.13), the Kalman state sequence $\hat{X}_{i-1}$ can be calculated as:

$$\hat{X}_{i+1} = O_{i-1}^{\dagger} \mathscr{P}_{i-1}^{\text{ref}} \tag{3.23}$$

From now on, the identification problem with **SSI-DATA** is straightforward. The system matrices A and C can now be calculated from following overdetermined set of linear equations, obtained by stacking the state-space models for time instants i to $i+N_k-1$:

$$\begin{bmatrix} \hat{X}_{i+1} \\ Y_{i|i} \end{bmatrix} = \begin{bmatrix} A \\ C \end{bmatrix} \hat{X}_i + \begin{bmatrix} W_i \\ V_i \end{bmatrix} \tag{3.24}$$

where $Y_{i|i} \in \mathbb{R}^{N_o \times N_k}$ is given by eq. (3.15), and $W_i \in \mathbb{R}^{n \times N_k}$ and $V_i \in \mathbb{R}^{N_o \times N_k}$ are the residuals. As the Kalman state sequence and the residuals are uncorrelated, the system matrices A and C can be computed in a linear least squares sense, as:

$$\begin{bmatrix} A \\ C \end{bmatrix} = \begin{bmatrix} \hat{X}_{i+1} \\ Y_{i|i} \end{bmatrix} \hat{X}_i^{\dagger} \tag{3.25}$$

These equations can be written in terms of the sub-matrices R and Q obtained with the QR factorization of the Hankel matrix (3.12). Substituting eqs. (3.13) and (3.15) into (3.25), and taking advantage of the orthogonality conditions of the Q factors, the system matrices A and C can be expressed as a function of the sub-matrices of the R factor only:

$$\begin{bmatrix} A \\ C \end{bmatrix} = \begin{bmatrix} O_{i-1}^{\dagger} R_{41} \\ R_{21} \\ R_{31} \end{bmatrix} \begin{bmatrix} R_{21} \\ R_{31} \\ R_{41} \end{bmatrix}^{\dagger} O_i \tag{3.26}$$

In practice, an important reduction of the computational time is verified if the Hankel matrix is replaced by the R factor. In this condition, the projections $\mathscr{P}_i^{\text{ref}}$ and $\mathscr{P}_{i-1}^{\text{ref}}$ can be computed using only the partitions of this matrix and neglecting Q sub-matrices in eqs. (3.13). This strategy avoids the calculation of the Q factors, resulting in a faster factorization of the Hankel matrix

H^{ref}. The Matlab® function `qr` (MathWorks, 2010) allows for the computation of R factor only. Once the system matrices A and C are computed by means of eq. (3.26), the covariances of the noise Q, R and S are computed as the covariances of the least squares residuals:

$$\begin{bmatrix} Q & S \\ S^T & R \end{bmatrix} = \begin{bmatrix} W_i \\ V_i \end{bmatrix} \begin{bmatrix} W_i^T & V_i^T \end{bmatrix} \tag{3.27}$$

and the stochastic system matrices G and R_0 are finally computed from the covariance matrices Q, R, S. The computation of the these system matrices starts by solving the Lyapunov equation for Σ:

$$\Sigma = A\Sigma A^T + Q \tag{3.28}$$

and then, they are finally computed as:

$$\begin{aligned} R_0 &= C\Sigma C^T + R \\ G &= A\Sigma C^T + S \end{aligned} \tag{3.29}$$

At this point all the system matrices A, C, G and R_0 are found. The system matrices A and C are sufficient to compute the discrete poles Λ_d and the observed mode shapes V, which are given by:

$$\begin{aligned} A &= \Psi \Lambda_d \Psi^{-1} \\ V &= C\Psi \end{aligned}$$

Once the model parameters are identified with the **SSI-COV** and **SSI-DATA** techniques, the approach described in Döhler and Mevel (2013) can be used to estimate their confidence intervals. In the context of the present thesis, however, the estimation of these uncertainties is performed by following another strategy, which takes advantage of the statistic properties of the **pMLE-MM**. This strategy will be detailed elaborated in Section 3.5.2.

3.2.3. Estimation of the Modal Responses and Prediction Errors

One of the main advantages of **SSI-DATA**, with regard to the other **OMA** estimators, is the possibility to estimate the responses of the identified modes and their contribution to the measured output responses by making use of the *Forward Innovation Model* discussed in Section 2.5.2. This approach can only be applied in conjunction with the **SSI-DATA** method, as the implementation of **SSI-COV** does not guarantee the positive realness of the identi-

fied covariance sequence and, therefore, it is not always possible to obtain a forward innovation model (Overchee and De-Moor, 1996; Peeters, 2000). The derivation of such approach starts by rewriting the discrete-time stochastic state-space model into the Forward Innovation form (2.81). This is accomplished by applying the steady-state Kalman Filter to the stochastic state-space model (2.72)(Peeters, 2000; Cara et al., 2013):

$$\begin{aligned} z_{k+1} &= Az_k + Ke_k \\ y_k &= Cz_k + e_k \end{aligned}$$

By pre-multiplying eqs. (3.2.3) by Ψ^{-1}, the following modal state-space model is obtained:

$$\begin{aligned} z_{m_{k+1}} &= \Lambda_d z_{m_k} + K_m e_k \\ y_k &= V\bar{z}_k + e_k \end{aligned} \tag{3.30}$$

where $z_{m_k} = \Psi^{-1} z_k \in \mathbb{C}^{n \times N_o}$ is the modal state vector containing the contributions of all modes and $K_m = \Psi^{-1} K \in \mathbb{C}^{n \times N_o}$ the *modal Kalman filter gain*. Isolating e_k in the second set of eqs. (3.30) and substituting the resulting equation into the first, yields:

$$\begin{aligned} z_{m_{k+1}} &= (\Lambda_d - K_m V) z_{m_k} + K_m y_k \\ e_k &= -V z_{m_k} + y_k \end{aligned} \tag{3.31}$$

As all matrices $(\Lambda_d - K_m, K_m, V)$ of the state-space model (3.31) are known, the modal state vector z_{m_k} and the innovation error sequence e_k are estimated using the output vector y_k as inputs. Once these vectors are estimated, it is possible to define a predicted output vector that contains the estimated output responses due to the identified modes:

$$\hat{y}_k = \sum_{m=1}^{N_m} \hat{y}_{k_m} = V z_{m_k} \tag{3.32}$$

where $\hat{y}_{k_m} \in \mathbb{C}^{N_o \times 1}$ is a predicted output vector containing the response of the m^{th} mode. Since Λ_d is a diagonal matrix containing the numerical and physical poles in complex conjugated pairs, it is possible to define a matrix $S_m \in \mathbb{R}^{n \times n}$ to select the modal response due to a certain mode m. Such matrix is composed by zeros, except the diagonal elements corresponding to eigenvalue m and its complex conjugate, which equal the unit. When the eigenvalues of matrix A are real, as there is no complex conjugate, only the element of diagonal of matrix S_m corresponding to the real eigenvalue equals the unit. By making use of this matrix, it is possible select only the set of physical the modes that contribute to the total response y_k. This is ac-

complished by reformulating eq. (3.32) into a summation of the contributions of the identified modes, as:

$$\hat{y}_k = \sum_{m=1}^{n} \hat{y}_{k_m} = \sum_{m=1}^{n} VS_m z_{m_k} \tag{3.33}$$

where m $(m = 1, 2, \ldots, n)$ corresponds to any of the n identified modes. Once the responses due to the modes are estimated, the measured response, y_k, at time instant k can be calculated as the summation of the estimated modal responses $\hat{y}_k$ plus the predicted error e_k:

$$y_k = \hat{y}_k + e_k \tag{3.34}$$

This expression can be reformulated in matrix notation for all N_k output samples, as:

$$Y = \hat{Y} + E \tag{3.35}$$

with

$$Y = \begin{bmatrix} y_1 & \cdots & y_{N_k} \end{bmatrix}^T \in \mathbb{R}^{N_k \times N_o}, \quad \hat{Y} = \begin{bmatrix} y_1 & \cdots & y_{N_k} \end{bmatrix}^T \in \mathbb{R}^{N_k \times N_o}, \quad E = \begin{bmatrix} e_1 & \cdots & e_{N_k} \end{bmatrix}^T \in \mathbb{R}^{N_k \times N_o} \tag{3.36}$$

where Y and $\hat{Y}$ are matrices containing all the measured and estimated output samples, respectively, and E is a matrix containing the corresponding predicted errors.

3.2.4. Contribution of the Estimated Modal Responses to the Measured Outputs

Once the responses due to each mode are estimated, it is possible to quantify the contributions of each mode to the measured output responses. In Cara et al. (2013), an index is proposed to quantify these contributions and its derivation starts by pre-multiplying eq. (3.35) by the transpose of the matrix containing the measured responses, Y, yielding:

$$Y^T Y = Y^T \hat{Y} + Y^T E \tag{3.37}$$

Retaining only the diagonal elements of $Y^T Y$, $Y^T \hat{Y}$ and $Y^T E$ which correspond, respectively, to the auto covariance of the measured outputs, cross covariance between the measured and estimated outputs, and cross covariance between the measured outputs and predicted errors, eq. (3.37) becomes:

$$(Y^T Y)_D = (Y^T \hat{Y})_D + (Y^T E)_D \tag{3.38}$$

where $(\bullet)_D$ stands for the diagonal operator: for a given a matrix M, the operator $(M)_D$ returns a matrix containing the elements of the main diagonal of M in its diagonal and zeros elsewhere. The diagonal elements of $(Y^T \hat{Y})_D$ and $(Y^T E)_D$ correspond to the cross covariance between the estimated and measured responses of output o, and to the cross covariance between predicted errors and the measured responses of output o, respectively. Normalizing eq. (3.38) by $(Y^T Y)_D^{-1}$ and retaining only the diagonal vectors of each term, yields:

$$\{1\}_{N_o} = \Delta_{\hat{y}} + \Delta_e \tag{3.39}$$

where $\{1\}_{N_o} = (Y^T Y)_D^{-1}(Y^T Y)_D$ is a column vector containing N_o elements equal to the unit, $\Delta_{\hat{y}} = (Y^T Y)_D^{-1}(Y^T \hat{Y})_D$ is a column vector containing the contribution of the identified modes to each measured response and $\Delta_e = (Y^T Y)_D^{-1}(Y^T E)_D$ is a column vector containing the contribution of the prediction errors to each measured response. Once the contributions $\Delta_{\hat{y}}$ and Δ_e are calculated, the *global contribution of the modes*, $\delta_{\hat{y}}$, and the *global contribution of the error*, δ_e, are calculated as the mean values of the components of these vectors:

$$\delta_{\hat{y}} = \frac{1}{N_o}\sum_{o=1}^{N_o} \Delta_{\hat{y}}^{(o)}, \quad \delta_e = \frac{1}{N_o}\sum_{o=1}^{N_o} \Delta_e^{(o)} \tag{3.40}$$

with $\Delta_{\hat{y}}^{(o)} \in \mathbb{R}$ denoting the contribution of the identified modes to output o and $\Delta_e^{(o)} \in \mathbb{R}$ the contribution of the predicted error to output o. The global contributions (3.40) quantify the degree of participation of the predicted responses due to the modes and the predicted errors on the measured outputs. Other useful information that can be extracted from the predicted modal responses is the degree of contribution of the response due to a certain identified mode to the measured responses. For instance, in the context the **OMA**, the analyst might be interested on assessing the modes which are likely to be more excited by environmental and/or operational conditions. The derivation of such contribution follows the same idea used to derive eq.(3.40) and starts by substituting eq. (3.32) into (3.34) and reformulating the resulting equation in matrix notation, yielding:

$$(Y^T Y)_D = (Y^T \hat{Y}_1)_D + (Y^T \hat{Y}_2)_D + \cdots + (Y^T \hat{Y}_{N_m})_D + (Y^T E)_D \tag{3.41}$$

Normalizing eq. (3.41) by $(Y^T Y)_D^{-1}$ and retaining only the diagonal vectors of the resulting

matrices, gives:

$$\{1\}_{N_o} = \Delta_{\hat{y}_1} + \Delta_{\hat{y}_2} + \cdots + \Delta_{\hat{y}_{N_m}} + \Delta_e \tag{3.42}$$

where $\{1\}_{N_o}$ is a column vector with N_o components, all equal to one and $\Delta_{\hat{y}_m} \in \mathbb{R}^{N_o \times 1}$ a column vector containing the contributions of mode m to each measured output. The modal contribution of mode m to the measured outputs, $\delta_{\hat{y}_m} \in \mathbb{R}$, is calculated as the mean value of the components of $\Delta_{\hat{y}_m}$:

$$\delta_{\hat{y}_m} = \frac{1}{N_o} \sum_{o=1}^{N_o} \Delta_{\hat{y}_m}^{(o)} \tag{3.43}$$

where $\Delta_{\hat{y}_m}^{(o)} \in \mathbb{R}$ is the contribution of mode m to output o. The relation between the global contribution of the modes, $\delta_{\hat{y}}$, and the contribution of each mode, $\delta_{\hat{y}_m}$, is given by:

$$\sum_{m=1}^{N_m} \delta_{\hat{y}_m} + \delta_e = \delta_{\hat{y}} + \delta_e = 1 \tag{3.44}$$

Example 7
The output responses contaminated with noise of **Example 3** is used by the **SSI-DATA** technique to the estimate the model parameters of the tower structure. The estimation with **SSI-DATA** starts by computing the Hankel matrix according to eq. (3.10). Next, the R-factor of this matrix is computed using eq. (3.12). The R-factor sub-matrices are then used compute the state-space matrices A and C, which are found by means of eq. (3.26). A stabilization diagram was constructed by identifying models with order n ranging from 2 to 50, as shown in Fig. 3.2a. The two zooms of Figs. 3.2b and 3.2c show that it is possible to identify the two pairs of close spaced modes around 1.29 and 3.9 Hz.

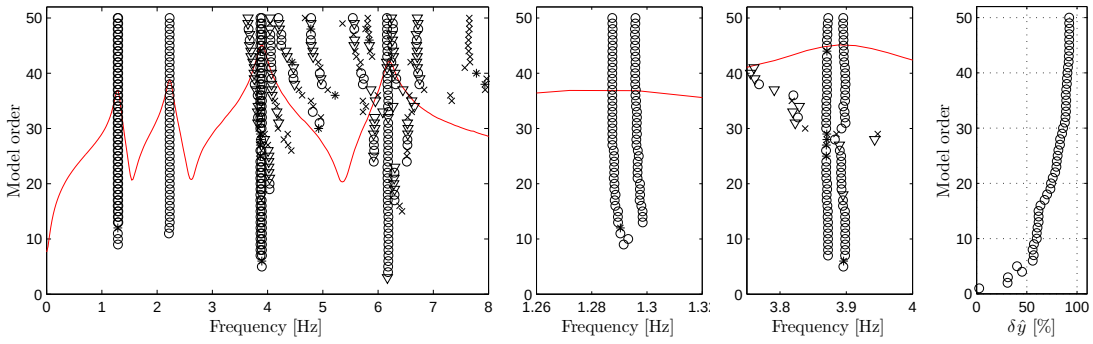

Fig. 3.2 – Stabilization diagram created with the **SSI-DATA** technique with $i = 20$ and $n_{max} = 50$ (a), detail of the two pair of close spaced modes around 1.29 (b) and 3.9 Hz (c), and variation of contribution of the identified modes to the total responses over the different model orders (d).

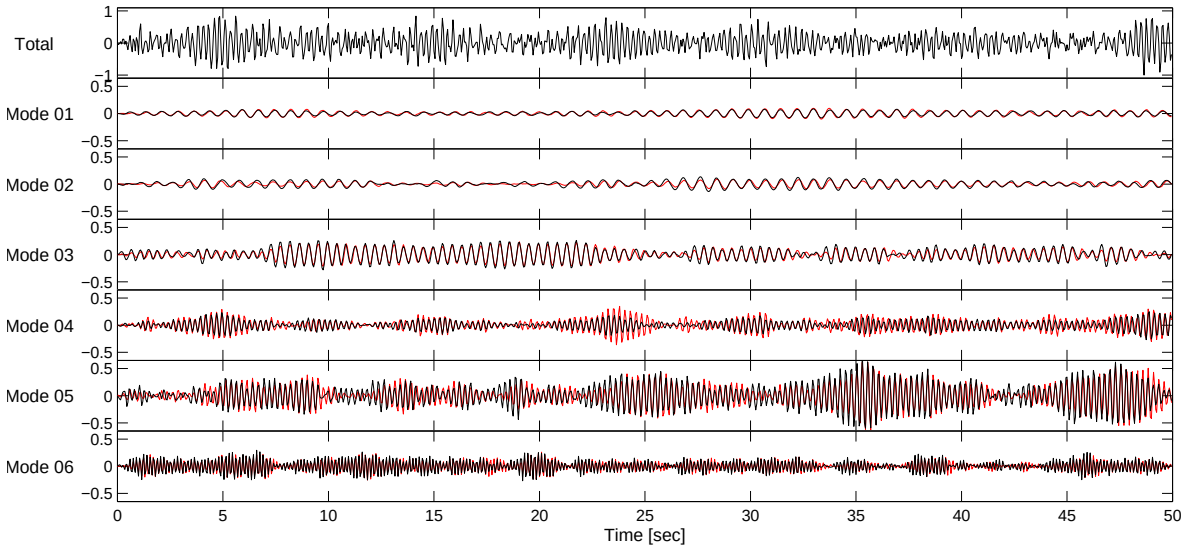

Fig. 3.3 – Modal responses of the tower example with normalized amplitudes measured at node 4 in *x*-axis direction: exact (black line) and estimated (red line) responses.

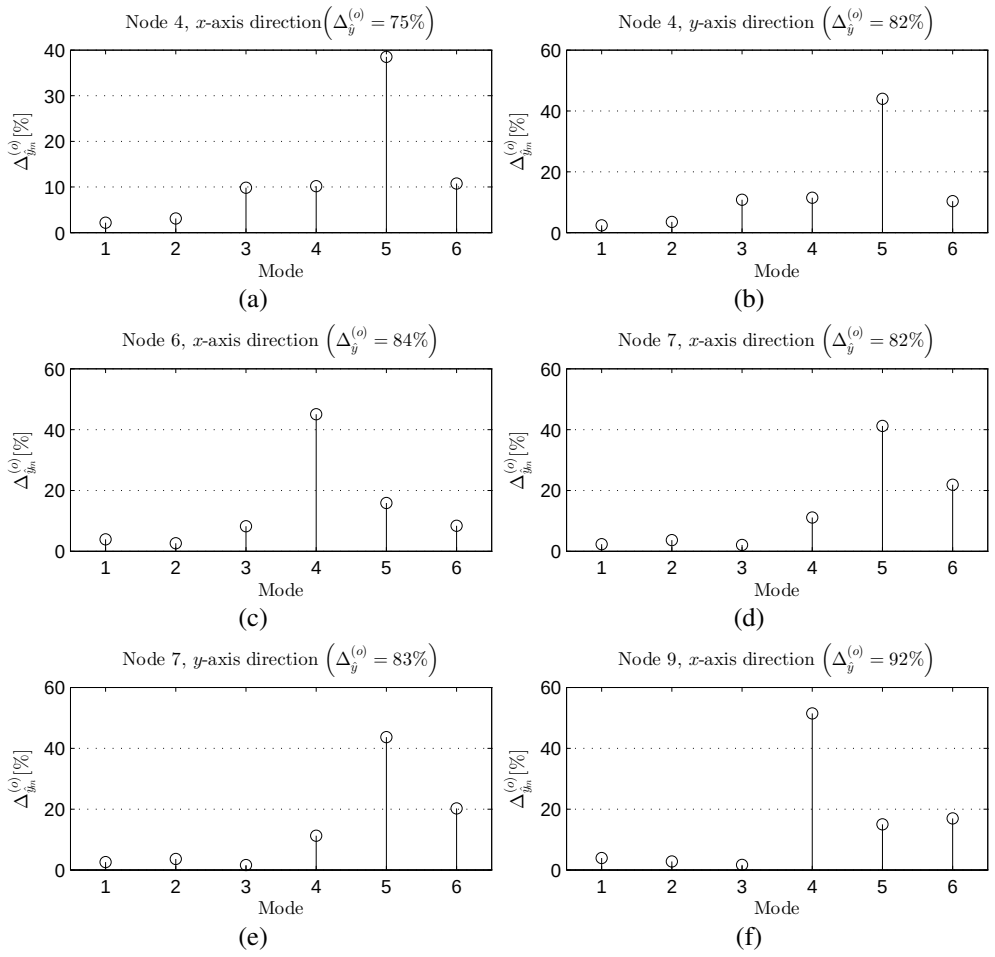

Fig. 3.4 – Contribution of the response of each identified mode to the total responses measured at: node 4 in *x* (a) and *y*-axis (b) directions, node 6 in *x*-axis (c) direction, node 7 in *x* (d) and *y*-axis (e) directions, and at node 9 in *x*-axis direction (f).

Afterwards the modal responses and their respective modal contributions were estimated using the procedure described in Section 3.2.4. The variation of the global contribution of the modes $\delta_{\hat{y}}$ with identified model orders is shown in Fig. 3.2d and the modal responses of **DOF** 4 in x-axis direction is compared to the exact response in Fig. 3.3.

In Figs. 3.4 and 3.5 are shown the contributions of these modal responses to the output responses measured at each **DOF**, $\Delta^{(o)}_{\hat{y}_m}$, and the global contribution of the identified modes to the measured output vector, $\delta_{\hat{y}}$, respectively. By inspecting these figures, it is verified that the 4th, 5th and 6th vibration modes are those which tend to be more excited by the white noise sequences used as inputs. The identification results obtained with the **SSI-DATA** technique are presented in Tab. 3.5 located at the end of Section 3.5.3.

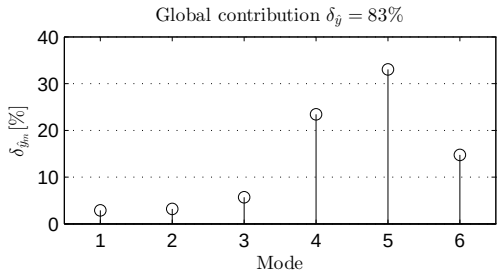

Fig. 3.5 – Global contribution of the identified modes to total measured responses.

3.3. Identification of Common Denominator Models

3.3.1. Least Squares Complex Frequency-domain Method

The Least Squares Complex Frequency-domain (Guillaume and Schoukens, 1998; Van-der Auweraer et al., 2001; Verboven et al., 2005; El-Kafafy, 2013) (**LSCF**) is an identification method commonly used in **EMA** and **OMA**. The basic idea of this technique is to identify the modal parameters by fitting the **FRF** matrix modelled by the common denominator model to the measured **FRF** matrix. As described in Section 2.10 the **FRF** matrix in common denominator model is expressed by:

$$\hat{H}_k(\Theta,\omega) = \frac{\mathbf{N}_k(\Theta,\omega)}{\mathbf{d}(\Theta,\omega)} \tag{3.45}$$

where the numerator matrix $\mathbf{N}_k(\Theta,\omega_f)$ and the denominator scalar $\mathbf{d}(\Theta,\omega)$ are given, respectively, by:

$$\mathbf{N}_k(\Theta,\omega) = \sum_{r=0}^{n} \beta_{kr}\Omega_r(\omega), \quad k = 1,2,\cdots,N_oN_i \tag{3.46}$$

and

$$\mathbf{d}(\Theta,\omega)=\sum_{r=0}^{n}\alpha_r\Omega_r(\omega) \tag{3.47}$$

where $\Omega_r(\omega)=\mathrm{z}^r$, with z denoting the z-domain polynomial basins, Δt represents the sampling time and ω_f the circular frequency. The coefficients α_r and β_{kr} are the unknown parameters to be estimated. For identification purposes, these coefficients are stacked on the top of each other as follows:

$$\Theta=\begin{bmatrix}\beta_1\\ \vdots\\ \beta_{N_oN_i}\\ \alpha\end{bmatrix},\quad \beta_k=\begin{bmatrix}\beta_{k0}\\ \vdots\\ \beta_{kn}\end{bmatrix},\quad \alpha=\begin{bmatrix}\alpha_0\\ \vdots\\ \alpha_n\end{bmatrix} \tag{3.48}$$

The estimates of the polynomial coefficients can be obtained by minimizing the following **N**on-linear **L**east-**S**quares (**NLS**) cost function with respect to the parameter Θ:

$$l_{NLS}\sum_{k=1}^{N_oN_i}\sum_{f=1}^{N_f}\left|E_k^{NLS}(\Theta,\omega_f)\right|^2 \tag{3.49}$$

with the non-linear equation error $E_k^{NLS}(\Theta,\omega_f)$ given by:

$$E_k^{NLS}(\Theta,\omega_f)=\frac{\mathbf{N}_k(\Theta,\omega_f)}{\mathbf{d}(\Theta,\omega_f)}-H_k(\omega_f) \tag{3.50}$$

where $H_k(\omega_f)$ is the element k $(k=1,2,\cdots,N_oN_i)$ of the measured **FRF** matrix, $\omega_f=2\pi f$ $\left(f=f_1,f_2,\cdots,f_{N_f}\right)$ are the discrete frequencies at which **FRF** measurements are available, with N_f denoting the number of frequency lines. The **NLS** cost function (3.49) can be approximated by a linear one by:

$$l_{LS}\sum_{k=1}^{N_oN_i}\sum_{f=1}^{N_f}\left|E_k^{LS}(\Theta,\omega_f)\right|^2 \tag{3.51}$$

with

$$E_k^{LS}(\Theta,\omega_f)=\mathbf{N}_k(\Theta,\omega_f)-\mathbf{d}(\Theta,\omega_f)H(\omega_f) \tag{3.52}$$

where $E_k^{LS}(\Theta,\omega_f)=\mathbf{d}(\Theta,\omega_f)E_k^{NLS}(\Theta,\omega_f)$ is the linearised equation error. Since eq. (3.52) is

linear in the parameters, it follows that:

$$J^H E(\Theta) = J^H J\Theta \approx 0, \quad E(\Theta) = \begin{bmatrix} E_k^{LS}(\Theta, \omega_1) \\ \vdots \\ E_k^{LS}(\Theta, \omega_{N_f}) \end{bmatrix} \tag{3.53}$$

where J is the so-called Jacobian matrix, which is given by:

$$J = \begin{bmatrix} X_1 & 0 & \cdots & 0 & Y_1 \\ 0 & X_2 & \cdots & 0 & Y_1 \\ \vdots & \vdots & \ddots & \vdots & \vdots \\ 0 & 0 & \cdots & X_{N_o N_i} & Y_{N_o N_i} \end{bmatrix} \tag{3.54}$$

with

$$X_k = \begin{bmatrix} \Omega_0(\omega_1) & \cdots & \Omega_1(\omega_1) & \Omega_n(\omega_1) \\ \vdots & \ddots & \vdots & \vdots \\ \Omega_0(\omega_{N_f}) & \cdots & \Omega_1(\omega_{N_f}) & \Omega_n(\omega_{N_f}) \end{bmatrix} \in \mathbb{C}^{N_f \times (n+1)} \tag{3.55}$$

and

$$Y_k = \begin{bmatrix} \Omega_0(\omega_1)H_k(\omega_1) & \cdots & \Omega_1(\omega_1)H_k(\omega_1) & \Omega_n(\omega_1)H_k(\omega_1) \\ \vdots & \ddots & \vdots & \vdots \\ \Omega_0(\omega_{N_f})H_k(\omega_{N_f}) & \cdots & \Omega_1(\omega_{N_f})H_k(\omega_{N_f}) & \Omega_n(\omega_{N_f})H_k(\omega_{N_f}) \end{bmatrix} \in \mathbb{C}^{N_f \times (n+1)} \tag{3.56}$$

Given the structure of the Jacobian matrix, the normal equations (3.53) can be reformulated as:

$$\begin{bmatrix} R_1 & 0 & \cdots & 0 & S_1 \\ 0 & R_2 & \cdots & 0 & S_2 \\ \vdots & \vdots & \ddots & \vdots & \vdots \\ 0 & 0 & \cdots & R_{N_o N_i} & S_{N_o N_i} \\ S_1^T & S_1^T & \cdots & S_{N_o N_i}^T & \sum_{k=1}^{N_o N_i} T_k \end{bmatrix} \begin{Bmatrix} \beta_1 \\ \beta_2 \\ \vdots \\ \beta_{N_o N_i} \\ \alpha \end{Bmatrix} = 0 \tag{3.57}$$

with

$$R_k = \mathrm{Re}\left(X_k^H X_k\right) \in \mathbb{R}^{(n+1)\times(n+1)}, \quad S_k = \mathrm{Re}\left(X_k^H Y_k\right) \in \mathbb{R}^{(n+1)\times(n+1)}, \quad T_k = \mathrm{Re}\left(Y_k^H Y_k\right) \in \mathbb{R}^{(n+1)\times(n+1)} \tag{3.58}$$

Due to their Toeplitz structure, the normal matrices R_k, S_k and T_k can be computed in a time efficient way by using the **FFT** (Cauberghe et al., 2004). Since the denominator polynomial coefficient α is sufficient to compute the poles, this parameter can be calculated by eliminating the numerator coefficients β_k from Eqs. (3.57). This elimination starts by calculating the numerator coefficients from the first set of equations (3.57):

$$\beta_k = -R_k^{-1} S_k \alpha \tag{3.59}$$

Afterwards, they are eliminated from the normal equations by substituting (3.59) into the last equation (3.57), yielding:

$$\sum_{k=1}^{N_o N_i} (T_k - S_k^T R_k^{-1} S_k)\alpha = 0 \tag{3.60}$$

or in a more compact form

$$M\alpha = 0 \tag{3.61}$$

with

$$M = \sum_{k=1}^{N_o N_i} (T_k - S_k^T R_k^{-1} S_k) \tag{3.62}$$

In order to avoid the trivial solution, a constraint has to be imposed to the α coefficients. This can be done by imposing one of the coefficients is equal to a non-zero constant value. Assuming, for instance, that the last coefficient is constrained to 1, eq. (3.61) becomes:

$$\alpha_{LS} = \begin{Bmatrix} -M_{[1:n,1:n]}^{-1} M_{[1:n,n+1]} \\ 1 \end{Bmatrix} \tag{3.63}$$

Once the denominator coefficients are found, back substitution based in eq. (3.59) can be done to compute the numerator coefficients β_k. At this point the identification problem is solved with **LSCF**. The poles are found as the roots of the denominator polynomial, **d**, and the modal

residues, $[Res]_r$, are obtained by following either of the two strategies described in Section 2.10. Although the confidence bounds on the **LSCF** estimates can be computed by using the approach presented in De Troyer et al. (2009a), another procedure is proposed in this thesis to estimate such uncertainties. This approach consists of using one Gauss-Newton iteration of the **MLE-MM**. This will be detailed described in Section 3.5.1.

3.3.2. Maximum Likelihood Estimator

One of the advantages of the **LS**-based identification techniques is their ability to handle a large amount of data and estimate the modal parameters in a reasonable computational time. Despite this efficiency, the estimates provided by these techniques are not always accurate enough. In such circumstances, more precise non-linear estimators as the **MLE** can be employed to improve the precision of these estimates (Guillaume, 1992; Pintelon and Schoukens, 2001). In this section, the implementation of the **MLE** formulated to estimate the parameters of the common denominator models (**MLE-CDM**) is presented. Two variants of the **MLE-CDM** exist and the difference between them relies upon the cost function to be minimized, which can be either a linear or logarithmic cost function, and on the type of the parameters to optimized, i.e, complex or real. Detailed discussion about these variants is found, for instance, in El-Kafafy (2013).

In this section, the **MLE-CDM** with logarithmic cost function and real coefficients is addressed. This logarithmic **ML** is more robust to the noise assumptions made as well as to outliers, and can handle measurements with a large dynamic range (Guillaume, 1992). Moreover, the logarithmic cost function tends to be smoother than the traditional non-linear least squares cost function resulting in a larger convergence region (Arruda, 1992). The **ML** estimate Θ_{ML} of the polynomial coefficients of the common denominator model is obtained in non-linear least squares sense using the estimated parameters from a preliminary **LS** identification as starting guess. This logarithmic weighted cost function is expressed by (Guillaume and Schoukens, 1998):

$$\sum_{k=1}^{N_o N_i} \sum_{f=1}^{N_f} l(\Theta)_{Log-ML-CDM} = \left| E_k^{\log}(\omega_f, \Theta) \right|^2 \tag{3.64}$$

with the logarithmic equation error $E_k^{\log}(\omega_f, \Theta)$ given as:

$$E_k^{\log}(\omega_f, \Theta) = \frac{\log\left(\hat{H}_k(\omega_f, \Theta)/H_k(\omega_f)\right)}{\sigma_{H_k(\omega_f)}/\left|H_k(\omega_f)\right|} \tag{3.65}$$

where $\hat{H}_k(\omega_f, \Theta)$ is the **FRF** to be fitted to the measured **FRF** $H_k(\omega_f)$ and $\sigma_{H_k(\omega_f)}$ is the stan-

dard deviation of the noise.

Gauss-Newton optimization

The advantage of the **MLE** with regard to the **LS**-based techniques is the possibility to take into account the quality of the measured **FRF**s during the parametric identification and, therefore, to provide the optimized modal parameters together with there uncertainty bounds. The **ML** parameters Θ_{ML} is obtained by minimizing eq. (3.65) in an iterative manner. This is done by means of a Gauss-Newton optimization algorithm, which takes advantage of the quadratic form of the logarithmic cost function (3.65). Each Gauss-Newton iteration is performed in two steps:

1. Solve the normal equations

$$J_i^H J_i \Delta\Theta_i = -J_i^H E_i \quad \text{for} \quad \Delta\Theta_i. \tag{3.66}$$

2. Compute an update of the previous solution

$$\Theta_{i+1} = \Theta_i + \Delta\Theta_i \tag{3.67}$$

with $E_i = E(\Theta_i)$ denoting the equation error and $J_i = \frac{\partial E(\Theta_i)}{\partial \Theta_i}$ the Jacobian matrix evaluated at the i^{th} iteration. The equation error or so-called residual vector, $E(\Theta)$, is computed at each iteration by:

$$E(\Theta_i) = \begin{Bmatrix} E_1^{\log}(\Theta_i) \\ E_2^{\log}(\Theta_i) \\ \vdots \\ E_{N_o N_i}^{\log}(\Theta_i) \end{Bmatrix} \in \mathbb{C}^{N_o N_i N_f \times 1}, \quad E_k^{\log}(\Theta_i) = \begin{Bmatrix} \frac{\log\left(\hat{H}_k(\omega_1,\Theta_i)/H_k(\omega_1)\right)}{\sigma_{H_k(\omega_1)}/|H_k(\omega_1)|} \\ \frac{\log\left(\hat{H}_k(\omega_2,\Theta_i)/H_k(\omega_2)\right)}{\sigma_{H_k(\omega_2)}/|H_k(\omega_2)|} \\ \vdots \\ \frac{\log\left(\hat{H}_k(\omega_{N_f},\Theta_i)/H_k(\omega_{N_f})\right)}{\sigma_{H_k(\omega_{N_f})}/\left|H_k(\omega_{N_f})\right|} \end{Bmatrix} \in \mathbb{C}^{N_f \times 1}, \quad k = 1,\ldots,N_o N_i \tag{3.68}$$

The Jacobian matrix in eq. (3.66) has the same structure as that of (3.54). The entries X_k and Y_k in this matrix, on the other hand, are calculated, respectively, by:

$$X_k = \begin{bmatrix} \frac{\Omega_0(\omega_1)|H_k(\omega_1)|}{\sigma_{H_k(\omega_1)}\mathbf{N}_k(\omega_1,\Theta)} & \frac{\Omega_1(\omega_1)|H_k(\omega_1)|}{\sigma_{H_k(\omega_1)}\mathbf{N}_k(\omega_1,\Theta)} & \cdots & \frac{\Omega_n(\omega_1)|H_k(\omega_1)|}{\sigma_{H_k(\omega_1)}\mathbf{N}_k(\omega_1,\Theta)} \\ \vdots & \vdots & \ddots & \vdots \\ \frac{\Omega_0(\omega_{N_f})\left|H_k(\omega_{N_f})\right|}{\sigma_{H_k(\omega_{N_f})}\mathbf{N}_k(\omega_{N_f},\Theta)} & \frac{\Omega_1(\omega_{N_f})\left|H_k(\omega_{N_f})\right|}{\sigma_{H_k(\omega_{N_f})}\mathbf{N}_k(\omega_{N_f},\Theta)} & \cdots & \frac{\Omega_n(\omega_{N_f})\left|H_k(\omega_{N_f})\right|}{\sigma_{H_k(\omega_{N_f})}\mathbf{N}_k(\omega_{N_f},\Theta)} \end{bmatrix} \in \mathbb{C}^{N_f \times (n+1)} \tag{3.69}$$

and

$$Y_k = \begin{bmatrix} \frac{-\Omega_0(\omega_1)|H_k(\omega_1)|}{\sigma_{H_k(\omega_1)}\mathbf{d}(\omega_1,\Theta)} & \frac{-\Omega_1(\omega_1)|H_k(\omega_1)|}{\sigma_{H_k(\omega_1)}\mathbf{d}(\omega_1,\Theta)} & \cdots & \frac{-\Omega_n(\omega_1)|H_k(\omega_1)|}{\sigma_{H_k(\omega_1)}\mathbf{d}(\omega_1,\Theta)} \\ \vdots & \vdots & \ddots & \vdots \\ \frac{-\Omega_0(\omega_{N_f})\left|H_k(\omega_{N_f})\right|}{\sigma_{H_k(\omega_{N_f})}\mathbf{d}(\omega_{N_f},\Theta)} & \frac{-\Omega_1(\omega_{N_f})\left|H_k(\omega_{N_f})\right|}{\sigma_{H_k(\omega_{N_f})}\mathbf{d}(\omega_{N_f},\Theta)} & \cdots & \frac{-\Omega_n(\omega_{N_f})\left|H_k(\omega_{N_f})\right|}{\sigma_{H_k(\omega_{N_f})}\mathbf{d}(\omega_{N_f},\Theta)} \end{bmatrix} \in \mathbb{C}^{N_f\times(n+1)} \tag{3.70}$$

Given the block structure of the Jacobian matrix, the normal equations (3.66) can be reformulated as:

$$\begin{bmatrix} R_1 & 0 & \cdots & 0 & S_1 \\ 0 & R_2 & \cdots & 0 & S_2 \\ \vdots & \vdots & \ddots & \vdots & \vdots \\ 0 & 0 & \cdots & R_{N_oN_i} & S_{N_oN_i} \\ S_1^T & S_1^T & \cdots & S_{N_oN_i}^T & \sum_{k=1}^{N_oN_i} T_k \end{bmatrix} \begin{Bmatrix} \Delta\beta_1 \\ \Delta\beta_2 \\ \vdots \\ \Delta\beta_{N_oN_i} \\ \Delta\alpha \end{Bmatrix} = \begin{Bmatrix} \mathrm{Re}\left(X_1^H E_1\right) \\ \mathrm{Re}\left(X_2^H E_2\right) \\ \vdots \\ \mathrm{Re}\left(X_{N_oN_i}^H E_{N_oN_i}\right) \\ \sum_{k=1}^{N_oN_i}\mathrm{Re}\left(Y_k^H E_k\right) \end{Bmatrix} \tag{3.71}$$

where $R_k = \mathrm{Re}\left(X_k^H X_k\right) \in \mathbb{R}^{(n+1)\times(n+1)}$, $S_k = \mathrm{Re}\left(X_k^H Y_k\right) \in \mathbb{R}^{(n+1)\times(n+1)}$ and $T_k = \mathrm{Re}\left(Y_k^H Y_k\right) \in \mathbb{R}^{(n+1)\times(n+1)}$. By taking advantage of the block structure of the normal equations (3.71), the numerator and the denominator coefficients can be isolated from each other and updated separately, as follows:

$$\Delta\beta_k = R_k^{-1}\left(\mathrm{Re}\left(X_k^H E_k\right) + S_k\Delta\alpha\right) \tag{3.72}$$

$$\sum_{k=1}^{N_oN_i}\left(T_k - S_k^T R_k^{-1} S_k\right)\Delta\alpha = -\sum_{k=1}^{N_oN_i}\left(\mathrm{Re}\left(Y_k^H E_k\right) - S_k^T R_k^{-1}\mathrm{Re}\left(X_k^H E_k\right)\right) \tag{3.73}$$

Once the denominator coefficients α are calculated in the last iteration by means of (3.73), eq. (3.72) can be used to compute the numerator coefficients β. The poles can be estimated as the roots of the common denominator $\mathbf{d}(\omega_f,\Theta)$ with the coefficients α, and the mode shapes and operational factors are computed by following the procedure described in Section 2.10.

Estimation of the uncertainty bounds

The **MLE-CDM** takes into account not only the measured **FRF**s, but also the noise information during the parametric estimation of the polynomial coefficients of the common denominator model, therefore, apart from providing optimized estimates of the modal parameters, they also yield the confidence intervals of these estimates. The estimation of these confidence intervals is given as the Cramér-Rao lower bound on the estimated modal parameters (Pintelon and Schoukens, 2001), assuming that the noise on the measured **FRF** is disseminated to the modal

parameters. As shown in Schoukens and Pintelon (1991), if real coefficients are used to model the parameters of the common denominator model, a good approximation of the covariance of the parameters Θ_{ML} is obtained by:

$$\mathrm{Cov}(\hat{\Theta}_{ML}) \simeq \left[2\mathrm{Re}\left(J_l^H J_l\right)\right]^{-1} \tag{3.74}$$

with J_l standing for the Jacobian matrix evaluated in the last iteration of the Gaussian-Newton algorithm. In practice, one is mainly interested in the uncertainty on the natural frequencies and the damping ratios and, therefore, only the covariance matrix of the denominator coefficients can be used to computed these uncertainties. In this case, the computation of these uncertainties is accomplished without significant loss in precision, but with considerable reduction of the computational time, by means of the following expression:

$$\mathrm{Cov}(\hat{\alpha}) \simeq \mathbf{E}\left[\Delta\alpha(\Delta\alpha)^H\right] \tag{3.75}$$

Assuming that the noise on the **FRF**s are uncorrelated and that no correlation exists between the residuals E_l, the covariance (3.75) reduces to:

$$\mathrm{Cov}(\hat{\alpha}) \simeq \left[\sum_{k=1}^{N_o N_i}\left(T_k - S_k^T R_k^{-1} S_k\right)\right]^{-1} \tag{3.76}$$

This strategy avoids the inversion of full matrix in eq. (3.71), resulting in a significant reduction of computational time. Once the covariance of the denominator coefficients are computed, the covariance of the natural frequencies and damping ratios can be estimated using the approach described in Pintelon et al. (2007).

Convergence of the ML Algorithm

The **MLE-CDM** optimizes iteratively the starting estimates provided by the **LSCF**. This is accomplished by setting a maximum number of iterations and a value for the relative error between two consecutive iterations (i.e. $|l(\Theta_{i+1}) - l(\Theta_i)|/l(\Theta_i)$, with l denoting the cost function to be minimized and i the iteration number). In order to avoid local minima and enlarge the convergence region of the Gauss-Newton algorithm, the following Levenberg-Marquardt form of eq. (3.66) should be used (Pintelon and Schoukens, 2001) to ensure that the cost function decreases during the performed iterations:

$$\left(J_i^H J_i + \lambda_{LM}(J_i^H J_i)_D\right) = -\Delta\Theta_i J_i^H E_i \tag{3.77}$$

Increasing the Levenberg-Marquardt parameter λ_{LM} in eq. (3.77) forces the cost function to decrease, but reduces the convergence speed. Normally $\lambda_{LM} = 0$ is used as an initial value and then it is adapted in every iteration according to the variation of the cost function. If the cost function increases, the value of parameter λ_{LM} is increased, otherwise, it is decreased (Cauberghe, 2004).

Example 8
The half spectra matrix of the lattice tower structure estimated with the correlogram approach (see Section 2.7) in **Example 4** is used to illustrate the identification with the **LSCF** method and **MLE-CDM**. Firstly, the parameters Θ of the common denominator model are estimated from the measured spectra matrix by means of the **LSCF** technique using a model with order $n = 70$. Afterwards these parameters are used as a starting guess by the **MLE-CDM**. The estimation with the **MLE-CDM** is only possible if the measured half spectra and their variances are taken into account in the cost function (3.64).

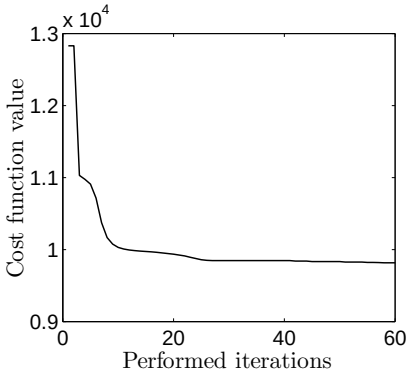

Fig. 3.6 – Convergence of the **MLE-CDM** cost function over the performed iterations.

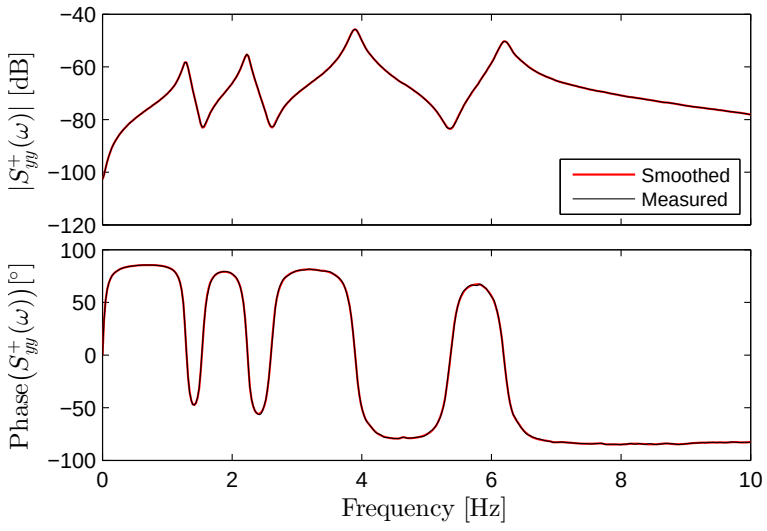

Fig. 3.7 – Elements (1,1) of the estimated half spectra matrix S^+_{yy} (red line) and the corresponding spectrum synthesized after 60 iterations of **MLE-CDM** (black line): absolute value (top) and phase (bottom).

As the noise information is not measurable during an output-only vibration test, the variances of the measured half spectra are estimated by using the square absolute of residual errors from the preliminary estimation with the **LSCF** estimator (see Section 2.7.1). These residual errors between the measured and modelled spectra are smoothed by making use of a Hanning window with shape parameter $\gamma = 41$.

Once the standard deviations of the half spectra are estimated, the optimization of the starting parameters with **MLE-CDM** was performed iteratively with the Guass-Newton algorithm combined with Levenberg-Marquardt approach to ensure that the cost function decreases with the performed iterations. A total of 60 iterations was performed to optimize the starting guess provided by the **LSCF** technique. The variation of the cost function over the performed iterations is shown in Fig. 3.6. In Fig. 3.7, the element(1,1) of measured spectra matrix is compared to the spectrum synthesized from the estimates provided by **MLE-CDM** after 60 iterations (smoothed spectrum).

3.4. Identification of Right Fraction Description Models

3.4.1. Poly-reference Least Squares Complex Frequency-domain Method

The Poly-reference Least Squares Complex Frequency-domain (**pLSCF**) technique, also known by its commercial name as PolyMAX (Peeters et al., 2004c), identifies the so-called **RMFD** models. In fact, this technique consists of a poly-reference version of the **LSCF** estimator and was initially proposed by Guillaume et al. (2003) for **EMA**. Afterwards the technique was also extended to **OMA** (Peeters et al., 2007). More details on the implementation of this technique are found, for instance, in (Peeters et al., 2004b,a). In case of **EMA**, the following equation is assumed to model the measured **FRF** matrix:

$$\hat{H}(\Theta, \omega_f) = \mathbf{N}(\Theta, \omega_f)\mathbf{D}(\Theta, \omega_f)^{-1} \tag{3.78}$$

where $\hat{H}(\Theta, \omega_f) \in \mathbb{C}^{N_o \times N_i}$ is the **FRF** matrix to be estimated, $\mathbf{N}(\Theta, \omega_f) \in \mathbb{C}^{N_o \times N_i}$ and $\mathbf{D}(\Theta, \omega_f) \in \mathbb{C}^{N_o \times N_i}$ are the numerator and the denominator polynomials, respectively. These matrices are parametrized, respectively, as:

$$\mathbf{N}(\Theta, \omega_f) = \sum_{r=0}^{n} \Omega_r(\omega_f)\beta_r, \quad \mathbf{D}(\Theta, \omega_f) = \sum_{r=0}^{n} \Omega_r(\omega_f)\alpha_r \tag{3.79}$$

where $\beta_r \in \mathbb{C}^{N_o \times N_i}$ and $\alpha_r \in \mathbb{C}^{N_i \times N_i}$ are the numerator and denominator polynomial coefficients, respectively. For a model having N_o outputs and N_i inputs, each row of the **RMFD** model is given as:

$$\hat{H}_o(\Theta, \omega_f) = \sum_{r=0}^{n} \Omega_r(\omega_f)\beta_{or}\left(\sum_{r=0}^{n} \Omega_r(\omega_f)\alpha_r\right)^{-1}, \quad o = 1, 2, \cdots, N_o \tag{3.80}$$

with $\hat{H}_o(\Theta, \omega_f)$ denoting the row vector containing the estimated **FRF**s of the output o and $\beta_{or} \in \mathbb{C}^{1\times N_i}$ the row vector containing the o^{th} row of the numerator matrix polynomial coefficient. These numerator matrices together with the denominator matrices α_r are the parameters to be estimated by the **pLSCF** method. All these coefficients are stacked on the top of each other, as follows:

$$\Theta = \begin{bmatrix} \beta_1 \\ \vdots \\ \beta_{N_o} \\ \alpha \end{bmatrix}, \quad \beta_o = \begin{bmatrix} \beta_{o0} \\ \vdots \\ \beta_{on} \end{bmatrix}, \quad \alpha = \begin{bmatrix} \alpha_0 \\ \vdots \\ \alpha_n \end{bmatrix} \tag{3.81}$$

The **MPE** with the **RMFD** models is accomplished by minimizing the following non-linear least-squares cost function with respect to parameter Θ:

$$l_{NLS} \sum_{o=1}^{N_o} \sum_{f=1}^{N_f} \left| E_o^{NLS}(\Theta, \omega_f) \right|^2 \tag{3.82}$$

with the non-linear equation error given as:

$$E_o^{NLS}(\Theta, \omega_f) = \mathbf{N}_o(\Theta, \omega_f)\mathbf{D}(\Theta, \omega_f)^{-1} - H_o(\omega_f) \tag{3.83}$$

where $H_o(\omega_f)$ denotes the row vector containing the measured **FRF**s of output o and $\mathbf{N}_o(\Theta, \omega_f)$ the row vector containing numerator matrix polynomial of output o. The non-linear cost function (3.82) can be approximated by a linear one by:

$$l_{LS} \sum_{o=1}^{N_o} \sum_{f=1}^{N_f} \left| E_o^{LS}(\Theta, \omega_f) \right|^2 \tag{3.84}$$

with $E_o^{LS} = E_o^{NLS}\mathbf{D}(\Theta, \omega_f)$ now representing the linearised equation error given by:

$$E_o^{LS}(\Theta, \omega_f) = \mathbf{W}_o(\omega_f) \left(\mathbf{N}_o(\Theta, \omega_f) - H_o(\omega_f)\mathbf{D}(\Theta, \omega_f) \right) \tag{3.85}$$

where $\mathbf{W}_o(\omega_f)$ is an optional diagonal frequency-dependent weighting matrix. Since eq. (3.85) is linear in the parameters, it follows that:

$$J^H E(\Theta) = J^H J\Theta \approx 0 \tag{3.86}$$

with

$$E(\Theta) = \begin{bmatrix} E_1(\Theta) \\ E_2(\Theta) \\ \vdots \\ E_{N_o}(\Theta) \end{bmatrix} \in \mathbb{C}^{N_o N_f \times N_i}, \quad E_o(\Theta) = \begin{bmatrix} E_o^{LS}(\Theta, \omega_1) \\ E_o^{LS}(\Theta, \omega_2) \\ \vdots \\ E_o^{LS}(\Theta, \omega_{N_f}) \end{bmatrix} \in \mathbb{C}^{N_f \times N_i}, \quad o = 1, 2, \ldots, N_o \tag{3.87}$$

and J denoting the so-called Jacobian matrix given as:

$$J = \begin{bmatrix} X_1 & 0 & \cdots & 0 & Y_1 \\ 0 & X_2 & \cdots & 0 & Y_2 \\ \vdots & \vdots & \ddots & \vdots & \vdots \\ 0 & 0 & \cdots & X_{N_o} & Y_{N_o} \end{bmatrix} \in \mathbb{C}^{N_o N_f \times (N_o + N_i)(n+1)} \tag{3.88}$$

The entries X_o and Y_o in eq. (3.88) are the derivatives of the equation error with respect to the unknown matrix coefficients β_o and α, respectively. These entries are calculated, respectively, by:

$$X_o = \begin{bmatrix} \mathbf{W}_o(\omega_1) \begin{pmatrix} \Omega_0(\omega_1) & \Omega_1(\omega_1) & \cdots & \Omega_n(\omega_1) \end{pmatrix} \\ \mathbf{W}_o(\omega_2) \begin{pmatrix} \Omega_0(\omega_2) & \Omega_1(\omega_2) & \cdots & \Omega_n(\omega_2) \end{pmatrix} \\ \vdots \\ \mathbf{W}_o(\omega_{N_f}) \begin{pmatrix} \Omega_0(\omega_{N_f}) & \Omega_1(\omega_{N_f}) & \cdots & \Omega_n(\omega_{N_f}) \end{pmatrix} \end{bmatrix} \in \mathbb{C}^{N_f \times (n+1)} \tag{3.89}$$

and

$$Y_o = \begin{bmatrix} -\mathbf{W}_o(\omega_1) \begin{pmatrix} \Omega_0(\omega_1) & \Omega_1(\omega_1) & \cdots & \Omega_n(\omega_1) \end{pmatrix} \otimes H_o(\omega_1) \\ -\mathbf{W}_o(\omega_2) \begin{pmatrix} \Omega_0(\omega_2) & \Omega_1(\omega_2) & \cdots & \Omega_n(\omega_2) \end{pmatrix} \otimes H_o(\omega_2) \\ \vdots \\ -\mathbf{W}_o(\omega_{N_f}) \begin{pmatrix} \Omega_0(\omega_{N_f}) & \Omega_1(\omega_{N_f}) & \cdots & \Omega_n(\omega_{N_f}) \end{pmatrix} \otimes H_o(\omega_{N_f}) \end{bmatrix} \in \mathbb{C}^{N_f \times N_i (n+1)} \tag{3.90}$$

where $\otimes$ denotes the Kronecker product. In the case of real-valued coefficients Θ, $J^H J$ can be replaced by its real part $\mathrm{Re}\left(J^H J\right)$. In such condition, the normal equations (3.86) can be reformulated in matrix notation, as:

$$\mathrm{Re}\left(J^H J\right)\Theta = \begin{bmatrix} R_1 & 0 & \cdots & 0 & S_1 \\ 0 & R_2 & \cdots & 0 & S_2 \\ \vdots & \vdots & \ddots & \vdots & \vdots \\ 0 & 0 & \cdots & R_{N_o} & S_{N_o} \\ S_1^T & S_1^T & \cdots & S_{N_o}^T & \sum_{o=1}^{N_o} T_o \end{bmatrix} \begin{Bmatrix} \beta_1 \\ \beta_2 \\ \vdots \\ \beta_{N_o} \\ \alpha \end{Bmatrix} = 0 \tag{3.91}$$

with R_o, S_o and T_o denoting the so-called normal matrices, which are computed, respectively, by:

$$\begin{aligned} R_o &= \mathrm{Re}\left(X_o^H X_o\right) \in \mathbb{R}^{(n+1)\times(n+1)} \\ S_o &= \mathrm{Re}\left(X_o^H Y_o\right) \in \mathbb{R}^{(n+1)\times N_i(n+1)} \\ T_o &= \mathrm{Re}\left(Y_o^H Y_o\right) \in \mathbb{R}^{N_i(n+1)\times N_i(n+1)} \end{aligned} \tag{3.92}$$

It is worth mentioning that these matrices have a block Toeplitz structure and, therefore, they can be calculated using the **FFT**, which reduces the memory as well as computational time required to run the **pLSCF** algorithm (Cauberghe, 2004). Since the denominator polynomial coefficient α is sufficient to compute the poles and operational factors, this parameter can be calculated by eliminating the numerator coefficients β_o from eqs. (3.91), as follows:

$$\beta_o = -R_o^{-1} S_o \alpha \tag{3.93}$$

Substitution of eq. (3.93) in the last set of equations (3.91) leads to the following reduced normal equations:

$$\left[\sum_{o=1}^{N_o} \left(T_o - S_o^T R_o^{-1} S_o\right)\right] \alpha = 0 \tag{3.94}$$

or, in a more compact form, to:

$$M\alpha = 0 \tag{3.95}$$

where $M = \left[\sum_{o=1}^{N_o} \left(T_o - S_o^T R_o^{-1} S_o\right)\right] \in \mathbb{R}^{N_i(n+1)\times N_i(n+1)}$ is computed solely from the measured **FRF**. This equation is solved for the denominator polynomial α in a least-squares sense, using the non-trivial solution which is obtained by imposing a constraint on these parameters. Such constraint consists of setting one of the polynomial coefficients α_r equal to the identity matrix I_{N_i}. More accurate estimates are obtained when the coefficient with highest order equals the identity matrix (e.g. $\alpha_n = I_{N_i}$) (El-Kafafy, 2013). Apart from avoiding the trivial solution, this

strategy also removes the parameter redundancy that exists in the **RMFD** model. By making use of such constraint strategy, eq. (3.95) can be solved for α in a least squares sense, as follows:

$$\alpha = \begin{bmatrix} -M^{-1}_{[1:nN_i,1:nN_i]} M_{[1:nN_i,nN_i+1:(n+1)N_i]} \\ I_{N_i} \end{bmatrix} \tag{3.96}$$

Once the denominator polynomial coefficients α_r are determined, the poles and modal participation factors are retrieved as the eigenvalues $\Lambda_d \in \mathbb{C}^{N_i n \times N_i n}$ and eigenvectors $\Psi \in \mathbb{C}^{N_i n \times N_i n}$ of their companion matrix A_o:

$$A_o \Psi = \begin{bmatrix} 0 & I_{N_i} & \cdots & 0 & 0 \\ 0 & 0 & \cdots & 0 & 0 \\ \vdots & \vdots & \ddots & \vdots & \vdots \\ 0 & 0 & \cdots & 0 & I_{N_i} \\ -\alpha_0^T & -\alpha_1^T & \cdots & -\alpha_{n-2}^T & -\alpha_{n-1}^T \end{bmatrix} \Psi = \Psi \Lambda_d \tag{3.97}$$

The modal participation factors L are the last N_i rows of Ψ and Λ_d contains the discrete-time poles $\mu_i = e^{-\lambda_i \Delta t}$ on its diagonal. The continuous-time poles λ_i are related to the eigenfrequencies ω_{n_i} [rad/s] and damping ratios ξ_{n_i}, as:

$$\lambda_i, \lambda_i^* = -\omega_{n_i} \xi_{n_r} \pm j \sqrt{1 - \xi_{n_i}^2} \omega_{n_i}, \quad i = 1, 2, \cdots, N_m \tag{3.98}$$

Once the poles and participation factors are found, the mode shapes, V, are obtained in a least squares sense by means of the **LSFD** estimator (see APPENDIX A.1). The confidence bounds on the **pLSCF** estimates can be computed by using the approach discussed in De Troyer et al. (2009b). In the context o the present thesis, however, another strategy is used to estimate such uncertainties. This strategy consists of using one Gauss-Newton iteration of the **pMLE-MM** and will be discussed in Section 3.5.2.

Example 9

The simulated responses of the tower structure is used to illustrate the application of the **pLSCF** technique to estimated the modal parameters from output-only measurements. Rather than using the half spectra matrix estimated with the correlogram approach in **Example 4**, the half spectra matrix synthesized after the optimization with the **MLE-CDM** (smoothed spectra) in **Example 8** is used as primary data by the **pLSCF** technique to estimate the modal parameters of the lattice tower. The combination of the **MLE-CDM** and **pLSCF** estimator is also known by its commercial version PolyMAX Plus (Peeters et al., 2012).

This combined estimator is used in **EMA** to estimate the modal parameters from noisy **FRF**s and is discussed in Section 3.6. The stabilisation diagram constructed with the **pLSCF** technique by identifying models with order $n = 2, 3, \ldots, 20$ is illustrated in Fig. 3.8. The two

zooms shown in Figs. 3.8b and 3.8c reveals that it is possible to distinguish the two pairs of close spaced modes around 1.29 and 3.9 Hz.

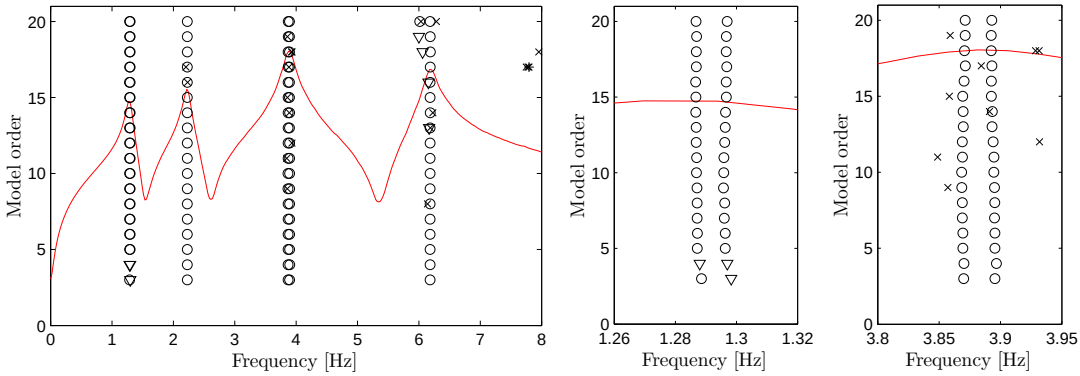

Fig. 3.8 – **MPE** of the lattice tower structure with the combined **MLE-CDM-pLSCF**: stabilization diagram created with the **pLSCF** by identifying models with order n ranging from 2 to 20 (a), and details of the two pairs of close spaced modes around 1.29 (b) and 3.9 Hz (c).

3.5. Identification of Modal Models

3.5.1. Proposed (Single-Reference) Maximum Likelihood Estimator in Modal Model Formulation

In this section, a single-reference implementation of the Maximum Likelihood Estimator formulated in (pole-residue) Modal Model (**MLE-MM**) is proposed. Differently from the poly-reference implementation found in El-Kafafy (2013) and discussed in Section 3.5.2, the approach proposed in this section is intended to identify the model model with enhanced residual model in pole-residue form, given by:

$$\hat{H}(\omega) = \sum_{r=1}^{N_m} \frac{[Res]_r}{j\omega - \lambda_r} + \frac{[Res]_r^*}{j\omega - \lambda_r^*} + \frac{[AR] + j\omega\,[BR] + (j\omega)^2\,[CR]}{d(\omega)} \tag{3.99}$$

with

$$d(\omega) = a + j\omega b + (j\omega)^2 c \tag{3.100}$$

As the modal model is highly non-linear in the parameters, the identification of the modal parameters is performed in a non-linear least square sense using the estimates provided by the **LSCF** method as starting guess. The optimization of these starting parameters are than performed iteratively by minimizing the following (negative) log-like cost function:

$$\sum_{k=1}^{N_o N_i} \sum_{f=1}^{N_f} l(\Theta)_{ML-MM} = \frac{\left|\hat{H}_k(\Theta, \omega_f) - H_k(\omega_f)\right|^2}{\sigma_{H_k(\omega_f)}} \tag{3.101}$$

where $H_k(\omega_f)$ and $\sigma_{H_k(\omega_f)}$ are, respectively, the measured **FRF** and its standard deviation, and $H_k(\Theta,\omega_f)$ is the modelled **FRF**; k ($k = 1, 2, \cdots, N_oN_i$) denotes any of the N_oN_i elements of the measured and estimated **FRF** matrices; N_f represents the number of frequency lines and $\omega_f = 2\pi f$ the angular frequency evaluated at frequency line f. The parameter Θ is a column vector containing the invariants of the pole residue modal model to be optimized by the **ML** algorithm and is given as follows:

$$\Theta = \begin{bmatrix} \theta_1 & \theta_2 & \cdots & \theta_{N_oN_i} & \theta_d & \theta_\lambda \end{bmatrix}^T \in \mathbb{R}^{1\times(2N_m+6)(N_oN_i+1)} \tag{3.102}$$

with

$$\theta_k = \begin{bmatrix} \mathrm{Re}\left([Res]_{1k}\right) & \cdots & \mathrm{Re}\left([Res]_{N_mk}\right) & \mathrm{Re}\left([AR]_k\right) & \mathrm{Re}\left([BR]_k\right) & \mathrm{Re}\left([CR]_k\right) & \cdots \\ \cdots & \mathrm{Im}\left([Res]_{1k}\right) & \cdots & \mathrm{Im}\left([Res]_{N_mk}\right) & \mathrm{Im}\left([AR]_k\right) & \mathrm{Im}\left([BR]_k\right) & \mathrm{Im}\left([CR]_k\right) \end{bmatrix} \tag{3.103}$$

$$\theta_d = \begin{bmatrix} \mathrm{Re}(a) & \mathrm{Re}(b) & \mathrm{Re}(c) & \mathrm{Im}(a) & \mathrm{Im}(b) & \mathrm{Im}(c) \end{bmatrix} \tag{3.104}$$

and

$$\theta_\lambda = \begin{bmatrix} \mathrm{Re}(f_{n_1}) & \cdots & \mathrm{Re}\left(f_{n_{N_m}}\right) & \mathrm{Im}(\xi_{n_1}) & \cdots & \mathrm{Im}\left(\xi_{n_{N_m}}\right) \end{bmatrix} \tag{3.105}$$

The **ML** estimates of the invariants of the modal model is given by minimizing the cost function (3.101) with respect to parameter Θ. Similarly to the **MLE-CDM** discussed in Section 3.3.2, this minimization is accomplished by means of a Gauss-Newton optimization algorithm combined with Levenberg-Marquardt approach to guarantee a continuous reduction of the cost function over the performed iterations. In case of real coefficients, each Gauss-Newton iteration is performed in two steps:

1. Solve the normal equations

$$\mathrm{Re}\left(J_i^H J_i\right)(\Delta\Theta_i) = -\mathrm{Re}\left(J_i^H E_i\right) \quad \text{for} \quad \Delta\Theta_i \tag{3.106}$$

2. Compute an update of the previous solution

$$\Theta_{i+1} = \Theta_i + \Delta\Theta_i \tag{3.107}$$

with $E_i = E(\Theta_i)$ representing the equation error, $J_i = \frac{\partial E(\Theta_i)}{\partial \Theta_i}$ the Jacobian matrix and $\Delta\Theta_i$ the perturbation on the parameters Θ evaluated at the i^{th} iteration. The error equation or so-called

residual vector is given by:

$$E(\Theta_i) = \begin{Bmatrix} E_1(\Theta_i) \\ E_2(\Theta_i) \\ \vdots \\ E_{N_oN_i}(\Theta_i) \end{Bmatrix} \in \mathbb{C}^{N_fN_oN_i \times 1}, \quad E_k(\Theta_i) = \begin{Bmatrix} \frac{\hat{H}_k(\omega_1,\Theta_i) - H_k(\omega_1)}{\sigma_{H_k(\omega_1)}} \\ \frac{\hat{H}_k(\omega_2,\Theta_i) - H_k(\omega_1)}{\sigma_{H_k(\omega_1)}} \\ \vdots \\ \frac{\hat{H}_k(\omega_{N_f},\Theta_i) - H_k(\omega_{N_f})}{\sigma_{H_k(\omega_{N_f})}} \end{Bmatrix} \in \mathbb{C}^{N_f \times 1}, \quad k = 1, 2, \cdots, N_oN_i \tag{3.108}$$

and the Jacobian matrix by:

$$J = \begin{bmatrix} Y_1 & 0 & \cdots & 0 & X_1^d & X_1^\lambda \\ 0 & Y_2 & \cdots & 0 & X_2^d & X_2^\lambda \\ \vdots & \vdots & \ddots & \vdots & \vdots & \vdots \\ 0 & 0 & \cdots & Y_{N_oN_i} & X_{N_oN_i}^d & X_{N_oN_i}^\lambda \end{bmatrix} \tag{3.109}$$

with Y_k containing the derivatives of the equation error (3.108) with respect to the real and imaginary parts of the k^{th} element of the residue matrices $[Res]_r$, and to the real and imaginary parts of the of the k^{th} element of the numerator matrix coefficients of the enhanced residual model $[AR]$, $[BR]$ and $[CR]$; X_k^d containing the derivatives with respect to real and imaginary parts of the denominator scalar coefficients of the enhanced residual model a, b and c; and X_k^λ the derivatives with respect to the natural frequencies and damping ratios. The entries Y_k, X_k^d and X_k^λ are computed, respectively, as follows:

$$Y_k = \begin{bmatrix} \frac{\partial E_k(\Theta)}{\partial \text{Re}([Res]_{1k})} & \cdots & \frac{\partial E_k(\Theta)}{\partial \text{Re}\left([Res]_{N_mk}\right)} & \frac{\partial E_k(\Theta)}{\partial \text{Re}([AR]_k)} & \frac{\partial E_k(\Theta)}{\partial \text{Re}([BR]_k)} & \frac{\partial E_k(\Theta)}{\partial \text{Re}([CR]_k)} & \cdots \\ \cdots & \frac{\partial E_k(\Theta)}{\partial \text{Im}([Res]_{1k})} & \cdots & \frac{\partial E_k(\Theta)}{\partial \text{Im}\left([Res]_{N_mk}\right)} & \frac{\partial E_k(\Theta)}{\partial \text{Im}([AR]_k)} & \frac{\partial E_k(\Theta)}{\partial \text{Im}([BR]_k)} & \frac{\partial E_k(\Theta)}{\partial \text{Im}([CR]_k)} \end{bmatrix} \tag{3.110}$$

$$X_k^d = \begin{bmatrix} \frac{\partial E_k(\Theta)}{\partial \text{Re}(a)} & \frac{\partial E_k(\Theta)}{\partial \text{Re}(b)} & \frac{\partial E_k(\Theta)}{\partial \text{Re}(c)} & \frac{\partial E_k(\Theta)}{\partial \text{Im}(a)} & \frac{\partial E_k(\Theta)}{\partial \text{Im}(b)} & \frac{\partial E_k(\Theta)}{\partial \text{Im}(c)} \end{bmatrix} \tag{3.111}$$

$$X_k^\lambda = \begin{bmatrix} \frac{\partial E_k(\Theta)}{\partial f_{n_1}} & \frac{\partial E_k(\Theta)}{\partial f_{n_2}} & \cdots & \frac{\partial E_k(\Theta)}{\partial f_{n_{N_m}}} & \frac{\partial E_k(\Theta)}{\partial \xi_{n_1}} & \frac{\partial E_k(\Theta)}{\partial \xi_{n_2}} & \cdots & \frac{\partial E_k(\Theta)}{\partial \xi_{n_{N_m}}} \end{bmatrix} \tag{3.112}$$

with the partial derivatives in each entry computed, respectively, by:

$$\frac{\partial E_k(\boldsymbol{\Theta})}{\partial \mathrm{Re}\left([Res]_{mk}\right)} = \begin{bmatrix} \frac{1}{\sigma_{H_k(\omega_1)}}\left(\frac{1}{(j\omega_1-\lambda_m)}+\frac{1}{(j\omega_1-\lambda_m^*)}\right) \\ \vdots \\ \frac{1}{\sigma_{H_k(\omega_{N_f})}}\left(\frac{1}{(j\omega_{N_f}-\lambda_m)}+\frac{1}{(j\omega_{N_f}-\lambda_m^*)}\right) \end{bmatrix}, \quad m=1,2,\cdots,N_m \tag{3.113}$$

$$\frac{\partial E_k(\boldsymbol{\Theta})}{\partial \mathrm{Im}\left([Res]_{mk}\right)} = \begin{bmatrix} \frac{j}{\sigma_{H_k(\omega_1)}}\left(\frac{1}{(j\omega_1-\lambda_m)}-\frac{1}{(j\omega_1-\lambda_m^*)}\right) \\ \vdots \\ \frac{j}{\sigma_{H_k(\omega_{N_f})}}\left(\frac{1}{(j\omega_{N_f}-\lambda_m)}-\frac{1}{(j\omega_{N_f}-\lambda_m^*)}\right) \end{bmatrix} \tag{3.114}$$

$$\frac{\partial E_k(\boldsymbol{\Theta})}{\partial \mathrm{Re}\left([AR]_k\right)} = \begin{bmatrix} \frac{1}{d(\omega_1)\sigma_{H_k(\omega_1)}} \\ \vdots \\ \frac{1}{d(\omega_{N_f})\sigma_{H_k(\omega_{N_f})}} \end{bmatrix}, \quad \frac{\partial E_k(\boldsymbol{\Theta})}{\partial \mathrm{Re}\left([BR]_k\right)} = \begin{bmatrix} \frac{j\omega_1}{d(\omega_1)\sigma_{H_k(\omega_1)}} \\ \vdots \\ \frac{j\omega_{N_f}}{d(\omega_{N_f})\sigma_{H_k(\omega_{N_f})}} \end{bmatrix}, \quad \frac{\partial E_k(\boldsymbol{\Theta})}{\partial \mathrm{Re}\left([CR]_k\right)} = \begin{bmatrix} \frac{-\omega_1^2}{d(\omega_1)\sigma_{H_k(\omega_1)}} \\ \vdots \\ \frac{-\omega_{N_f}^2\delta_{i1}}{d(\omega_{N_f})\sigma_{H_k(\omega_{N_f})}} \end{bmatrix} \tag{3.115}$$

$$\frac{\partial E_k(\boldsymbol{\Theta})}{\partial \mathrm{Im}\left([AR]_k\right)} = \begin{bmatrix} \frac{j}{d(\omega_1)\sigma_{H_{o1}(\omega_1)}} \\ \vdots \\ \frac{j}{d(\omega_{N_f})\sigma_{H_{o1}(\omega_{N_f})}} \end{bmatrix}, \quad \frac{\partial E_k(\boldsymbol{\Theta})}{\partial \mathrm{Im}\left([BR]_k\right)} = \begin{bmatrix} \frac{-\omega_1}{d(\omega_1)\sigma_{H_k(\omega_1)}} \\ \vdots \\ \frac{-\omega_{N_f}}{d(\omega_{N_f})\sigma_{H_k(\omega_{N_f})}} \end{bmatrix}, \quad \frac{\partial E_k(\boldsymbol{\Theta})}{\partial \mathrm{Im}\left([CR]_k\right)} = \begin{bmatrix} \frac{-j\omega_1^2}{d(\omega_1)\sigma_{H_k(\omega_1)}} \\ \vdots \\ \frac{-j\omega_{N_f}^2}{d(\omega_{N_f})\sigma_{H_k(\omega_{N_f})}} \end{bmatrix} \tag{3.116}$$

$$\frac{\partial E_k(\boldsymbol{\Theta})}{\partial \mathrm{Re}\left(a\right)} = \begin{bmatrix} \frac{-N_k(\omega_1)}{d(\omega_1)^2\sigma_{H_k(\omega_1)}} \\ \vdots \\ \frac{-N_k(\omega_{N_f})}{d(\omega_{N_f})^2\sigma_{H_k(\omega_{N_f})}} \end{bmatrix}, \quad \frac{\partial E_k(\boldsymbol{\Theta})}{\partial \mathrm{Re}\left(b\right)} = \begin{bmatrix} \frac{-j\omega_1 N_k(\omega_1)}{d(\omega_1)^2\sigma_{H_k(\omega_1)}} \\ \vdots \\ \frac{-j\omega_{N_f} N_k(\omega_{N_f})}{d(\omega_{N_f})^2\sigma_{H_k(\omega_{N_f})}} \end{bmatrix}, \quad \frac{\partial E_k(\boldsymbol{\Theta})}{\partial \mathrm{Re}\left(c\right)} = \begin{bmatrix} \frac{\omega_1^2 N_k(\omega_1)}{d(\omega_1)^2\sigma_{H_k(\omega_1)}} \\ \vdots \\ \frac{\omega_{N_f}^2 N_k(\omega_{N_f})}{d(\omega_{N_f})^2\sigma_{H_k(\omega_{N_f})}} \end{bmatrix} \tag{3.117}$$

$$\frac{\partial E_k(\Theta)}{\partial \mathrm{Im}\,(a)} = \begin{bmatrix} \frac{-jN_k(\omega_1)}{d(\omega_1)^2\sigma_{H_k(\omega_1)}} \\ \vdots \\ \frac{-jN_k(\omega_{N_f})}{d(\omega_{N_f})^2\sigma_{H_k(\omega_{N_f})}} \end{bmatrix}, \quad \frac{\partial E_k(\Theta)}{\partial \mathrm{Im}\,(b)} = \begin{bmatrix} \frac{\omega_1 N_k(\omega_1)}{d(\omega_1)^2\sigma_{H_{o1}(\omega_1)}} \\ \vdots \\ \frac{\omega_{N_f} N_k(\omega_{N_f})}{d(\omega_{N_f})^2\sigma_{H_k(\omega_{N_f})}} \end{bmatrix}, \quad \frac{\partial E_k(\Theta)}{\partial \mathrm{Im}\,(c)} = \begin{bmatrix} \frac{j\omega_1^2 N_k(\omega_1)}{d(\omega_1)^2\sigma_{H_k(\omega_1)}} \\ \vdots \\ \frac{j\omega_{N_f}^2 N_k(\omega_{N_f})}{d(\omega_{N_f})^2\sigma_{H_k(\omega_{N_f})}} \end{bmatrix} \tag{3.118}$$

$$\frac{\partial E_k(\Theta)}{\partial f_{n_m}} = \begin{bmatrix} \frac{2\pi}{|\lambda_m|\sigma_{H_k(\omega_1)}}\left(\frac{[Res]_{km}\lambda_m}{(j\omega_1-\lambda_m)^2} + \frac{[Res]^*_{km}\lambda^*_m}{(j\omega_1-\lambda^*_m)^2}\right) \\ \vdots \\ \frac{2\pi}{|\lambda_m|\sigma_{H_k(\omega_{N_f})}}\left(\frac{[Res]_{km}\lambda_m}{(j\omega_{N_f}-\lambda_m)^2} + \frac{[Res]^*_{km}\lambda^*_m}{(j\omega_{N_f}-\lambda^*_m)^2}\right) \end{bmatrix} \tag{3.119}$$

and

$$\frac{\partial E_k(\Theta)}{\partial \xi_{n_m}} = \begin{bmatrix} \frac{j|\lambda_m|}{\mathrm{Im}(\lambda_m)\sigma_{H_k(\omega_1)}}\left(\frac{[Res]_{km}\lambda_m}{(j\omega_1-\lambda_m)^2} - \frac{[Res]^*_{km}\lambda^*_m}{(j\omega_1-\lambda^*_m)^2}\right) \\ \vdots \\ \frac{j|\lambda_m|}{\mathrm{Im}(\lambda_m)\sigma_{H_k(\omega_{N_f})}}\left(\frac{[Res]_{km}\lambda_m}{(j\omega_{N_f}-\lambda_m)^2} - \frac{[Res]^*_{km}\lambda^*_m}{(j\omega_{N_f}-\lambda^*_m)^2}\right) \end{bmatrix} \tag{3.120}$$

By taking advantage of the block structure of the Jacobean matrix, the normal equations (3.106) are rewritten as follows:

$$\begin{bmatrix} R_1 & 0 & \cdots & 0 & S_1^d & S_1^\lambda \\ 0 & R_2 & \cdots & 0 & S_2^d & S_2^\lambda \\ \vdots & \vdots & \ddots & \vdots & \vdots & \vdots \\ 0 & 0 & \cdots & R_{N_o} & S_k^d & S_{N_oN_i}^\lambda \\ S_1^{dT} & S_2^{dT} & \cdots & S_{N_oN_i}^{dT} & \sum_{k=1}^{N_oN_i} T_k^d & \sum_{k=1}^{N_oN_i} T_k^{d\lambda} \\ S_1^{\lambda T} & S_2^{\lambda T} & \cdots & S_{N_oN_i}^{\lambda T} & \sum_{k=1}^{N_oN_i} T_k^{\lambda d} & \sum_{k=1}^{N_oN_i} T_k^\lambda \end{bmatrix} \begin{Bmatrix} \Delta\theta_1 \\ \Delta\theta_1 \\ \vdots \\ \Delta\theta_{N_oN_i} \\ \Delta\theta_d \\ \Delta\theta_\lambda \end{Bmatrix} = - \begin{Bmatrix} \mathrm{Re}\left(Y_1^H E_1\right) \\ \mathrm{Re}\left(Y_2^H E_2\right) \\ \vdots \\ \mathrm{Re}\left(Y_{N_oN_i}^H E_{N_oN_i}\right) \\ \sum_{k=1}^{N_oN_i} \mathrm{Re}\left(\left(X_k^d\right)^H E_k\right) \\ \sum_{k=1}^{N_oN_i} \mathrm{Re}\left(\left(X_k^\lambda\right)^H E_k\right) \end{Bmatrix} \tag{3.121}$$

with

$$R_k = \mathrm{Re}\left(Y_k^H Y_k\right) \in \mathbb{R}^{2(N_m+6)\times 2(N_m+6)}$$
$$S_k^d = \mathrm{Re}\left(Y_k^H X_k^d\right) \in \mathbb{R}^{2(N_m+6)\times 6}$$
$$S_k^\lambda = \mathrm{Re}\left(Y_k^H X_k^\lambda\right) \in \mathbb{R}^{2(N_m+6)\times 2N_m}$$
$$T_k^d = \mathrm{Re}\left(\left(X_k^d\right)^H X_k^d\right) \in \mathbb{R}^{6\times 6}$$
$$T_k^\lambda = \mathrm{Re}\left(\left(X_k^\lambda\right)^H X_k^\lambda\right) \in \mathbb{R}^{2N_m\times 2N_m}$$
$$T_k^{d\lambda} = \mathrm{Re}\left(\left(X_k^d\right)^H X_k^\lambda\right) \in \mathbb{R}^{6\times 2N_m}$$
$$T_k^{\lambda d} = \mathrm{Re}\left(\left(X_k^\lambda\right)^H X_k^d\right) \in \mathbb{R}^{2N_m\times 6}$$

From eqs. (3.121), the perturbation on the coefficients $\Delta\theta_k$ (i.e. the perturbations on the real and imaginary parts of the residues, and on the real and imaginary parts of the numerator matrices of the enhanced residual model) can be written as a function of the perturbation on the denominator coefficients of the enhanced residual model $\Delta\theta_d$ and perturbation on the poles, $\Delta\theta_\lambda$, as:

$$\Delta\theta_k = -R_k^{-1}\left(\mathrm{Re}\left(Y_k^H E_k\right) + S_k^d \Delta\theta_d + S_k^\lambda \Delta\theta_\lambda\right) \tag{3.122}$$

By making use of eq. (3.122), the perturbations $\Delta\theta_k$ can eliminated from the normal equations (3.121), yielding:

$$\begin{bmatrix} \sum_{k=1}^{N_o N_i} T_k^d - \left(S_k^d\right)^T R_k^{-1} S_k^d & \sum_{k=1}^{N_o N_i} T_k^{d\lambda} - \left(S_k^d\right)^T R_k^{-1} S_k^\lambda \\ \sum_{k=1}^{N_o N_i} T_k^{\lambda d} - \left(S_k^\lambda\right)^T R_k^{-1} S_k^d & \sum_{k=1}^{N_k} T_k^\lambda - \left(S_k^\lambda\right)^T R_k^{-1} S_k^\lambda \end{bmatrix} \begin{Bmatrix} \Delta\theta_d \\ \Delta\theta_\lambda \end{Bmatrix} = \begin{bmatrix} \sum_{k=1}^{N_o N_i} \left(S_k^d\right)^T R_k^{-1} \mathrm{Re}\left(Y_k^H E_k\right) - \mathrm{Re}\left(\left(X_k^d\right)^H E_k\right) \\ \sum_{k=1}^{N_o N_i} \left(S_k^\lambda\right)^T R_k^{-1} \mathrm{Re}\left(Y_k^H E_k\right) - \mathrm{Re}\left(\left(X_k^\lambda\right)^H E_k\right) \end{bmatrix} \tag{3.123}$$

or in a more compact form

$$\begin{bmatrix} M_1 & M_2 \\ M_3 & M_4 \end{bmatrix} \begin{Bmatrix} \Delta\theta_d \\ \Delta\theta_\lambda \end{Bmatrix} = \begin{bmatrix} M_5 \\ M_6 \end{bmatrix} \tag{3.124}$$

with

$$M_1 = \sum_{k=1}^{N_o N_i} T_k^d - \left(S_k^d\right)^T R_k^{-1} S_k^d, \quad M_3 = \sum_{k=1}^{N_o N_i} T_k^{\lambda d} - \left(S_k^\lambda\right)^T R_k^{-1} S_k^d, \quad M_5 = \sum_{k=1}^{N_o N_i} \left(S_k^d\right)^T R_k^{-1} \mathrm{Re}\left(Y_k^H E_k\right) - \mathrm{Re}\left(\left(X_k^d\right)^H E_k\right)$$
$$M_2 = \sum_{k=1}^{N_o N_i} T_k^{d\lambda} - \left(S_k^d\right)^T R_k^{-1} S_k^\lambda, \quad M_4 = \sum_{k=1}^{N_o N_i} T_k^\lambda - \left(S_k^\lambda\right)^T R_k^{-1} S_k^\lambda, \quad M_6 = \sum_{k=1}^{N_o N_i} \left(S_k^\lambda\right)^T R_k^{-1} \mathrm{Re}\left(Y_k^H E_k\right) - \mathrm{Re}\left(\left(X_k^\lambda\right)^H E_k\right)$$

This elimination decreases the memory, as well as the time required to run the algorithm. As for the **MLE-CDM**, an efficient implementation of the **MLE-MM** is only possible if the variances are taken into account in the cost function (3.101). Once the perturbations on the natural frequencies, damping ratios and denominator coefficients of the enhanced residual model are calculated in the last iteration by means of eq. (3.123), then perturbations on the modal residues and numerator matrix coefficients of the enhanced residual model are computed using eq. (3.122).

Estimation of the uncertainty bounds

One of the main advantages of the **ML**-based algorithms is the possibility to estimate the confidence intervals for the identified modal parameters using the noise information measured together with the **FRF**s during the vibration tests. As shown in Schoukens and Pintelon (1991), a good approximation of the covariance of the **ML** parameters Θ_{ML-MM} is obtained by:

$$\mathrm{Cov}([Res],[AR],[BR],[CR],a,b,c,\lambda) \simeq \left[2\mathrm{Re}\left(J_l^H J_l\right)\right]^{-1} \tag{3.125}$$

with J_l standing for the Jacobean matrix evaluated in the last iteration of the Gaussian-Newton algorithm. Taking advantage of the structure of the Jacobean matrix and using the matrix inversion lemma (Kailath, 1980), the covariance of the denominator scalar coefficients of the enhanced residual model, and the covariance of the natural frequencies and damping ratios can be estimated independently from the covariance of the residues and from the covariance of the numerator matrix coefficients of the enhanced residual model, as follows:

$$\mathrm{Cov}(a,b,c) \simeq M_1^{-1} + M_1^{-1} M_2 \Delta_1^{-1} M_3 M_1^{-1} \tag{3.126}$$

$$\mathrm{Cov}(f_n,\xi_n) \simeq \Delta_1^{-1} \tag{3.127}$$

with

$$\Delta_1 = M_4 - M_3 M_1^{-1} M_2 \tag{3.128}$$

The advantage of the parametrization used in eq. (3.102) is that the covariance of the natural frequencies and damping ratios are computed directly from the from the normal matrices and, therefore, the use of explicit linearisation formulas is avoided. If one is interested on the variances of the real and imaginary parts of the poles, they can be estimated means of the following linearisation formulas:

$$\begin{aligned}
\mathrm{Var}(\mathrm{Re}\,(\lambda_m)) &\simeq 4\pi^2 \begin{bmatrix} f_{n_m} \\ \xi_{n_m} \end{bmatrix}^T \mathrm{Cov}(f_{n_m},\xi_{n_m}) \begin{bmatrix} f_{n_m} \\ \xi_{n_m} \end{bmatrix} \\
\mathrm{Var}(\mathrm{Im}\,(\lambda_m)) &\simeq 4\pi^2 (1-\xi_{n_m}^2) \begin{bmatrix} 1 \\ \frac{-f_{n_m}\xi_{n_m}}{1-\xi_{n_m}^2} \end{bmatrix}^T \mathrm{Cov}(f_{n_m},\xi_{n_m}) \begin{bmatrix} 1 \\ \frac{-f_{n_m}\xi_{n_m}}{1-\xi_{n_m}^2} \end{bmatrix}
\end{aligned} \tag{3.129}$$

The covariance of the residues and the numerator matrix coefficients of the enhanced residual model are estimated as:

$$\mathrm{Cov}([Res]_k,[AR]_k,[BR]_k,[CR]_k) \simeq R_k^{-1} + Z_k \tag{3.130}$$

with

$$\begin{aligned}
Z_k &= Z_{1k}\left(S_k^d\right)^H R_k^{-1} + Z_{2k}\left(S_k^\lambda\right)^H R_k^{-1} \\
Z_{1k} &= R_k^{-1}\left[S_k^d\left(M_1 - M_2M_4^{-1}M_3\right)^{-1} - S_k^\lambda\left(M_4 - M_3M_1^{-1}M_2\right)^{-1}M_3M_1\right] \\
Z_{2k} &= R_k^{-1}\left[S_k^\lambda\left(M_4 - M_3M_1^{-1}M_2\right)^{-1} - S_k^dM_1^{-1}M_2\left(M_4 - M_3M_1^{-1}M_2\right)^{-1}\right]
\end{aligned}$$

Once the covariance of real and imaginary parts of the residues are computed, the covariance of the mode shapes and operational factors are estimated by following the procedure presented in Pintelon et al. (2007).

Example 10
At this point another structure is introduced to validate the proposed **MLE-MM** discussed in Section 3.5.1. The structure is used to perform a simulated **EMA** and corresponds to a five-**DOF** system illustrated in Fig. 3.9. This system was used by Böswald et al. (2006) to compare different modal parameter estimation techniques in terms of their sensitivity to statistical errors. It is composed by 5 masses supported by cantilever beans and connected among themselves by arch springs. The exact natural frequencies, damping ratios and modal masses of the system are given in Tab. 3.1, whist the real modes are shown in Tab. 3.2. These properties were used to generate the **FRF**s used in simulated **EMA**.

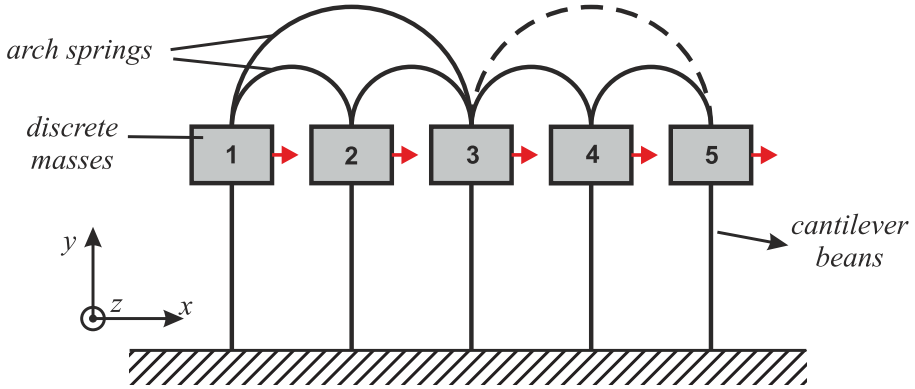

Fig. 3.9 – Five-**DOF** system connected with arch springs (Böswald et al., 2006).

The system was exited by a white Gaussian noise at masses 1 and 2, and the responses were measured at all **DOF**s, resulting in **FRF** matrix with two columns and five rows. These **FRF**s were calculated in the frequency range of 0-80 Hz with a resolution of 0.1 Hz. Afterwards, a colored noise was introduced in the **FRF** matrix with a standard deviation of 10%. The noise was added to the real and imaginary parts independently. This was achieved by adding

a complex random number to the **FRF** at each frequency line. This number is computed so that its amplitude is a random element of a normal distribution (with $\sigma(\omega) = 10\%|H(\omega)|$) and phase is an uniform random number between 0 and 2π (Peeters et al., 2012).

Tab. 3.1 – Eigenfrequencies, damping ratios and modal masses of the five-**DOF** system.

Mode	f_n [Hz]	ξ_n [%]	m_i [Kg]
1	26.06	2	2.52
2	36.84	2	2.97
3	51.47	2	0.90
4	56.21	2	1.09
5	62.60	2	1.05

Tab. 3.2 – Real modes of the five-**DOF** system.

DOF/Mode	1	2	3	4	5
1	0.7147	1.0000	-0.0911	-0.9230	-0.6083
2	0.7166	0.9999	-0.1493	1.0000	-0.1937
3	0.7981	0.2257	0.1554	-0.1518	1.0000
4	0.8518	-0.5166	1.0000	0.1231	-0.3936
5	1.0000	-0.8590	-0.5860	0.0196	-0.2041

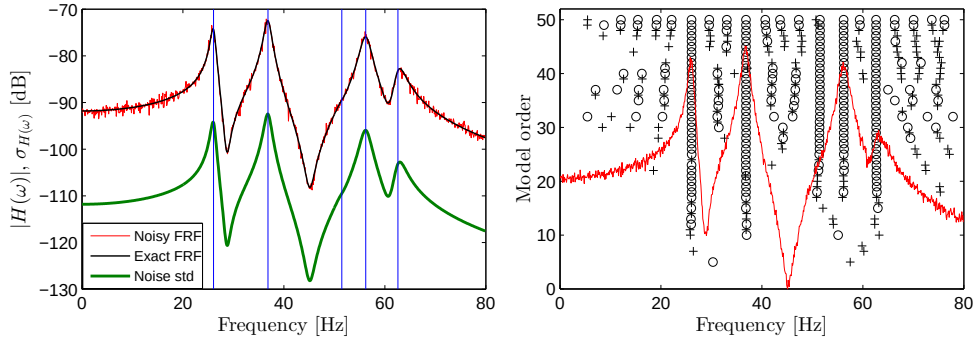

(a) (b)

Fig. 3.10 – Element(1,1) of the **FRF** matrix contaminated with 10% noise: exact and noisy **FRF**, noise standard deviation and exact natural frequencies (vertical lines) (a); and stabilization diagram constructed with the **LSCF** estimator (b).

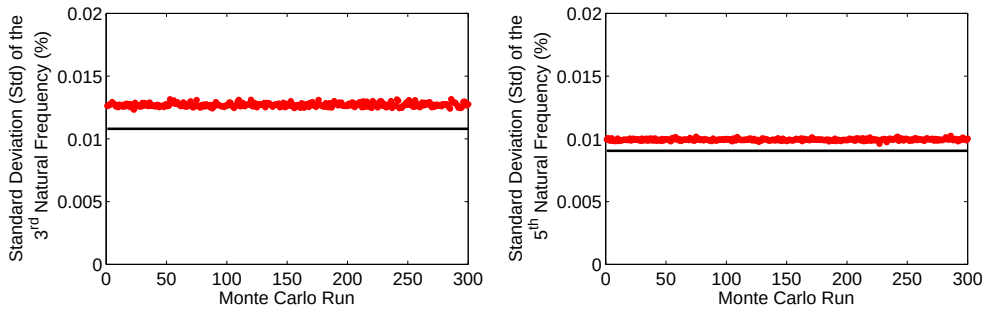

(a) (b)

Fig. 3.11 – Monte Carlo simulation results for the natural frequencies of the 3rd (a) and 5th modes with 10% of noise level: predicted standard deviation with the proposed **MLE-MM** (dots) and sample standard deviation (solid line).

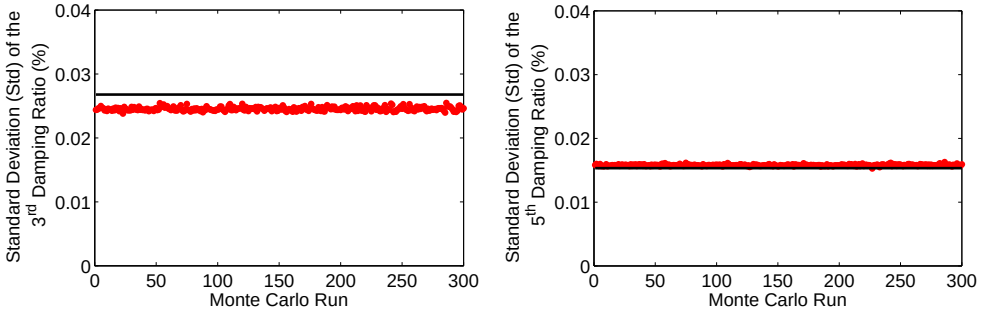

(a) (b)

Fig. 3.12 – Monte Carlo simulation results for the damping ratios of the 3rd (a) and 5th (b) modes with 10% of noise level: predicted standard deviation with the proposed **MLE-MM** (dots) and sample standard deviation (solid line).

The exact and noisy element (1,1) of the **FRF** matrix, and the corresponding "true" standard deviation of the noise are shown in Fig. 3.10a. A set of 300 **FRF**s contaminated with noise was generated to perform Monte Carlo simulations in order to assess the efficiency of the proposed **MLE-MM**. The modal parameters of each dataset were identified with the **LSCF** and **LSFD** estimators and then used as starting values to be optimized by the **MLE-MM** algorithm. The identification of each dataset was performed using the full frequency band, i.e., with no upper and lower residual terms. A typical stabilization diagram constructed with the **LSCF** method from the noisy **FRF** is shown in Fig. 3.10.

In a final step of the identification process, 10 iterations of the **MLE-MM** were performed to optimize the modal parameters of each dataset and estimate their standard deviations. The standard deviations of the natural frequencies and damping ratios of the 3rd and 5th modes estimated with the proposed **MLE-MM** are compared to their respective sample standard deviations in Figs. 3.11 and 3.12. From these figures, it is verified that the standard deviations provided by the proposed **MLE-MM** are in good agreement with the sample standard deviations. These results are also verified in Figs. 3.13 and Tab. 3.3, where the estimated and sample standard deviations of all the identified natural frequencies and damping ratios are compared.

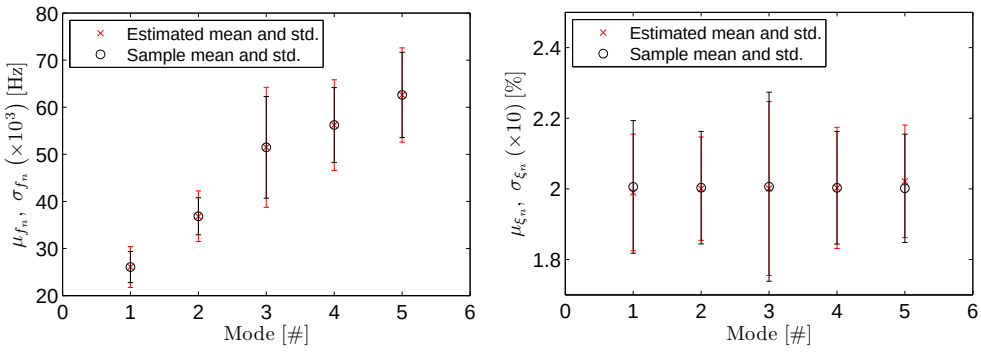

(a) (b)

Fig. 3.13 – Monte Carlo simulation results for the identified natural frequencies and damping ratios: sample (black line) and estimated (red line) means and standard deviations of natural frequencies (a) and damping ratios (b) provided by the proposed **MLE-MM** method after 10 iterations.

Tab. 3.3 – Results obtained from the simulated **EMA** of the five-**DOF** system with the proposed **MLE-MM**.

Mode	Sample Mean and Std.				Estimated Mean and Std.			
	$\mu_{\hat{f}_n}$(Hz)	$\sigma_{\hat{f}_n}$(Hz) $\times 10^3$	$\mu_{\hat{\xi}_n}$(%)	$\sigma_{\hat{\xi}_n}$(%) $\times 10^2$	$\hat{\mu}_{\hat{f}_n}$(Hz)	$\hat{\sigma}_{\hat{f}_n}$(Hz) $\times 10^3$	$\hat{\mu}_{\hat{\xi}_{n(\%)}}$	$\hat{\sigma}_{\hat{\xi}_n}$(%) $\times 10^2$
1	26.0602	3.31	2.0057	1.88	26.0571	4.35	1.9898	1.65
2	36.8399	3.94	2.0034	1.59	36.8345	5.37	2.0008	1.46
3	51.4682	10.80	2.0061	2.68	51.4730	12.75	2.0011	2.46
4	56.2114	7.96	2.0031	1.59	56.2026	9.63	2.0029	1.72
5	62.6011	9.04	2.0016	1.53	62.5989	10.01	2.0215	1.59

3.5.2. Poly-reference Maximum Likelihood Estimator in Modal Model Formulation

The first implementation of the of the poly-reference Maximum Likelihood in Modal Model (**pMLE-MM**) formulation was derived by El-Kafafy (2013) in order to optimize the estimates provided the **pLSCF** technique and yield the uncertainties on these optimized estimates. In this derivation, the following model with enhanced residual terms is assumed to represent the measured **FRF**s:

$$\hat{H}(\omega) = \sum_{i=1}^{N_m} \frac{v_i l_i^T}{j\omega - \lambda_i} + \frac{v_i^* l_i^H}{j\omega - \lambda_i^*} + \frac{N(\omega)}{d(\omega)} \tag{3.131}$$

with

$$N(\omega) = [AR] + j\omega\,[BR] + (j\omega)^2\,[CR] \tag{3.132}$$

The idea behind the **pMLE-MM** is to optimize the modal parameters estimated with the **pLSCF** and **LSFD** estimators, by fitting the parameters of the modal model as in eq. (3.131) to the measured **FRF**. One of the main advantages of the **pMLE-MM** with regard to its single-reference counterpart, proposed in Section 3.5.1, is the possibility to retain and improve the precision of the poly-reference estimates provided by the **pLSCF** estimator. The optimization of the starting parameters with the **pMLE-MM** is accomplished by minimizing the following (negative) log-like cost function:

$$\sum_{o=1}^{N_o} \sum_{f=1}^{N_f} l(\Theta)_{pML-MM} = E_o(\Theta, \omega_f) E_o^H(\Theta, \omega_f) \tag{3.133}$$

with $E_o(\Theta, \omega_f)$ denoting the row vector error between the measured and estimated **FRF**s for

output o, which is given as:

$$E_o(\Theta,\omega_f)=\left\langle \frac{\hat{H}_{o1}(\Theta,\omega_f)-H_{o1}(\omega_f)}{\sigma_{H_{o1}(\omega_f)}}\cdots\frac{\hat{H}_{oN_i}(\Theta,\omega_f)-H_{oN_i}(\omega_f)}{\sigma_{H_{oN_i}(\omega_f)}}\right\rangle \tag{3.134}$$

where $\hat{H}_o(\Theta,\omega_f)\in\mathbb{C}^{1\times N_i}$ and $H_o(\omega_f)\in\mathbb{C}^{1\times N_i}$ denote the o^{th} rows of the estimated and measured **FRF**s, and $\sigma_{H_o(\omega_f)}\in\mathbb{R}^{1\times N_i}$ is the standard deviation of the noise. The parameter Θ is a column vector with all the parameters to be optimized by means of the Gauss-Newton algorithm and is given as:

$$\Theta=\begin{bmatrix}\theta_1 & \theta_2 & \cdots & \theta_{N_o} & \theta_L & \theta_d & \theta_\lambda\end{bmatrix}^T\in\mathbb{R}^{2N_m(N_o+N_i)+6(N_oN_i+1)} \tag{3.135}$$

with

$$\theta_o=\begin{bmatrix}\theta_{V_o} & \theta_{A_o} & \theta_{B_o} & \theta_{C_o}\end{bmatrix}\in\mathbb{C}^{2N_m+6N_i},\quad o=1,2,\cdots,N_o \tag{3.136}$$

The parameter $\theta_{V_o}\in\mathbb{C}^{2N_m}$ is a vector with the real and imaginary parts of the mode shape elements corresponding to the o^{th} output, and is given by:

$$\theta_{V_o}=\begin{bmatrix}\text{Re}(v_{o1}) & \text{Re}(v_{o2}) & \cdots & \text{Re}(v_{oN_m}) & \text{Im}(v_{o1}) & \text{Im}(v_{o2}) & \cdots & \text{Im}(v_{oN_m})\end{bmatrix} \tag{3.137}$$

The parameters θ_{A_o}, θ_{B_o}, $\theta_{C_o}\in\mathbb{C}^{2N_i}$, in eq. (3.136), are vectors containing the real and imaginary parts of the o^{th} row of the numerator matrix coefficients of the residual model (3.132), and are given, respectively, by:

$$\begin{aligned}
\theta_{A_o}&=\begin{bmatrix}\text{Re}([AR]_{o1}) & \text{Im}([AR]_{o1}) & \text{Re}([AR]_{o2}) & \text{Im}([AR]_{o2}) & \cdots & \text{Re}([AR]_{oN_i}) & \text{Im}([AR]_{oN_i})\end{bmatrix}\\
\theta_{B_o}&=\begin{bmatrix}\text{Re}([BR]_{o1}) & \text{Im}([BR]_{o1}) & \text{Re}([BR]_{o2}) & \text{Im}([BR]_{o2}) & \cdots & \text{Re}([BR]_{oN_i}) & \text{Im}([BR]_{oN_i})\end{bmatrix}\\
\theta_{C_o}&=\begin{bmatrix}\text{Re}([CR]_{o1}) & \text{Im}([CR]_{o1}) & \text{Re}([CR]_{o2}) & \text{Im}([CR]_{o2}) & \cdots & \text{Re}([CR]_{oN_i}) & \text{Im}([CR]_{oN_i})\end{bmatrix}
\end{aligned} \tag{3.138}$$

The parameters $\theta_d\in\mathbb{C}^6$, $\theta_L\in\mathbb{R}^{2N_m(N_i-1)}$ and $\theta_\lambda\in\mathbb{C}^{2N_m}$ in eq. (3.135) are column vectors containing, respectively, the real and imaginary parts of the denominator coefficients of the new residual model, the real and imaginary parts of all elements of the modal participation factor matrix L, and the real and imaginary parts of the poles. These parameters are defined,

respectively, as:

$$\theta_d = \begin{bmatrix} \mathrm{Re}(a) & \mathrm{Im}(a) & \mathrm{Re}(b) & \mathrm{Im}(b) & \mathrm{Re}(c) & \mathrm{Im}(c) \end{bmatrix} \tag{3.139}$$

$$\theta_L = \begin{bmatrix} \mathrm{Re}(l_{11}) & \cdots & \mathrm{Re}(l_{N_k 1}) & \mathrm{Im}(l_{11}) & \cdots & \mathrm{Im}(l_{N_k 1}) & \cdots \\ \cdots & \mathrm{Re}(l_{1N_m}) & \cdots & \mathrm{Re}(l_{N_k N_m}) & \mathrm{Im}(l_{1N_m}) & \cdots & \mathrm{Im}(l_{N_k N_m}) \end{bmatrix} \tag{3.140}$$

and

$$\theta_\lambda = \begin{bmatrix} \mathrm{Re}(\lambda_{n_1}) & \mathrm{Im}(\lambda_{n_1}) & \mathrm{Re}(\lambda_{n_2}) & \mathrm{Im}(\lambda_{n_2}) & \cdots & \mathrm{Re}(\lambda_{n_{N_m}}) & \mathrm{Im}(\lambda_{n_{N_m}}) \end{bmatrix} \tag{3.141}$$

where $l_{km} \in \mathbb{C}$ is the k^{th} element of the modal participation factor vector corresponding to the m^{th} vibration mode, with $k = 1, 2, \cdots, N_k$, and $N_k = N_i - 1$, which means that only the operational factors that differ from 1 are optimized by the algorithm during the performed iterations. As each identified modal participation factor vector is normalized by its highest component in the identification with the **pLSCF**, the derivatives of the elements that equals 1 are not evaluated and, therefore, are not included in the vector defined by eq. (3.140). In fact, this works like a constraint, since the operational factors elements that equal 1 are not updated during the minimization of the cost function (3.133). The employment of this constraint, on the one hand, improves the numerical stability of the normal equations and, on other the hand, reduces the time and the memory required to run the algorithm.

Similarly to the **MLE-CDM** discussed in Section 3.3.2, the optimization of the parameters Θ with the **pMLE-MM** is accomplished by minimizing the cost function (3.133) in a non-linear least squares sense. This is performed by means of the Gauss-Newton optimization algorithm combined with Levenberg-Marquardt approach (Pintelon and Schoukens, 2001) in two steps:

1. Solve the normal equations

$$J_i^H J_i \mathrm{vec}(\Delta\Theta_i) = -J_i^H E_i \quad \text{for} \quad \mathrm{vec}(\Delta\Theta_i). \tag{3.142}$$

2. Compute an update of the previous solution

$$\Theta_{i+1} = \Theta_i + \Delta\Theta_i \tag{3.143}$$

where $\text{vec}(\Delta\Theta_i) \in \mathbb{R}^{2N_m(N_o+N_i)+6(N_oN_i+1)}$ is the perturbation on the modal parameters, E_i is the error between the measured quantity and the parametric model (i.e. **FRF** equation in modal model formulation (3.131)), J_i is the Jacobian matrix evaluated at the i^{th} iteration and $\text{vec}(\bullet)$ stands for the column stacking operator. The equation error calculated at the i^{th} iteration $E_i = E(\Theta_i)$ is given by:

$$E_i = \left\{ \begin{array}{c} \text{vec}(E_1(\Theta_i)) \\ \text{vec}(E_2(\Theta_i)) \\ \vdots \\ \text{vec}(E_{N_o}(\Theta_i)) \end{array} \right\} \in \mathbb{R}^{N_f N_o N_i \times 1}, \quad E_o(\Theta_i) = \left[\begin{array}{c} E_o(\Theta_i, \omega_1) \\ E_o(\Theta_i, \omega_2) \\ \vdots \\ E_o(\Theta_i, \omega_{N_f}) \end{array} \right] \in \mathbb{R}^{N_f \times N_i} \quad , \quad o = 1, \ldots, N_o \tag{3.144}$$

and the corresponding Jacobian matrix by:

$$J_i = \left[\frac{\partial E(\Theta_i)}{\partial \Theta_i} \right] \in \mathbb{R}^{N_f N_o N_i \times 2N_m(N_o+N_i)+6(N_oN_i+1)} \tag{3.145}$$

with Θ_i representing the parameters (3.135) at the i^{th} iteration. The Jacobian matrix has the following structure:

$$J = \begin{bmatrix} Y_1 & 0 & \cdots & 0 & X_1^d & X_1^L & X_1^\lambda \\ 0 & Y_2 & \cdots & 0 & X_2^d & X_2^L & X_2^\lambda \\ \vdots & \vdots & \ddots & \vdots & \vdots & \vdots & \vdots \\ 0 & 0 & \cdots & Y_{N_o} & X_{N_o}^d & X_{N_o}^L & X_{N_o}^\lambda \end{bmatrix} \tag{3.146}$$

where X_o^L, X_o^d and X_o^λ are matrices containing the partial derivatives of the equation error (3.134) with respect to the real and imaginary parts of the modal participation factors, real and imaginary parts of the denominator coefficients of the enhanced residual, and to the real and imaginary parts of the poles, respectively. Y_o is a matrix containing the derivatives with respect to the real and imaginary parts of the mode shapes, and to the real and imaginary parts of the numerator matrix coefficients of the enhanced residual model, $[AR]$, $[BR]$ and $[CR]$. The matrices X_o^L and X_o^d are computed, respectively, as:

$$X_o^L = \begin{bmatrix} X_o^{l_1} & X_o^{l_2} & \cdots & X_o^{l_{N_m}} \end{bmatrix} \tag{3.147}$$

and

$$X_o^d = \begin{bmatrix} X_o^a & X_o^b & X_o^c \end{bmatrix} \tag{3.148}$$

with $X_o^{l_m}$ containing the derivatives of the equation error with respect to the real and imaginary parts of the components of the modal participation factor vector corresponding to the m^{th} mode, and X_o^a, X_o^b and X_o^c the derivatives with regard to the real and imaginary parts of the denominator coefficients a, b and c of the enhanced residual model (3.100), respectively. The sub-matrices X_o^λ is calculated as:

$$X_o^\lambda = \begin{bmatrix} \text{vec}\left\{\frac{\partial E_o(\Theta)}{\partial \text{Re}(\lambda_{n_1})}\right\} & \text{vec}\left\{\frac{\partial E_o(\Theta)}{\partial \text{Im}(\lambda_{n_1})}\right\} & \text{vec}\left\{\frac{\partial E_o(\Theta)}{\partial \text{Re}(\lambda_{n_2})}\right\} & \text{vec}\left\{\frac{\partial E_o(\Theta)}{\partial \text{Im}(\lambda_{n_2})}\right\} & \cdots & \text{vec}\left\{\frac{\partial E_o(\Theta)}{\partial \text{Re}(\lambda_{n_{N_m}})}\right\} & \text{vec}\left\{\frac{\partial E_o(\Theta)}{\partial \text{Im}(\lambda_{n_{N_m}})}\right\} \end{bmatrix} \tag{3.149}$$

with the partial derivatives of the equation error with respect to the real and imaginary parts of the pole corresponding to the m^{th} mode given, respectively, as follows:

$$\frac{\partial E_o(\Theta)}{\partial \text{Re}(\lambda_m)} = \begin{bmatrix} \frac{1}{\sigma_{H_{o1}(\omega_1)}}\left(\frac{v_{om}l_{1m}}{(j\omega_1-\lambda_m)^2}+\frac{v_{om}^*l_{1m}^*}{(j\omega_1-\lambda_m^*)^2}\right) & \cdots & \frac{1}{\sigma_{H_{oN_i}(\omega_1)}}\left(\frac{v_{om}l_{N_im}}{(j\omega_1-\lambda_m)^2}+\frac{v_{om}^*l_{N_im}^*}{(j\omega_1-\lambda_m^*)^2}\right) \\ \vdots & \vdots & \vdots \\ \frac{1}{\sigma_{H_{o1}(\omega_{N_f})}}\left(\frac{v_{om}l_{1m}}{(j\omega_{N_f}-\lambda_m)^2}+\frac{v_{om}^*l_{1m}^*}{(j\omega_{N_f}-\lambda_m^*)^2}\right) & \cdots & \frac{1}{\sigma_{H_{oN_i}(\omega_{N_f})}}\left(\frac{v_{om}l_{N_im}}{(j\omega_{N_f}-\lambda_m)^2}+\frac{v_{om}^*l_{N_im}^*}{(j\omega_{N_f}-\lambda_m^*)^2}\right) \end{bmatrix} \tag{3.150}$$

and

$$\frac{\partial E_o(\Theta)}{\partial \text{Im}(\lambda_m)} = \begin{bmatrix} \frac{j}{\sigma_{H_{o1}(\omega_1)}}\left(\frac{v_{om}l_{1m}}{(j\omega_1-\lambda_m)^2}-\frac{v_{om}^*l_{1m}^*}{(j\omega_1-\lambda_m^*)^2}\right) & \cdots & \frac{j}{\sigma_{H_{oN_i}(\omega_1)}}\left(\frac{v_{om}l_{N_im}}{(j\omega_1-\lambda_m)^2}-\frac{v_{om}^*l_{N_im}^*}{(j\omega_1-\lambda_m^*)^2}\right) \\ \vdots & \vdots & \vdots \\ \frac{j}{\sigma_{H_{o1}(\omega_{N_f})}}\left(\frac{v_{om}l_{1m}}{(j\omega_{N_f}-\lambda_m)^2}-\frac{v_{om}^*l_{1m}^*}{(j\omega_{N_f}-\lambda_m^*)^2}\right) & \cdots & \frac{j}{\sigma_{H_{oN_i}(\omega_{N_f})}}\left(\frac{v_{om}l_{N_im}}{(j\omega_{N_f}-\lambda_m)^2}-\frac{v_{om}^*l_{N_im}^*}{(j\omega_{N_f}-\lambda_m^*)^2}\right) \end{bmatrix} \tag{3.151}$$

The sub-matrices $X_o^{l_m}$ in eq. (3.147) are computed as:

$$X_o^{l_m} = \begin{bmatrix} \text{vec}\left\{\frac{\partial E_o(\Theta)}{\partial \text{Re}(l_{1m})}\right\} & \cdots & \text{vec}\left\{\frac{\partial E_o(\Theta)}{\partial \text{Re}(l_{N_km})}\right\} & \text{vec}\left\{\frac{\partial E_o(\Theta)}{\partial \text{Im}(l_{1m})}\right\} & \cdots & \text{vec}\left\{\frac{\partial E_o(\Theta)}{\partial \text{Im}(l_{N_km})}\right\} \end{bmatrix} \tag{3.152}$$

with $N_k = N_i - 1$. It is worth noting that the same constraint strategy used in the definition

of eq. (3.140) must be used to calculate the derivatives in eq. (3.152). Therefore, only the derivatives with respect to the elements of the participation factor which are different from 1 are included in this equation. In eq. (3.152), the partial derivatives of the equation error with respect to the real and imaginary parts of each component of the m^{th} participation factor vector are given, respectively, by:

$$\frac{\partial E_o(\Theta)}{\partial \text{Re}\,(l_{km})} = \begin{bmatrix} \frac{\delta_{k1}}{\sigma_{H_{o1}(\omega_1)}}\left(\frac{v_{om}}{(j\omega_1-\lambda_m)}+\frac{v_{om}^*}{(j\omega_1-\lambda_m^*)}\right) & \cdots & \frac{\delta_{kN_i}}{\sigma_{H_{oN_i}(\omega_1)}}\left(\frac{v_{om}}{(j\omega_1-\lambda_m)}+\frac{v_{om}^*}{(j\omega_1-\lambda_m^*)}\right) \\ \vdots & \vdots & \vdots \\ \frac{\delta_{k1}}{\sigma_{H_{o1}(\omega_{N_f})}}\left(\frac{v_{om}}{(j\omega_{N_f}-\lambda_m)}+\frac{v_{om}^*}{(j\omega_{N_f}-\lambda_m^*)}\right) & \cdots & \frac{\delta_{kN_i}}{\sigma_{H_{oN_i}(\omega_{N_f})}}\left(\frac{v_{om}}{(j\omega_{N_f}-\lambda_m)}+\frac{v_{om}^*}{(j\omega_{N_f}-\lambda_m^*)}\right) \end{bmatrix} \tag{3.153}$$

and

$$\frac{\partial E_o(\Theta)}{\partial \text{Im}\,(l_{km})} = \begin{bmatrix} \frac{j\delta_{k1}}{\sigma_{H_{o1}(\omega_1)}}\left(\frac{v_{om}}{(j\omega_1-\lambda_m)}-\frac{v_{om}^*}{(j\omega_1-\lambda_m^*)}\right) & \cdots & \frac{j\delta_{kN_i}}{\sigma_{H_{oN_i}(\omega_1)}}\left(\frac{v_{om}}{(j\omega_1-\lambda_m)}-\frac{v_{om}^*}{(j\omega_1-\lambda_m^*)}\right) \\ \vdots & \vdots & \vdots \\ \frac{j\delta_{k1}}{\sigma_{H_{o1}(\omega_{N_f})}}\left(\frac{v_{om}}{(j\omega_{N_f}-\lambda_m)}-\frac{v_{om}^*}{(j\omega_{N_f}-\lambda_m^*)}\right) & \cdots & \frac{j\delta_{kN_i}}{\sigma_{H_{oN_i}(\omega_{N_f})}}\left(\frac{v_{om}}{(j\omega_{N_f}-\lambda_m)}-\frac{v_{om}^*}{(j\omega_{N_f}-\lambda_m^*)}\right) \end{bmatrix} \tag{3.154}$$

where δ_{ki} is the Kronecker delta which equals unity if $k = i$ (i.e., where the derivative is evaluated) and zero otherwise. In eq. (3.148), the sub-matrices X_o^a, X_o^b and X_o^c are defined, respectively, as follows:

$$X_o^a = \begin{bmatrix} \text{vec}\left\{\frac{\partial E_o(\Theta)}{\partial \text{Re}(a)}\right\} & \text{vec}\left\{\frac{\partial E_o(\Theta)}{\partial \text{Im}(a)}\right\} \end{bmatrix} \tag{3.155}$$

$$X_o^b = \begin{bmatrix} \text{vec}\left\{\frac{\partial E_o(\Theta)}{\partial \text{Re}(b)}\right\} & \text{vec}\left\{\frac{\partial E_o(\Theta)}{\partial \text{Im}(b)}\right\} \end{bmatrix} \tag{3.156}$$

$$X_o^c = \begin{bmatrix} \text{vec}\left\{\frac{\partial E_o(\Theta)}{\partial \text{Re}(c)}\right\} & \text{vec}\left\{\frac{\partial E_o(\Theta)}{\partial \text{Im}(c)}\right\} \end{bmatrix} \tag{3.157}$$

The partial derivatives in entries X_o^a, X_o^b, X_o^c are given by:

$$\frac{\partial E_o(\Theta)}{\partial \mathrm{Re}(a)} = \begin{bmatrix} \frac{-N_{o1}(\omega_1)}{d(\omega_1)^2\sigma_{H_{o1}(\omega_1)}} & \cdots & \frac{-N_{oN_i}(\omega_1)}{d(\omega_1)^2\sigma_{H_{oN_i}(\omega_1)}} \\ \vdots & \vdots & \vdots \\ \frac{-N_{o1}(\omega_{N_f})}{d(\omega_{N_f})^2\sigma_{H_{o1}(\omega_{N_f})}} & \cdots & \frac{-N_{oN_i}(\omega_{N_f})}{d(\omega_{N_f})^2\sigma_{H_{oN_i}(\omega_{N_f})}} \end{bmatrix} \tag{3.158}$$

$$\frac{\partial E_o(\Theta)}{\partial \mathrm{Im}(a)} = \begin{bmatrix} \frac{-jN_{o1}(\omega_1)}{d(\omega_1)^2\sigma_{H_{o1}(\omega_1)}} & \cdots & \frac{-jN_{oN_i}(\omega_1)}{d(\omega_1)^2\sigma_{H_{oN_i}(\omega_1)}} \\ \vdots & \vdots & \vdots \\ \frac{-jN_{o1}(\omega_{N_f})}{d(\omega_{N_f})^2\sigma_{H_{o1}(\omega_{N_f})}} & \cdots & \frac{-jN_{oN_i}(\omega_{N_f})}{d(\omega_{N_f})^2\sigma_{H_{oN_i}(\omega_{N_f})}} \end{bmatrix} \tag{3.159}$$

$$\frac{\partial E_o(\Theta)}{\partial \mathrm{Re}(b)} = \begin{bmatrix} \frac{-j\omega_1 N_{o1}(\omega_1)}{d(\omega_1)^2\sigma_{H_{o1}(\omega_1)}} & \cdots & \frac{-j\omega_1 N_{oN_i}(\omega_1)}{d(\omega_1)^2\sigma_{H_{oN_i}(\omega_1)}} \\ \vdots & \vdots & \vdots \\ \frac{-j\omega_{N_f} N_{o1}(\omega_{N_f})}{d(\omega_{N_f})^2\sigma_{H_{o1}(\omega_{N_f})}} & \cdots & \frac{-j\omega_{N_f} N_{oN_i}(\omega_{N_f})}{d(\omega_{N_f})^2\sigma_{H_{oN_i}(\omega_{N_f})}} \end{bmatrix} \tag{3.160}$$

$$\frac{\partial E_o(\Theta)}{\partial \mathrm{Im}(b)} = \begin{bmatrix} \frac{\omega_1 N_{o1}(\omega_1)}{d(\omega_1)^2\sigma_{H_{o1}(\omega_1)}} & \cdots & \frac{\omega_1 N_{oN_i}(\omega_1)}{d(\omega_1)^2\sigma_{H_{oN_i}(\omega_1)}} \\ \vdots & \vdots & \vdots \\ \frac{\omega_{N_f} N_{o1}(\omega_{N_f})}{d(\omega_{N_f})^2\sigma_{H_{o1}(\omega_{N_f})}} & \cdots & \frac{\omega_{N_f} N_{oN_i}(\omega_{N_f})}{d(\omega_{N_f})^2\sigma_{H_{oN_i}(\omega_{N_f})}} \end{bmatrix} \tag{3.161}$$

and

$$\frac{\partial E_o(\Theta)}{\partial \mathrm{Re}(c)} = \begin{bmatrix} \frac{\omega_1^2 N_{o1}(\omega_1)}{d(\omega_1)^2\sigma_{H_{o1}(\omega_1)}} & \cdots & \frac{\omega_1^2 N_{oN_i}(\omega_1)}{d(\omega_1)^2\sigma_{H_{oN_i}(\omega_1)}} \\ \vdots & \vdots & \vdots \\ \frac{\omega_{N_f}^2 N_{o1}(\omega_{N_f})}{d(\omega_{N_f})^2\sigma_{H_{o1}(\omega_{N_f})}} & \cdots & \frac{\omega_{N_f}^2 N_{oN_i}(\omega_{N_f})}{d(\omega_{N_f})^2\sigma_{H_{oN_i}(\omega_{N_f})}} \end{bmatrix} \tag{3.162}$$

$$\frac{\partial E_o(\Theta)}{\partial \mathrm{Im}(c)} = \begin{bmatrix} \frac{j\omega_1^2 N_{o1}(\omega_1)}{d(\omega_1)^2\sigma_{H_{o1}(\omega_1)}} & \cdots & \frac{j\omega_1^2 N_{oN_i}(\omega_1)}{d(\omega_1)^2\sigma_{H_{oN_i}(\omega_1)}} \\ \vdots & \vdots & \vdots \\ \frac{j\omega_{N_f}^2 N_{o1}(\omega_{N_f})}{d(\omega_{N_f})^2\sigma_{H_{o1}(\omega_{N_f})}} & \cdots & \frac{j\omega_{N_f}^2 N_{oN_i}(\omega_{N_f})}{d(\omega_{N_f})^2\sigma_{H_{oN_i}(\omega_{N_f})}} \end{bmatrix} \tag{3.163}$$

with $N_o(\omega_f)$ corresponding to the o^{th} row of the numerator matrix and $d(\omega_f)$ the denominator of the enhanced residual model. In eq. (3.146), Y_o is given by:

$$Y_o = \begin{bmatrix} Y_o^V & Y_o^A & Y_o^B & Y_o^C \end{bmatrix} \tag{3.164}$$

where Y_o^V is a sub-matrix containing the derivatives of the equation error with respect to the real and imaginary parts of the o^{th} mode shape elements, and Y_o^A, Y_o^B and Y_o^C sub-matrices containing the derivatives with regard to the real and imaginary parts of the o^{th} row of the numerator residual matrices $[AR]$, $[BR]$ and $[CR]$, respectively. These sub-matrices are computed, respectively, as follows:

$$Y_o^V = \begin{bmatrix} \text{vec}\left\{\frac{\partial E_o(\Theta)}{\partial \text{Re}(v_{o1})}\right\} & \cdots & \text{vec}\left\{\frac{\partial E_o(\Theta)}{\partial \text{Re}(v_{oN_m})}\right\} & \text{vec}\left\{\frac{\partial E_o(\Theta)}{\partial \text{Im}(v_{o1})}\right\} & \cdots & \text{vec}\left\{\frac{\partial E_o(\Theta)}{\partial \text{Im}(v_{oN_m})}\right\} \end{bmatrix} \tag{3.165}$$

$$Y_o^A = \begin{bmatrix} \text{vec}\left\{\frac{\partial E_o(\Theta)}{\partial \text{Re}([AR]_{o1})}\right\} & \cdots & \text{vec}\left\{\frac{\partial E_o(\Theta)}{\partial \text{Re}([AR]_{oN_i})}\right\} & \text{vec}\left\{\frac{\partial E_o(\Theta)}{\partial \text{Im}([AR]_{o1})}\right\} & \cdots & \text{vec}\left\{\frac{\partial E_o(\Theta)}{\partial \text{Im}([AR]_{oN_i})}\right\} \end{bmatrix} \tag{3.166}$$

$$Y_o^B = \begin{bmatrix} \text{vec}\left\{\frac{\partial E_o(\Theta)}{\partial \text{Re}([BR]_{o1})}\right\} & \cdots & \text{vec}\left\{\frac{\partial E_o(\Theta)}{\partial \text{Re}([BR]_{oN_i})}\right\} & \text{vec}\left\{\frac{\partial E_o(\Theta)}{\partial \text{Im}([BR]_{o1})}\right\} & \cdots & \text{vec}\left\{\frac{\partial E_o(\Theta)}{\partial \text{Im}([BR]_{oN_i})}\right\} \end{bmatrix} \tag{3.167}$$

$$Y_o^C = \begin{bmatrix} \text{vec}\left\{\frac{\partial E_o(\Theta)}{\partial \text{Re}([CR]_{o1})}\right\} & \cdots & \text{vec}\left\{\frac{\partial E_o(\Theta)}{\partial \text{Re}([CR]_{oN_i})}\right\} & \text{vec}\left\{\frac{\partial E_o(\Theta)}{\partial \text{Im}([CR]_{o1})}\right\} & \cdots & \text{vec}\left\{\frac{\partial E_o(\Theta)}{\partial \text{Im}([CR]_{oN_i})}\right\} \end{bmatrix} \tag{3.168}$$

with

$$\frac{\partial E_o(\Theta)}{\partial \text{Re}\,(v_{om})} = \begin{bmatrix} \frac{1}{\sigma_{H_{o1}(\omega_1)}}\left(\frac{l_{1m}}{(j\omega_1-\lambda_m)} + \frac{l_{1m}^*}{(j\omega_1-\lambda_m^*)}\right) & \cdots & \frac{1}{\sigma_{H_{oN_i}(\omega_1)}}\left(\frac{l_{N_im}}{(j\omega_1-\lambda_m)} + \frac{l_{N_im}^*}{(j\omega_1-\lambda_m^*)}\right) \\ \vdots & \vdots & \vdots \\ \frac{1}{\sigma_{H_{o1}(\omega_{N_f})}}\left(\frac{l_{1m}}{(j\omega_{N_f}-\lambda_m)} + \frac{l_{1m}^*}{(j\omega_{N_f}-\lambda_m^*)}\right) & \cdots & \frac{1}{\sigma_{H_{oN_i}(\omega_{N_f})}}\left(\frac{l_{N_im}}{(j\omega_{N_f}-\lambda_m)} + \frac{l_{N_im}^*}{(j\omega_{N_f}-\lambda_m^*)}\right) \end{bmatrix} \tag{3.169}$$

$$\frac{\partial E_o(\Theta)}{\partial \mathrm{Im}\,(v_{om})} = \begin{bmatrix} \frac{j}{\sigma_{H_{o1}(\omega_1)}}\left(\frac{l_{1m}}{(j\omega_1-\lambda_m)}-\frac{l^*_{1m}}{(j\omega_1-\lambda^*_m)}\right) & \cdots & \frac{j}{\sigma_{H_{oN_i}(\omega_1)}}\left(\frac{l_{N_im}}{(j\omega_1-\lambda_m)}-\frac{l^*_{N_im}}{(j\omega_1-\lambda^*_m)}\right) \\ \vdots & \vdots & \vdots \\ \frac{j}{\sigma_{H_{o1}(\omega_{N_f})}}\left(\frac{l_{1m}}{(j\omega_{N_f}-\lambda_m)}-\frac{l^*_{1m}}{(j\omega_{N_f}-\lambda^*_m)}\right) & \cdots & \frac{j}{\sigma_{H_{oN_i}(\omega_{N_f})}}\left(\frac{l_{N_im}}{(j\omega_{N_f}-\lambda_m)}-\frac{l^*_{N_im}}{(j\omega_{N_f}-\lambda^*_m)}\right) \end{bmatrix} \tag{3.170}$$

$$\frac{\partial E_o(\Theta)}{\partial \mathrm{Re}\,([AR]_{oi})} = \begin{bmatrix} \frac{\delta_{i1}}{d(\omega_1)\sigma_{H_{o1}(\omega_1)}} & \cdots & \frac{\delta_{iN_i}}{d(\omega_1)\sigma_{H_{oN_i}(\omega_1)}} \\ \vdots & \vdots & \vdots \\ \frac{\delta_{i1}}{d(\omega_{N_f})\sigma_{H_{o1}(\omega_{N_f})}} & \cdots & \frac{\delta_{iN_i}}{d(\omega_{N_f})\sigma_{H_{oN_i}(\omega_{N_f})}} \end{bmatrix} \tag{3.171}$$

$$\frac{\partial E_o(\Theta)}{\partial \mathrm{Im}\,([AR]_{oi})} = \begin{bmatrix} \frac{j\delta_{i1}}{d(\omega_1)\sigma_{H_{o1}(\omega_1)}} & \cdots & \frac{j\delta_{iN_i}}{d(\omega_1)\sigma_{H_{oN_i}(\omega_1)}} \\ \vdots & \vdots & \vdots \\ \frac{j\delta_{i1}}{d(\omega_{N_f})\sigma_{H_{o1}(\omega_{N_f})}} & \cdots & \frac{j\delta_{iN_i}}{d(\omega_{N_f})\sigma_{H_{oN_i}(\omega_{N_f})}} \end{bmatrix} \tag{3.172}$$

$$\frac{\partial E_o(\Theta)}{\partial \mathrm{Re}\,([BR]_{oi})} = \begin{bmatrix} \frac{j\omega_1\delta_{i1}}{d(\omega_1)\sigma_{H_{o1}(\omega_1)}} & \cdots & \frac{j\omega_1\delta_{iN_i}}{d(\omega_1)\sigma_{H_{oN_i}(\omega_1)}} \\ \vdots & \vdots & \vdots \\ \frac{j\omega_{N_f}\delta_{i1}}{d(\omega_{N_f})\sigma_{H_{o1}(\omega_{N_f})}} & \cdots & \frac{j\omega_{N_f}\delta_{iN_i}}{d(\omega_{N_f})\sigma_{H_{oN_i}(\omega_{N_f})}} \end{bmatrix} \tag{3.173}$$

$$\frac{\partial E_o(\Theta)}{\partial \mathrm{Im}\,([BR]_{oi})} = \begin{bmatrix} \frac{-\omega_1\delta_{i1}}{d(\omega_1)\sigma_{H_{o1}(\omega_1)}} & \cdots & \frac{-\omega_1\delta_{iN_i}}{d(\omega_1)\sigma_{H_{oN_i}(\omega_1)}} \\ \vdots & \vdots & \vdots \\ \frac{-\omega_{N_f}\delta_{i1}}{d(\omega_{N_f})\sigma_{H_{o1}(\omega_{N_f})}} & \cdots & \frac{-\omega_{N_f}\delta_{iN_i}}{d(\omega_{N_f})\sigma_{H_{oN_i}(\omega_{N_f})}} \end{bmatrix} \tag{3.174}$$

$$\frac{\partial E_o(\Theta)}{\partial \mathrm{Re}\,([CR]_{oi})} = \begin{bmatrix} \frac{-\omega_1^2\delta_{i1}}{d(\omega_1)\sigma_{H_{o1}(\omega_1)}} & \cdots & \frac{-\omega_1^2\delta_{iN_i}}{d(\omega_1)\sigma_{H_{oN_i}(\omega_1)}} \\ \vdots & \vdots & \vdots \\ \frac{-\omega_{N_f}^2\delta_{i1}}{d(\omega_{N_f})\sigma_{H_{o1}(\omega_{N_f})}} & \cdots & \frac{-\omega_{N_f}^2\delta_{iN_i}}{d(\omega_{N_f})\sigma_{H_{oN_i}(\omega_{N_f})}} \end{bmatrix} \tag{3.175}$$

$$\frac{\partial E_o(\Theta)}{\partial \mathrm{Im}\,([CR]_{oi})} = \begin{bmatrix} \frac{-j\omega_1^2\delta_{i1}}{d(\omega_1)\sigma_{H_{o1}(\omega_1)}} & \cdots & \frac{-j\omega_1^2\delta_{iN_i}}{d(\omega_1)\sigma_{H_{oN_i}(\omega_1)}} \\ \vdots & \vdots & \vdots \\ \frac{-j\omega_{N_f}^2\delta_{i1}}{d(\omega_{N_f})\sigma_{H_{o1}(\omega_{N_f})}} & \cdots & \frac{-j\omega_{N_f}^2\delta_{iN_i}}{d(\omega_{N_f})\sigma_{H_{oN_i}(\omega_{N_f})}} \end{bmatrix} \tag{3.176}$$

Given the block structure of the Jacobean matrix, the normal equations (3.142) are rewritten as follows:

$$\begin{bmatrix} R_1 & 0 & \cdots & 0 & S_1^d & S_1^L & S_1^\lambda \\ 0 & R_2 & \cdots & 0 & S_2^d & S_2^L & S_2^\lambda \\ \vdots & \vdots & \ddots & \vdots & \vdots & \vdots & \vdots \\ 0 & 0 & \cdots & R_{N_o} & S_{N_o}^d & S_{N_o}^L & S_{N_o}^\lambda \\ S_1^{dT} & S_2^{dT} & \cdots & S_{N_o}^{d\ T} & \sum_{o=1}^{N_o} T_o^d & \sum_{o=1}^{N_o} T_o^{dL} & \sum_{o=1}^{N_o} T_o^{d\lambda} \\ S_1^{LT} & S_2^{LT} & \cdots & S_{N_o}^{L\ T} & \sum_{o=1}^{N_o} T_o^{Ld} & \sum_{o=1}^{N_o} T_o^{L} & \sum_{o=1}^{N_o} T_o^{L\lambda} \\ S_1^{\lambda T} & S_2^{\lambda T} & \cdots & S_{N_o}^{\lambda\ T} & \sum_{o=1}^{N_o} T_o^{\lambda L} & \sum_{o=1}^{N_o} T_o^{\lambda d} & \sum_{o=1}^{N_o} T_o^{\lambda} \end{bmatrix} \begin{Bmatrix} \text{vec}(\Delta\theta_1) \\ \text{vec}(\Delta\theta_1) \\ \vdots \\ \text{vec}(\Delta\theta_{N_o}) \\ \text{vec}(\Delta\theta_d) \\ \text{vec}(\Delta\theta_L) \\ \text{vec}(\Delta\theta_\lambda) \end{Bmatrix} = - \begin{Bmatrix} \text{Re}\left(Y_1^H \text{vec}(E_1)\right) \\ \text{Re}\left(Y_2^H \text{vec}(E_2)\right) \\ \vdots \\ \text{Re}\left(Y_{N_o}^H \text{vec}(E_{N_o})\right) \\ \sum_{o=1}^{N_o} \text{Re}\left(X_o^{dH} \text{vec}(E_o)\right) \\ \sum_{o=1}^{N_o} \text{Re}\left(X_o^{LH} \text{vec}(E_o)\right) \\ \sum_{o=1}^{N_o} \text{Re}\left(X_o^{\lambda H} \text{vec}(E_o)\right) \end{Bmatrix} \tag{3.177}$$

with

$$\begin{aligned} R_o &= \text{Re}\left(Y_o^H Y_o\right) \in \mathbb{R}^{2(N_m+3N_i)\times 2(N_m+3N_i)} \\ S_o^d &= \text{Re}\left(Y_o^H X_o^d\right) \in \mathbb{R}^{2(N_m+3N_i)\times 6} \\ S_o^L &= \text{Re}\left(Y_o^H X_o^L\right) \in \mathbb{R}^{2(N_m+3N_i)\times 2N_m(N_i-1)} \\ S_o^\lambda &= \text{Re}\left(Y_o^H X_o^\lambda\right) \in \mathbb{R}^{2(N_m+3N_i)\times 2N_m} \\ T_o^d &= \text{Re}\left(X_o^{dH} X_o^d\right) \in \mathbb{R}^{6\times 6} \\ T_o^L &= \text{Re}\left(X_o^{LH} X_o^L\right) \in \mathbb{R}^{2N_m(N_i-1)\times 2N_m(N_i-1)} \\ T_o^\lambda &= \text{Re}\left(X_o^{\lambda H} X_o^\lambda\right) \in \mathbb{R}^{2N_m\times 2N_m} \end{aligned}$$

$$\begin{aligned} T_o^{dL} &= \text{Re}\left(X_o^{dH} X_o^L\right) \in \mathbb{R}^{6\times 2N_m(N_i-1)} \\ T_o^{d\lambda} &= \text{Re}\left(X_o^{dH} X_o^\lambda\right) \in \mathbb{R}^{6\times 2N_m} \\ T_o^{Ld} &= \text{Re}\left(X_o^{LH} X_o^d\right) \in \mathbb{R}^{2N_m(N_i-1)\times 6} \\ T_o^{L\lambda} &= \text{Re}\left(X_o^{LH} X_o^\lambda\right) \in \mathbb{R}^{2N_m(N_i-1)\times 2N_m} \\ T_o^{\lambda d} &= \text{Re}\left(X_o^{\lambda H} X_o^d\right) \in \mathbb{R}^{2N_m\times 6} \\ T_o^{\lambda L} &= \text{Re}\left(X_o^{\lambda H} X_o^L\right) \in \mathbb{R}^{2N_m\times 2N_m(N_i-1)} \end{aligned}$$

From eqs. (3.177), the perturbation on the coefficients $\text{vec}(\Delta\theta_o)$ (i.e. the perturbations on the real and imaginary parts of the mode shape elements, and on the real and imaginary parts of the numerator matrices of the residual model) can be written as a function of the perturbation on the denominator coefficients of the residual model $\text{vec}(\Delta\theta_d)$, operational factors $\text{vec}(\Delta\theta_L)$ and on the poles $\text{vec}(\Delta\theta_\lambda)$, as:

$$\text{vec}(\Delta\theta_o) = -R_o^{-1}\left(\text{Re}\left(Y_o^H \text{vec}(E_o)\right) + S_o^d \text{vec}(\Delta\theta_d) + S_o^L \text{vec}(\Delta\theta_L) + S_o^\lambda \text{vec}(\Delta\theta_\lambda)\right) \tag{3.178}$$

By making use of eq. (3.178), the perturbations $\text{vec}(\Delta\theta_o)$ can be eliminated from the normal equations (3.177), yielding:

$$\begin{bmatrix} \sum_{o=1}^{N_o} T_o^d - S_o^{dT} R_o^{-1} S_o^d & \sum_{o=1}^{N_o} T_o^{dL} - S_o^{dT} R_o^{-1} S_o^L & \sum_{o=1}^{N_o} T_o^{d\lambda} - S_o^{dT} R_o^{-1} S_o^\lambda \\ \sum_{o=1}^{N_o} T_o^{Ld} - S_o^{LT} R_o^{-1} S_o^d & \sum_{o=1}^{N_o} T_o^{L} - S_o^{LT} R_o^{-1} S_o^L & \sum_{o=1}^{N_o} T_o^{L\lambda} - S_o^{LT} R_o^{-1} S_o^\lambda \\ \sum_{o=1}^{N_o} T_o^{\lambda d} - S_o^{\lambda T} R_o^{-1} S_o^d & \sum_{o=1}^{N_o} T_o^{\lambda L} - S_o^{\lambda T} R_o^{-1} S_o^L & \sum_{o=1}^{N_o} T_o^{\lambda} - S_o^{\lambda T} R_o^{-1} S_o^\lambda \end{bmatrix} \begin{Bmatrix} \mathrm{vec}(\Delta\theta_d) \\ \mathrm{vec}(\Delta\theta_L) \\ \mathrm{vec}(\Delta\theta_\lambda) \end{Bmatrix} = \begin{bmatrix} \sum_{o=1}^{N_o} S_o^{dT} R_o^{-1} \mathrm{Re}\left(Y_o^H \mathrm{vec}(E_o)\right) - \mathrm{Re}\left(X_o^{dH} \mathrm{vec}(E_o)\right) \\ \sum_{o=1}^{N_o} S_o^{LT} R_o^{-1} \mathrm{Re}\left(Y_o^H \mathrm{vec}(E_o)\right) - \mathrm{Re}\left(X_o^{LH} \mathrm{vec}(E_o)\right) \\ \sum_{o=1}^{N_o} S_o^{\lambda T} R_o^{-1} \mathrm{Re}\left(Y_o^H \mathrm{vec}(E_o)\right) - \mathrm{Re}\left(X_o^{\lambda H} \mathrm{vec}(E_o)\right) \end{bmatrix} \tag{3.179}$$

or in a more compact form:

$$\begin{bmatrix} M_1 & M_2 & M_3 \\ M_4 & M_5 & M_6 \\ M_7 & M_8 & M_9 \end{bmatrix} \begin{Bmatrix} \mathrm{vec}(\Delta\theta_d) \\ \mathrm{vec}(\Delta\theta_L) \\ \mathrm{vec}(\Delta\theta_\lambda) \end{Bmatrix} = \begin{bmatrix} M_{10} \\ M_{11} \\ M_{12} \end{bmatrix} \tag{3.180}$$

with

$$M_1 = \sum_{o=1}^{N_o} T_o^d - S_o^{dT} R_o^{-1} S_o^d, \quad M_4 = \sum_{o=1}^{N_o} T_o^{Ld} - S_o^{LT} R_o^{-1} S_o^d, \quad M_7 = \sum_{o=1}^{N_o} T_o^{\lambda d} - S_o^{\lambda T} R_o^{-1} S_o^d, \quad M_{10} = \sum_{o=1}^{N_o} S_o^{dT} R_o^{-1} \mathrm{Re}\left(Y_o^H \mathrm{vec}(E_o)\right) - \mathrm{Re}\left(X_o^{dH} \mathrm{vec}(E_o)\right)$$

$$M_2 = \sum_{o=1}^{N_o} T_o^{dL} - S_o^{dT} R_o^{-1} S_o^L, \quad M_5 = \sum_{o=1}^{N_o} T_o^{L} - S_o^{LT} R_o^{-1} S_o^L, \quad M_8 = \sum_{o=1}^{N_o} T_o^{\lambda L} - S_o^{\lambda T} R_o^{-1} S_o^L, \quad M_{11} = \sum_{o=1}^{N_o} S_o^{LT} R_o^{-1} \mathrm{Re}\left(Y_o^H \mathrm{vec}(E_o)\right) - \mathrm{Re}\left(X_o^{LH} \mathrm{vec}(E_o)\right)$$

$$M_3 = \sum_{o=1}^{N_o} T_o^{d\lambda} - S_o^{dT} R_o^{-1} S_o^\lambda, \quad M_6 = \sum_{o=1}^{N_o} T_o^{L\lambda} - S_o^{LT} R_o^{-1} S_o^\lambda, \quad M_9 = \sum_{o=1}^{N_o} T_o^{\lambda} - S_o^{\lambda T} R_o^{-1} S_o^\lambda, \quad M_{12} = \sum_{o=1}^{N_o} S_o^{\lambda T} R_o^{-1} \mathrm{Re}\left(Y_o^H \mathrm{vec}(E_o)\right) - \mathrm{Re}\left(X_o^{\lambda H} \mathrm{vec}(E_o)\right)$$

This elimination decreases the memory and computational time required to run the algorithm. As for the **MLE-CDM**, an efficient implementation of the frequency domain **MLE** in modal model formulation is only possible if the variances are taken into account in the cost function (3.133). Once the perturbation on the poles, participation factors and on the denominator residuals are calculated in the last iteration by means of eq. (3.179), then the perturbations on the mode shapes and numerator residuals are computed using eq. (3.178).

Estimation of the uncertainty bounds

A good approximation of the covariance of the **ML** parameters Θ_{ML-MM} is obtained by inverting the Fisher information matrix (Pintelon and Schoukens, 2001):

$$\mathrm{Cov}(V,[AR],[BR],[CR],a,b,c,L,\lambda) \simeq \left[2\mathrm{Re}\left(J_l^H J_l\right)\right]^{-1} \tag{3.181}$$

with J_l the Jacobean matrix computed in the last iteration of the Gaussian-Newton algorithm. Taking advantage of the structure of the Jacobean matrix and using the matrix inversion lemma (Kailath, 1980), the covariance of the denominator coefficients of the residual model, the covariance of the participation factors and the covariance of poles can be estimated, independently, as follows:

$$\text{Cov}(a,b,c) \simeq M_1^{-1} + M_1^{-1} \begin{bmatrix} M_2 & M_3 \end{bmatrix} \begin{bmatrix} Z_1 & Z_2 \\ Z_3 & \Delta_1^{-1} \end{bmatrix} \begin{bmatrix} M_4 \\ M_7 \end{bmatrix} M_1^{-1} \tag{3.182}$$

$$\text{Cov}(L) \simeq Z_1 \tag{3.183}$$

$$\text{Cov}(\lambda) \simeq \Delta_1^{-1} \tag{3.184}$$

with

$$Z_1 = -(M_5 - M_4 M_1^{-1} M_2)^{-1} \left[I_{2N_m(N_i-1)} + (M_6 - M_4 M_1^{-1} M_3) \quad -\Delta_1 \begin{bmatrix} M_4 \\ M_7 \end{bmatrix} (M_5 - M_4 M_1^{-1} M_2)^{-1} \right]$$

$$\Delta_1 = \left(M_9 - M_7 M_1^{-1} M_3\right) - \left(M_8 - M_7 M_1^{-1} M_2\right) \left(M_5 - M_4 M_1^{-1} M_2\right)^{-1} \left(M_6 - M_4 M_1^{-1} M_3\right)$$

$$Z_2 = -\left(M_5 - M_4 M_1^{-1} M_2\right)^{-1} \left(M_6 - M_4 M_1^{-1} M_3\right) \Delta_1^{-1}$$

and

$$Z_3 = -\Delta_1^{-1} \left(M_8 - M_7 M_1^{-1} M_2\right)^{-1} \left(M_5 - M_4 M_1^{-1} M_2\right)$$

The covariance of the mode shapes and numerator matrices of the residual model, on the other hand, is estimated by means of the following expressions:

$$\text{Cov}(V_o, [AR]_o, [BR]_o, [CR]_o) \simeq R_o^{-1} + \left(\alpha_o S_o^{d\,T} + \beta_o S_o^{d\,T} + \gamma_o S_o^{\lambda\,T} \right) R_o^{-1} \tag{3.185}$$

where α_o, β_o and γ_o are given, respectively, as follows:

$$\alpha_o = R_o^{-1} \left(S_o^d Z_4 + S_o^L Z_5 + S_o^\lambda Z_6 \right)$$

$$\beta_o = R_o^{-1} \left(S_o^d Z_7 + S_o^L Z_1 + S_o^\lambda Z_3 \right)$$

and

$$\gamma_o = R_o^{-1}\left(S_o^d Z_8 + S_o^L Z_2 + S_o^\lambda \Delta_1^{-1}\right)$$

with

$$Z_4 = M_1^{-1} + \left[\left(M_1^{-1}M_2Z_1 + M_1^{-1}M_3Z_3\right)M_4M_1^{-1} + \left(M_1^{-1}M_2Z_2 + M_1^{-1}M_3\Delta^{-1}\right)M_7M_1^{-1}\right]$$

$$Z_5 = -\left(Z_1M_4 + Z_2M_7\right)M_1^{-1}, \quad Z_6 = -\left(Z_3M_4 + \Delta_1^{-1}M_7\right)M_1^{-1}$$

$$Z_7 = -\left(M_1^{-1}M_2Z_1 + M_1^{-1}M_3Z_3\right), \quad Z_8 = -\left(M_1^{-1}M_2Z_2 + M_1^{-1}M_3\Delta^{-1}\right)$$

The strategy used for partitioning the normal matrices in eq. (3.177) was proposed by El-Kafafy (2013) to improve the conditioning of these matrices and, therefore, the precision of the estimates provided by the **pMLE-MM**. Once the covariance of the poles are estimated using eq. (3.184), the covariance of corresponding natural frequencies and damping ratios can be estimated using the following linearisation formulas (Guillaume et al., 1989; Pintelon et al., 2007):

$$\begin{aligned}
\mathrm{Var}(f_{n_m}) &\simeq \frac{1}{(2\pi)^2}\begin{bmatrix}0 & 1\end{bmatrix}\mathrm{Cov}\left((\lambda_m)_{\mathrm{re}}\right)\begin{bmatrix}0\\1\end{bmatrix} \\
\mathrm{Var}(\xi_{n_m}) &\simeq \frac{\left(\mathrm{Im}\left(\lambda_m\right)\right)^2}{|\lambda|^6}\begin{bmatrix}-\mathrm{Im}\left(\lambda_m\right) & \mathrm{Re}\left(\lambda_m\right)\end{bmatrix}\mathrm{Cov}\left((\lambda_m)_{\mathrm{re}}\right)\begin{bmatrix}-\mathrm{Im}\left(\lambda_m\right)\\ \mathrm{Re}\left(\lambda_m\right)\end{bmatrix}
\end{aligned} \tag{3.186}$$

with

$$(\lambda_m)_{\mathrm{re}} = \begin{Bmatrix}\mathrm{Re}\left(\lambda_m\right)\\ \mathrm{Im}\left(\lambda_m\right)\end{Bmatrix} \tag{3.187}$$

*3.5.3. Proposed Implementation of the **pMLE-MM***

In this section, another implementation of the **pMLE-MM** is proposed as an alternative to the derivation introduced by El-Kafafy (2013) and discussed in Section 3.5.2. The alternative implementation of the **pMLE-MM** proposed in this section addresses optimization process in a similar manner, but with the derivatives of the equation error taken directly with respect to the natural frequencies and damping ratios, real and imaginary parts of the denominator coefficients of the residual model, real and imaginary parts of the participation factors, real and imaginary parts of mode shapes, and to the real and imaginary parts of the numerator coefficients of the residual model.

One of the main advantages of this alternative strategy is the possibility to estimate the uncertainties on the identified modal natural frequencies and damping ratios directly from the Jacobian matrix, avoiding the necessity of estimating these uncertainties in a second step, i.e. by means of explicit linearization formulas. The data flow of this alternative implementation of the **pMLE-MM** is compared to the original implementation proposed by El-Kafafy (2013) in Fig. 3.14.

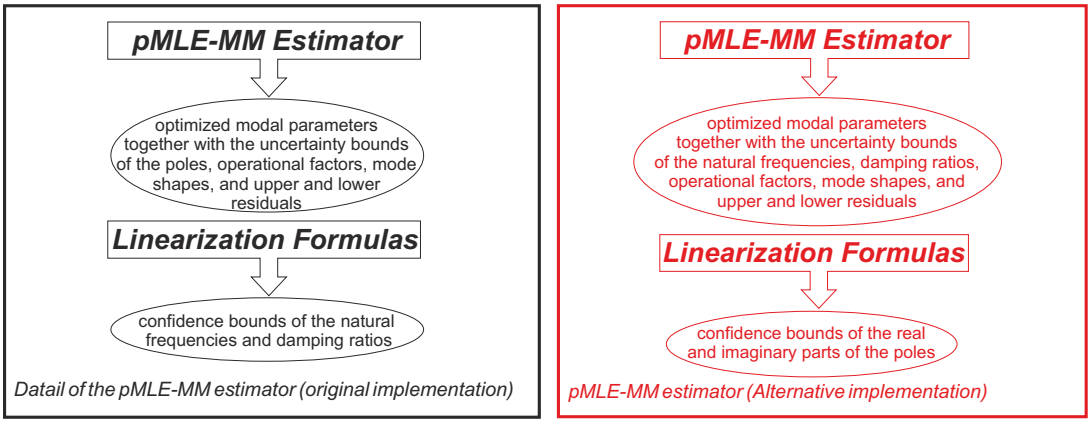

(a) (b)

Fig. 3.14 – Data flows of the implementation of the algorithm of the **pMLE-MM** introduced by El-Kafafy (2013) (a) and of the proposed algorithm (b).

In this proposed implementation the invariants of the modal model are parametrized as follows:

$$\Theta = \begin{bmatrix} \theta_1 & \theta_2 & \cdots & \theta_{N_o} & \theta_d & \theta_L & \theta_\lambda \end{bmatrix}^T \in \mathbb{R}^{2N_m(N_o+N_i+1)+6N_oN_i+6} \tag{3.188}$$

where the parameter θ_λ is now given by:

$$\theta_\lambda = \begin{bmatrix} f_{n_1} & f_{n_2} & \cdots & f_{n_{N_m}} & \xi_{n_1} & \xi_{n_2} & \cdots & \xi_{n_{N_m}} \end{bmatrix} \tag{3.189}$$

and the entries X_o^λ of the Jacobian matrix (3.146) given by:

$$X_o^\lambda = \begin{bmatrix} \text{vec}\left\{\frac{\partial E_o(\Theta)}{\partial f_{n_1}}\right\} & \text{vec}\left\{\frac{\partial E_o(\Theta)}{\partial f_{n_2}}\right\} & \cdots & \text{vec}\left\{\frac{\partial E_o(\Theta)}{\partial f_{n_{N_m}}}\right\} & \text{vec}\left\{\frac{\partial E_o(\Theta)}{\partial \xi_{n_1}}\right\} & \text{vec}\left\{\frac{\partial E_o(\Theta)}{\partial \xi_{n_2}}\right\} & \cdots & \text{vec}\left\{\frac{\partial E_o(\Theta)}{\partial \xi_{n_{N_m}}}\right\} \end{bmatrix} \tag{3.190}$$

with

$$\frac{\partial E_o(\Theta)}{\partial f_{n_m}} = \begin{bmatrix} \frac{2\pi}{|\lambda_m|\sigma_{H_{o1}(\omega_1)}}\left(\frac{v_{om}l_{1m}\lambda_m}{(j\omega_1-\lambda_m)^2}+\frac{v_{om}^*l_{1m}^*\lambda_m^*}{(j\omega_1-\lambda_m^*)^2}\right) & \cdots & \frac{2\pi}{|\lambda_m|\sigma_{H_{oN_i}(\omega_1)}}\left(\frac{v_{om}l_{N_im}\lambda_m}{(j\omega_1-\lambda_m)^2}+\frac{v_{om}^*l_{N_im}^*\lambda_m^*}{(j\omega_1-\lambda_m^*)^2}\right) \\ \vdots & \vdots & \vdots \\ \frac{2\pi}{|\lambda_m|\sigma_{H_{o1}(\omega_{N_f})}}\left(\frac{v_{om}l_{1m}\lambda_m}{(j\omega_{N_f}-\lambda_m)^2}+\frac{v_{om}^*l_{1m}^*\lambda_m^*}{(j\omega_{N_f}-\lambda_m^*)^2}\right) & \cdots & \frac{2\pi}{|\lambda_m|\sigma_{H_{oN_i}(\omega_{N_f})}}\left(\frac{v_{om}l_{N_im}\lambda_m}{(j\omega_{N_f}-\lambda_m)^2}+\frac{v_{om}^*l_{N_im}^*\lambda_m^*}{(j\omega_{N_f}-\lambda_m^*)^2}\right) \end{bmatrix} \tag{3.191}$$

$$\frac{\partial E_o(\Theta)}{\partial \xi_{n_m}} = \begin{bmatrix} \frac{j|\lambda_m|}{\mathrm{Im}(\lambda_m)\sigma_{H_{o1}(\omega_1)}}\left(\frac{v_{om}l_{1m}\lambda_m}{(j\omega_1-\lambda_m)^2}-\frac{v^*_{om}l^*_{1m}\lambda^*_m}{(j\omega_1-\lambda^*_m)^2}\right) & \cdots & \frac{j|\lambda_m|}{\mathrm{Im}(\lambda_m)\sigma_{H_{oN_i}(\omega_1)}}\left(\frac{v_{om}l_{N_im}\lambda_m}{(j\omega_1-\lambda_m)^2}-\frac{v^*_{om}l^*_{N_im}\lambda^*_m}{(j\omega_1-\lambda^*_m)^2}\right) \\ \vdots & \vdots & \vdots \\ \frac{j|\lambda_m|}{\mathrm{Im}(\lambda_m)\sigma_{H_{o1}(\omega_{N_f})}}\left(\frac{v_{om}l_{1m}\lambda_m}{(j\omega_{N_f}-\lambda_m)^2}-\frac{v^*_{om}l^*_{1m}\lambda^*_m}{(j\omega_{N_f}-\lambda^*_m)^2}\right) & \cdots & \frac{j|\lambda_m|}{\mathrm{Im}(\lambda_m)\sigma_{H_{oN_i}(\omega_{N_f})}}\left(\frac{v_{om}l_{N_im}\lambda_m}{(j\omega_{N_f}-\lambda_m)^2}-\frac{v^*_{om}l^*_{N_im}\lambda^*_m}{(j\omega_{N_f}-\lambda^*_m)^2}\right) \end{bmatrix} \tag{3.192}$$

The remaining entries Y_o, X_o^d, X_o^L are computed in the same way as in eqs. (3.164), (3.148) and (3.147). Once all entries of the Jacobian matrix are computed, the perturbations $\Delta\Theta_o$, $\Delta\Theta_d$, $\Delta\Theta_L$ and $\Delta\Theta_\lambda$ are computed in the same way as that described in Section 3.5.2.

Estimation of the uncertainty bounds

Despite the different parametrization adopted in the alternative implementation of **pMLE-MM**, the covariance of the invariants of the modal model can be computed independently from each other by following the same strategy as for the **pMLE-MM** discussed in Section 3.5.2. Due to the different parametrization chosen, however, the covariance of the natural frequency and damping ratios are computed directly from the normal matrices by means of the following expression:

$$\mathrm{Cov}(f_n, \xi_n) \simeq \Delta_1^{-1} \tag{3.193}$$

The main advantage of this alternative implementation of the **pMLE-MM** is that the uncertainties on the natural frequencies and damping ratios are computed directly from the Jacobian matrix, without using the explicit linearisation formulas found in Pintelon and Schoukens (2001). Instead, the linearisation are performed implicitly during the computation of the Jacobian matrix. If one is interested on the covariance of the poles, they can be estimated using the following expressions:

$$\begin{aligned} \mathrm{Var}\left(\mathrm{Re}\left(\lambda_m\right)\right) &\simeq 4\pi^2 \begin{bmatrix} f_{n_m} \\ \xi_{n_m} \end{bmatrix}^T \mathrm{Cov}\left(f_{n_m}, \xi_{n_m}\right) \begin{bmatrix} f_{n_m} \\ \xi_{n_m} \end{bmatrix} \\ \mathrm{Var}\left(\mathrm{Im}\left(\lambda_m\right)\right) &\simeq 4\pi^2 \left(1-\xi_{n_m}^2\right) \begin{bmatrix} 1 \\ \frac{-f_{n_m}\xi_{n_m}}{1-\xi_{n_m}^2} \end{bmatrix}^T \mathrm{Cov}\left(f_{n_m}, \xi_{n_m}\right) \begin{bmatrix} 1 \\ \frac{-f_{n_m}\xi_{n_m}}{1-\xi_{n_m}^2} \end{bmatrix} \end{aligned} \tag{3.194}$$

Logarithmic pMLE-MM

Another variant of the proposed implementation of the **pMLE-MM** can be derived by minimizing the following logarithmic cost function:

$$l(\Theta)_{Log-pML-MM} = \sum_{o=1}^{N_o} \sum_{f=1}^{N_f} E_o^{\log}(\Theta,\omega_f) E_o^{\log^H}(\Theta,\omega_f) \tag{3.195}$$

where $E_o^{\log}(\Theta,\omega_f) \in \mathbb{C}^{1\times N_i}$ is the logarithmic equation error given by:

$$E_o^{\log}(\Theta,\omega_f) = \left\langle \frac{\log(\hat{H}_{o1}(\Theta,\omega_f)) - \log(H_{o1}(\omega_f))}{\sigma^{\log}_{H_{o1}(\omega_f)}} \cdots \frac{\log(\hat{H}_{oN_i}(\Theta,\omega_f)) - \log(H_{oN_i}(\omega_f))}{\sigma^{\log}_{H_{oN_i}(\omega_f)}} \right\rangle \tag{3.196}$$

with $\sigma^{\log}_{H_o(\omega_f)}$ denoting the standard deviation of the logarithmic **FRF** matrix. The relationship between this standard deviation and the measured one is given as follows:

$$\sigma^{\log}_{H_{oi}(\omega_f)} = \frac{\sigma_{H_{oi}(\omega_f)}}{\left|H_{oi}(\omega_f)\right|}, \quad i = 1,2,\ldots,N_i. \tag{3.197}$$

The strategy used to minimize the cost function (3.133) can be employed to eq. (3.195) and the partial derivatives of the logarithmic error equation (3.196) with respect to the invariants of the modal model, are calculated as follows:

$$\frac{\partial E_o(\Theta)}{\partial f_{n_m}} = \frac{2\pi}{|\lambda_m|} \begin{bmatrix} \frac{|H_{o1}(\omega_1)|}{\hat{H}_{o1}(\Theta,\omega_1)\sigma_{H_{o1}(\omega_1)}} \left(\frac{v_{om} l_{1m} \lambda_m}{(j\omega_1-\lambda_m)^2} + \frac{v^*_{om} l^*_{1m} \lambda^*_m}{(j\omega_1-\lambda^*_m)^2} \right) & \cdots & \frac{\left|H_{oN_i}(\omega_1)\right|}{\hat{H}_{oN_i}(\Theta,\omega_1)\sigma_{H_{oN_i}(\omega_1)}} \left(\frac{v_{om} l_{N_i m} \lambda_m}{(j\omega_1-\lambda_m)^2} + \frac{v^*_{om} l^*_{N_i m} \lambda^*_m}{(j\omega_1-\lambda^*_m)^2} \right) \\ \vdots & \vdots & \vdots \\ \frac{\left|H_{o1}(\omega_{N_f})\right|}{\hat{H}_{o1}(\Theta,\omega_{N_f})\sigma_{H_{o1}(\omega_{N_f})}} \left(\frac{v_{om} l_{1m} \lambda_m}{(j\omega_{N_f}-\lambda_m)^2} + \frac{v^*_{om} l^*_{1m} \lambda^*_m}{(j\omega_{N_f}-\lambda^*_m)^2} \right) & \cdots & \frac{\left|H_{oN_i}(\omega_{N_f})\right|}{\hat{H}_{oN_i}(\Theta,\omega_{N_f})\sigma_{H_{oN_i}(\omega_{N_f})}} \left(\frac{v_{om} l_{N_i m} \lambda_m}{(j\omega_{N_f}-\lambda_m)^2} + \frac{v^*_{om} l^*_{N_i m} \lambda^*_m}{(j\omega_{N_f}-\lambda^*_m)^2} \right) \end{bmatrix} \tag{3.198}$$

$$\frac{\partial E_o(\Theta)}{\partial \xi_{n_m}} = \frac{|\lambda_m|}{\mathrm{Im}\,(\lambda_m)} \begin{bmatrix} \frac{j|H_{o1}(\omega_1)|}{\hat{H}_{o1}(\Theta,\omega_1)\sigma_{H_{o1}(\omega_1)}} \left(\frac{v_{om} l_{1m} \lambda_m}{(j\omega_1-\lambda_m)^2} - \frac{v^*_{om} l^*_{1m} \lambda^*_m}{(j\omega_1-\lambda^*_m)^2} \right) & \cdots & \frac{j\left|H_{oN_i}(\omega_1)\right|}{\hat{H}_{oN_i}(\Theta,\omega_1)\sigma_{H_{oN_i}(\omega_1)}} \left(\frac{v_{om} l_{N_i m} \lambda_m}{(j\omega_1-\lambda_m)^2} - \frac{v^*_{om} l^*_{N_i m} \lambda^*_m}{(j\omega_1-\lambda^*_m)^2} \right) \\ \vdots & \vdots & \vdots \\ \frac{j\left|H_{o1}(\omega_{N_f})\right|}{\hat{H}_{o1}(\Theta,\omega_{N_f})\sigma_{H_{o1}(\omega_{N_f})}} \left(\frac{v_{om} l_{1m} \lambda_m}{(j\omega_{N_f}-\lambda_m)^2} - \frac{v^*_{om} l^*_{1m} \lambda^*_m}{(j\omega_{N_f}-\lambda^*_m)^2} \right) & \cdots & \frac{j\left|H_{oN_i}(\omega_{N_f})\right|}{\hat{H}_{oN_i}(\Theta,\omega_{N_f})\sigma_{H_{oN_i}(\omega_{N_f})}} \left(\frac{v_{om} l_{N_i m} \lambda_m}{(j\omega_{N_f}-\lambda_m)^2} - \frac{v^*_{om} l^*_{N_i m} \lambda^*_m}{(j\omega_{N_f}-\lambda^*_m)^2} \right) \end{bmatrix} \tag{3.199}$$

$$\frac{\partial E_o(\Theta)}{\partial \mathrm{Re}\,(l_{km})} = \begin{bmatrix} \frac{\delta_{k1}|H_{o1}(\omega_1)|}{\hat{H}_{o1}(\Theta,\omega_1)\sigma_{H_{o1}(\omega_1)}}\left(\frac{v_{om}}{(j\omega_1-\lambda_m)}+\frac{v_{om}^*}{(j\omega_1-\lambda_m^*)}\right) & \cdots & \frac{\delta_{kN_i}\left|H_{oN_i}(\omega_1)\right|}{\hat{H}_{oN_i}(\Theta,\omega_1)\sigma_{H_{oN_i}(\omega_1)}}\left(\frac{v_{om}}{(j\omega_1-\lambda_m)}+\frac{v_{om}^*}{(j\omega_1-\lambda_m^*)}\right) \\ \vdots & \vdots & \vdots \\ \frac{\delta_{k1}\left|H_{o1}(\omega_{N_f})\right|}{\hat{H}_{o1}(\Theta,\omega_{N_f})\sigma_{H_{o1}(\omega_{N_f})}}\left(\frac{v_{om}}{(j\omega_{N_f}-\lambda_m)}+\frac{v_{om}^*}{(j\omega_{N_f}-\lambda_m^*)}\right) & \cdots & \frac{\delta_{kN_i}\left|H_{oN_i}(\omega_{N_f})\right|}{\hat{H}_{oN_i}(\Theta,\omega_{N_f})\sigma_{H_{oN_i}(\omega_{N_f})}}\left(\frac{v_{om}}{(j\omega_{N_f}-\lambda_m)}+\frac{v_{om}^*}{(j\omega_{N_f}-\lambda_m^*)}\right) \end{bmatrix} \tag{3.200}$$

$$\frac{\partial E_o(\Theta)}{\partial \mathrm{Im}\,(l_{km})} = \begin{bmatrix} \frac{j\delta_{k1}|H_{o1}(\omega_1)|}{\hat{H}_{o1}(\Theta,\omega_1)\sigma_{H_{o1}(\omega_1)}}\left(\frac{v_{om}}{(j\omega_1-\lambda_m)}-\frac{v_{om}^*}{(j\omega_1-\lambda_m^*)}\right) & \cdots & \frac{j\delta_{kN_i}\left|H_{oN_i}(\omega_1)\right|}{\hat{H}_{oN_i}(\Theta,\omega_1)\sigma_{H_{oN_i}(\omega_1)}}\left(\frac{v_{om}}{(j\omega_1-\lambda_m)}-\frac{v_{om}^*}{(j\omega_1-\lambda_m^*)}\right) \\ \vdots & \vdots & \vdots \\ \frac{j\delta_{k1}\left|H_{o1}(\omega_{N_f})\right|}{\hat{H}_{o1}(\Theta,\omega_{N_f})\sigma_{H_{o1}(\omega_{N_f})}}\left(\frac{v_{om}}{(j\omega_{N_f}-\lambda_m)}-\frac{v_{om}^*}{(j\omega_{N_f}-\lambda_m^*)}\right) & \cdots & \frac{j\delta_{kN_i}\left|H_{oN_i}(\omega_{N_f})\right|}{\hat{H}_{oN_i}(\Theta,\omega_{N_f})\sigma_{H_{oN_i}(\omega_{N_f})}}\left(\frac{v_{om}}{(j\omega_{N_f}-\lambda_m)}-\frac{v_{om}^*}{(j\omega_{N_f}-\lambda_m^*)}\right) \end{bmatrix} \tag{3.201}$$

$$\frac{\partial E_o(\Theta)}{\partial \mathrm{Re}\,(a)} = \begin{bmatrix} \frac{-N_{o1}(\omega_1)|H_{o1}(\omega_1)|}{d(\omega_1)^2\hat{H}_{o1}(\Theta,\omega_1)\sigma_{H_{o1}(\omega_1)}} & \cdots & \frac{-N_{oN_i}(\omega_1)\left|H_{oN_i}(\omega_1)\right|}{d(\omega_1)^2\hat{H}_{oN_i}(\Theta,\omega_1)\sigma_{H_{oN_i}(\omega_1)}} \\ \vdots & \vdots & \vdots \\ \frac{-N_{o1}(\omega_{N_f})\left|H_{o1}(\omega_{N_f})\right|}{d(\omega_{N_f})^2\hat{H}_{o1}(\Theta,\omega_{N_f})\sigma_{H_{o1}(\omega_{N_f})}} & \cdots & \frac{-N_{oN_i}(\omega_{N_f})\left|H_{oN_i}(\omega_{N_f})\right|}{d(\omega_{N_f})^2\hat{H}_{oN_i}(\Theta,\omega_{N_f})\sigma_{H_{oN_i}(\omega_{N_f})}} \end{bmatrix} \tag{3.202}$$

$$\frac{\partial E_o(\Theta)}{\partial \mathrm{Im}\,(a)} = \begin{bmatrix} \frac{-jN_{o1}(\omega_1)|H_{o1}(\omega_1)|}{d(\omega_1)^2\hat{H}_{o1}(\Theta,\omega_1)\sigma_{H_{o1}(\omega_1)}} & \cdots & \frac{-jN_{oN_i}(\omega_1)\left|H_{oN_i}(\omega_1)\right|}{d(\omega_1)^2\hat{H}_{oN_i}(\Theta,\omega_1)\sigma_{H_{oN_i}(\omega_1)}} \\ \vdots & \vdots & \vdots \\ \frac{-jN_{o1}(\omega_{N_f})\left|H_{o1}(\omega_{N_f})\right|}{d(\omega_{N_f})^2\hat{H}_{o1}(\Theta,\omega_{N_f})\sigma_{H_{o1}(\omega_{N_f})}} & \cdots & \frac{-jN_{oN_i}(\omega_{N_f})\left|H_{oN_i}(\omega_{N_f})\right|}{d(\omega_{N_f})^2\hat{H}_{oN_i}(\Theta,\omega_{N_f})\sigma_{H_{oN_i}(\omega_{N_f})}} \end{bmatrix} \tag{3.203}$$

$$\frac{\partial E_o(\Theta)}{\partial \mathrm{Re}\,(b)} = \begin{bmatrix} \frac{-j\omega_1 N_{o1}(\omega_1)|H_{o1}(\omega_1)|}{d(\omega_1)^2\hat{H}_{o1}(\Theta,\omega_1)\sigma_{H_{o1}(\omega_1)}} & \cdots & \frac{-j\omega_1 N_{oN_i}(\omega_1)\left|H_{oN_i}(\omega_1)\right|}{d(\omega_1)^2\hat{H}_{oN_i}(\Theta,\omega_1)\sigma_{H_{oN_i}(\omega_1)}} \\ \vdots & \vdots & \vdots \\ \frac{-j\omega_{N_f} N_{o1}(\omega_{N_f})\left|H_{o1}(\omega_{N_f})\right|}{d(\omega_{N_f})^2\hat{H}_{o1}(\Theta,\omega_{N_f})\sigma_{H_{o1}(\omega_{N_f})}} & \cdots & \frac{-j\omega_{N_f} N_{oN_i}(\omega_{N_f})\left|H_{oN_i}(\omega_{N_f})\right|}{d(\omega_{N_f})^2\hat{H}_{oN_i}(\Theta,\omega_{N_f})\sigma_{H_{oN_i}(\omega_{N_f})}} \end{bmatrix} \tag{3.204}$$

$$\frac{\partial E_o(\Theta)}{\partial \mathrm{Im}\,(b)} = \begin{bmatrix} \frac{\omega_1 N_{o1}(\omega_1)|H_{o1}(\omega_1)|}{d(\omega_1)^2\hat{H}_{o1}(\Theta,\omega_1)\sigma_{H_{o1}(\omega_1)}} & \cdots & \frac{\omega_1 N_{oN_i}(\omega_1)\left|H_{oN_i}(\omega_1)\right|}{d(\omega_1)^2\hat{H}_{oN_i}(\Theta,\omega_1)\sigma_{H_{oN_i}(\omega_1)}} \\ \vdots & \vdots & \vdots \\ \frac{\omega_{N_f} N_{o1}(\omega_{N_f})\left|H_{o1}(\omega_{N_f})\right|}{d(\omega_{N_f})^2\hat{H}_{o1}(\Theta,\omega_{N_f})\sigma_{H_{o1}(\omega_{N_f})}} & \cdots & \frac{\omega_{N_f} N_{oN_i}(\omega_{N_f})\left|H_{oN_i}(\omega_{N_f})\right|}{d(\omega_{N_f})^2\hat{H}_{oN_i}(\Theta,\omega_{N_f})\sigma_{H_{oN_i}(\omega_{N_f})}} \end{bmatrix} \tag{3.205}$$

$$\frac{\partial E_o(\Theta)}{\partial \mathrm{Re}\,(c)} = \begin{bmatrix} \frac{{\omega_1}^2 N_{o1}(\omega_1)|H_{o1}(\omega_1)|}{d(\omega_1)^2 \hat{H}_{o1}(\Theta,\omega_1)\sigma_{H_{o1}(\omega_1)}} & \cdots & \frac{{\omega_1}^2 N_{oN_i}(\omega_1)\left|H_{oN_i}(\omega_1)\right|}{d(\omega_1)^2 \hat{H}_{oN_i}(\Theta,\omega_1)\sigma_{H_{oN_i}(\omega_1)}} \\ \vdots & \vdots & \vdots \\ \frac{-j\omega_{N_f} N_{o1}(\omega_{N_f})\left|H_{o1}(\omega_{N_f})\right|}{d(\omega_{N_f})^2 \hat{H}_{o1}(\Theta,\omega_{N_f})\sigma_{H_{o1}(\omega_{N_f})}} & \cdots & \frac{{\omega_{N_f}}^2 N_{oN_i}(\omega_{N_f})\left|H_{oN_i}(\omega_{N_f})\right|}{d(\omega_{N_f})^2 \hat{H}_{oN_i}(\Theta,\omega_{N_f})\sigma_{H_{oN_i}(\omega_{N_f})}} \end{bmatrix} \tag{3.206}$$

$$\frac{\partial E_o(\Theta)}{\partial \mathrm{Im}\,(c)} = \begin{bmatrix} \frac{j{\omega_1}^2 N_{o1}(\omega_1)|H_{o1}(\omega_1)|}{d(\omega_1)^2 \hat{H}_{o1}(\Theta,\omega_1)\sigma_{H_{o1}(\omega_1)}} & \cdots & \frac{j{\omega_1}^2 N_{oN_i}(\omega_1)\left|H_{oN_i}(\omega_1)\right|}{d(\omega_1)^2 \hat{H}_{oN_i}(\Theta,\omega_1)\sigma_{H_{oN_i}(\omega_1)}} \\ \vdots & \vdots & \vdots \\ \frac{j\omega_{N_f}^2 N_{o1}(\omega_{N_f})\left|H_{o1}(\omega_{N_f})\right|}{d(\omega_{N_f})^2 \hat{H}_{o1}(\Theta,\omega_{N_f})\sigma_{H_{o1}(\omega_{N_f})}} & \cdots & \frac{j\omega_{N_f}^2 N_{oN_i}(\omega_{N_f})\left|H_{oN_i}(\omega_{N_f})\right|}{d(\omega_{N_f})^2 \hat{H}_{oN_i}(\Theta,\omega_{N_f})\sigma_{H_{oN_i}(\omega_{N_f})}} \end{bmatrix} \tag{3.207}$$

$$\frac{\partial E_o(\Theta)}{\partial \mathrm{Re}\,(v_{om})} = \begin{bmatrix} \frac{|H_{o1}(\omega_1)|}{\hat{H}_{o1}(\Theta,\omega_1)\sigma_{H_{o1}(\omega_1)}}\left(\frac{l_{1m}}{(j\omega_1-\lambda_m)}+\frac{l_{1m}^*}{(j\omega_1-\lambda_m^*)}\right) & \cdots & \frac{\left|H_{oN_i}(\omega_1)\right|}{\hat{H}_{oN_i}(\Theta,\omega_1)\sigma_{H_{oN_i}(\omega_1)}}\left(\frac{l_{N_im}}{(j\omega_1-\lambda_m)}+\frac{l_{N_im}^*}{(j\omega_1-\lambda_m^*)}\right) \\ \vdots & \vdots & \vdots \\ \frac{\left|H_{o1}(\omega_{N_f})\right|}{\hat{H}_{o1}(\Theta,\omega_{N_f})\sigma_{H_{o1}(\omega_{N_f})}}\left(\frac{l_{1m}}{(j\omega_{N_f}-\lambda_m)}+\frac{l_{1m}^*}{(j\omega_{N_f}-\lambda_m^*)}\right) & \cdots & \frac{\left|H_{oN_i}(\omega_{N_f})\right|}{\hat{H}_{oN_i}(\Theta,\omega_{N_f})\sigma_{H_{oN_i}(\omega_{N_f})}}\left(\frac{l_{N_im}}{(j\omega_{N_f}-\lambda_m)}+\frac{l_{N_im}^*}{(j\omega_{N_f}-\lambda_m^*)}\right) \end{bmatrix} \tag{3.208}$$

$$\frac{\partial E_o(\Theta)}{\partial \mathrm{Im}\,(v_{om})} = \begin{bmatrix} \frac{j|H_{o1}(\omega_1)|}{\hat{H}_{o1}(\Theta,\omega_1)\sigma_{H_{o1}(\omega_1)}}\left(\frac{l_{1m}}{(j\omega_1-\lambda_m)}-\frac{l_{1m}^*}{(j\omega_1-\lambda_m^*)}\right) & \cdots & \frac{j\left|H_{oN_i}(\omega_1)\right|}{\hat{H}_{oN_i}(\Theta,\omega_1)\sigma_{H_{oN_i}(\omega_1)}}\left(\frac{l_{N_im}}{(j\omega_1-\lambda_m)}-\frac{l_{N_im}^*}{(j\omega_1-\lambda_m^*)}\right) \\ \vdots & \vdots & \vdots \\ \frac{j\left|H_{o1}(\omega_{N_f})\right|}{\hat{H}_{o1}(\Theta,\omega_{N_f})\sigma_{H_{o1}(\omega_{N_f})}}\left(\frac{l_{1m}}{(j\omega_{N_f}-\lambda_m)}-\frac{l_{1m}^*}{(j\omega_{N_f}-\lambda_m^*)}\right) & \cdots & \frac{j\left|H_{oN_i}(\omega_{N_f})\right|}{\hat{H}_{oN_i}(\Theta,\omega_{N_f})\sigma_{H_{oN_i}(\omega_{N_f})}}\left(\frac{l_{N_im}}{(j\omega_{N_f}-\lambda_m)}-\frac{l_{N_im}^*}{(j\omega_{N_f}-\lambda_m^*)}\right) \end{bmatrix} \tag{3.209}$$

$$\frac{\partial E_o(\Theta)}{\partial \mathrm{Re}\,([AR]_{oi})} = \begin{bmatrix} \frac{\delta_{i1}|H_{o1}(\omega_1)|}{d(\omega_1)\hat{H}_{o1}(\Theta,\omega_1)\sigma_{H_{o1}(\omega_1)}} & \cdots & \frac{\delta_{iN_i}\left|H_{oN_i}(\omega_1)\right|}{d(\omega_1)\hat{H}_{oN_i}(\Theta,\omega_1)\sigma_{H_{oN_i}(\omega_1)}} \\ \vdots & \vdots & \vdots \\ \frac{\delta_{i1}\left|H_{o1}(\omega_{N_f})\right|}{d(\omega_{N_f})\hat{H}_{o1}(\Theta,\omega_{N_f})\sigma_{H_{o1}(\omega_{N_f})}} & \cdots & \frac{\delta_{iN_i}\left|H_{oN_i}(\omega_{N_f})\right|}{d(\omega_{N_f})\hat{H}_{oN_i}(\Theta,\omega_{N_f})\sigma_{H_{oN_i}(\omega_{N_f})}} \end{bmatrix} \tag{3.210}$$

$$\frac{\partial E_o(\Theta)}{\partial \mathrm{Im}\,([AR]_{oi})} = \begin{bmatrix} \frac{j\delta_{i1}|H_{o1}(\omega_1)|}{d(\omega_1)\hat{H}_{o1}(\Theta,\omega_1)\sigma_{H_{o1}(\omega_1)}} & \cdots & \frac{j\delta_{iN_i}\left|H_{oN_i}(\omega_1)\right|}{d(\omega_1)\hat{H}_{oN_i}(\Theta,\omega_1)\sigma_{H_{oN_i}(\omega_1)}} \\ \vdots & \vdots & \vdots \\ \frac{j\delta_{i1}\left|H_{o1}(\omega_{N_f})\right|}{d(\omega_{N_f})\hat{H}_{o1}(\Theta,\omega_{N_f})\sigma_{H_{o1}(\omega_{N_f})}} & \cdots & \frac{j\delta_{iN_i}\left|H_{oN_i}(\omega_{N_f})\right|}{d(\omega_{N_f})\hat{H}_{oN_i}(\Theta,\omega_{N_f})\sigma_{H_{oN_i}(\omega_{N_f})}} \end{bmatrix} \tag{3.211}$$

$$\frac{\partial E_o(\Theta)}{\partial \mathrm{Re}\left([BR]_{oi}\right)} = \begin{bmatrix} \frac{j\omega_1 \delta_{i1} |H_{o1}(\omega_1)|}{d(\omega_1)\hat{H}_{o1}(\Theta,\omega_1)\sigma_{H_{o1}(\omega_1)}} & \cdots & \frac{j\omega_1 \delta_{iN_i} \left|H_{oN_i}(\omega_1)\right|}{d(\omega_1)\hat{H}_{oN_i}(\Theta,\omega_1)\sigma_{H_{oN_i}(\omega_1)}} \\ \vdots & \vdots & \vdots \\ \frac{j\omega_{N_f} \delta_{i1} \left|H_{o1}(\omega_{N_f})\right|}{d(\omega_{N_f})\hat{H}_{o1}(\Theta,\omega_{N_f})\sigma_{H_{o1}(\omega_{N_f})}} & \cdots & \frac{j\omega_{N_f} \delta_{iN_i} \left|H_{oN_i}(\omega_{N_f})\right|}{d(\omega_{N_f})\hat{H}_{oN_i}(\Theta,\omega_{N_f})\sigma_{H_{oN_i}(\omega_{N_f})}} \end{bmatrix} \tag{3.212}$$

$$\frac{\partial E_o(\Theta)}{\partial \mathrm{Im}\left([BR]_{oi}\right)} = \begin{bmatrix} \frac{-\omega_1 \delta_{i1} |H_{o1}(\omega_1)|}{d(\omega_1)\hat{H}_{o1}(\Theta,\omega_1)\sigma_{H_{o1}(\omega_1)}} & \cdots & \frac{-\omega_1 \delta_{iN_i} \left|H_{oN_i}(\omega_1)\right|}{d(\omega_1)\hat{H}_{oN_i}(\Theta,\omega_1)\sigma_{H_{oN_i}(\omega_1)}} \\ \vdots & \vdots & \vdots \\ \frac{-\omega_{N_f} \delta_{i1} \left|H_{o1}(\omega_{N_f})\right|}{d(\omega_{N_f})\hat{H}_{o1}(\Theta,\omega_{N_f})\sigma_{H_{o1}(\omega_{N_f})}} & \cdots & \frac{-\omega_{N_f} \delta_{iN_i} \left|H_{oN_i}(\omega_{N_f})\right|}{d(\omega_{N_f})\hat{H}_{oN_i}(\Theta,\omega_{N_f})\sigma_{H_{oN_i}(\omega_{N_f})}} \end{bmatrix} \tag{3.213}$$

$$\frac{\partial E_o(\Theta)}{\partial \mathrm{Re}\left([CR]_{oi}\right)} = \begin{bmatrix} \frac{-\omega_1^2 \delta_{i1} |H_{o1}(\omega_1)|}{d(\omega_1)\hat{H}_{o1}(\Theta,\omega_1)\sigma_{H_{o1}(\omega_1)}} & \cdots & \frac{-\omega_1^2 \delta_{iN_i} \left|H_{oN_i}(\omega_1)\right|}{d(\omega_1)\hat{H}_{oN_i}(\Theta,\omega_1)\sigma_{H_{oN_i}(\omega_1)}} \\ \vdots & \vdots & \vdots \\ \frac{-\omega_{N_f}^2 \delta_{i1} \left|H_{o1}(\omega_{N_f})\right|}{d(\omega_{N_f})\hat{H}_{o1}(\Theta,\omega_{N_f})\sigma_{H_{o1}(\omega_{N_f})}} & \cdots & \frac{-\omega_{N_f}^2 \delta_{iN_i} \left|H_{oN_i}(\omega_{N_f})\right|}{d(\omega_{N_f})\hat{H}_{oN_i}(\Theta,\omega_{N_f})\sigma_{H_{oN_i}(\omega_{N_f})}} \end{bmatrix} \tag{3.214}$$

$$\frac{\partial E_o(\Theta)}{\partial \mathrm{Im}\left([CR]_{oi}\right)} = \begin{bmatrix} \frac{-j\omega_1^2 \delta_{i1} |H_{o1}(\omega_1)|}{d(\omega_1)\hat{H}_{o1}(\Theta,\omega_1)\sigma_{H_{o1}(\omega_1)}} & \cdots & \frac{-j\omega_1^2 \delta_{iN_i} \left|H_{oN_i}(\omega_1)\right|}{d(\omega_1)\hat{H}_{oN_i}(\Theta,\omega_1)\sigma_{H_{oN_i}(\omega_1)}} \\ \vdots & \vdots & \vdots \\ \frac{-j\omega_{N_f}^2 \delta_{i1} \left|H_{o1}(\omega_{N_f})\right|}{d(\omega_{N_f})\hat{H}_{o1}(\Theta,\omega_{N_f})\sigma_{H_{o1}(\omega_{N_f})}} & \cdots & \frac{-j\omega_{N_f}^2 \delta_{iN_i} \left|H_{oN_i}(\omega_{N_f})\right|}{d(\omega_{N_f})\hat{H}_{oN_i}(\Theta,\omega_{N_f})\sigma_{H_{oN_i}(\omega_{N_f})}} \end{bmatrix} \tag{3.215}$$

Example 11

The five-**DOF** system introduced in **Example 10** is again used to validate the implementation of the **pMLE-MM** presented in Section 3.5.3. A set of 200 **FRF**s contaminated with noise was generated to perform Monte Carlo simulations in order to assess the proposed implementation and compare its efficiency with the implementation introduced by El-Kafafy (2013) presented in Section 3.5.2. The noisy **FRF**s were generated by following the procedure described in **Example 10**.

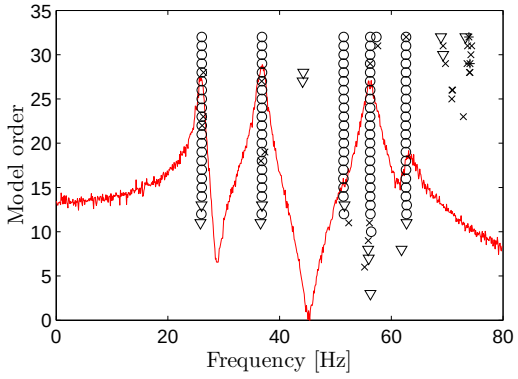

Fig. 3.15 – Typical stabilization diagram constructed with the **pLSCF** from the noisy **FRF**s.

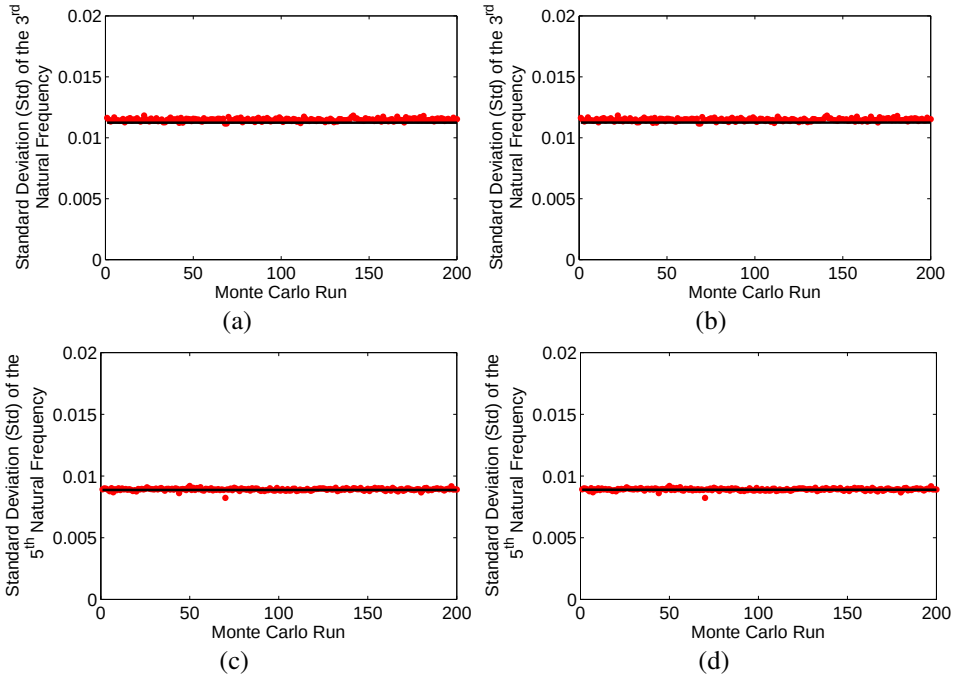

Fig. 3.16 – Monte Carlo simulation results for the natural frequencies of the 3rd and 5th modes with 10% of noise level: predicted standard deviation (dots) and sample standard deviation (solid line) with the proposed implementation of the **pMLE-MM** ((a) and (c)) and the implementation proposed by (El-Kafafy, 2013) ((b) and (d)).

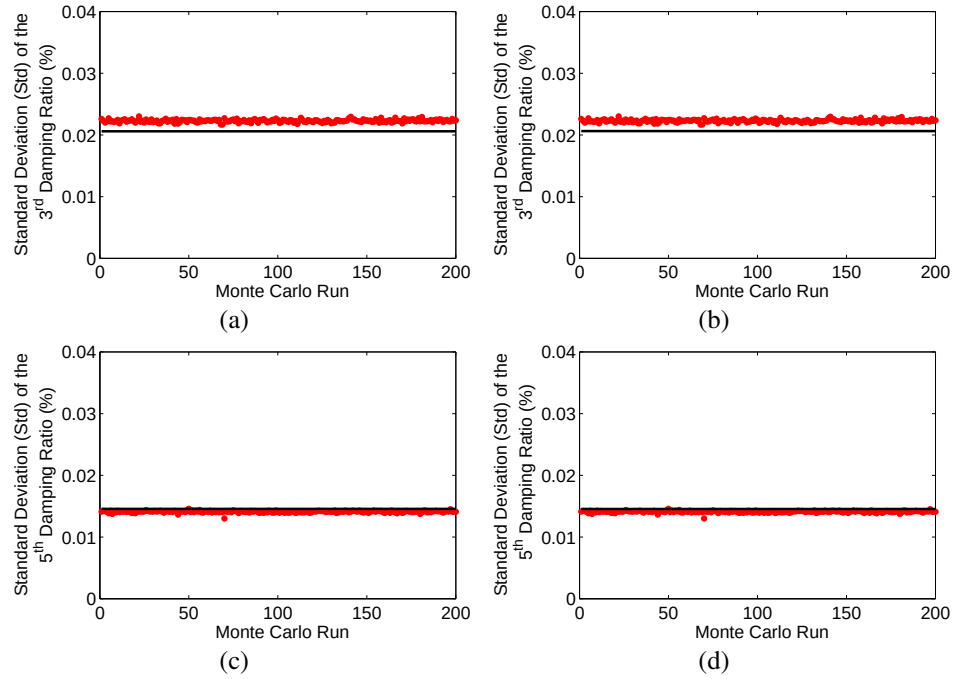

Fig. 3.17 – Monte Carlo simulation results for the damping ratios of the 3rd and 5th modes with 10% of noise level: predicted standard deviation (dots) and sample standard deviation (solid line) with the proposed implementation of the **pMLE-MM** ((a) and (c)) and the implementation proposed by (El-Kafafy, 2013) ((b) and (d)).

The modal parameters of each dataset were identified with the **pLSCF** and **LSFD** estimators and then used as starting values to be optimized by both implementations of the **pMLE-MM**. Similarly to **Example 10**, the identification of each dataset was performed by using the full frequency band, i.e., with no upper and lower residuals.

A typical stabilization diagram constructed with the **pLSCF** method from the **FRF**s contaminated with noise is shown in Fig. 3.15. This diagram was created by identifying models with order n ranging from 2 to 36. In a final step of the identification process, 15 iterations of the **pMLE-MM** were performed to optimize the modal parameters of each dataset and estimate their standard deviations. The standard deviations of the 3$^{\text{rd}}$ and 5$^{\text{th}}$ natural frequencies and damping ratios estimated with both algorithms of the **pMLE-MM** are compared in Figs. 3.16 and 3.17. In these figures, the standard deviations of the parameters estimated for each of the 200 simulated **FRF**s are compared to their respective sample standard deviations.

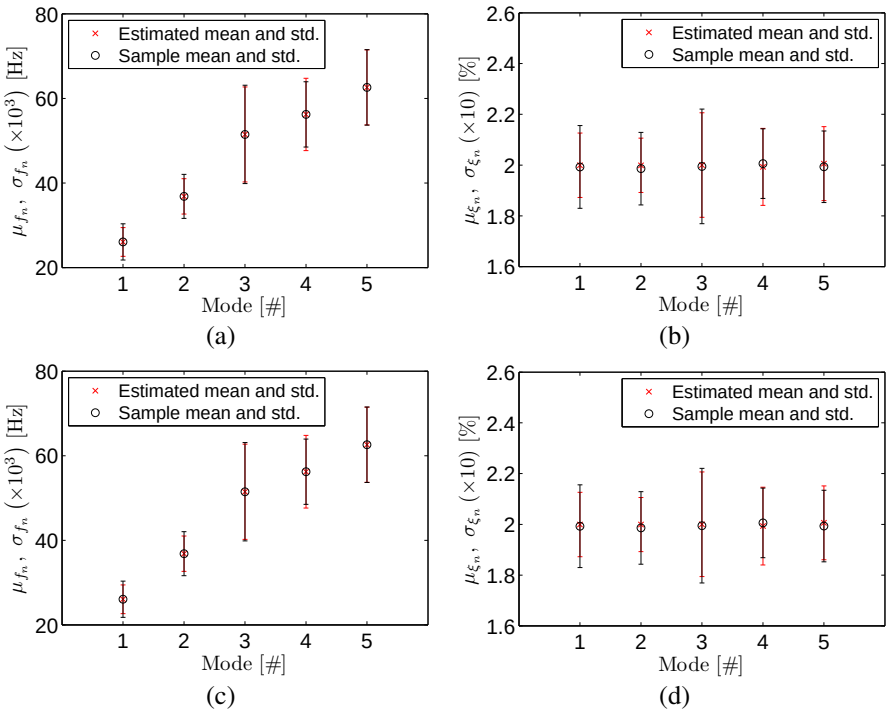

Fig. 3.18 – Monte Carlo simulation results obtained with the proposed implementation of the **pMLE-MM** (top) and with the implementation proposed by (El-Kafafy, 2013) (bottom): comparison of the sample (black line) and estimated means and standard deviations (red line) of the natural frequencies (a and c) and damping ratios (b and d).

Comparing the standard deviations estimated with both implementations of the **pMLE-MM** shown in such figures, it is verified that they are in very good agreement with each other. It is also verified, from these figures, that both implementations provide good estimates of the sample standard deviations. The results of the analysis carried out with both implementations of **pMLE-MM**, as well as with the proposed **MLE-MM** introduced in Section 3.5.1 are summarized in Tab. 3.4. In this table, the estimated standard deviations of the natural frequencies and damping ratios identified with both implementations of the **pMLE-MM** and of the **MLE-MM** are compared to each other, as well as to their corresponding sample standard deviations.

As seen in this table, the results provided by both **pMLE-MM** algorithms are very similar,

which demonstrates that the proposed implementation is as efficient and accurate as the implementation proposed by El-Kafafy (2013). With regard to the estimation of the uncertainties on the modal parameters, it is verified in Tab. 3.4 that the 3rd mode presents the highest uncertainties, since this mode is poorly exited compared to the other identified modes.

Tab. 3.4 – Comparison of the results from the simulated **EMA** of the five-**DOF** system obtained with the proposed implementation of the **pMLE-MM** to those provided by the implementation proposed by El-Kafafy (2013) and by the proposed **MLE-MM**.

MLE-MM	Mode	Sample Mean and Std.				Estimated Mean and Std.			
		$\mu_{\hat{f}_n}$(Hz)	$\sigma_{\hat{f}_n}$(Hz) $\times 10^3$	$\mu_{\hat{\xi}_n}$(%)	$\sigma_{\hat{\xi}_n}$(%) $\times 10^2$	$\hat{\mu}_{\hat{f}_n}$(Hz)	$\hat{\sigma}_{\hat{f}_n}$(Hz) $\times 10^3$	$\hat{\mu}_{\hat{\xi}_n}$(%)	$\hat{\sigma}_{\hat{\xi}_n}$(%) $\times 10^2$
Proposed **pMLE-MM**	1	26.0598	3.39	1.9995	1.27	26.0580	4.28	1.9927	1.63
	2	36.8402	4.18	1.9991	1.07	36.8362	5.21	1.9861	1.43
	3	51.4708	11.24	2.0003	2.06	51.4776	11.63	1.9948	2.26
	4	56.2081	8.55	1.9930	1.52	56.2191	7.72	2.0058	1.37
	5	62.6003	8.86	2.0059	1.46	62.6106	8.92	1.9935	1.41
pMLE-MM (El-Kafafy, 2013)	1	26.0598	3.40	1.9995	1.27	26.0580	4.28	1.9927	1.63
	2	36.8403	4.18	1.9992	1.07	36.8362	5.21	1.9861	1.43
	3	51.4709	11.25	2.0003	2.06	51.4776	11.63	1.9948	2.26
	4	56.2081	8.59	1.9932	1.53	56.2192	7.72	2.0058	1.37
	5	62.6004	8.88	2.0061	1.45	62.6106	8.92	1.9935	1.41
Proposed **MLE-MM**	1	26.0602	3.31	2.0057	1.88	26.0571	4.35	1.9898	1.65
	2	36.8399	3.94	2.0034	1.59	36.8345	5.37	2.0008	1.46
	3	51.4682	10.80	2.0061	2.68	51.4730	12.75	2.0011	2.46
	4	56.2114	7.96	2.0031	1.59	56.2026	9.63	2.0029	1.72
	5	62.6011	9.04	2.0016	1.53	62.5989	10.01	2.0215	1.59

3.6. The Combined MLE-CDM-pLSCF-pMLE-MM Method

3.6.1. Introduction

Recently, new improvements were added to the estimation with the **pLSCF** to overpass the loss of precision and robustness observed when dealing with very noisy **FRF**s and poorly exited modes (El-Kafafy et al., 2012a; El-Kafafy, 2013; Peeters et al., 2012). It is verified that, under these circumstances, the **pLSCF** is not so robust and tends to overestimate the damping ratios. This new variant of the **pLSCF** technique consists of a 3-step approach proposed by El-Kafafy (2013) to address these issues and is also known by its commercial name as PolyMAX Plus (Peeters et al., 2012).

In fact, this approach consists of a combination of three different estimators, namely, the **MLE-CDM**, the **pLSCF** and the **pMLE-MM**. The combination of these three estimators enhances the **MPE** by taking advantage of the specific features of each one of them, as, for instance, the statistical features of the of the **MLE-CDM** in the first step of the identification process, the fast and clear stabilization diagrams provided by the **pLSCF** method, and the precision and

numeric stability of the **pMLE-MM** which is used to improve the accuracy of the identified modal parameters and estimate their confidence intervals.

*3.6.2. Structure of the Combined **MLE-CDM-pLSCF-pMLE-MM** Method*

The identification process with the combined **MLE-CDM-pLSCF-pMLE-MM** basically consists of the following steps: (1) smoothing the noisy **FRF** (**EMA**) or half spectrum (**OMA**) with the **MLE-CDM**; (2) identification of the poles and operational factors from the smoothed spectrum in the first step with the **pLSCF** estimator, and estimation of the corresponding mode shapes of vibration together with the lower and upper residuals in a least squares sense with the **LSFD** estimator; and, finally, (3) optimization of the model parameters provided by the **pLSCF** and **LSFD** estimators, and estimation of the their uncertainty bounds with the **pMLE-MM**. The structure of the combined **MLE-pLSCF-pMLE-MM** is synthesized in Fig.3.19.

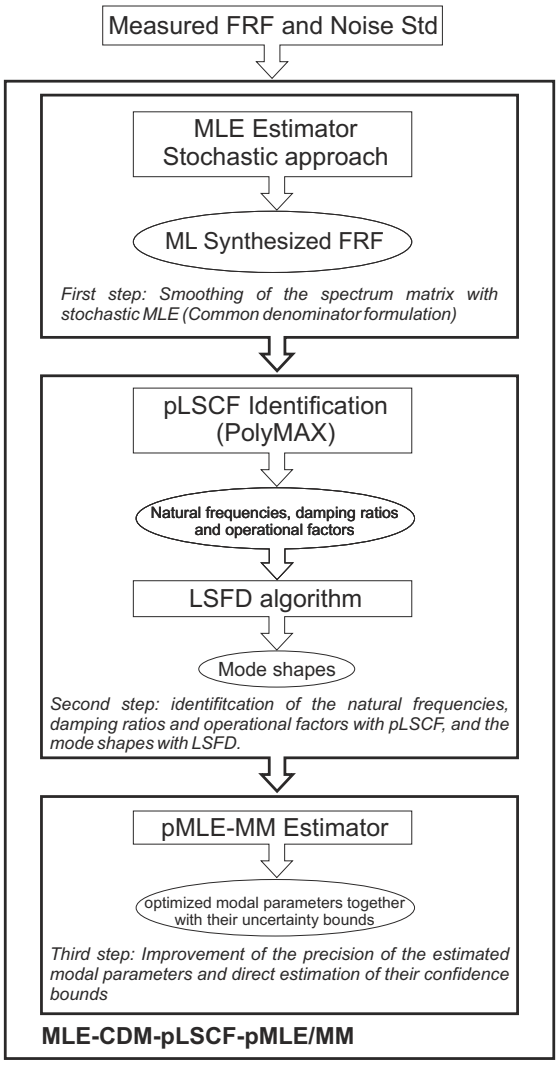

Fig. 3.19 – Data flow of the implementation of the combined **MLE-CDM-pLSCF-pMLE-MM**.

In the first step of the identification, the **MLE-CDM** is applied in a "blind" way, i.e. a fixed model order is specified for the common-denominator model and the **FRF**s are synthesized without prior selection of the physical modes. The third step of the of this combined estimator was originally proposed by (El-Kafafy et al., 2012b) and is described in Section 3.5.2. The alternative implementation ot the **pMLE-MM** introduced in Section 3.5.3 can also be used in the third step of this combined estimator to optimize the modal parameters provided by the **pLSCF** technique and estimate their confidence intervals. One of the main advantages of this alternative strategy is the possibility to estimate the uncertainties on the identified modal natural frequencies and damping ratios directly from the normal matrices, avoiding the necessity of estimating these uncertainties in a second step, by means of explicit linearisation formulas.

Moreover, in practical **EMA** and **OMA**, one is more interested on the confidence intervals of the estimated natural frequency and damping ratios rather than on the uncertainties on the estimated poles.

3.6.3. Lack of Prior Noise Information

When the noise information is not available, a residual error approach can be adopted to estimate the variance of the measured **FRF**s (**EMA**) or half spectra (**OMA**). This approach estimates the noise on the **FRF**s by smoothing the residual errors between the measured **FRF**s and the estimated (synthesized) **FRF**s by making use of a window function (see Section 2.7.1). These estimated **FRF**s are, for instance, obtained from a preliminary **LS** estimation with the **LSCF** technique. It is also possible to perform some **MLE-CDM** iterations without taking into account the variance, then calculate the variances by means of the residual error approach from the difference between the measured and modelled **FRF**s, and finally, perform some more **MLE** iterations with noise weighting. The advantage of the residual error approach is that it can also be applied to **OMA**.

3.7. The Combined SSI-DATA-pMLE-MM and SSI-COV-pMLE-MM

Following the same idea of the combined **MLE-CDM-pLSCF-pMLE-MM** discussed in Section 3.6, two other combined estimators are proposed in the present work. These approaches consist of combinations of the **SSI-DATA** and **SSI-COV** techniques with the **pMLE-MM**. In such approaches both **SSI** methods are used to estimate the poles and mode shapes, which are subsequently used to estimate the operational factors by means of the **LSFD** estimator in the first step of the identification process. Next, these estimates are used as starting guess by the **pMLE-MM**, which optimizes iteratively these parameters in frequency-domain and provides their uncertainty bounds, in a second step of the identification process.

Similarly to the combined **MLE-CDM-pLSCF-pMLE-MM**, the variance of the measured half spectra can be estimated by making use of the residual error approach discussed in Section 2.7.1. The data flows of the **MPE** with the combined **SSI-DATA-pMLE-MM** and **SSI-COV-pMLE-MM** are illustrated in Figs. 3.20a and 3.20b, respectively.

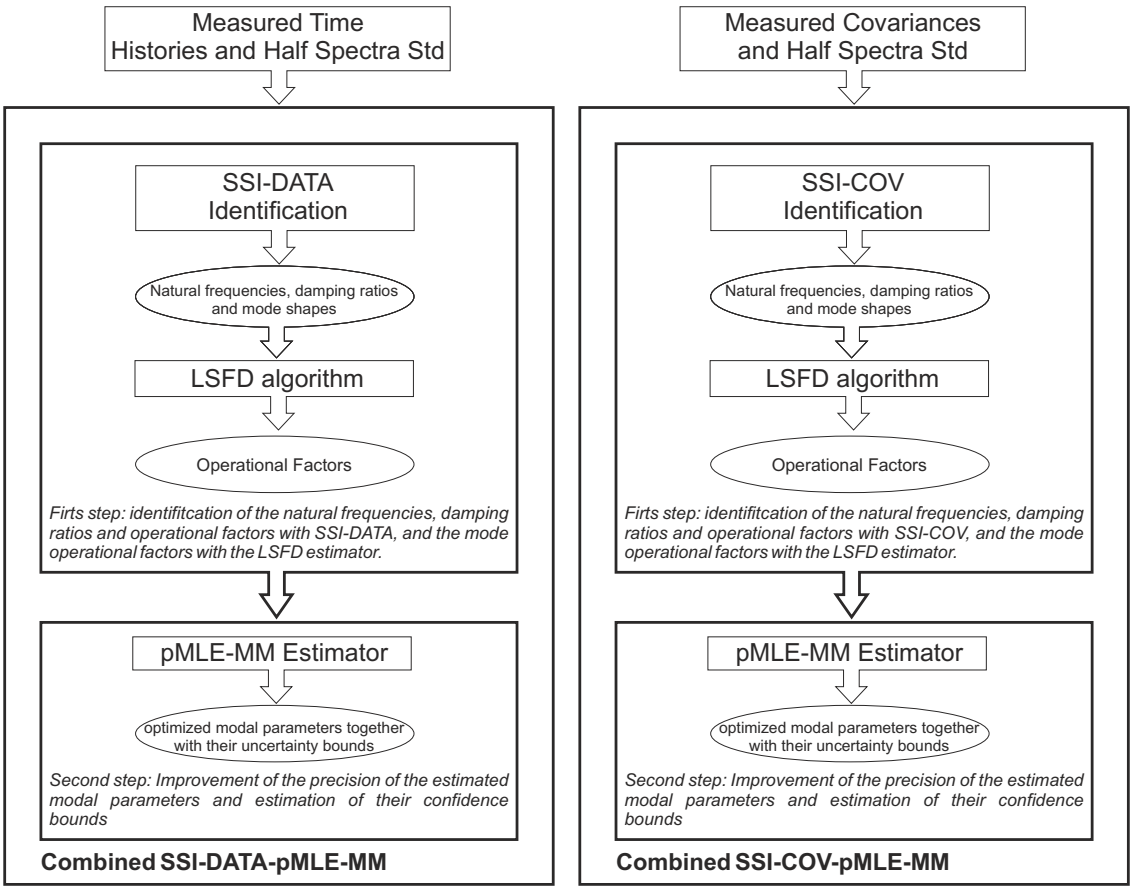

Fig. 3.20 – Data flow of the implementation of the combined **SSI-DATA-pMLE-MM** (a) and **SSI-COV-pMLE-MM** (b).

Example 12

The proposed implementation of the **pMLE-MM** is now applied to the lattice tower structure introduced in **Example 1**. The modal parameters estimated with the **SSI-DATA**, **SSI-COV** and combined **MLE-CDM-pLSCF** in **Examples 6**, **7** and **9** are now used as starting guess by the **pMLE-MM** to estimate their uncertainties, improve their precision and estimate the confidence intervals of the optimized estimates. Firstly, one iteration of the **pMLE-MM** was applied to estimate the confidence intervals of the estimates provided by such identification techniques. Afterwards, a total of 50 iterations of the Gauss-Newton algorithm was performed to optimize these estimates and compute the standard deviations of the optimized parameters.

As the optimization with the **pMLE-MM** is only possible if the noise information is taken into account in the cost function (3.133), the same residual error variance estimated in **Example** 8 was taken into account in the optimization of the **SSI-DATA** and **SSI-COV** estimates. The optimization of the starting estimates provided by the **pLSCF**, **SSI-DATA** and **SSI-COV** techniques was performed within the frequency range of 0.1-10 Hz. The variations of the cost

function value computed over the iterations performed to optimize the parameters estimated with **SSI-DATA**, **SSI-COV** and combined **MLE-CDM-pLSCF** are shown in Fig. 3.21.

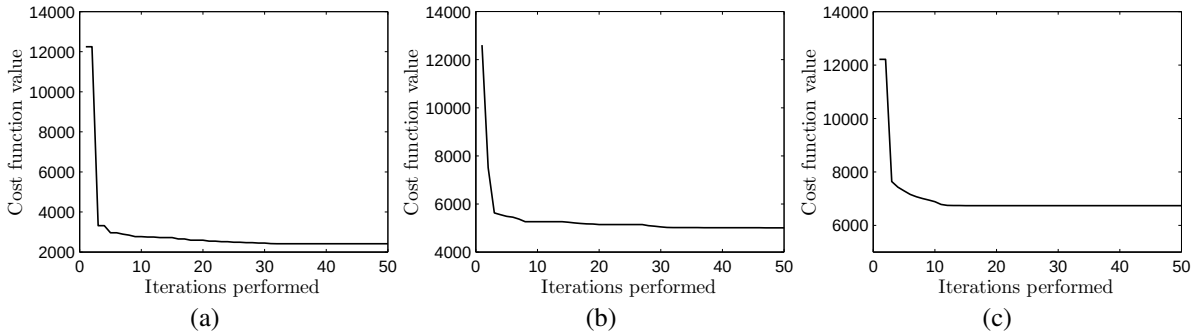

Fig. 3.21 – Variation of the **pMLE-MM** cost function value over the performed iterations computed from the starting estimates provided by the **SSI-DATA** (a), **SSI-COV** (b) and **MLE-CDM-pLSCF** (c) identification techniques.

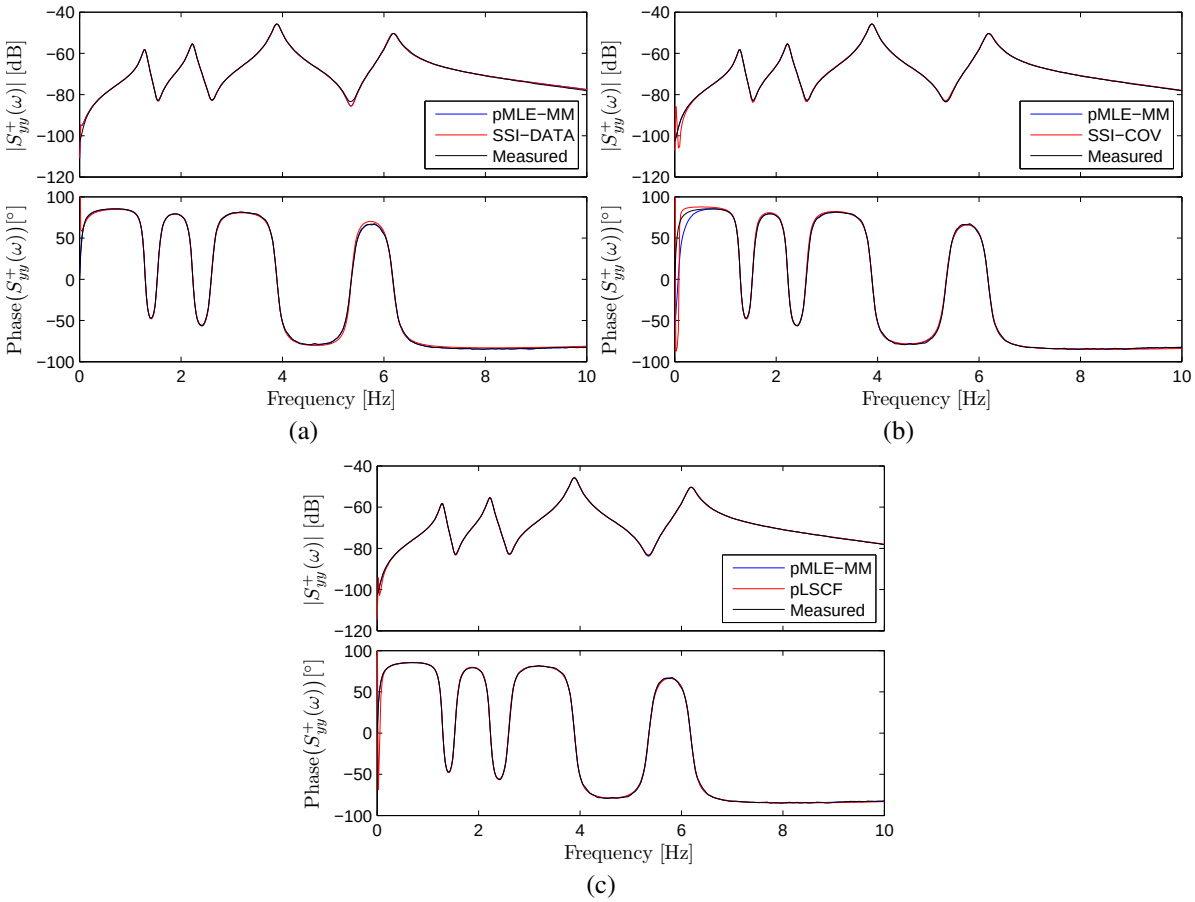

Fig. 3.22 – Comparison of element (1,1) of measured half spectra matrix, S_{yy}^{+}, to the spectrum synthesized from the estimates provided by the **SSI-DATA** (a), **SSI-COV** (b) and combined **MLE-CDM-pLSCF** (c), as well as to the spectrum synthesized after 50 Gauss-Newton iterations of the **pMLE-MM**.

In Figs. 3.22, element (1,1) of the measured half spectra matrix, S_{yy}^{+}, is compared to the spectra synthesized from the parameters identified with **SSI-DATA**, **SSI-COV** and combined **MLE-**

CDM-pLSCF, as well as to the spectra synthesized after 50 Gauss-Newton iterations of the **pMLE-MM**. As seen in these figures, the spectrum synthesized from the parameters optimized with the **pMLE-MM** are in very good agreement with the measured spectrum. The natural frequencies and damping ratios together with their standard deviations estimated before and after the optimization with the **pMLE-MM** are shown in Figs. 3.23 and 3.24, respectively.

Comparing these parameters to their optimized counterparts, it is verified that, whist no significant variation is observed for the natural frequencies, a noticeable difference is seen for the damping ratios estimates. The identification results obtained with the three different techniques combined with **pMLE-MM** shown in Figs. 3.23 and 3.24 are summarised in Tab. 3.5. Comparing the results presented in such table, it is verified that they are consistent with each other.

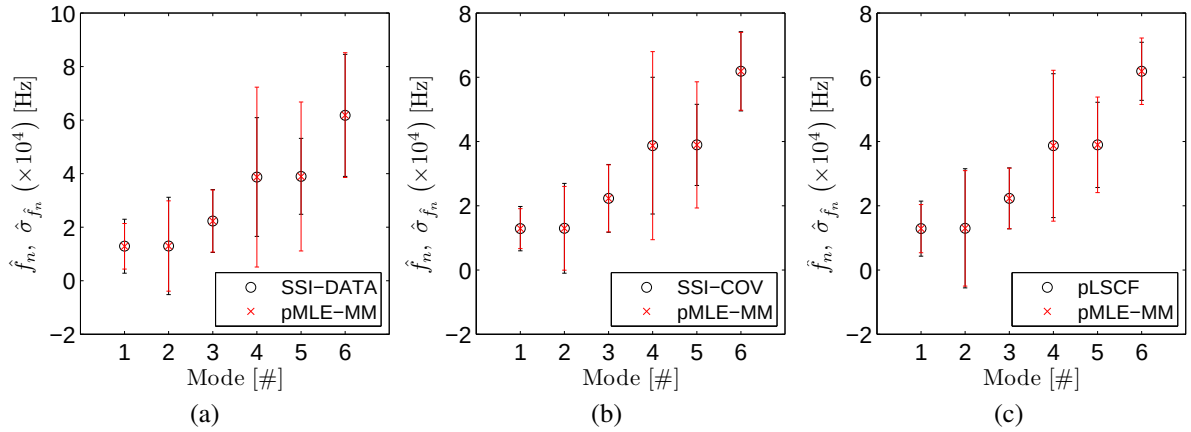

Fig. 3.23 – Natural frequencies identified with the **SSI-DATA** (a), **SSI-COV** (b) and combined **MLE-CDM-pLSCF** (c) together with their standard deviation before (black line) and after the optimization with **pMLE-MM**. The standard deviations are multiplied by a factor of 10^4 to improve their visibility within the figure.

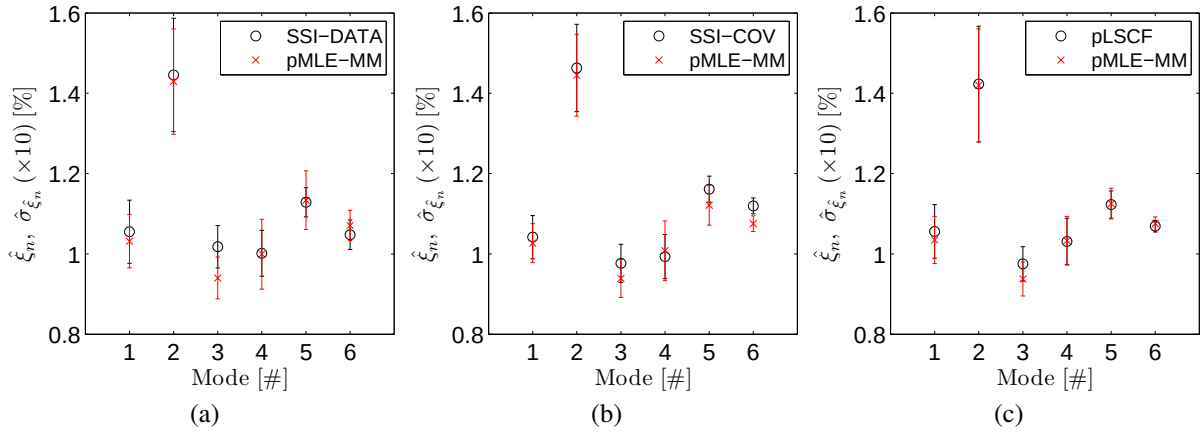

Fig. 3.24 – Damping ratios identified with the **SSI-DATA** (a), **SSI-COV** (b) and combined **MLE-CDM-pLSCF** (c) together with their standard deviation before (black line) and after the optimization with **pMLE-MM**. The standard deviations are multiplied by a factor of 10 to improve their visibility within the figure.

Tab. 3.5 – Results obtained for the simulated **OMA** of the tower structure with the **SSI-DATA**, **SSI-COV** and **MLE-pLSCF** combined with the alternative implementation of the **pMLE-MM**.

Method	Mode	**pMLE-MM** Estimates (1 iteration)				**pMLE-MM** Estimates (50 iterations)			
		$\hat{f}_n$ [Hz]	$\hat{\sigma}_{\hat{f}_n}$ [Hz] $(\times 10^4)$	$\hat{\xi}_n$ [%]	$\hat{\sigma}_{\hat{\xi}_n}$ [%] $(\times 10^2)$	$\hat{f}_n$ [Hz]	$\hat{\sigma}_{\hat{f}_n}$ [Hz] $(\times 10^4)$	$\hat{\xi}_n$ [%]	$\hat{\sigma}_{\hat{\xi}_n}$ [%] $(\times 10^2)$
SSI-DATA	1	1.28763	1.01	1.0553	0.79	1.28662	0.85	1.0316	0.66
	2	1.29615	1.82	1.4457	1.41	1.29652	1.69	1.4291	1.31
	3	2.22752	1.17	1.0178	0.53	2.22802	1.16	0.9401	0.52
	4	3.87063	2.22	1.0016	0.57	3.86998	3.36	0.9993	0.87
	5	3.89552	1.42	1.1286	0.36	3.89222	2.78	1.1339	0.73
	6	6.17518	2.28	1.0479	0.37	6.18328	2.33	1.0710	0.38
SSI-COV	1	1.28697	0.69	1.0418	0.54	1.28667	0.62	1.0268	0.49
	2	1.29661	1.40	1.4630	1.09	1.29676	1.30	1.4450	1.02
	3	2.22724	1.06	0.9765	0.48	2.22785	1.04	0.9388	0.47
	4	3.86926	2.13	0.9934	0.55	3.86986	2.93	1.0079	0.74
	5	3.89435	1.26	1.1613	0.32	3.89257	1.96	1.1212	0.50
	6	6.18498	1.23	1.1195	0.20	6.18384	1.21	1.0754	0.20
MLE-CDM-pLSCF	1	1.28693	0.86	1.0560	0.67	1.28665	0.75	1.0348	0.59
	2	1.29621	1.85	1.4229	1.44	1.29646	1.80	1.4201	1.41
	3	2.22751	0.95	0.9753	0.43	2.22792	0.94	0.9376	0.42
	4	3.86970	2.24	1.0310	0.58	3.86873	2.35	1.0330	0.61
	5	3.89393	1.33	1.1229	0.34	3.89424	1.49	1.1255	0.38
	6	6.18418	0.91	1.0691	0.15	6.18410	1.03	1.0755	0.17

3.8. Merging Strategies For Multi-dataset OMA

In this section the mode shape re-scaling strategies used in multi-dataset non-stationary **OMA** is discussed. These strategies are often used in multi-dataset **EMA** and **OMA** to glue the mode shape parts of each dataset and provide the global modal configurations of the tested structures. The difference between these strategies relies, essentially, on when the rescaling is applied in order to uniform the different scales of the mode shapes ordinates of each dataset, which can take place either before or after the estimation of the modal parameters. There exist three approaches for this purpose: the **Pre G**lobal **E**stimation **R**e-scaling (**PreGER**), the **P**ost **S**eparate **E**stimation **R**e-scaling (**PoSER**) and the **Po**st **G**lobal **E**stimation **R**e-scaling (**PoGER**), and the their advantages and drawbacks are briefly discussed in the following sections. Further details about these merging strategies are found, for instance, in Parloo (2003), Reynders et al. (2009) and Döhler et al. (2010).

*3.8.1. Post-Separate Estimation Re-scaling (**PoSER**) Approach*

The **PoSER**, also known as the "classic" approach, consists of a merging strategy in which the spectrum or the covariance of each dataset is identified independently. Once the modal

parameters are estimated, the mode shapes of each dataset are re-scaled with regard to one these mode shapes, which is previously chosen as reference. In practice, the mode shapes of the first the dataset is usually chosen reference. The re-scaling procedure with **PoSER** is illustrated in Fig. 3.25. The main drawback of this approach is that the number of identified modes may differ from dataset to dataset due to the non-stationary character of the operational excitations and to the few **DOF**s measured during the test.

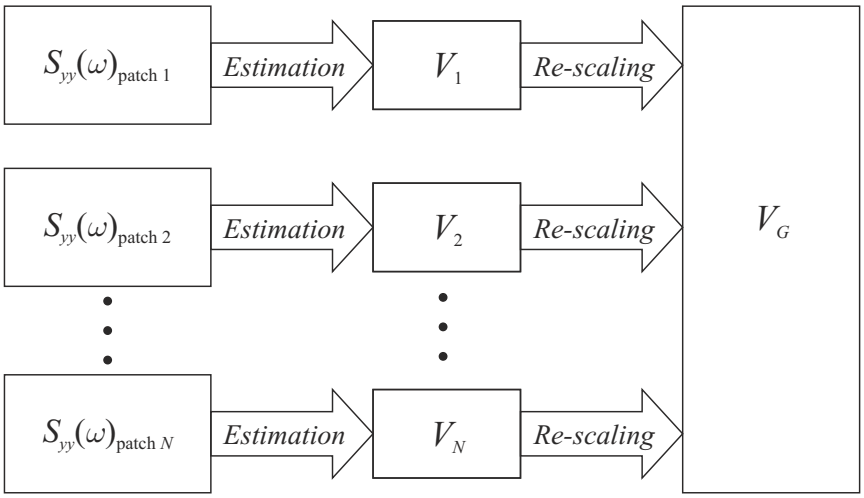

Fig. 3.25 – Merging partial mode shape estimates V_k, $k = 1, ..., N$ into a global mode shape estimate V_G using the **PoSER** approach.

In such conditions, it may be not possible to yield the global mode shapes of all the identified modes in the frequency band of interest. Another disadvantage of this merging approach is that the analyst needs to identify each dataset separately. If the number of datasets collected in vibration tests is large, this task may be very tiresome and time consuming. Moreover, the mode pairing between different datasets is only possible if the modes to be merged are identified in all datasets. When dealing with close spaced modes, however, the mode pairing between different datasets may be very difficult, since these modes may not be identified in all datasets. Given these difficulties, the **PoGER** and **PreGER** can be used to the estimate the global mode shapes using a single stabilization diagram.

*3.8.2. Pre-Global Estimation Re-scaling (**PreGER**) Approach*

The idea behind the **PreGER** approach is to yield the re-scaled global mode shapes directly from the global spectrum matrix. This is accomplished by re-scaling the spectrum matrix of each dataset prior to stacking and assembling the global spectrum matrix as illustrated in Fig. 3.26. One of the main advantages of this approach is that it provides the re-scaled global mode shapes directly from the global spectrum matrix and no further post-processing is required after the identification of the modal parameters. The main drawback, however, is that it is not so

robust to non-stationary excitations from dataset to dataset (Reynders et al., 2009), particularly if used in conjunction with the time-domain identification techniques such as **SSI-COV**.

In such circumstances, a different strategy discussed in Mevels et al. (2002) and Döhler et al. (2010) can be used in conjunction with the correlation-driven identification methods to overpass this limitation.

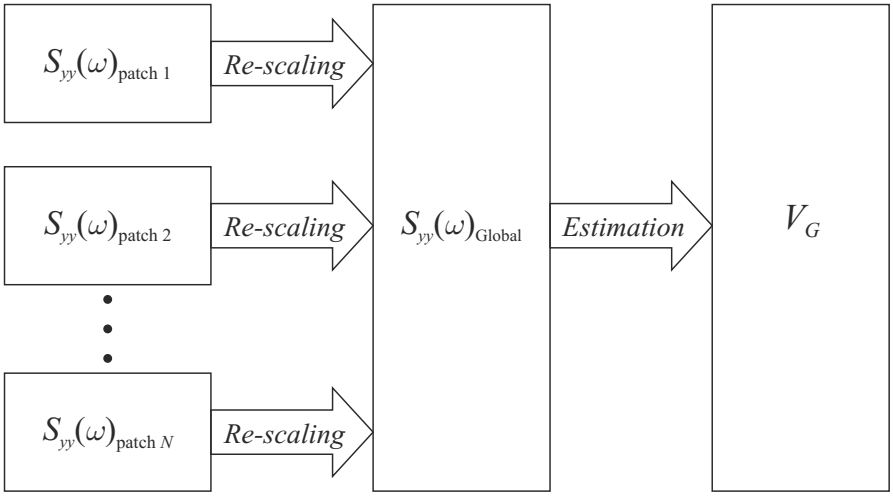

Fig. 3.26 – Merging partial mode shape estimates V_k, $k = 1, ..., N$ into a global mode shape estimate V_G using the **PreGER** approach.

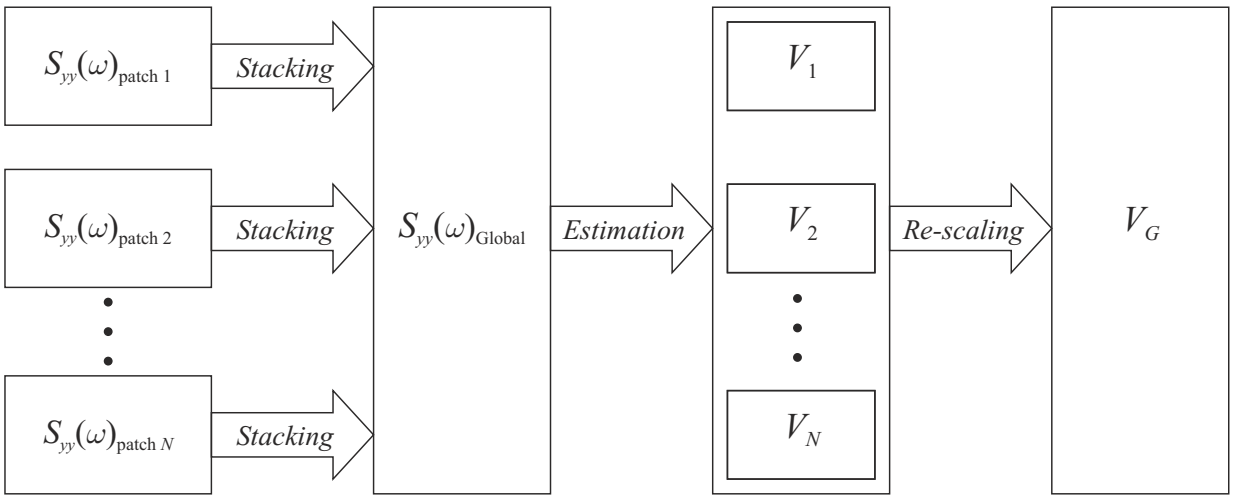

Fig. 3.27 – Merging partial mode shape estimates V_k, $k = 1, ..., N$ into a global mode shape estimate V_G using the **PoGER** approach.

*3.8.3. Post-Global Estimation Re-scaling (**PoGER**) Approach*

In the **PoGER** merging strategy, the re-scaling is applied to the mode shape parts of each dataset only after the identification of the modal parameters. In this merging strategy, the global spectra or covariance matrices are constructed by stacking the spectrum or covariance of each dataset on

the top of each order. Afterwards, these matrices are used as primary data by the system identification techniques to estimate the modal parameters. Once these parameters are estimated, the mode shapes parts of each dataset are than re-scaled with regard to one of the parts previously chosen as reference. The purpose of this procedure is to uniform the scales of each mode shape part to yield the global mode shapes of the tested structure. The main advantage of this approach is that it is more robust to the non-stationary inputs. The data flow of the identification with the **PoGER** merging strategy is illustrated in Fig. 3.27.

3.9. Conclusions

In this Chapter, some of the state-of-the-art input-output and output-only identification techniques were reviewed. Especial attention was dedicated to the time-domain estimators **SSI-DATA** and **SSI-COV**, as well as to the frequency-domain techniques **pLSCF**, **MLE-CDM**, **MLE-MM**, **pMLE-MM**. The main characteristics, advantages and drawbacks of these techniques were occasionally highlighted. Apart from this review, two approaches were proposed in the framework of the **ML** estimators. The first consists of a single reference **ML**-based identification technique formulated in pole-residual modal model and the second corresponds to an alternative implementation of the **pMLE-MLE** originally proposed by El-Kafafy (2013). Aiming at assessing the efficiency of the first approach, the proposed estimator was applied to a simulated **EMA** of a five-**DOF** system and the results obtained have demonstrated that the single reference **MLE-MM** can be efficiently used to optimize the modal parameters provided by the **LSCF** and estimate their uncertainty bounds.

With regard to the second approach, the same five-**DOF** system was used to assess the efficiency of the proposed implementation of the **pMLE-MM**. The modal parameters of this system and their respective standard deviations provided by such implementation were in very good agreement with the estimates obtained with the **pMLE-MM** proposed by (El-Kafafy, 2013), which demonstrates that the alternative approach can be used without loss of efficiency and precision. One of the main advantages of this alternative approach is the possibility to estimate the uncertainties on the identified natural frequencies and damping ratios directly from the normal matrices, avoiding the use of explicit linearisation formulas in a final step of the identification process.

Comparing the poly-reference implementation of the **ML-MM** estimator to its single reference counterpart, it is verified that main advantage of the former is the possibility to retain and improve the poly-reference precision provided by the **pLSCF** estimator. The main disadvantage, however, is that it demands a much longer time to compute the normal matrices. The main benefit of using the single reference **MLE-MM** is that it results in a faster algorithm. The main

disadvantages, on the other hand, are, in fact, related to the modal model in its pole residue form, as well as to the shortcomings of a single reference method. These disadvantages include: (1) difficulty of distinguishing between close spaced modes; and (2) impossibility to synthesize the spectrum, once the mode shapes and operational factors are estimated from the residue matrices by means of the **SVD**.

In Döhler and Mevel (2013) is presented an efficient approach to estimate the confidence intervals of the modal parameters provided by the **SSI**-based identification methods. In this Chapter, however, a new strategy in frequency-domain was followed to the estimate the uncertainties on the **SSI-COV** and **SSI-DATA** estimates. This strategy follows the same idea of the combined **MLE-CDM-pLSCF-pMLE-MM** and consists of: (1) compute the variance of the measured half spectra by making use of the residual error approach (see Section 2.7.1); (2) identifying the poles and the observed mode shapes by means of the stabilization diagrams; (3) computing the reference operational factors with the **LSFD** estimator; and, finally, (4) estimating the confidence intervals of the estimated modal parameters with the **pMLE-MM**. This strategy was applied to a simulated tower structure and it was shown that the confidence intervals estimated for the modal parameters provided by the **SSI-DATA** and **SSI-COV** were in good agreement with those estimated for the **pLSCF** estimates (see **Example 12**).

Chapter 4

VIBRATION-BASED DAMAGE DETECTION UNDER VARYING ENVIRONMENTAL CONDITIONS

In this chapter, the main procedures and techniques used to detect damage from data acquired by vibration-based monitoring systems are discussed. The first part of the chapter is dedicated to the strategies applied to vibration data to automatically identify the modal properties of the monitored structures, which are subsequently used as observed features to detect structural damage. The final part of the chapter discusses some of the techniques commonly used to model the environmental and operational effects and remove their influence from the observed features used as indicators of structural change and damage.

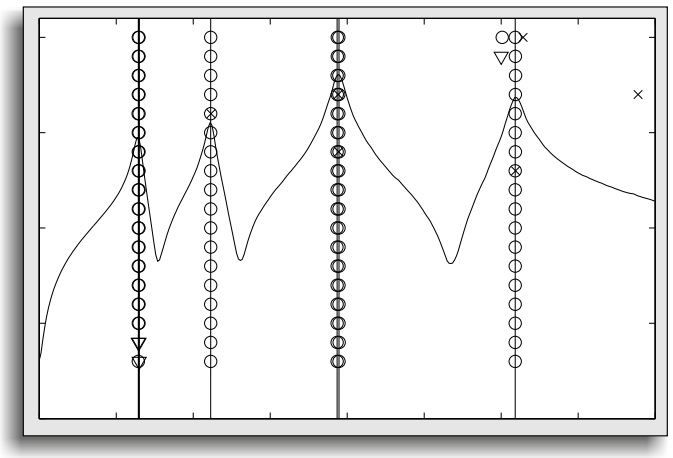

4.1. Introduction

The benefits to be gained in detecting damage by monitoring the structural dynamic responses of structures justifies the great interest shown by the civil, mechanical, and aerospace engineering communities over the last years in this subject area. These benefits include the possibility to detect early stage structural change and damage, to avoid unnecessary inspections and to reduce the overall maintenance costs of civil structures. The main obstacle to stablish a reliable monitoring system to assess the health condition of civil structures based on the vibration responses is the identification of structural changes in presence of varying environmental and operational conditions.

One of the key steps to achieve this goal is the development of reliable autonomous applications which are capable of transforming the raw data measurements continuously collected in such monitoring into useful and conclusive information regarding the health condition of the monitored structures. In previous chapters, the **MPE** was addressed with the assumption of constant environmental and operational conditions. In practical situations, however, structures are subjected to changes in such in conditions (e.g., temperature, humidity, wind, traffic, etc.). Therefore, if the these properties are intended to be used as damage indicators, the variations induced by such conditions must be taken into account, otherwise they may mask the structural changes caused by damage.

If such variations are not accounted in damage assessment, false-positive or negative damage diagnosis may occur so that vibration-based health monitoring becomes inefficient or unreliable. Accordingly, during the last years, several strategies have been proposed to assess the component of variation of these properties due to environmental conditions. A detailed overview of these strategies is found, for instance, in Doebling et al. (1996). In the context of civil engineering, a commonly used strategy consists of detecting damage by monitoring the variations in modal features extracted from vibration measurements permanently acquired over the course of the monitoring campaigns. Such strategies are based on the fact that damage is characterised by changes in the modal parameters, i.e., natural frequencies, modal damping ratios and mode shapes.

Given the few amount of sensors generally used in **SHM** of civil structures, in the context of civil engineering, these strategies are normally applied to model the influence of the environmental and operational effects on the modal features. Such application aims at removing this influence, so that the changes in these features due to damage can be efficiently detected. Such strategies have yet proven to be very effective as verified, for instance, in Peeters (2000), and have been increasingly used to detect damage in civil engineering (Magalhães, 2010; Hu, 2011).

In this context, this chapter discusses some of the most relevant techniques used to transform the vibration data acquired under varying environmental and operational conditions into useful information regarding the health condition of the monitored structures.

4.2. Automated OMA

The automated **OMA** plays a fundamental role in the context of damage detection based on vibration responses. In fact, a successful assessment of the health condition based on this approach is only possible if the modal properties are accurately extracted from the raw vibration data acquired over the course of the monitoring period. Given the huge amount of datasets acquired in such monitoring, this task needs to be performed by automated applications which are capable of tracking, amongst other useful information, the modal properties from these data. Once they are initially configured, it is required that such applications are capable of extracting these information with no further intervention. The automation of this procedure depends on the identification techniques applied to estimate the modal parameters from the collected datasets, which can be non-parametric and parametric techniques.

With regard to the non-parametric techniques, the **FFD** method has been often used in automated **OMA**. The application of the automated **FFD** in the context of damage detection is discussed, for instance, in Magalhães (2010) and Hu (2011). In the case of parametric techniques, this automation can be achieved by making use of different algorithms to automatically interpret the stabilization diagrams by separating the physical modal parameters from the numerical ones. Some of the most widely used techniques for this purpose are, for instance the **G**enetic **A**lgorithm **GA** (Chou and Ghabouss, 2001; Gomes and Silva, 2008), **F**uzzy **C**-**M**eans (**FCM**) (Carden and Brownjoh, 2008) clustering and **H**ierarchical **C**lustering (**HC**) algorithm (Magalhães, 2010; Reynders et al., 2012).

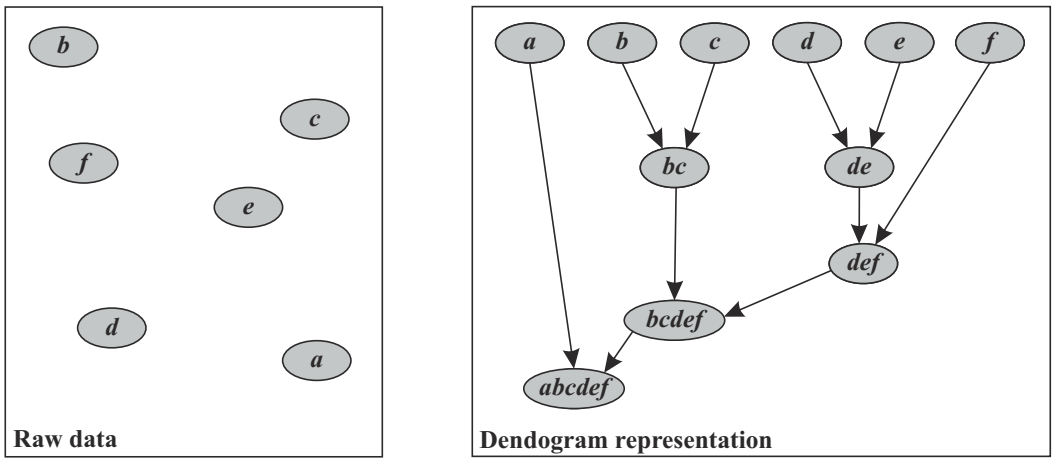

Fig. 4.1 – Schematic example of an agglomerative clustering: raw data (left) and hierarchical clustering dendrogram (right).

4.2.1. Hierarchical Clustering for Automated **OMA**

Hierarchical clustering is one of the most popular algorithms applied to cluster multi-dimensional data. Detailed description about this clustering technique is found, for instance in Olson (1995). This method starts with a set of distinct points, each of which is considered an individual cluster. Next, the two clusters which are closest according to a metric distance, are merged into a single cluster, originating an *agglomerate*. This procedure is repeated until all of the points are agglomerated into one hierarchically constructed cluster, as illustrated in Fig. 4.1. The final hierarchical cluster structure is called *dendogram* and consists of a tree that shows the clusters which were agglomerated at each generation. An example of a typical dendogram is illustrated in Fig. 4.2.

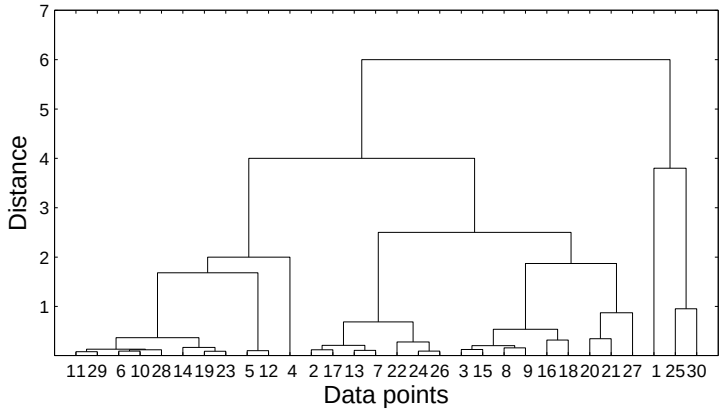

Fig. 4.2 – Typical dendogram showing how the clusters are merged hierarchically.

Different variants of the hierarchical clustering algorithm can be used to select the physical modal parameters from the poles of stabilisation diagrams. One of the main differences among these variants relies upon the criteria used to measure the degree of similarities of the mean properties of two clusters. Several strategies are found in literature to measure these similarities, as for instance, in Magalhães et al. (2009a) and Reynders et al. (2012). Despite the good results obtained with these strategies, in the autonomous application developed in the framework of this thesis it was followed a similar approach, but adopting slightly different criteria to measure the similarities between two cluster centres. These criteria are defined by the following expressions:

$$F(f_i, f_j) = 2\frac{|f_i - f_j|}{f_i + f_j}$$
$$V(v_i, v_j) = 1 - MAC(v_i, v_j), \tag{4.1}$$

where $F(f_i, f_j)$ and $V(v_i, v_j)$ are scalars that measure the degree of similarity between the mean

natural frequencies and mean modal vectors of two distinct clusters denoted by indexes i and j, and f_i and f_j are the mean natural frequencies of these clusters. $MAC(v_i, v_j)$ is the modal assurance criterion used to calculate the correlation between two modal vectors by means of the following equation:

$$MAC(v_i, v_j) = \frac{|v_i^H v_j|^2}{(v_i^H v_i)(v_j^H v_j)} \tag{4.2}$$

where v_i and v_j are, respectively, the mean modal vectors of the clusters i and j. The summation of eqs. (4.1) yields:

$$S_{ij} = F(f_i, f_j) + V(v_i, v_j) \tag{4.3}$$

where S_{ij} is a value that measures the total degree of similarity between the mean properties of clusters i and j. The closer this value is to zero, the more similar the clusters of poles denoted by indexes i and j are. An interesting property of the equation used to calculate the differences in the natural frequencies is the fact of providing a quantification of the relative difference that does not depend on the order of comparison of the evaluated clusters (e.g., order ij or ji). It is believed that this stability may provide more accurate results on gathering the clusters of poles with similar modal properties.

*4.2.2. Fuzzy C-Means clustering for Automated **OMA***

The **F**uzzy **C**-**M**eans (**FCM**) clustering is another algorithm widely used to automatically interpret stability diagrams and separate the physical from the numerical modes (Verboven, 2002; Scionti and Lanslots, 2005; Carden and Brownjoh, 2008). It was originally developed by Bezdek (1981) and is the essentially concerned with the separation of a dataset into overlapping subsets. The number of subsets is specified by the analyst a priori and is typically denoted by C, hence the name of the clustering technique. The algorithm begins by assuming a set of cluster centers denoted by v_i and minimizing the following cost function:

$$l_{FCM} = \sum_{i=1}^{C} \sum_{k=1}^{N_d} u_{ik}^m (x_k - v_i)^T (x_k - v_i) \tag{4.4}$$

where u_{ik} denotes the elements of the membership matrix $\boldsymbol{U}$, N_d is the number of members within the dataset and m is an exponent that determines the fuzziness of the clusters or degree of membership of data points to multiple clusters. A typical value chosen for m is 2. The goal of the algorithm is to update the cluster centres and the membership function iteratively to find

a minimum. The implementation of **FCM** is found in the Matlab Fuzzy Logic Toolbox (MathWorks, 2010).

Example 13
In order to illustrate the clustering technique used in this thesis from a practical point of view, the poles of the stabilisation diagram constructed with the **pLSCF** method presented in **Example 9** are used as raw data to be clustered. These poles are hierarchically clustered using the criteria defined by eqs. (4.1). The triplet functions `pdist, linkage and cluster` of MATLAB's Statistic Processing Toolbox can be used for this purpose. The function `pdist` allows for computing the pairwise distance between two clusters by making use of a customized function with additional criteria. A dendogram tree is constructed from the poles of the stabilization diagram illustrated in Fig. 3.8 is shown in Fig. 4.3. This dendogram is cut using a threshold distance $S_{ij}^{\max} = 2.1$ as indicated in such figure and only the nodes formed at or bellow this limit are retained.

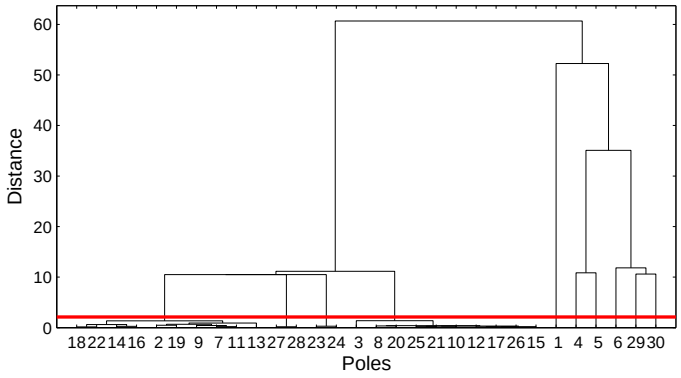

Fig. 4.3 – Dendogram tree (black line) constructed from the poles of the stabilization diagram illustrated in Fig. 3.8 and cut with a threshold distance $S_{ij}^{\max} = 2.1$ (red line).

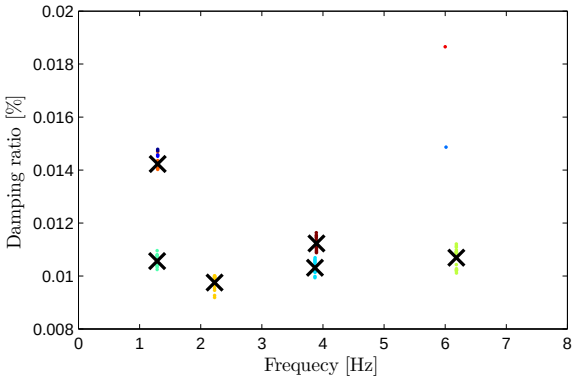

Fig. 4.4 – Automated **MPE** of the lattice tower structure: natural frequencies and damping ratios of the poles within the each agglomerate cluster (dots), and mean natural frequencies and damping ratios of the physical poles (cross).

The natural frequencies of the poles within each retained cluster are plotted against their corresponding damping ratios in Fig. 4.4. The variation of number of poles within each retained cluster as a function of the cluster's mean natural frequency is illustrated in 4.5. It is verified from this figure that, since the physical poles tend to stabilize over the different model orders,

the clusters with higher number of elements are those containing the physical poles, whereas the clusters with fewer elements are those which agglomerate the numerical poles. By defining a minimum number of elements within each agglomerate cluster as a criterion, the clusters with the physical poles can be sorted out from those with the numerical ones.

As indicated in Fig. 4.5, in other to retain only the clusters with physical poles, this number was set equal to 10. The centres of clusters with physical natural frequencies and damping ratios are marked with crosses in Fig. 4.4. The result of the automated identification of the physical poles of the lattice tower structure with the hierarchical cluster algorithm is illustrated by vertical lines in the stabilisation diagram of Fig. 4.6. These lines represents the natural frequencies of the identified physical modes.

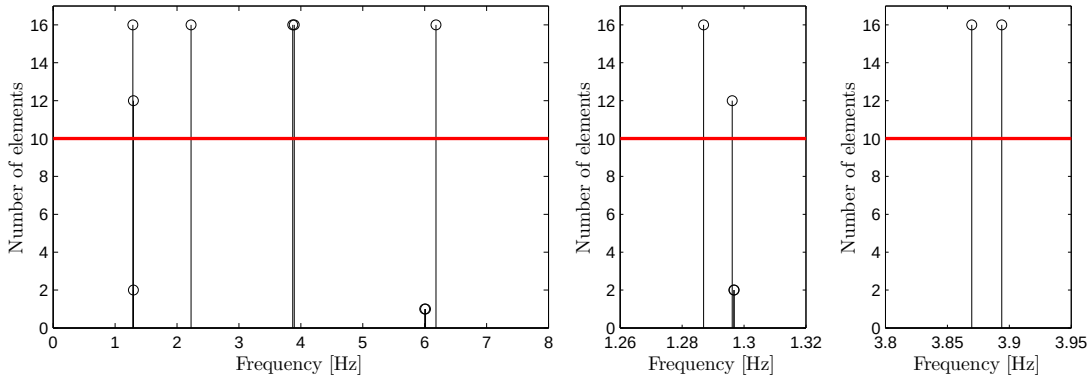

Fig. 4.5 – Automated interpretation of the stabilization diagram constructed for the tower structure with the **pLSCF** technique: number of elements as a function of the mean natural frequency of each agglomerate cluster (a), and details of the poles agglomerated around 1.29 (b) and 3.875 Hz (c).

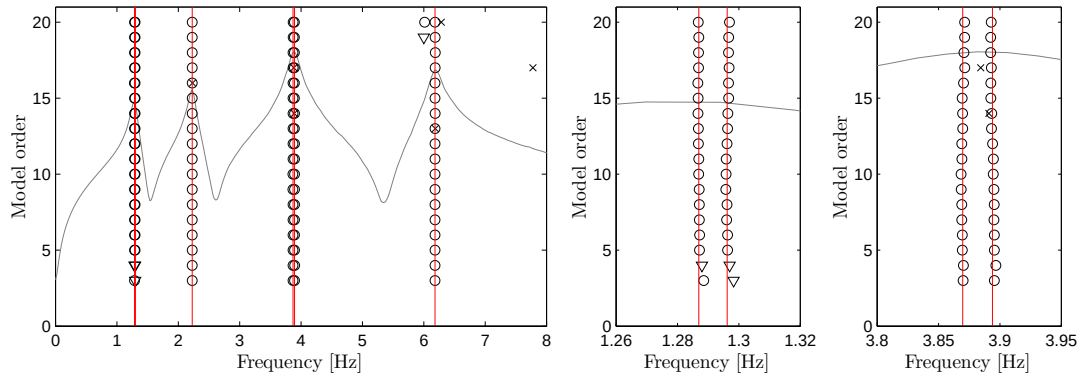

Fig. 4.6 – Automated interpretation of the stabilization diagram constructed for the tower structure with the **pLSCF** technique: physical modes automatically identified with hierarchical cluster algorithm (a), and details of the close spaced modes identified around 1.29 (b) and 3.875 Hz (c).

.

4.3. Removal of the Environmental and Operational Effects from the Identified Natural Frequencies

Apart from the applications developed to automatically identify the model properties of the monitored structures discussed in previous section, another key step towards the development of a reliable **SHM** application based on the vibration responses consists of removing the influence of the environmental effect from the modal parameters identified over the course of the monitoring period. Such step relies upon the application of environment models to the estimated modal properties so that the damage events can be distinguished from environmental effects. The basic idea is that, if the monitored structure has changed due to damage, its corresponding modal parameters estimates will significantly deviate from those estimated in its undamaged state. Several strategies can be used to mitigate the influence of the environmental effects on the modal properties of the monitored structures and assess damage. Detailed description about these strategies are found, for instance, in Doebling et al. (1996), Doebling et al. (1998) and Sohn et al. (2004).

The application of these strategies depends on the level of damage assessment which are basically divided into four categories: (1) damage detection, (2) damage localization, (3) damage quantification, and (4) prediction of the remaining life time of the structure. Given the few amount of sensors generally used in **SHM** of civil engineering structures, the damage assessment by means of the permanent monitoring of the vibration responses is normally based on level 1, which is suitable to detect the abnormal structural changes due to damage events and trigger further detailed investigations that may then demand higher levels of damage assessment. A commonly used approach to mitigate the influence of the environmental and operational effects in this level of damage assessment is the application of environmental models directly to the modal properties identified over the course of the monitored period, in order to remove the component of the deviation due to these effects.

4.3.1. Input-Output Methods

The input-output models is widely used in **SHM** to mitigate the influence of the environmental and operational conditions. These models are commonly based in linear regression analysis between the environmental or operational actions (inputs) and the estimated natural frequencies extracted from the vibration responses permanently acquired by the dynamic monitoring systems (outputs). The main difference among these models relies upon the complexity of the linear regressions used to model the input-output relationships. Apart from these models, other input-output models based on non-linear regressions or based on the statistic learning theory (Vapnik, 1999) are found in literature review, as, for instance, the **S**upport **V**ector **M**achine

(**SVM**) or **N**eural **N**etworks (**NN**). The efficiency of **SVM** algorithm and of the non-linear regression models in the context of the structural health monitoring are discussed, for instance, in Ni et al. (2005) and Steenackers and Guillaume (2005).

Multiple Linear Regressions

The linear regression models are based on a statistical technique used to analyse the relation between a single dependent variable and several independent variables. The basic concept of a regression analysis is to stablish the relation between the observed feature, y_k (the output quantity to be modelled), and the entire set of n_p variables z_{k1}, z_{k2} and z_{kn_p} that best achieves the objective of the specific multivariate analysis (inputs). This relations can be mathematically expressed by the following linear combination:

$$\hat{y}_k = \theta_1 z_{k1} + \theta_2 z_{k2} + \ldots + \theta_{n_p} z_{kn_p} \tag{4.5}$$

where θ_p $(p = 1, 2, \ldots, n_p)$ are the parameters to be determined by the multivariate technique, z_{kn_p} denotes the inputs, n_p the model order and k $(k = 1, 2, , \ldots, N_k)$ designates the modelled sample, with N_k denoting the number of observed samples. The main objective of regression analysis is then to estimate the parameters θ_p. Once these parameters are obtained, the model can be used to predict the outputs y_k for any given set of inputs. In the context of **SHM**, the environmental models based on multivariate linear regression can be used to predict the natural frequencies (output) by making use of the measured environmental actions such as temperature, wind velocity, humidity, etc., which are used as inputs. The estimation of the parameters θ_p are performed by minimizing the following equation error in a least squares sense:

$$E(\Theta) = Y - \hat{Y} = Y - Z\Theta \tag{4.6}$$

with

$$Z = \begin{bmatrix} Z_1 \\ Z_2 \\ \vdots \\ Z_{N_k} \end{bmatrix} \in \mathbb{R}^{N_k \times n_p} \quad \Theta = \begin{Bmatrix} \theta_1 \\ \theta_2 \\ \vdots \\ \theta_{n_p} \end{Bmatrix} \in \mathbb{R}^{n_p \times 1} \quad \hat{Y} = \begin{Bmatrix} \hat{y}_1 \\ \hat{y}_2 \\ \vdots \\ \hat{y}_{N_k} \end{Bmatrix} \in \mathbb{R}^{N_k \times 1} \quad Y = \begin{Bmatrix} y_1 \\ y_2 \\ \vdots \\ y_{N_k} \end{Bmatrix} \in \mathbb{R}^{N_k \times 1} \tag{4.7}$$

where Z is a matrix containing the inputs, $\hat{Y}$ a matrix containing the modelled features (predicted quantities) $\hat{y}_k$, Y a matrix containing the observed features y_k and Z_k a row vector with predictors

(inputs) corresponding to sample k, which is given by:

$$Z_k = \left\langle z_{k1} \quad z_{k2} \quad \dots \quad z_{kn_p} \right\rangle \in \mathbb{R}^{1\times n_p}, \quad k = 1, 2, \dots, N_k \tag{4.8}$$

It is straightforward to solve eq. (4.6) for Θ, which is obtained as:

$$\hat{\Theta} = \left(Z^T Z\right)^{-1} Z^T Y \tag{4.9}$$

Once the parameters of the environmental model (4.5) are found, the estimated residuals $\hat{E}$, i.e. the difference between the observed and predicted quantities, are computed as:

$$\hat{E} = \left(I - Z\left(Z^T Z\right)^{-1} Z^T\right) Y \tag{4.10}$$

These estimated residuals are assumed to have the following properties:

$$\mu_{\hat{E}} = \mathbf{E}[\hat{E}] = 0, \quad \mathrm{Cov}(\hat{E}) = \sigma_{\hat{E}}\left(I - Z\left(Z^T Z\right)^{-1} Z^T\right), \quad \mathbf{E}\left[\hat{E}^T \hat{E}\right] = (N_k - n_p)\sigma_{\hat{E}} \tag{4.11}$$

with the unbiased estimate of $\sigma^2_{\hat{E}}$ given by:

$$\sigma^2_{\hat{E}} = \frac{1}{N_k - n_p} \sum_{k=1}^{N_k} \hat{e}_k^2 \tag{4.12}$$

The quality of the model can be measured by means of the coefficient of multiple determination, R^2, which is estimated as:

$$R^2 = 1 - \frac{\sum_{k=1}^{N_k} \hat{e}_k^2}{\sum_{k=1}^{N_k} (y_k - \bar{y})^2} = \frac{\sum_{k=1}^{N_k} (\hat{y}_k - \bar{y})^2}{\sum_{k=1}^{N_k} (y_k - \bar{y})^2} \tag{4.13}$$

The coefficient R^2 indicates the proportion of the variability in the observed features that can be attributed to changes in the predictor variables. It ranges from zero, when the predictor variables have no influence on the dependent variable, to one, when the fitted equation passes through all data points. Once the parameters Θ are estimated using eq. (4.9), the model (4.5) can be used to predict values of future observations. The predicted observations, denoted as $\hat{y}_0$, are estimated by:

$$\hat{y}_0 = Z_0\hat{\Theta}, \quad Z_0 = \left\langle z_{01} \quad z_{02} \quad \cdots \quad z_{0n_p} \right\rangle \tag{4.14}$$

where Z_0 designates the input values not considered in the construction of the model. The future observations, y_0 at $Z_k = Z_0$, are expected to fall within the confidence interval given by:

$$\hat{y}_0 \pm t_{N_k - n_p, \alpha/2} \sqrt{\left[1 + Z_0^T (Z^T Z)^{-1} Z_0\right] \hat{\sigma}_E^2} \tag{4.15}$$

or in a more synthetic form by:

$$\hat{y}_0 \pm I_{Z_0}, \quad \text{with} \quad I_{Z_0} = t_{N_k - n_p, \alpha/2} \sqrt{\left[1 + Z_0^T (Z^T Z)^{-1} Z_0\right] \hat{\sigma}_E^2} \tag{4.16}$$

where $t_{N_k - n_p, \alpha/2}$ is the upper $100(\alpha/2)$ percentile of a t-distribution with $N_k - n_p$ degrees of freedom. When $N_k - n_p$ is greater than 30 the t-distribution tends to approximate the normal distribution. If the future observed natural frequency, y_0, falls in the confidence interval estimated with eq. (4.16), then it is considered to be related to the structure in its undamaged state, otherwise it may be associated either to a frequency incorrectly identified or to a frequency influenced by other events not predictable by regression model, such as structural change due to damage.

If each row of matrix Z containing the inputs is normalized with regard to the inputs suited in the first column, then the first model parameter, θ_1, becomes the mean of the predicted observations, i.e. $\mu_{\hat{y}_0}$, and the confidence interval expressed by eq. (4.16) can be rewritten as:

$$\mu_{\hat{y}_0} - I_{Z_0} < y_0 - \sum_{p=2}^{n_p} \hat{\theta}_p z_{0p} < \mu_{\hat{y}_0} + I_{Z_0} \tag{4.17}$$

Multivariate Linear Regressions Models

The linear regression model (4.5) can be extended to a multivariate model, i.e., to the situation where N_o outputs $Y_1, Y_2 \ldots, Y_{N_o}$ are observed at the same time. In a multivariate model, each response Y_o ($o = 1, 2, \ldots, N_o$) follows its own regression model, which is given by the following expression:

$$\hat{Y} = Z\Theta \tag{4.18}$$

where Y and Θ are now given by:

$$\hat{Y} = \begin{bmatrix} \hat{Y}_1 & \hat{Y}_2 & \cdots & \hat{Y}_{N_o} \end{bmatrix} \in \mathbb{R}^{N_k \times N_o}, \quad \Theta = \begin{bmatrix} \Theta_1 & \Theta_2 & \cdots & \Theta_{N_o} \end{bmatrix} \in \mathbb{R}^{n_p \times N_o} \tag{4.19}$$

with

$$\hat{Y}_o = \begin{Bmatrix} \hat{y}_{o1} \\ \hat{y}_{o2} \\ \vdots \\ \hat{y}_{oN_k} \end{Bmatrix} \in \mathbb{R}^{1 \times N_k}, \quad \Theta_o = \begin{Bmatrix} \theta_{1o} \\ \theta_{2o} \\ \vdots \\ \theta_{n_p o} \end{Bmatrix} \in \mathbb{R}^{1 \times n_p} \tag{4.20}$$

Similarly to the univariate linear regression models, the parameters Θ are estimated in a linear least squares sense, as:

$$\hat{\Theta} = \left(Z^T Z\right)^{-1} Z^T Y \tag{4.21}$$

After the estimation of the model parameters, the residuals are estimated by:

$$\hat{E} = Y - \hat{Y} = \left(I - Z\left(Z^T Z\right)^{-1} Z^T\right) Y \in \mathbb{R}^{\in \mathbb{R}^{N_k \times N_o}} \tag{4.22}$$

The prediction of future observations and the estimation of uncertainty intervals for the multivariate case are accomplished by following the same strategy used for the univariate linear regression models.

Dynamic regression models

Depending on the type of relation they describe, the regression models can be categorized into two types: static and dynamic regression models. Differently from the static models discussed in Section 4.3.1, which consider that the dependent variables estimated at a certain time instant are only influenced by the inputs observed at the same instant, the dynamic models assume that these variables can also be influenced by the inputs observed at previous time instants. The application of the dynamic regression models are particularly more efficient on modelling, for instance, the deviations dynamically induced on the natural frequencies by the daily temperature variations.

The ARX Models

Auto-**R**egressive output and an e**X**ogeneous (**ARX**) input part consists of a dynamic regression model that can be used to predict the observed features considering also previous values of the dependent variables Ljung (1999). A detailed description of this model and its application in

the context of **SHM** of civil engineering is found, for instance, in Peeters (2000) and Zhang (2007). If a multiple-input and single output relationship is described, this model is expressed by:

$$\hat{y}_k = -\left(a_1 y_{k-1} + \ldots + a_{n_a} y_{k-n_a}\right) + b_1 z_{k-n_k} + b_2 z_{k-n_k-1} + \ldots + b_{n_b} z_{k-n_k-n_b+1} + \varepsilon_k \tag{4.23}$$

where a_i $(i = 1, 2, \ldots, n_a)$ and b_j $(j = 1, 2, \ldots, n_b)$ are the model parameters to be found; n_a is the auto-regressive order, n_b the exogeneous order and n_k the pure time delay between input and output; and ε_k is the residual error term modelling the disturbances that act on the input-output process. This residual error is not known, but it is assumed that it is white noise, with zero mean ($\mathbf{E}[\varepsilon_k] = 0$) and covariance $\mathbf{E}[\varepsilon_k \varepsilon_{k-i}] = R_\varepsilon \delta_i$, with δ_i denoting the Kronecker symbol (i.e., $i = 0 \Rightarrow \delta_i = 1$, $i \neq 0 \Rightarrow \delta_i = 0$). Aiming at establishing confidence intervals for the predicted observations, it is assumed that ε_k is normally distributed. Writing down eq. (4.23) for the N_k input-output samples and formulating the resulting relations in a single matrix equation, yields:

$$\hat{Y} = Z\Theta + E \tag{4.24}$$

where

$$\begin{aligned} Z &= \begin{bmatrix} Z_1^T & Z_2^T & \cdots & Z_{N_k}^T \end{bmatrix}^T \in \mathbb{R}^{N_k \times (n_a + n_b)} \\ \Theta &= \begin{bmatrix} a_1 & \cdots & a_{n_a} & b_1 & \cdots & b_{n_b} \end{bmatrix}^T \in \mathbb{R}^{(n_a+n_b)\times 1} \end{aligned} \tag{4.25}$$

with

$$Z_k = \begin{bmatrix} -y_{k-1} & \cdots & -y_{k-n_a} & z_{k-n_k} & \cdots & z_{k-n_k-n_a-1} \end{bmatrix} \tag{4.26}$$

The model parameters, Θ, are found by solving eq. (4.24) in linear least squares sense. Once the **ARX** model is obtained, future observations and their corresponding confidence intervals of are estimated by following the procedure described in Peeters (2000) and Ljung (1999).

4.3.2. Output Only Methods

One of the main advantages of the output-only environmental models with regard to the their input-output counterparts is that they do not require to measure environmental actions to re-

move their influence from the modal properties. The output-only model commonly used in the framework of damage detection is based on the **P**rincipal **C**omponent **A**nalysis (**PCA**). The application of this technique has proven to be very efficient on removing the environmental and operational effects from the natural frequencies as verified in Yan et al. (2005a,b) and Deraemaekera et al. (2008).

Principal Components Analysis

The **PCA** consists of an output-only multivariate statistical method which is also known as Karhunen-Loève transform or proper orthogonal decomposition (Krzanowski, 2000). Applications of **PCA** in the context of **SHM** are found, for instance, in Manson (2002), Manson et al. (2004), Yan et al. (2005a), Yan et al. (2005b), De Boe and Golinval (2003), as well as in the monitoring campaigns of the Pedro and Inês footbridge (Hu, 2011), and Infante D. Herinque bridge (Magalhães, 2010). Essential to stablish a environmental model based on **PCA** is the definition of the so-called score matrix $X \in \mathbb{R}^{N_k \times n_p}$. This matrix results from the linear transformation of the measured or observed data to be modelled into a new coordinate system. This score matrix contains new values expressed in the principal component base and is defined as:

$$X = Y\Upsilon \tag{4.27}$$

where $Y \in \mathbb{R}^{N_k \times n_p}$ is a matrix containing the observed features in its columns and $\Upsilon \in \mathbb{R}^{n_p \times n_p}$ the loading matrix. Similarly to the linear regression models, the dimension n_p can be interpreted as the number of combined environmental factors that may represent important influence on the observed features and, therefore, are significantly correlated with their deviations. The loading matrix Υ can be computed as the eigenvector of the covariance of the matrix containing the observed features. Since the data covariance $\Sigma_Y \in \mathbb{R}^{n_p \times n_p}$ is symmetric, its eigenvalue decomposition is given as follows:

$$\Sigma_Y = \mathrm{Cov}(Y) = \mathbf{E}[Y^T Y] = Y^T Y = \Psi \Lambda \Psi^T \tag{4.28}$$

where $\Lambda \in \mathbb{R}^{n_p \times n_p}$ is a diagonal matrix containing the eigenvalues of the covariance matrix Σ_Y and $\Psi \in \mathbb{R}^{n_p \times n_p}$ is a orthogonal matrix $\left(\Psi\Psi^T = \Psi^T\Psi = I\right)$ with the corresponding eigenvectors. Generally, matrix Υ may be calculated by extracting the main m eigenvectors of the covariance matrix Σ_Y. Alternatively, a more practical method to compute this matrix is to perform a **SVD** of Σ_Y:

$$Y^T Y = US^2U^T \tag{4.29}$$

with

$$UU^T = U^T U = I, \quad S = \begin{bmatrix} S_1 & 0 \\ 0 & S_2 \end{bmatrix} \tag{4.30}$$

where $U \in \mathbb{R}^{n_p \times n_p}$ is an orthonormal matrix and $S \in \mathbb{R}^{n_p \times n_p}$ a matrix containing the n_p singular values in its diagonal. The diagonal terms of S_1 ($\sigma_1, \sigma_2, \ldots, \sigma_m$) are assumed to represent the active energy of the associated principal components, whereas the terms in the diagonal of S_2 ($\sigma_{m+1}, \sigma_{m+1}, \ldots, \sigma_{n_p}$) are likely to be less significant than the diagonal elements of S_1, but they are not equal to zero due to the effect of noise and/or the presence of non-linear effects. The idea is that only few of these elements, i.e. the first m singular values, have significant influence on the vibration features and, therefore, should be taken into account. The other singular values whose influence is not so significant (e.g., noise and non-linearities) can be simply neglected. The number of significant singular values m can be theoretically obtained by plotting all the singular values of S in ascending order and looking for a gap in the plot. In practical applications, however, it is not always easy to identify this gap. Therefore, a more practical procedure used to determine this value consists of computing the following ratio:

$$I_m = \frac{\sum_{p=1}^{m} s_p}{\sum_{p=1}^{n_p} s_p} \tag{4.31}$$

where I_m can be set equal to a certain value used as criterion that accounts for the most significant components of the variance of the observed data and m is determined such that the sum of the first singular values match this criterion. In some applications, the temperature is the most significant effect to be considered as principal components in the context of damage detection based on frequency shifts. In such circumstances, the number of principal components with significant influence, m, is simply chosen as 1 (Yan et al., 2005a). The matrix Υ can be obtained as the eigenvectors associated to the first m principal components. Once this matrix is computed, it can be used to estimate the observed features by re-projecting data back to the original space:

$$\hat{Y} = X\Upsilon^T = Y\Upsilon\Upsilon^T \tag{4.32}$$

where $\hat{Y}$ denotes the feature to be modelled (e.g. the natural frequencies). The loss of information in the linear transformation (4.27) can be assessed by the residual error matrix E, which is computed by:

$$\hat{E} = \hat{Y} - Y = Y\left(\Upsilon\Upsilon^T - I\right) \tag{4.33}$$

Once the observed features are estimated with eq. (4.32), they can be subsequently used to remove the influence of environmental and operational effects from the observed features. This procedure will be described in Chapter 6 using a real-life application of the **PCA** technique. From the prediction equation (4.33), the error vector E_k obtained for the sample unit k can be used to define a Novelty Index used to detect abnormal changes on the monitored structures that might be associated to the existence of a structural damage. The application of such index in the context of damage detection is discussed in Section 4.3.3 and described from practical point of view in Chapter 6.

4.3.3. Control Charts

Control charts are very useful in the context of damage detection to distinguish between the environmental effects and the events not predictable by the environmental models, such as damage events. They are a tool of statistical quality control suitable to detect if the processes are out of control. In these charts, the quality characteristic of the controlled features are plotted as a function of the evaluated samples. When an unpredictable event occurs, the variability of the sample unit associated to this event is expected to be plotted out of the range previously defined as control limits. In these situation, an alarm can be triggered to indicate that an abnormal event has occurred. Several control charts for damage detection are found in literature. The basic difference among them relies on statistics used to control the abnormal occurrences.

An extensive discussion about different types of control charts and their applications is found in Montgomery (2005). The application of these control charts in the context of damage detection is discussed in Kullaa (2003) and their efficiency in the context of **SHM** is demonstrated, for instance, in Deraemaekera et al. (2008), Magalhães (2010), as well as in Hu et al. (2012). Amongst the most commonly used control charts in damage detection, are the $\bar{X}$-Chart (or X-bar chart) and the so-called *Shewhart* or T^2-Chart. The $\bar{X}$-Chart is constructed by plotting the individual observations or the mean of sub-samples of observations in time order and by drawing three horizontal lines parallel to each other: a **C**entre **L**ine (**CL**) and two lines that correspond to the **U**pper and **L**ower **C**ontrol **L**imits, usually labelled **UCL** and **LCL**, respectively. These upper and lower control limits as well as the central line are defined by the following expressions:

$$\begin{aligned} \mathbf{UCL} &= \bar{\bar{x}} + \alpha\sigma \\ \mathbf{LCL} &= \bar{\bar{x}} - \alpha\sigma \\ \mathbf{CL} &= \bar{\bar{x}} \end{aligned} \tag{4.34}$$

where x is generally used either to designate the observed feature itself, if a single features is controlled, or a **N**ovelty **I**ndex (**NI**), if several features are controlled at once; the coefficient α is usually taken equal to 3, which corresponds to a confidence interval of 99.7% with the assumption of a normal distribution; and $\bar{\bar{x}}$ denotes the sample mean and σ the sample standard deviation when single observations are controlled. When the means of sub-samples containing r samples are controlled, however, σ equals the sample standard deviation divided by $\sqrt{r}$. If $\bar{X}$-Chart is used after the application of **PCA** to control the observations of a single feature, than, apart from designating the feature itself, variable x can also be used to control the **NI**, which is normally computed either as the Euclidian norm of the residues:

$$x_k^E = \|E_k\| \tag{4.35}$$

or as the Mahalanobis norm:

$$x_k^E = \sqrt{E_k^T R^{-1} E_k}, \quad R = \frac{1}{N_k} Y^T Y \tag{4.36}$$

with $R \in \mathbb{R}$ representing the covariance of the matrix containing the observed features. If a multivariate model is used, the T^2-Chart can be used to control the observations of the set of features. Similarly to X-Chart, the T^2-Chart can be used either to control a single observation or a sub-sample of observations at once. In both situations, the observed features are controlled by means of the so-called T^2-statistic. If a single observation is controlled at a time, the T^2-statistic is computed by:

$$T^2 = \frac{N_k}{N_k + 1} (x - \bar{\bar{x}}) R^{-1} (x - \bar{\bar{x}})^T \tag{4.37}$$

where N_k is the number of observations collected during the reference period (i.e. period within which the observations were obtained with the monitored structure in its undamaged condition). Since **CL** and **LCL** are not used in the construction of T^2-Charts, these horizontal lines are considered to be coincident with x-axis. The **UCL**, on the other hand, is given by the following expression:

$$\mathbf{UCL} = \frac{(N_k - 1)m}{N_k - m} F_{n_p, n_p - m}(\alpha) \tag{4.38}$$

with $F_{m,n_p-m}(\alpha)$ denoting the α percentage point of the F-distribution with m and $n_p - m$ degrees of freedom. If sub-samples containing r observations of x are controlled, the T^2-statistic is computed by:

$$T^2 = r(\bar{x} - \bar{\bar{x}}) R_{ss}^{-1} (\bar{x} - \bar{\bar{x}})^T \tag{4.39}$$

where $\bar{x}$ is the is the sub-sample average; $\bar{\bar{x}}$ is the process average, i.e, the mean over the sub-sample averages computed within the reference period at which the process is under control; and R_{ss} is the matrix consisting of the average of the sub-sample variances and covariances. The **UCL**, on the other hand, is computed by:

$$\mathbf{UCL} = \frac{m(n_s + 1)(r - 1)}{n_s r - n_s - m + 1} F_{m, n_s r - n_s - m + 1}(\alpha) \tag{4.40}$$

with n_s denoting the number of sub-samples observed during the reference period. A practical application of $\bar{X}$ and T^2-Charts in the context damage detection of civil engineering structures is described in Chapter 6.

4.4. Conclusions

In this chapter, the main procedures and techniques used to detect damage in civil engineering structures under varying environmental conditions were discussed. In the first part of the chapter, it was presented the automated strategy used in the framework of this thesis to automatically track the modal parameters. A simulated example was used to assess the efficiency and robustness of such strategy and it was shown the identification procedure was capable of automatically interpreting the stabilization diagram and tracking the physical modes of the simulated structure. In the final part of the chapter the techniques used to remove the environmental effects from the identified modal parameters were discussed. Special attention was dedicated to **PCA** as this technique is applied to remove the environmental effects from the identified natural frequencies and detect damage in the context of the present work. The application of **PCA** technique to detect damage- induced structural changes in a real structure will be covered in detail in Chapter 6.

Chapter 5

OPERATIONAL MODAL ANALYSIS OF THE BRAGA STADIUM SUSPENSION ROOF

In this chapter, the modal identification techniques discussed in Chapter 3 are applied to the data acquired in an ambient vibration test of a real structure. The main purposes of the test were to perform a multi-patch **OMA** to estimate the modal properties of the tested structure together with their uncertainty bounds, as well as to assess the modes which were more sensitive to the underlying environmental and operational conditions. The chapter is divided into three parts: the first discusses the strategy used to pre-process the data recorded in each patch; the second addresses the time and frequency-domain analyses performed to extract the dynamic properties from each dataset; and the third part presents the results of the **OMA** performed to estimate the modal parameters of the tested structure with high spatial resolution for the mode shapes of vibration.

5.1. Introduction

In operational modal analysis engineers are usually confronted with the challenge of extracting as much information as possible from the data collected in the **A**mbient **V**ibration **T**ests (**AVT**s) in order to characterize the modal behaviour of the tested structures under environmental and operational conditions. In this context, this chapter describes the strategies and techniques employed, and the results obtained from the **OMA** performed to identify the modal properties of a football stadium suspension roof. Aiming at extracting relevant information regarding the dynamic behaviour of the roof structure, the state-of-the-art modal identification techniques discussed in Chapter 3 were applied to estimate the modal parameters of the roof structure with high spatial resolution for the mode shapes of vibration together with their uncertainties bounds. Apart from the modal identification, a sensitivity analysis based on the estimated modal responses was carried to assess the modes which are likely to be more sensitive to the underlying environmental and operational conditions during the test.

One of the main purposes of the test was to create a baseline reference result to be used by the autonomous monitoring system installed in one of the slabs of the roof in the beginning of 2009, by the Laboratory of Vibrations and Structural Monitoring (**ViBest**, www.fe.up.pt/vibest) of the **F**aculty of **E**ngineering of **U**niversity of **P**orto (**FEUP**) (Magalhães et al., 2009b). The test was carried out by measuring the vertical responses induced by environmental sources (e.g. wind and the traffic in the surroundings of the stadium) with two different acquisition systems. The employment of robust pre-processing techniques to synchronize the data collected by both acquisition systems, as well as of the combination of some of the state-of-art parametric **OMA** techniques, provided an accurate estimation of a large number of modes of the roof structure in the frequency range of 0-2 Hz with high spatial resolution for the corresponding modes shapes of vibration and with confidence intervals for the estimated natural frequencies and modal damping ratios.

5.2. Description of the Structure

The tested structure is located in the city of Braga, Portugal, and corresponds to one of the stadia that were constructed to host some of the matches of the European Football Championship that took place in 2004, in Portugal (Fig. 5.1). The structure is known for its innovative architectural design elaborated by the design office of the Portuguese architect Eduardo Souto Moura, who has won the Pritzker prize of architecture in 2011, in collaboration with the structural design office AFA Consult (Furtado et al., 2005). The stadium is considered a masterpiece of architecture not only because of its innovative concepts and architectonic characteristics, but also for the perfect integration in the surrounding environment. The structure was constructed in the

slopes of a hill known as “Monte Castro” which is located in a peaceful rural area.

Fig. 5.1 – Braga Municipal Sports Stadium: top view of the stadium (a); lateral view from the East side (b); top view of the roof from the West side (c); and lateral view of the East stand (d).

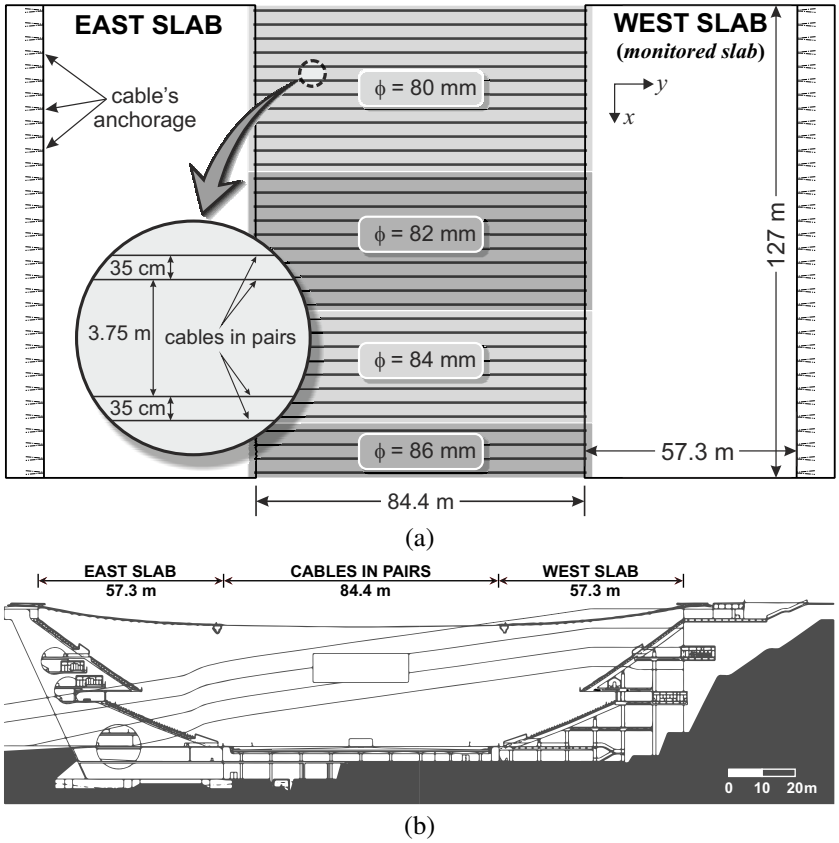

Fig. 5.2 – Braga Municipal Sports Stadium: distribution of the suspension cables of the roof structure (a) and cross section (b).

The stadium has capacity of accommodating 30000 spectators and is essentially composed by two stands located in both side of the pitch and a concrete roof suspended by cables. The most interesting element of the stadium, from the structural engineering point of view, is the suspension roof which is composed by two concrete slabs suspended by a set of 34 pairs of cables with diameters ranging from 80 to 86 mm. The distance between the cables in each pair and the distance between adjacent pairs of cables are, respectively, of 0.35 and 3.75 m as illustrated in Fig. 5.2a. The two concrete slabs of $127 \times 57.3 \times 0.245$ m are suspended by cables spanning a distance of 202 m, therefore, the remaining 88.4 m of the central part are free (Fig. 5.2b). The roof cables are anchored in two large beams at the top of both stands - East and West.

The East stand is structurally formed by 50 m high concrete walls, whose geometry was defined in order to minimize the unbalanced moments at the level of the foundation, induced by the combination of the gravitational action of the stand and the high forces transmitted by the roof cables. In the West stand, the concrete walls are anchored to the rock and the roof cables' tension forces are transmitted to the foundation by pre-stressing tendons embedded in the concrete (Magalhães et al., 2008).

5.3. Ambient Vibration Test

The acquisition of the operational responses of the suspension roof took place on the 6^{th} of July, 2011 on the West slab as indicated in Fig. 5.2a, and was carried out by using two different data acquisition systems to collect the vertical acceleration of the slab: the first consists of a set of 6 tri-axial seismographs and the second comprises a data acquisition system and a set of 6 accelerometers that was installed on the roof in the beginning of 2009 and that has been used to assess the long term health condition of this structure by means of the variation of the dynamic properties over the time. The test was conducted with a total of 15 datasets, which were used to measure vertical acceleration of 90 points on the slab, as indicated in Fig. 5.3a.

The seismographs were used as moving sensors and were placed on the tested slab according to each of the 15 different setups adopted in the ambient vibration test, as illustrated in Figs. 5.3a and 5.3b. The accelerometers of the dynamic monitoring system, on the other hand, were used as reference sensors and remained at the same position throughout the test. One of the main advantages of using both systems is that more sensors are available, allowing the test to be conducted in a rather shorter time period than with using only the sensors of the seismographs. The drawback of using different acquisition systems, however, is that the acquisition of the measured responses are triggered differently, requiring the signals acquired by both systems to be synchronized prior to the employment of the normal procedures used in ordinary multiple

dataset **OMA**.

The signals were acquired with sampling frequencies of 100 and 20 Hz for the moving sensors and reference sensors, respectively, and the sampling period was set 20 minutes for each of the 15 acquired datasets. Despite these differences in acquisition characteristics, a good synchronization of the signals acquired by both systems could be established thanks to the very precise built-in clocks, which are constantly updated by means of the GPS receivers embedded in both systems.

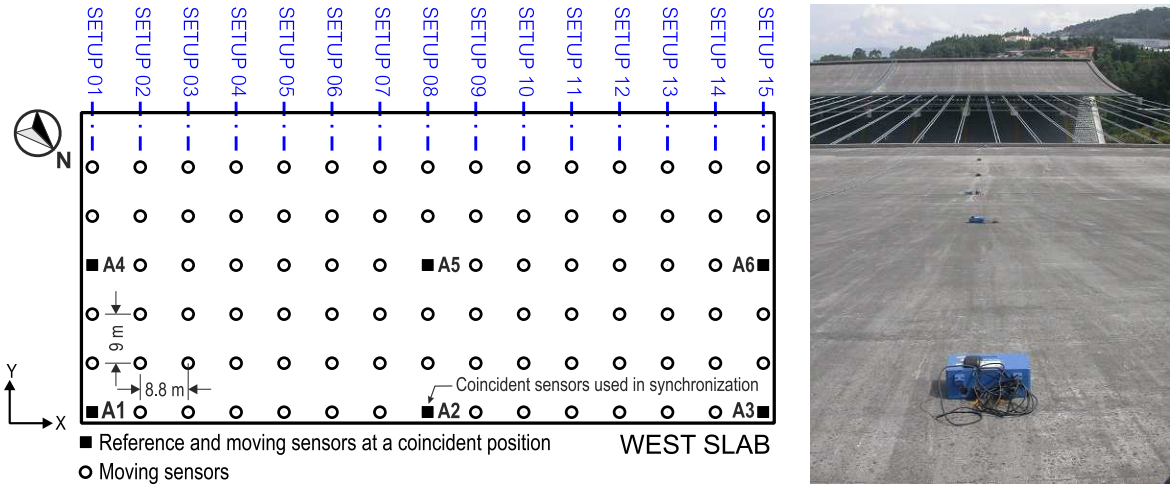

(a) (b)

Fig. 5.3 – Test plan: Distribution of the datasets along the tested slab (a) and placement of the sensors in one of these datasets (b).

5.4. Pre-processing and Non-parametric Estimation of the Spectrum Matrix of Each Setup

The different acquisition and triggering mechanisms available in each data acquisition system used in the test implies that the acquisition of the signals acquired by these systems start differently, resulting in a time delay between two types of time series acquired. This delay, on its turn, resulted in a phase between the corresponding **PSD**s that needed to be reduced, as much as possible, prior to use the time series acquired by both systems to identify the modal parameters of the slab. In order to correct this time delay, the acceleration time series acquired at the same point by a seismograph and an accelerometer were assessed. These sensors were placed, approximately, in the middle of the longer edge of the West slab, as indicated in Fig. 5.3.

As the sampling frequency of all seismographs was set to 100 Hz, the time series acquired by this type of acquisition system were filtered out using a low pass filter with a cut-off frequency equal to one half of the sampling frequency of the fixed acquisition system (i.e., 20 Hz). Once the sampling frequencies of both types of signals were evenly adjusted with regard to each other, the time delay was estimated by calculating the phase angle of the estimated transfer function

between the assessed signals. The transfer function was evaluated by means of the following equation:

$$T_{xy}(\omega) = \frac{S_{yx}(\omega)}{S_{xx}(\omega)} \tag{5.1}$$

where $S_{xy}(\omega)$ stands for the cross **PSD** between the signals acquired by the moving and reference sensor, and $S_{xx}(\omega)$ for the auto **PSD** of the signal acquired by a moving sensor. These cross and auto **PSD**s were calculated with the periodogram approach by making use of Hanning window to reduce the leakage and adopting 50% of overlapping between adjacent segments. In the context of the present **OMA**, the time series used to estimate the time delay between two types of signals were split in 18 time data segments with 1024 points.

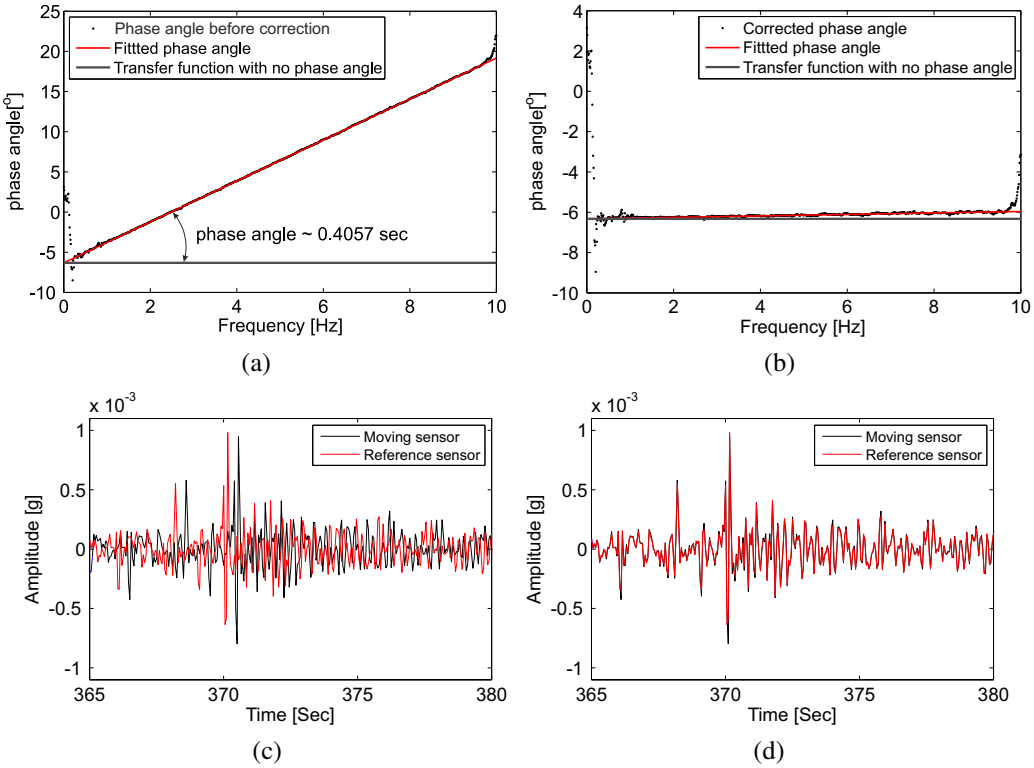

Fig. 5.4 – Correction of the existing phase angle between the signals acquired by reference and moving sensors: phase angle before (a) and after the correction (b), and the time series measured at the same point by the reference and moving sensors before (c) and after (d) correction.

The phase angle of the transfer function estimated by means of eq. (5.1) in the range of 0-10 Hz is shown in Fig. 5.4a. This estimated phase angle corresponds, approximately, to 0.4057 seconds, and was used to correct the time data signals collected by the seismographs with regard to those acquired by the reference sensors. As the time series obtained by the seismographs were acquired at a sampling interval of $\Delta t = 0.01$ sec, these time series were simply shifted towards left in time scale by $4\Delta t$ to reduce the existing time delay between the two types of signals. The phase angle of the transfer function estimated after the correction of the time delay is shown in

Fig. 5.4b. Although this time delay could not be completely removed, a good synchronization could be established between both type of signals as seen in the time series acquired before and after the delay correction shown in Figs. 5.4c and 5.4d. Since the **OMA** of the suspension roof was carried out in the frequency range of 0-2 Hz, the residual phase of 0.057 sec corresponds to 11.4% of the period associated to the upper frequency limit (i.e. 0.5 sec). Therefore, it is not expected that this residual phase influence significantly the estimation of the modal parameters suited in frequency band of interest.

5.5. Modal Parameter Estimation of Each Dataset

5.5.1. Identification of the Modal Parameters and Their Uncertainties

The identification of the modal parameters was performed from the acceleration responses of each dataset in time and frequency-domain using the modal identification techniques discussed in Chapter 3, namely, the **SSI-DATA**, **SSI-COV**, **pLSCF** and **pMLE-MM**. This identification was carried out aiming at accurately estimating the modal parameters together with their confidence intervals, as well as to assess the variation of these estimates over the test duration. The **MPE** of each dataset was performed in two steps. Firstly, these parameters were identified with the **SSI-DATA**, **SSI-COV** and **pLSCF** methods. Afterwards the estimates obtained with such techniques were used by the **pMLE-MM** to yield their confidence intervals.

The variance of the measured half spectra were estimated by making use of the residual error approach discussed in Section 2.7.1. Such estimation was carried out in three steps: (1) the numerator and denominator polynomials of the common denominator model were estimated with the **LSCF** technique from the measured half spectra using a model with order $n = 70$; (2) The half spectra were synthesized in a "blind" way from the estimated numerator and denominator polynomials, i.e., without prior classification of the physical and numerical poles; and (3) the variance, $\sigma^2_{S^+_{yy}}$, was computed by smoothing the residual error between the measured and synthesized half spectra with a Hanning window defined by the shape parameter $\gamma = 21$.

The **MPE** from each dataset was carried out in the frequency range of 0-1 Hz, using only the reference responses collected, i.e., the accelerations measured by sensors **A1**, **A2**, **A3**, **A4**, **A5** and **A6** (see Fig. 5.3a). The time series of each setup were filtered with a cutoff frequency of 1.14 Hz. The correlation matrices used to obtain the modal properties with **SSI-COV** were estimated for each dataset with 1024 correlation points. The identification with both **SSI** techniques was performed by means of stabilization diagrams constructed by identifying models with time lag $i = 20$ and order n ranging from 2 to 70. In the identification with **SSI-DATA**, apart form the modal parameters, the modal responses and their corresponding contributions to the measured outputs were also computed in order to assess the modes which were more excited

by the operational conditions.

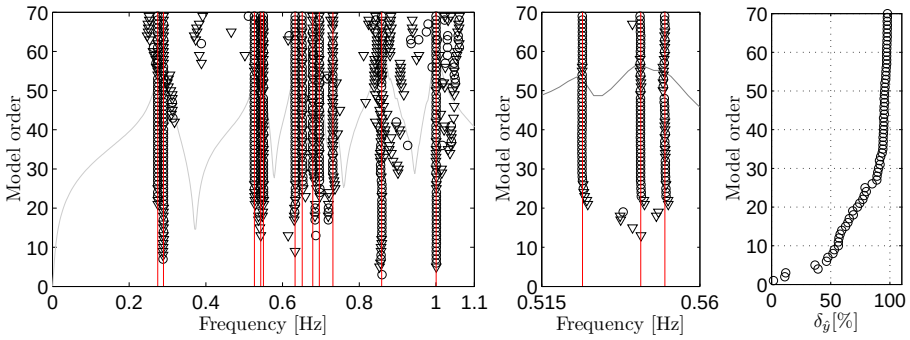

(a) (b) (c)

Fig. 5.5 – Stabilization diagram created with the **SSI-DATA** technique from the reference responses acquired with setup 2 (a), and detail of the close spaced modes around 0.53 Hz (b) and variation of contribution of the identified modes to the total responses over the different model orders (c).

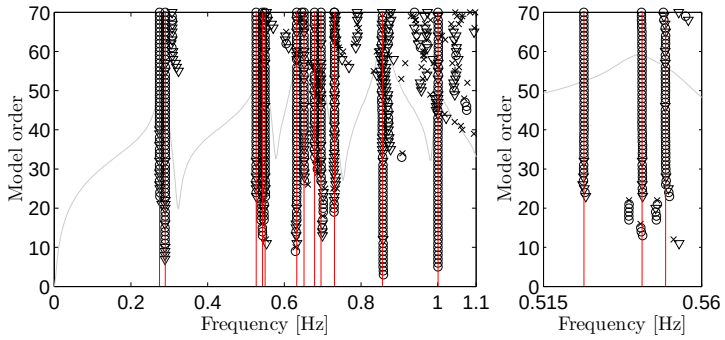

(a) (b)

Fig. 5.6 – Stabilization diagram created with the **SSI-COV** technique from the reference responses acquired with setup 2 (a), and detail of the close spaced modes around 0.53 Hz (b).

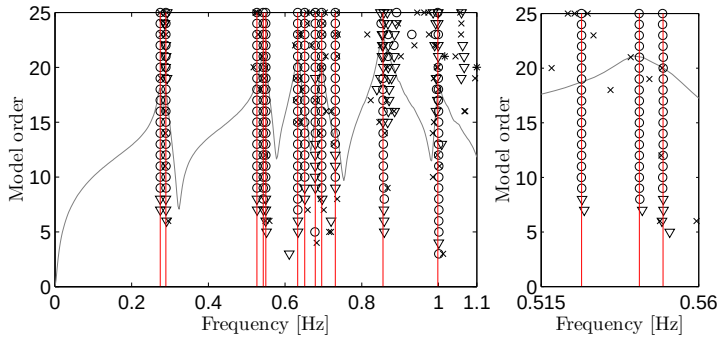

(a) (b)

Fig. 5.7 – Stabilization diagram created with the **pLSCF** technique from the reference responses acquired with setup 2 (a), and detail of the close spaced modes around 0.53 Hz (b).

The stabilization diagram constructed with **SSI-DATA** from the vibration responses acquired with setup 2 is shown in Figs. 5.5a. As seen in this figure, a total of 12 vibration modes were

clearly identified in the frequency range of 0-1 Hz, three of which closely concentrated around 0.53 Hz, as shown in Fig. 5.5b. The variation of the contribution of the modal responses to the measured outputs over the identified model orders is shown in Fig. 5.5c. Analysing such figure, it is verified that the responses of the modes identified with model orders greater than 30 represent more than 90% of the measured responses, which suggests that a model order of 30 could be chosen to estimate the modal parameters and the responses due to the modes, $\hat{y}_m$, as well as the contributions $\Delta_{\hat{y}_m}$, $\delta_{\hat{y}_m}$ and $\delta_{\hat{y}}$.

In Figs. 5.6a, it is shown the stabilization diagram constructed with the **SSI-COV** technique. As seen in such figure, 12 modes were also clearly identified in the frequency range of 0-1 Hz, including the three closed spaced modes around 0.53 Hz as shown in Fig. 5.5b. The identification with the **pLSCF** was performed by using a half spectra matrix containing 512 frequency lines as primary data. This matrix was computed by means of the correlogram approach described in Section 2.7 and using an exponential window with a decay rate of 99.99%, in order to minimize the leakage and the spurious effects of the higher covariance lags. Afterwards, a stabilization diagram was constructed by identifying models with orders n ranging from 2 to 25, as illustrated in Fig. 5.7. The same 12 vibration modes were clearly identified from this diagram with aid of the automated application described in Section 4.2.1, including the three close spaced modes suited around 0.53 Hz, as seen in the zoom illustrated in Fig. 5.7b.

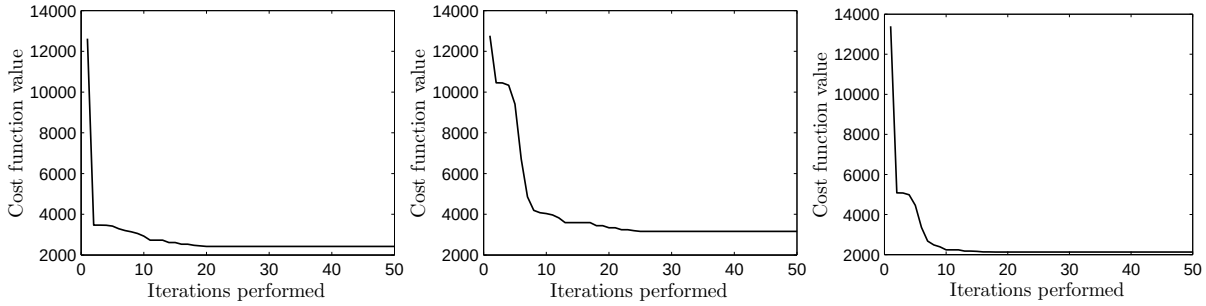

Fig. 5.8 – Variation of the **pMLE-MM** cost function value over the performed iterations computed from the starting estimates provided by the **SSI-DATA** (a), **SSI-COV** (b) and **pLSCF** (c) identification techniques.

Once the modal parameters of the suspension roof were automatically identified from the stabilization diagrams of Figs. 5.5a, 5.6a and 5.7a, they were used as starting values by the **pMLE-MM** to estimate their uncertainty bounds, which were obtained with only one iteration Gauss-Newton algorithm. Next, 50 iterations of the **pMLE-MM** were used to optimize these starting values and compute confidence intervals of the optimized modal parameters. The optimization was carried out in the frequency range of 0.01-1.1 Hz. The variation of the cost function value

over the iterations performed to optimize the starting parameters obtained with the **SSI-DATA**, **SSI-COV** and **pLSCF** methods are shown in Figs.5.8a, 5.8b and 5.8c, respectively.

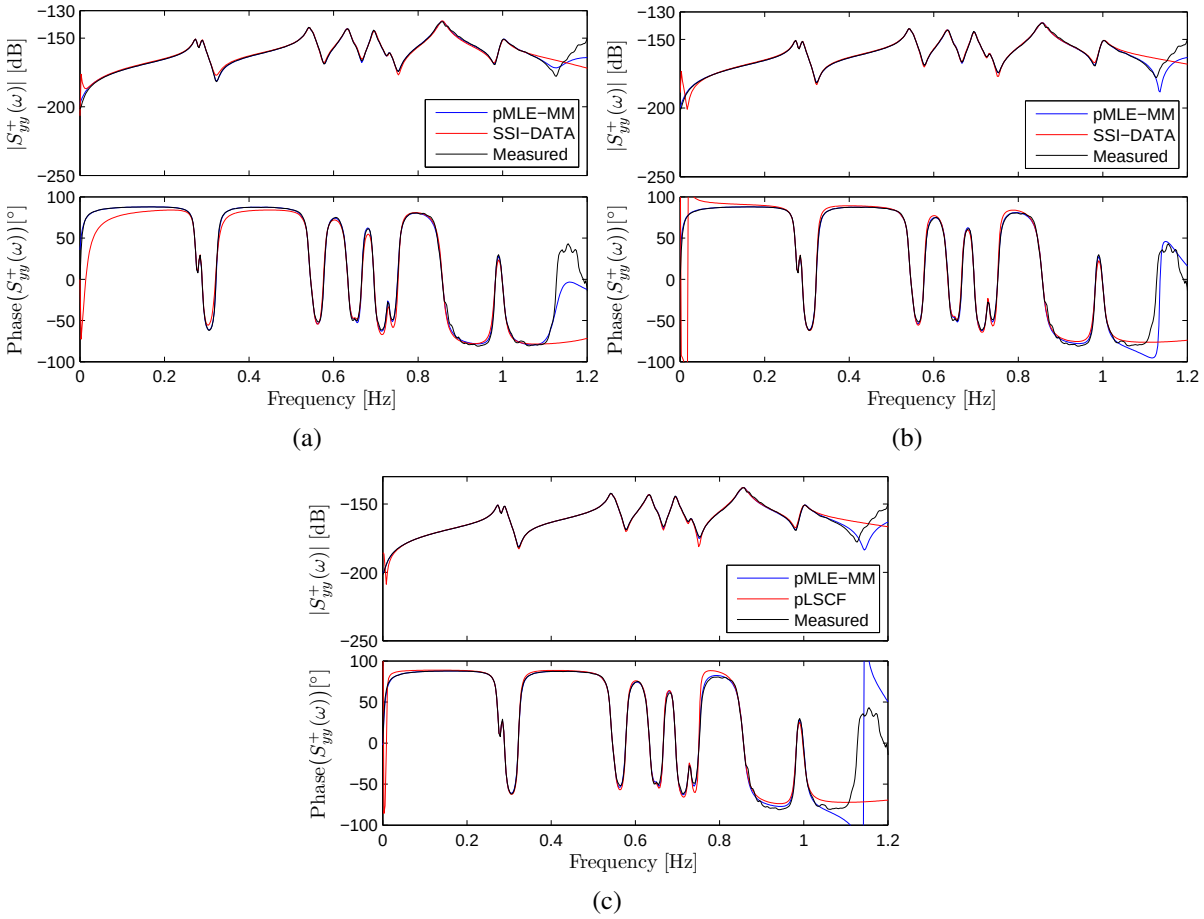

Fig. 5.9 – Comparison of element (1,1) of the measured half spectra matrix, S_{yy}^{+}, to the corresponding spectrum synthesized from the parameters identified with the **SSI-DATA** (a), **SSI-COV** (b) and **pLSCF** (c), as well as to the spectrum synthesized after 50 Gauss-Newton iterations of the **pMLE-MM**.

As observed in these figures, considerable reductions of the cost function values are verified after 50 Gauss-Newton iterations of the **pMLE-MM**, outcome of the approximation of the spectra matrices synthesized after every iteration to the measured spectra. These results are seen in Figs. 5.9a, 5.9b and 5.9c where the element (1,1) of the measured half spectra matrix, S_{yy}^{+}, is compared to the corresponding spectrum synthesized before and after the optimization of the starting parameters with the **pMLE-MM**. As verified in these figures, the spectrum synthesized after the optimization of the starting parameters are in good agreement with the measured spectrum, which demonstrates the efficiency of the optimization carried out with the **pMLE-MM**.

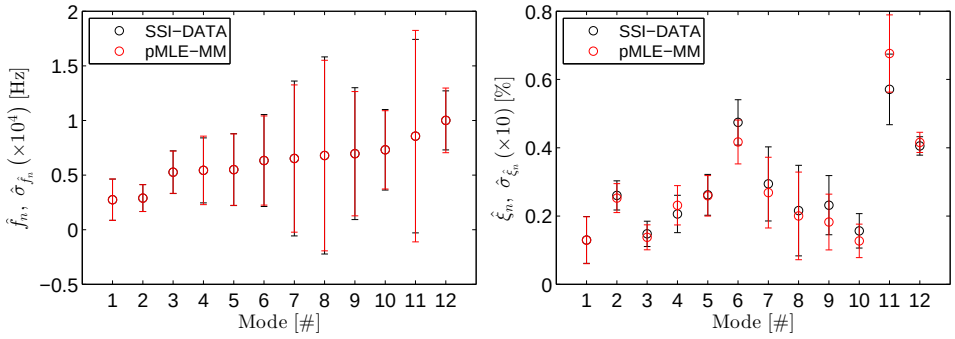

(a) (b)

Fig. 5.10 – Natural frequencies (a) and damping ratios (b) identified with **SSI-DATA** together with their standard deviation estimated before (black line) and after (red line) the optimization with the **pMLE-MM**. The standard deviations of the natural frequencies and damping ratios are multiplied by 10^4 and 10, respectively, to improve their visibility within the figure.

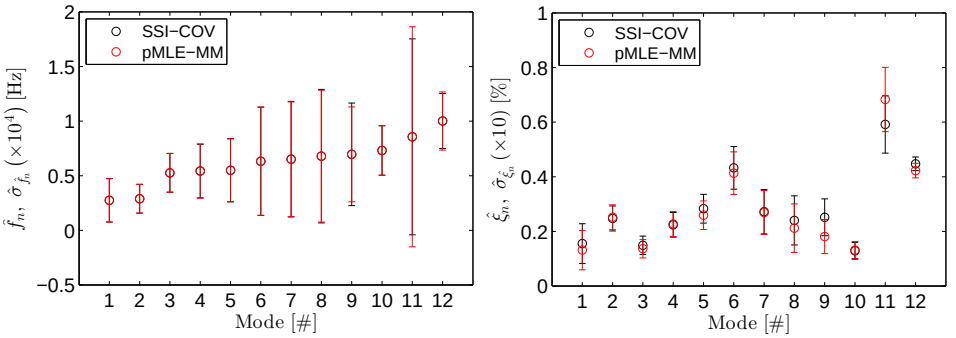

(a) (b)

Fig. 5.11 – Natural frequencies (a) and damping ratios (b) identified with **SSI-COV** together with their standard deviation estimated before (black line) and after (red line) the optimization with the **pMLE-MM**. The standard deviations of the natural frequencies and damping ratios are multiplied by 10^4 and 10, respectively, to improve their visibility within the figure.

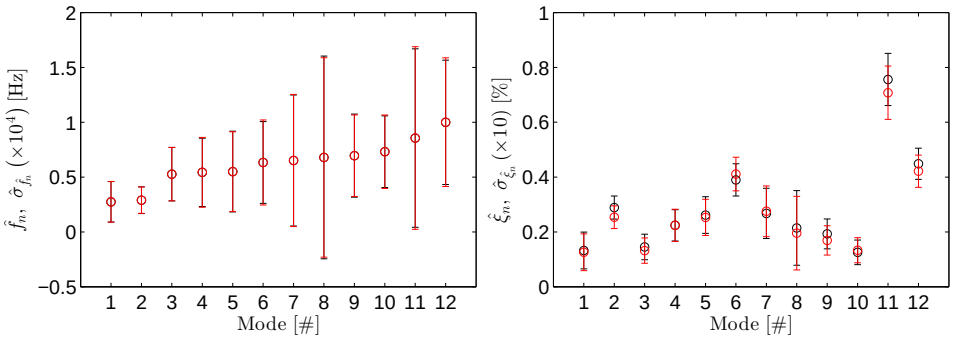

(a) (b)

Fig. 5.12 – Natural frequencies (a) and damping ratios (b) identified with **pLSCF** together with their standard deviation estimated before (black line) and after (red line) the optimization with the **pMLE-MM**. The standard deviations of the natural frequencies and damping ratios are multiplied by 10^4 and 10, respectively, to improve their visibility within the figure.

Tab. 5.1 – Identification results obtained from setup 2 with the **SSI-DATA**, **SSI-COV** and **pLSCF** methods combined with the alternative implementation of the **pMLE-MM**.

Method	Mode	**pMLE-MM** Estimates (1 iteration)				**pMLE-MM** Estimates (50 iterations)			
		$\hat{f}_n$ [Hz]	$\hat{\sigma}_{\hat{f}_n}$ [Hz] $(\times 10^4)$	$\hat{\xi}_n$ [%]	$\hat{\sigma}_{\hat{\xi}_n}$ [%] $(\times 10^2)$	$\hat{f}_n$ [Hz]	$\hat{\sigma}_{\hat{f}_n}$ [Hz] $(\times 10^4)$	$\hat{\xi}_n$ [%]	$\hat{\sigma}_{\hat{\xi}_n}$ [%] $(\times 10^2)$
SSI-DATA	1	0.27456	0.19	0.1298	0.69	0.27452	0.19	0.1290	0.69
	2	0.28940	0.12	0.2604	0.43	0.28928	0.12	0.2524	0.42
	3	0.52654	0.20	0.1478	0.37	0.52651	0.19	0.1376	0.37
	4	0.54315	0.30	0.2061	0.55	0.54305	0.31	0.2314	0.58
	5	0.54984	0.33	0.2620	0.60	0.54959	0.33	0.2592	0.59
	6	0.63285	0.42	0.4742	0.66	0.63300	0.41	0.4169	0.64
	7	0.65172	0.71	0.2940	1.09	0.65126	0.67	0.2685	1.03
	8	0.67942	0.90	0.2158	1.33	0.67877	0.87	0.2003	1.28
	9	0.69613	0.60	0.2318	0.87	0.69539	0.57	0.1823	0.82
	10	0.73150	0.37	0.1565	0.50	0.73107	0.36	0.1271	0.49
	11	0.85662	0.89	0.5711	1.03	0.85657	0.97	0.6762	1.13
	12	1.00090	0.27	0.4053	0.27	1.00045	0.30	0.4157	0.30
SSI-COV	1	0.27458	0.20	0.1555	0.73	0.27452	0.20	0.1314	0.72
	2	0.28943	0.13	0.2471	0.46	0.28928	0.13	0.2517	0.46
	3	0.52649	0.18	0.1489	0.34	0.52651	0.18	0.1363	0.33
	4	0.54303	0.25	0.2237	0.45	0.54305	0.25	0.2273	0.46
	5	0.54972	0.29	0.2830	0.53	0.54956	0.29	0.2590	0.52
	6	0.63224	0.50	0.4327	0.78	0.63296	0.50	0.4130	0.78
	7	0.65141	0.53	0.2719	0.81	0.65121	0.52	0.2691	0.81
	8	0.67873	0.61	0.2400	0.90	0.67872	0.60	0.2116	0.89
	9	0.69556	0.47	0.2517	0.68	0.69533	0.43	0.1809	0.62
	10	0.73085	0.23	0.1289	0.31	0.73100	0.23	0.1316	0.31
	11	0.85578	0.90	0.5915	1.05	0.85657	1.01	0.6829	1.18
	12	1.00073	0.25	0.4474	0.25	1.00045	0.27	0.4226	0.27
pLSCF	1	0.27452	0.18	0.1322	0.67	0.27454	0.19	0.1259	0.67
	2	0.28932	0.12	0.2888	0.42	0.28929	0.12	0.2535	0.41
	3	0.52651	0.24	0.1451	0.46	0.52650	0.24	0.1317	0.46
	4	0.54300	0.31	0.2239	0.57	0.54306	0.32	0.2240	0.59
	5	0.54978	0.37	0.2614	0.67	0.54957	0.36	0.2530	0.66
	6	0.63294	0.37	0.3896	0.59	0.63300	0.39	0.4111	0.61
	7	0.65124	0.60	0.2675	0.92	0.65116	0.60	0.2754	0.93
	8	0.67878	0.92	0.2145	1.36	0.67876	0.91	0.1955	1.34
	9	0.69546	0.38	0.1928	0.54	0.69528	0.37	0.1691	0.53
	10	0.73106	0.33	0.1254	0.45	0.73101	0.34	0.1332	0.46
	11	0.85553	0.81	0.7559	0.95	0.85615	0.83	0.7076	0.97
	12	0.99845	0.57	0.4485	0.57	1.00032	0.59	0.4214	0.59

The identification results obtained for setup 2 before and after the optimization with this esti-

mator are shown in Figs. 5.10, 5.11 and 5.12. In these figures, the starting estimates provided by the **SSI-DATA**, **SSI-COV** and **pLSCF** methods, and their uncertainty bounds are compared to the estimates obtained after 50 iterations of the **pMLE-MM**. As seen in such figures, the main noticeable differences between the starting and optimized estimates are verified on the damping ratios and their corresponding standard deviations, fact that is explained by the higher uncertainty generally involved on the estimation of the damping coefficients by the **LS**-based techniques like **SSI-DATA**, **SSI-COV** and **pLSCF**. The identification results obtained from setup 2 are summarized in Tab. 5.1. Comparing these results, one verifies a clear tendency of the starting estimates obtained with the three different identification techniques to converge to the same results after the optimization with the **pMLE-MM**.

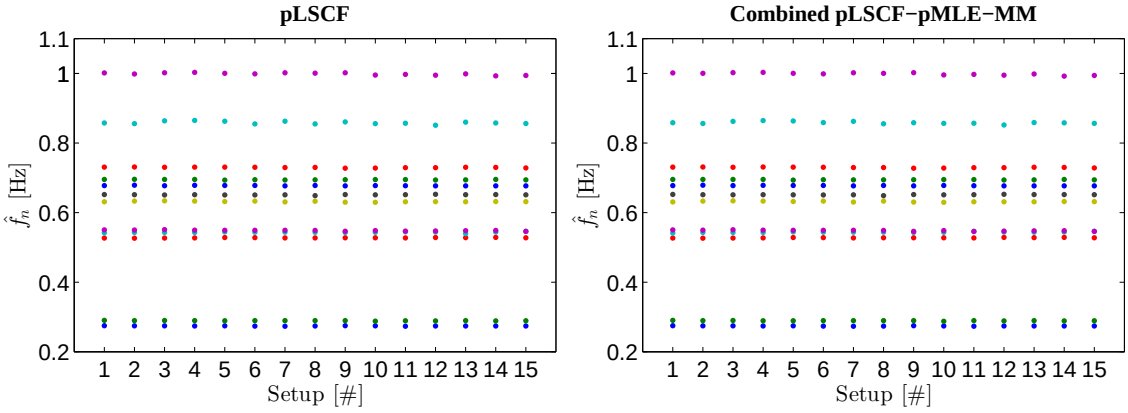

Fig. 5.13 – Variation of the natural frequencies experimentally identified in the range of 0-1 Hz with the **pLSCF** (a) and combined **pLSCF-pMLE-MM** (b) methods over the acquired datasets.

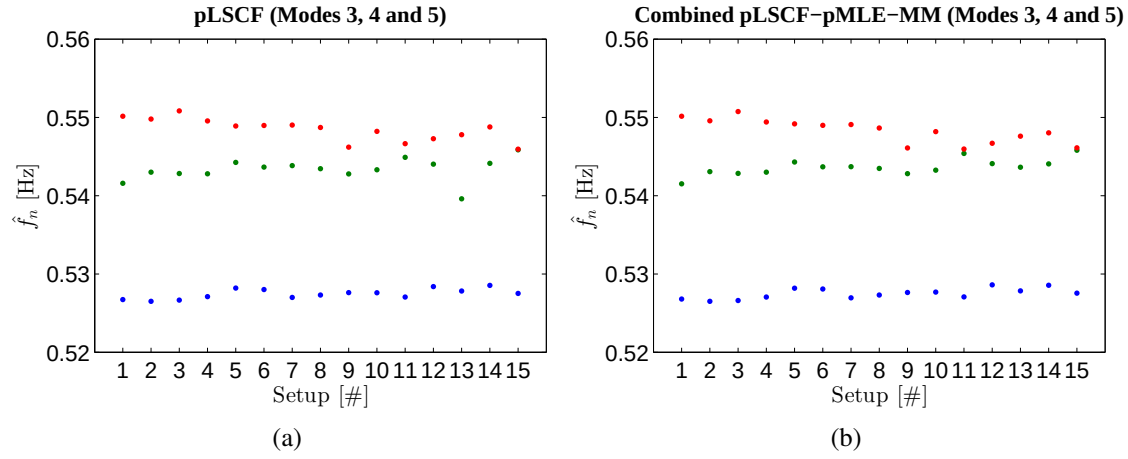

Fig. 5.14 – Detail of the variation of natural frequencies of the 3rd, 4th and 5th modes experimentally identified in the frequency range of 0-1 Hz with the **pLSCF** (a) and combined **pLSCF-pMLE-MM** (b) methods over the acquired datasets.

The procedures and settings previously described to estimate and optimize the modal parameters from data acquired with setup 2 were applied to all datasets collected in the test. In order to avoid figure redundancies, only the overall results obtained with the **pLSCF** method combined with the **pMLE-MM** will be presented, since these results are very similar to those obtained with the **SSI-DATA** and **SSI-COV** methods. The variations of the natural frequencies estimated with the **pLSCF** and the combined **pLSCF-pMLE-MM** in the range of 0-1 Hz over the 15 acquired datasets are shown in Figs. 5.13a and 5.13b. From these figures, one verifies no significant differences in the variation of the natural frequencies.

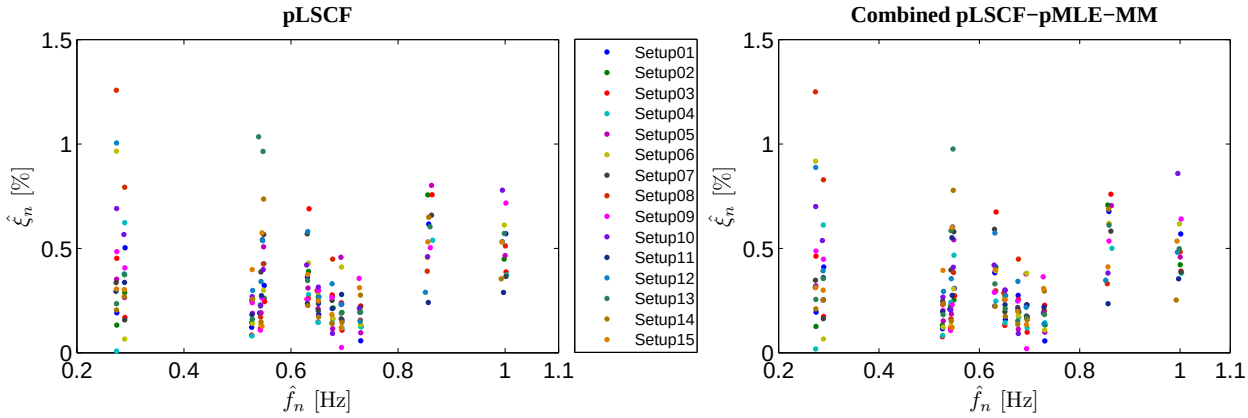

Fig. 5.15 – Variation of the damping coefficients with the natural frequencies identified in the range of 0-1 Hz with the **pLSCF** (a) and the combined **pLSCF-pMLE-MM** (b).

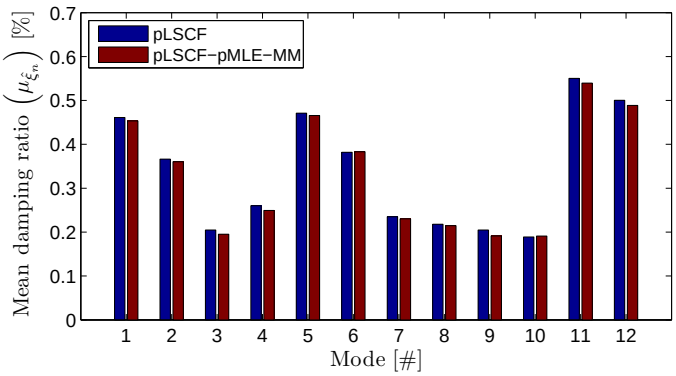

Fig. 5.16 – Variation of the mean values of the damping coefficients identified from the reference responses of the 15 setups with the **pLSCF** and the combined **pLSCF-pMLE-MM** methods.

Inspecting the details of variation of modes 3, 4 and 5 in Figs. 5.14a and 5.14b , however, it is observed that the estimate of the 4th natural frequency provided by the optimization algorithm from dataset 13 is more consistent with the estimates associated with the adjacent datasets. With regard to the damping ratios estimates, comparing the patterns of variation of these parameters

to those of the natural frequencies in Figs. 5.15, it is verified that they exhibit a significant scatter, even after the optimization with the **pMLE-MM**. In Fig. 5.16 is represented the variation of the mean values of the damping coefficients estimated with **pLSCF** and the combined **pLSCF-pMLE-MM** over the 15 setups. Analysing these results, it is verified that a slight reduction on the optimized damping ratio estimates has occurred, which also demonstrates the efficiency of the optimization with the **pMLE-MM** algorithm.

5.5.2. Modal Responses and Their Contributions to the Measured Responses

The approaches described in Sections 3.2.3 and 3.2.4 were used to estimate the modal responses of the Braga Stadium suspension roof and assess their contributions to the outputs measured during the vibration test. In order to evaluate the variation of the modal responses and their respective contributions over the different datasets, only the responses acquired with the reference sensors were taken into account in these analyses (see Fig. 5.3a).

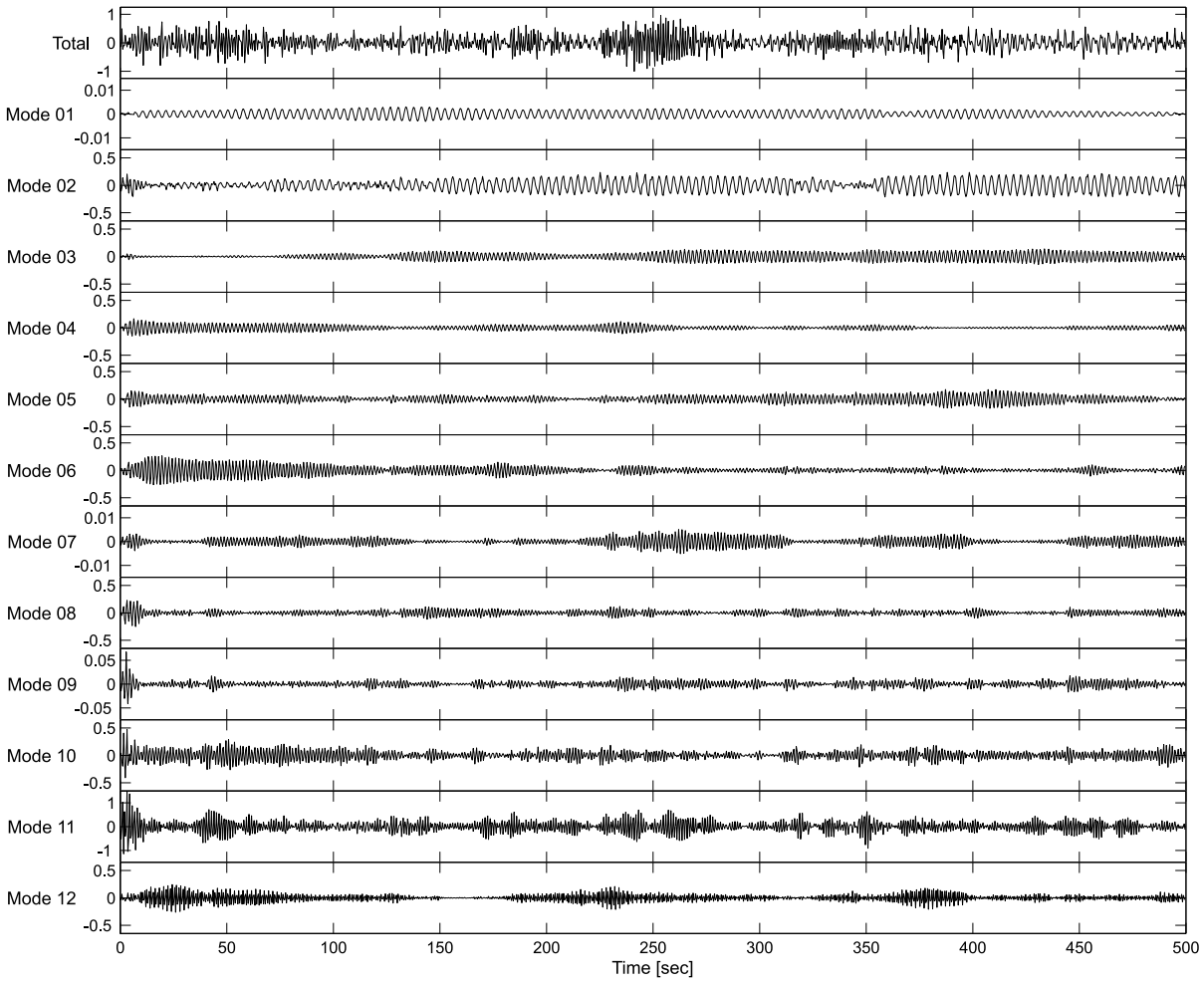

Fig. 5.17 – Contribution of the modal responses of the identified modes to the total response measured by sensor **A3** acquired with setup 2.

The main objective of this analysis was to determine the modes which were more excited by the operational conditions during the test. For this purpose, the estimated responses, $\hat{y}$ and $\hat{y}_m$, and the contributions $\Delta_{\hat{y}}^{(o)}$, $\Delta_{\hat{y}_m}^{(o)}$, $\delta_{\hat{y}}$ and $\delta_{\hat{y}_m}$ were estimated according to the procedures discussed in Sections 3.2.3 and 3.2.4. The poles and observed mode shapes obtained from a model with order $n = 30$ were used to compute these estimates.

Next, the modal responses of each identified mode were sorted out from the responses due to the numerical modes. The modal responses, $\hat{y}_m^{(o)}$, estimated for the output measured by sensor **A3** is represented in Fig. 5.17. Based on these estimates, the modal contributions, $\Delta_{\hat{y}_m}^{(o)}$, were computed to analyse the degree of participation of the identified modes on the outputs measured by each reference sensor used in setup 2. The result of this analysis is shown in Figs 5.18 where it is verified that modes 2, 11 and 12 are those which contributed more to the responses measured with setup 2. The results presented in Fig. 5.18 are synthesized by the global contributions of the modes, $\delta_{\hat{y}_m}$, shown in Fig. 5.19.

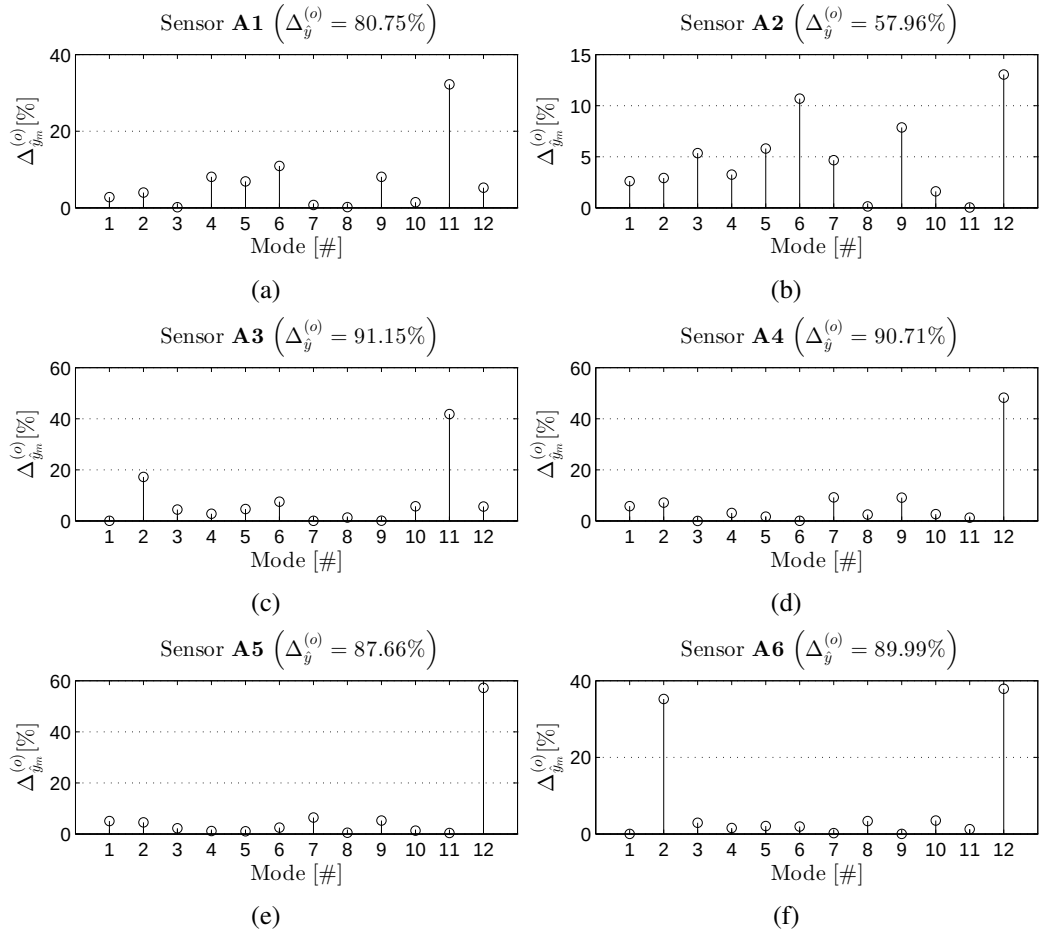

Fig. 5.18 – Modal contributions of each identified mode to the responses measured in setup 2 by sensors **A1**(a), **A2**(b), **A3**(c), **A4**(d), **A5**(e) and **A6**(f).

As seen in this figure, the responses due to modes 2, 11 and 12 contributed more to the responses measured with setup 2. The analysis carried out to assess the modal responses and their contributions to the outputs measured with setup 2 was extended to all setups adopted in the vibration test and the results obtained are synthesized in Fig. 5.19b. This figure shows the variation of the modal contributions, $\delta_{\hat{y}_m}$, over the different setups adopted in the test. Analysing these results, it is observed that modes 1 and 2 played a dominant role on the measured responses, which reveals that these modes were more excited by the operational conditions during the test.

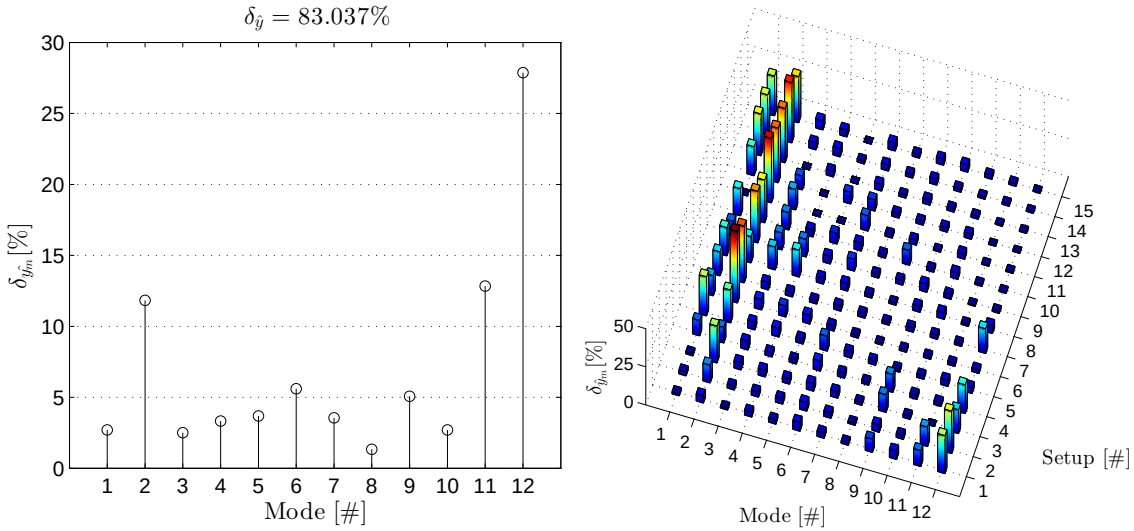

Fig. 5.19 – Modal contribution, $\delta_{\hat{y}_m}$, to the outputs measured with setup 2 (a) and its variation over the identified datasets (b).

5.6. MPE with High Spatial Resolution for the Mode Shapes of Vibration

In this section, the procedures and techniques applied to estimate the global modal parameters of the suspension roof are described. The main goal of this analysis was to estimate the modal parameters of this structure with high spatial resolution for the mode shapes in the frequency range of 0-2 Hz. Since the number of identified modes within the frequency band of 1-2 Hz differed from dataset to dataset, the identification with **PoSER** merging strategy was not possible. Therefore, the **PreGER** and **PoGER** merging strategies discussed in Section 3.8 were used in combination with the **SSI-COV**, **pLSCF** and **pMLE-MM** to estimate the global modal parameters of suspension roof by means of a single stabilization diagram and then obtain their uncertainty bounds. For this purpose, the spectra and covariance matrices of each dataset were estimated by following the approaches described in Sections 2.7.

Aiming at estimating the modal parameters of the suspension roof in the frequency range of 0-2 Hz, two covariance and two spectra matrices were estimated from the vibration raw data

acquired with each setup. The two covariance matrices were estimated with 1024 and 2048 lags, whist the two half spectra matrices were estimated with 512 and 1024 spectral lines by means of the correlogram approach discussed in Section 2.7. In order to minimize the leakage and the influence of the higher covariance lags, an exponential window with a decay rate of 99.99% was used to estimate the spectra matrix. The residual error variances of both spectra matrices were estimated according to the procedure described in Section 5.5.1 by making use of a Hanning window with shape parameter $\gamma = 21$.

The strategies applied to identify the modal properties of the suspension roof together with their confidence intervals with the aforementioned techniques are detailed described in the following sections.

*5.6.1. **pLSCF** with **PreGER** Approach*

In the **OMA** carried out with the combined **PreGER**-**pLSCF** the spectra matrix of each dataset was re-scaled with regard to a common spectra matrix. In this analysis, the spectra matrix of the first dataset was chosen as reference to re-scale the matrices of the other datasets. Once all matrices were re-scaled, they were stacked on the top of each other to construct the global spectra matrix, which was subsequently used as primary data by the **pLSCF** estimator. Next, the identification of the modal parameters was performed in the frequency range of 0-2 Hz in two steps. At first, a stabilization diagram was constructed in the frequency range of 0-1 Hz to identify the vibration modes suited in this frequency band. This first diagram was constructed by identifying models with order n ranging from 2 to 30.

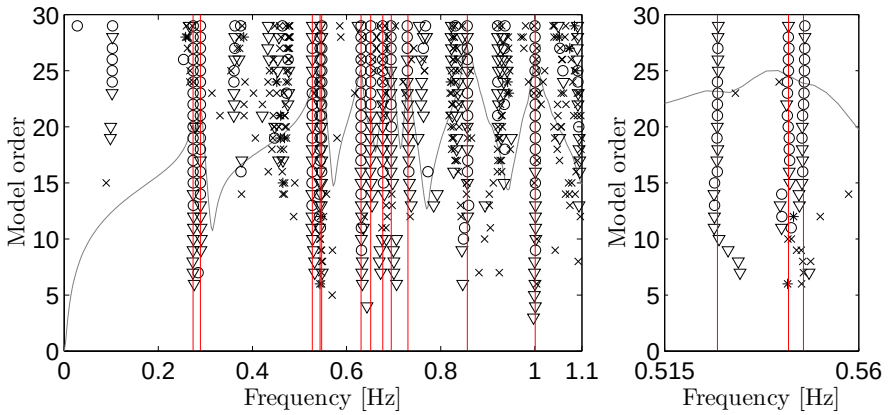

Fig. 5.20 – Stabilization diagram constructed with the **PreGER** and **pLSCF** techniques in the frequency range of 0-1 Hz (a) and detail of the three closed spaced modes concentrated around 0.53 Hz (b). The vertical lines indicate the natural frequencies of the identified vibration modes.

.

Afterwards, the modes with natural frequencies in the band of 1-2 Hz were identified by means

of a second stabilization diagram constructed in the frequency range of 0-2 Hz by identifying models with order n ranging from 2 to 60. The stabilization diagram constructed in range of 0-1 Hz is shown in Fig. 5.20. Although this diagram is not very clear, it was possible to identify the expected 12 vibration modes. These modes were successfully identified with the aid of the automated algorithm described in Section 4.2.1, as indicated by the vertical lines in Figs. 5.20a and 5.20b. Due to the high computational load and memory demanded by the **pMLE-MM** algorithm, only the confidence intervals of the first twelve modes were estimated with one Gauss-Newton iteration of the **pMLE-MM**.

Moreover, due to the few number of modes identified in the band of 1-2 Hz, it was not possible to derive a good starting guess to estimate the confidence intervals for the modal parameters identified in this frequency band.

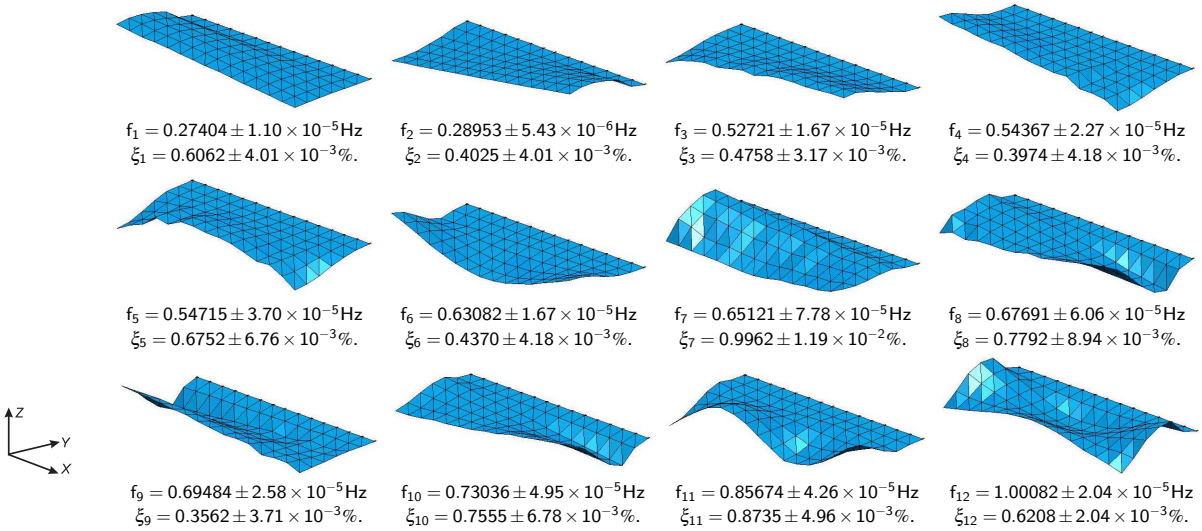

Fig. 5.21 – Natural frequencies, damping coefficients and the corresponding modal configurations of the West slab experimentally identified in the range of 0-1 Hz with the **PreGER** merging strategy and the **pLSCF** identification technique.

The identification results obtained with the combination of the **PreGER** merging strategy and the **pLSCF** method in the frequency range of 0-1 Hz are shown in Fig. 5.21. A total of 24 modes were identified by means of the two stabilization diagrams. The modes identified in the band of 1-2 Hz by means of the second stabilization diagram are presented in Fig. B.1 of APPENDIX B.1.

*5.6.2. **SSI-COV** with **PoGER** approach*

The estimation of the global modal parameters using the **PoGER** strategy and the **SSI-COV** identification technique was performed in the frequency band of 0-2 Hz by following a strategy similar to that used in the identification with the combined **PreGER-pLSCF** described in

Section 5.6.1. Two stabilization diagrams were created: the first used to identify the modal parameters in the frequency range of 0-1 Hz and the second, in the range 0-2 Hz, to estimate the modes with natural frequencies suited within the band of 1-2 Hz. The first diagram was constructed by identifying models with the number of time lags $i = 20$ and model order n ranging from 2 to 40, and the second with $i = 50$ and n ranging from 2 to 120. As shown in Figs. 5.22a and 5.22b, 12 modes were clearly identified with the first diagram. The modes with natural frequencies in the band of 1-2 Hz were identified by means of the second stabilization diagram created in the frequency range of 0-2 Hz.

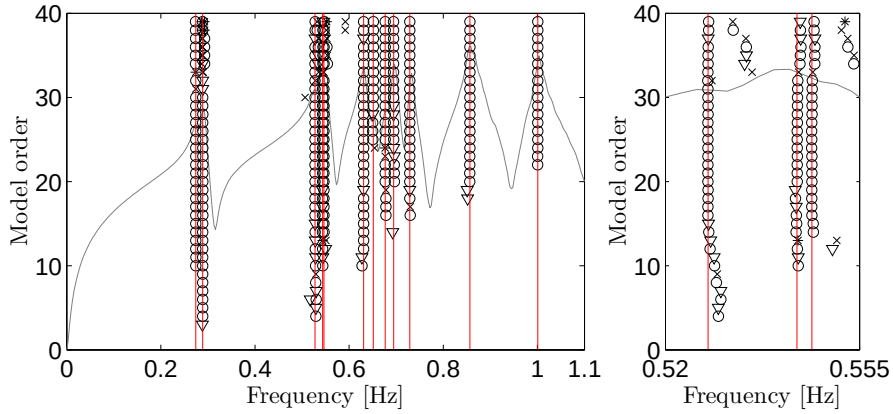

Fig. 5.22 – Stabilization diagram constructed with the **PoGER** and **SSI-COV** techniques in the frequency range of 0-1 Hz (a) and detail of the three closed spaced modes concentrated around 0.53 Hz (b). The vertical lines indicate the natural frequencies of the identified vibration modes.

.

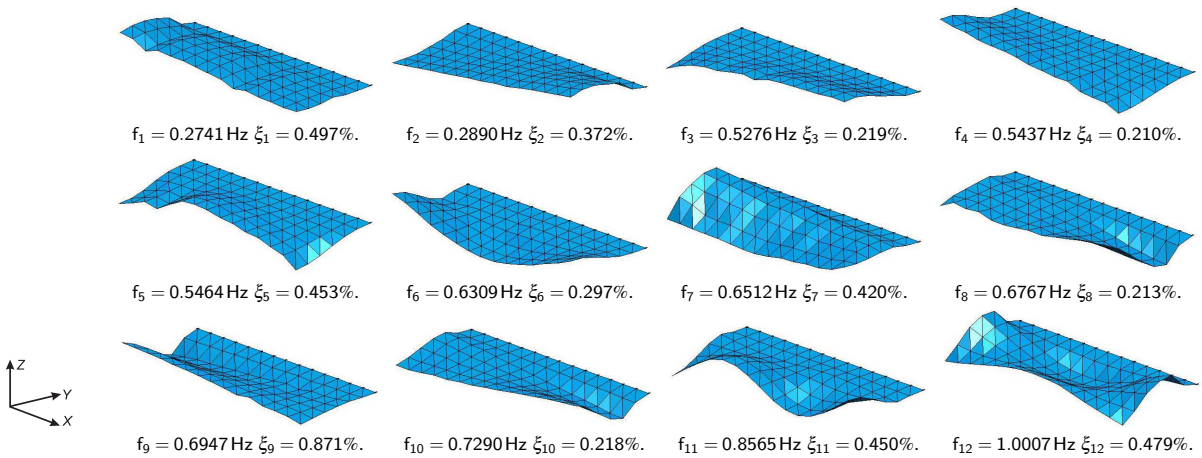

Fig. 5.23 – Natural frequencies, damping coefficients and the corresponding modal configurations of the West slab experimentally identified in the range of 0-1 Hz with the **PoGER** merging strategy and the **SSI-COV** identification technique.

Although several modes were estimated from both stabilization diagrams, only 26 modes presented well defined modal configurations. The first 12 vibration modes identified in the range of 0-1 Hz by means of the first diagram are shown in Fig. 5.23. The modes identified in the frequency range of 1-2 Hz are shown in Fig. B.2 (see APPENDIX B.2). It should mentioned that, given the dimensions of the global spectra matrix computed with the **PoGER** approach, it was not possible to estimate the operational factors by means of the **LSFD** algorithm due to the heavy computational load involved in such operation. Therefore, it was not possible the synthesize the global spectra matrix and the confidence bounds on the modal parameters estimated with the combined **PoGER-SSI-COV** were not computed.

*5.6.3. **pLSCF** with **PoGER** approach*

Similarly to the identification with combined the **PreGER-pLSCF** and **PoGER-SSI-COV**, the **MPE** of the suspension roof with the **PoGER** combined with the **pLSCF** method was carried out by means of two stabilization diagrams: one constructed in the frequency range of 0-1 Hz to identify the first vibration modes and the other to estimate the modes with natural frequencies suited in the range of 1-2 Hz. The first 12 vibration modes were clearly identified by means of the first diagram, as shown in Fig. 5.24a and in the detail of Fig. 5.24b. Several modes were identified in the range of 0-2 Hz, but only 30 modes presented well defined mode shapes.

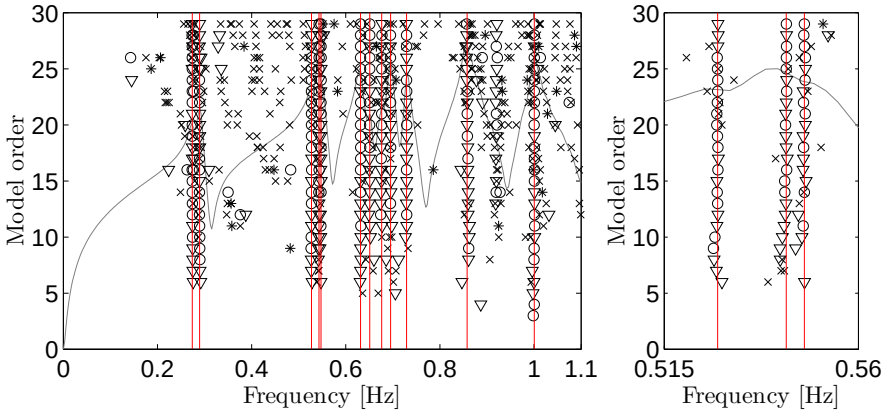

Fig. 5.24 – Stabilization diagram constructed with the **PoGER** and **pLSCF** techniques in the frequency range of 0-1 Hz (a) and detail of the three closed spaced modes concentrated around 0.53 Hz (b). The vertical lines indicate the natural frequencies of the identified vibration modes.

.

The modes with undefined modal configurations might be related to the modes of the slab which are not well excited, to the modes that only involve the slab that was not instrumented and/or to individual modes of the cables. Once identified, these modes were used as starting guess to compute their confidence intervals by means of one Gauss-Newton iteration of the **pMLE-MM**.

The first 12 modes identified in the band of 0-1 Hz by means of the first stabilization diagram together with their confidence intervals are shown in Fig. 5.25. The overall identification results obtained with the **PoGER** merging strategy and the **pLSCF** identification technique in the frequency range of 0-2 Hz are shown in Fig. B.3 (see APPENDIX B.3).

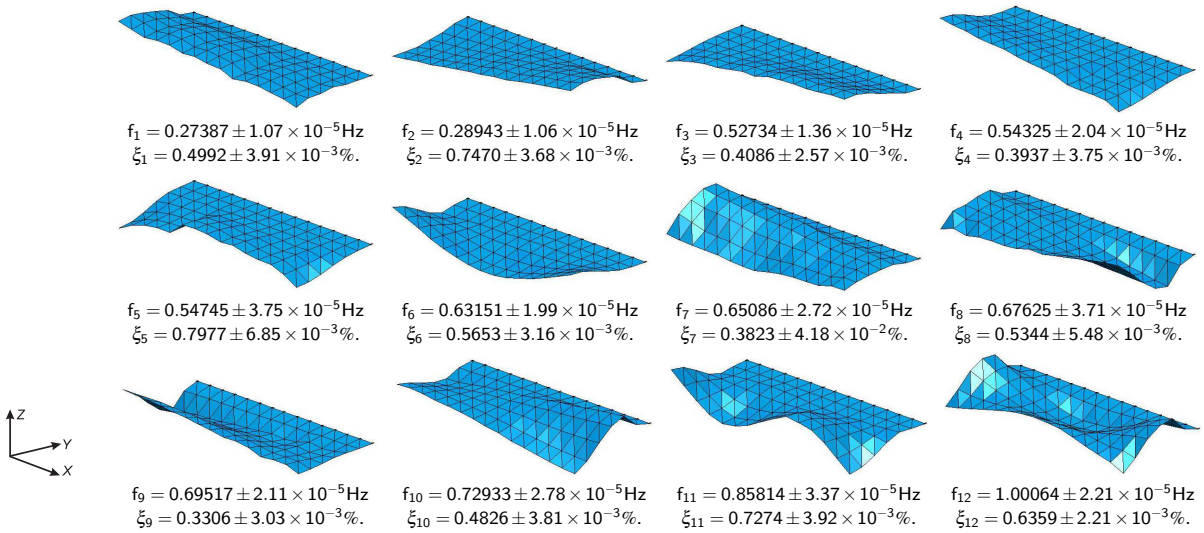

Fig. 5.25 – Natural frequencies, damping coefficients and the corresponding modal configurations of the West slab experimentally identified in the range of 0-1 Hz with the **PoGER** merging strategy and the **pLSCF** identification technique.

5.7. Correlation with FE Results

In order to assess the experimental results obtained with the high spatial resolution **OMA** of the suspension roof presented in previous sections, these results are compared to those obtained by means of a numerical model of the structure. This model is based on three-dimensional finite elements and was developed during the early stage of the structural design of the roof structure, amongst other purposes, to assess its structural behaviour during the construction process (Caetano et al., 2010). Afterwards this model was refined based on the experimental results obtained from the **AVT** of the suspension roof performed in 2007 (Magalhães et al., 2008). The model is formed by a total of 34 cables spaced at 3.75 m intervals, which were idealised as 89 truss elements each. These are linked by shell elements, simulating the slabs, which were only activated after full application of the corresponding weight, and are also connected by transversal truss girders at the ends of the slabs, simulating the lattice structures used to accommodate the floodlights and loudspeakers.

The sliding between the cables and slabs permitted by the materialised connection was simulated by the definition of different layers of nodes for the cables and slabs, which were constrained to identical vertical displacements. The 1% slope along the transversal direction to

drain the rain water was achieved by gradual modification of successive cables lengths. The modal parameters (natural frequencies and mode shapes) were calculated using the tangent stiffness matrix of the global structure after application of permanent loads, which was evaluated taking into account the geometric non-linear characteristics of this cable structure and simulating the progressive application of loads during the construction phase (Magalhães et al., 2009b). The first six mode shapes are represented in Figs. 5.26.

Comparing these results to those obtained from the high spatial **OMA** of the suspension roof represented in Figs. 5.21, 5.23 and 5.25, it is verified a very good correlation for the first vibration modes, both in terms of natural frequencies and modal configurations.

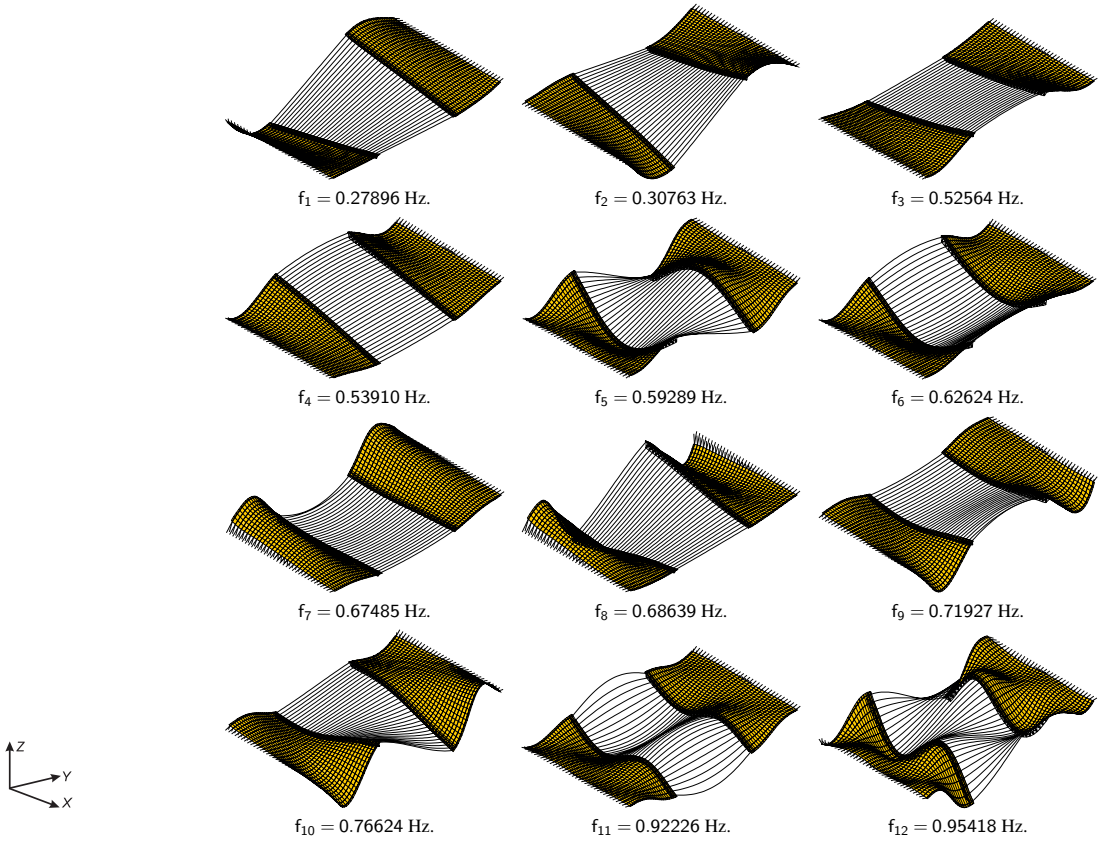

Fig. 5.26 – Natural frequencies and the corresponding modal configurations of the suspension roof provided by the **FE** model.

5.8. GUI-Toolbox For Multi-patch OMA

The identification of the modal parameters of the Braga stadium suspension roof was performed by using a Matlab **GUI**-Toolbox created for multi-patch **OMA** of civil engineering structures, which is called ***O**perational **M**odal **A**nalysis **Studio*** (**OMA Studio**) (Fig. 5.27). Initially designed for multi-patch **OMA** using the **PoSER** approach (Amador, 2007), this **GUI**-Toolbox

was afterwards extended to estimate the modal parameters of civil engineering structures by using the **PreGER** and **PoGER** merging strategies (Amador, 2010).

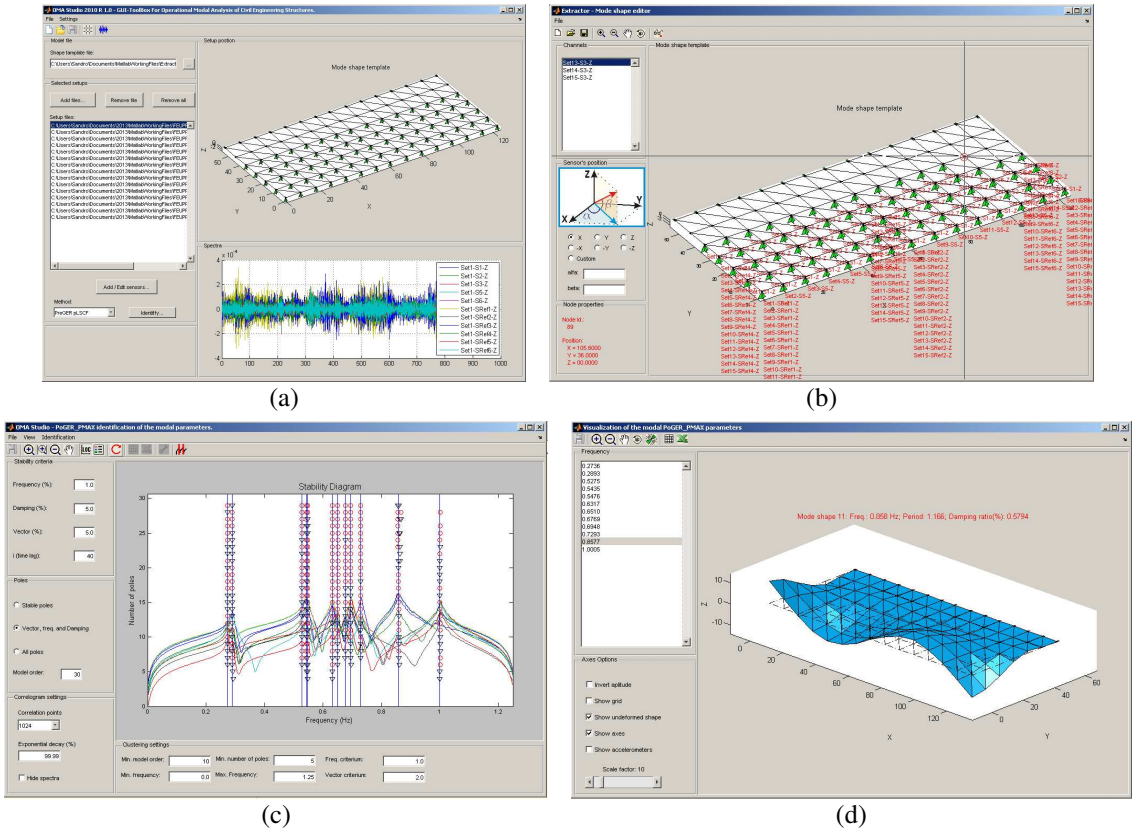

Fig. 5.27 – **OMA** Studio 2010: Main (a) and sensors (b) windows, and identification (c) and results (d) windows.

The **GUI**-Toolbox is basically composed by five main windows:

(i) pre-processing window: intended for analysis and pre-processing of the raw data files collected in the **AVT**s, and for estimation of the covariances and spectra matrices used as primary data by the modal identification methods implemented in the Toolbox;

(ii) settings window: used to configure the criteria, methods and parameters used to track the modal parameters from the raw data files collected in the **AVT**s;

(iii) sensors window: used to define the position and direction of measurement of the sensors used in the **AVT** within a schematic model of the tested structure previously created in order to yield global modal configurations of the identified modes;

(iv) identification window: comprises several tools used to estimate the modal parameters and their confidence intervals from the raw data acquired in vibration tests by means of the identification methods **SSI-COV** and **pLSCF**, and of the combined techniques **MLE-**

CDM-pLSCF-pMLE-MM and **SSI-COV-pMLE-MM**; and

(v) results window: used to visualize the modal parameters experimentally estimated with the identification window.

5.9. Conclusions

The procedures and strategies employed to estimate the modal parameters of the Braga stadium suspension roof with high spatial resolution for the mode shapes of vibration were described in this chapter. Two different acquisition systems and a total of 12 sensors were used to collect the vibration responses of one of the slabs of the roof structure. These sensors were used in a way such that the tested slab could be covered by a minimum number of setups, allowing the test to be conducted in rather shorter time period than with using only the sensors of the seismographs. It turns out, though, that this strategy demanded the employment of additional pre-processing techniques due to the differences in the built-in acquisition characteristics of data acquisition systems, which, in turn, implied a delay in the time series acquired by the seismographs with regard to those collected by the fixed acquisition system.

Despite the differences in acquisition characteristics, a good synchronization of the signals acquired by both systems could be established. Concerning the analysis performed individually on each of the 15 acquired datasets, it was verified that modes 1 and 2 were those which were more excited by the environmental actions during the test. Apart from these conclusions, the analysis of the optimized identification results obtained with the combined techniques **pLSCF-pMLE-MM**, **SSI-DATA-pMLE-MM** and **SSI-COV-pMLE-MM** revealed that, whist no significant variation on the natural frequencies were verified with respect to the starting estimates, a noticeable difference was observed on the damping ratio estimates and their standard deviations. Furthermore, comparing the starting estimates to their optimized counterparts, one verifies a clear tendency of the parameters provided by the three identification techniques to converge to the same results after the optimization with the **pMLE-MM**.

With regard to the multi-patch **OMA**, several modes were clearly identified in the frequency range of 0-2 Hz using **PreGER** and **PoGER** merging approaches combined with the **SSI-COV** and **pLSCF** identification techniques, but not all of them presented well defined modal configurations. The modes with undefined shapes be related to the modes of the slab which are not well excited, to the modes that only involve the slab that was not instrumented or to individual modes of the cables. Despite the heavy computational load demanded to process the global spectra matrix containing the merged setups, the alternative implementation of the **pMLE-MM** introduced in Chapter 3 was successfully applied to compute the confidence intervals for modal parameters estimated with the **pLSCF** identification technique.

Chapter 6

CONTINUOUS MONITORING OF THE BRAGA STADIUM SUSPENSION ROOF

In this Chapter, the techniques discussed in Chapter 4 to estimate the dynamic properties and assess the health condition of civil structures under varying environmental conditions are applied to a real structure. The Braga Stadium Suspension Roof described in Chapter 5 has been continuously monitored by two different monitoring systems with the aim of assessing its health condition and its structural behaviour under operational conditions over the time. The chapter is organized as follows. The motivation of the study is discussed in Section 6.1. In Sections 6.2 and 6.3, the main characteristics of the two monitoring systems installed on the suspension roof are described. The capabilities and results provided by these systems are discussed in Section 6.4 and 6.5. In Section 6.6, the application of a environmental model based on **PCA** to detect structural changes on the roof structure is demonstrated from a practical point of view. Finally, Section 6.7 concludes the chapter.

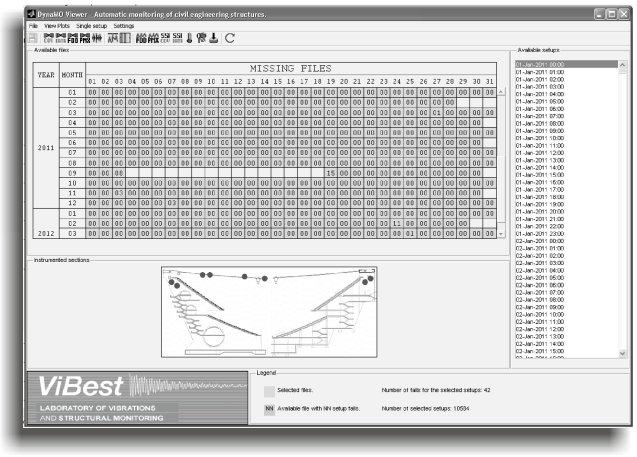

6.1. Introduction

One of the main obstacles to assess the structural condition of civil engineering structures by means of vibration responses relies on the transformation of the data continuously collected by the monitoring systems into relevant information regarding the structural condition of the monitored structures. The most important step to achieve this goal is the implementation of a robust and accurate automated monitoring application to process the raw data files and extract such information from the large amount of data collected over the monitoring period. Considerable efforts have been made towards the development of robust and fully automated monitoring systems as seen, for instance, in Magalhães (2010), Hu (2011) and Reynders et al. (2012). In this context, this chapter discusses the main features of the autonomous monitoring system implemented to assess the structural condition of the suspension roof described in Chapter 5.

Given the particular characteristics of this structure, several studies were carried out to assess its structural behaviour under varying environmental conditions since the beginning of the structural design (Magalhães et al., 2008; Caetano et al., 2010; Magalhães et al., 2009b). The results provided by such studies, as well as those obtained from the numerical simulations and wind tunnel tests performed during the early stage of the structural design have demonstrated that the structure could be susceptible to aero-elastic instabilities (Caetano and Cunha, 2001). These conclusions suggested a strict control of the influence of the environmental factors on the structural behaviour which, in turn, led to the installation of static, dynamic and wind monitoring systems during the construction of the structure (Furtado et al., 2005).

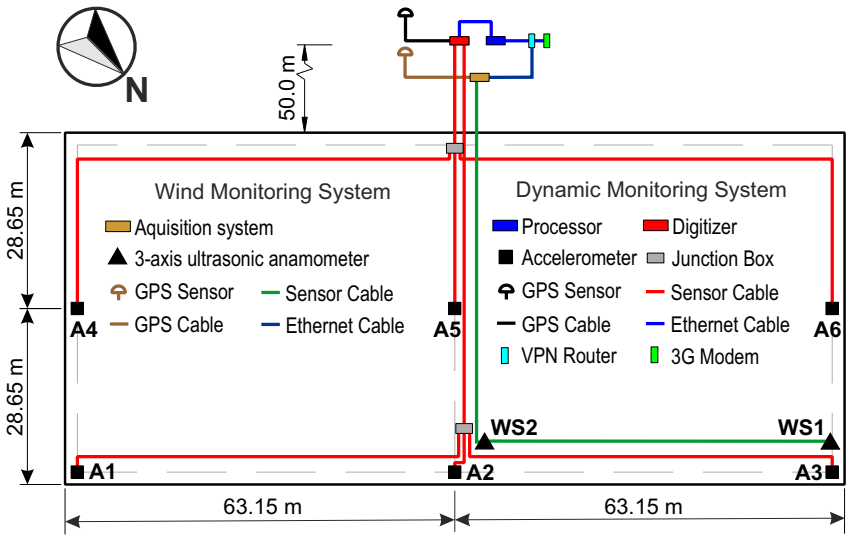

Fig. 6.1 – Location of components of the two monitoring systems installed for wind measurements and acquisition of vertical accelerations on the Braga stadium suspension roof (top view of the west slab).

These systems were essential during the construction, particularly the static monitoring sys-

tem which comprised a series of load cells installed in the cable anchorages, embedded instrumentation of the concrete structure (strain gauges, inclinometers and thermometers) and the instrumentation of the rock massifs and foundations with load cells installed in the anchors to the earth and in-place inclinometers. Aiming at investigating the sensitivity of the structure to ambient effects, **ViBest/FEUP** has installed two complementary monitoring systems on the West slab. One of which consists of a dynamic system installed to measure the acceleration responses (Magalhães et al., 2009b; Amador et al., 2011) and the other of a system to collect wind and temperature data (Martins et al., 2012).

The analysis of the data provided by the latter, in combination with the data from former, provided interesting results regarding the effects of wind on the dynamic properties of the suspension roof (Amador et al., 2012; Martins et al., 2014). The installation of both monitoring systems comprised several elements as described in Fig. 6.1.

6.2. Description of the Dynamic Monitoring System

The permanent dynamic monitoring system consists of a data acquisition system installed on the West slab of the suspension roof and of a autonomous monitoring application which was specially developed to automatically handle the great volume of data available in a permanent dynamic monitoring. One of the key elements the permanent monitoring system is the autonomous monitoring application which was initially developed in Matlab® platform and, afterwards converted into a java® platform application (Oracle, 2012), fact that is justified by the well-known robustness and flexibility on performing database and remote operations of this platform. The monitoring system, shown in Fig. 6.2 (Magalhães, 2010) is composed by a digitizer, a robust field processor and six force balance accelerometers with the following characteristics: dynamic range of 145 dB, frequency range from DC to 200 Hz, user-selectable measuring range that can vary from +/-0.25 to +/-4 g and extremely low levels of noise.

In the dynamic monitoring of the roof structure, the measuring range was fixed to +/-0.25 g, aiming at optimising the sensitivity (80 V/g for the used configuration) of the sensors and consequently reduce the effect of the noise introduced by the measuring chain, while keeping a conservative acceleration range. The digitizers allow the connection of six dynamic channels and 4 auxiliary static channels. This digitizer comprises 4 data ports that permit simultaneous real-time telemetry of the acquired data to a central site and transference to local recording units, and are equipped with a 24-bit analogue-to-digital converter, to take profit from the large dynamic range of the accelerometers. The field processor is a rugged, ultra-low power, multipurpose processor designed for field deployments in extreme operating conditions.

This field processor gathers the data packets produced by the digitizer to create text files with the

acceleration time series of all sensors. In order to allow for the creation of a local data backup, the used unit has a storage capacity of 15 Gbytes, materialized by Compact Flash cards, which can be accessible from **FEUP** by **F**ile **T**ransfer **P**rotocol (**FTP**) connection (Magalhães et al., 2009b). The system is set to acquire the vertical acceleration at six points on the West slab with a sampling frequency of 20 Hz (see Fig. 6.1).

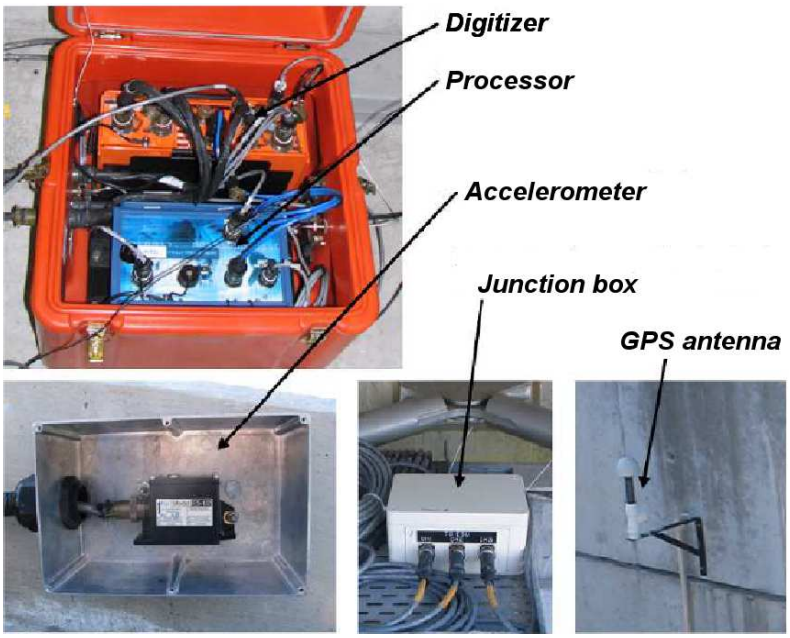

Fig. 6.2 – Main components of the acquisition system installed to measure and collect the vertical acceleration of the Braga stadium suspension roof.

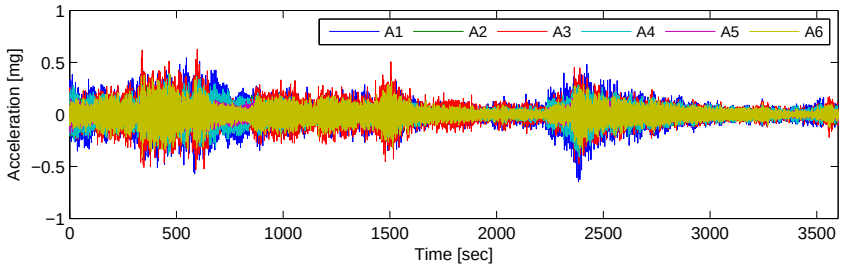

Fig. 6.3 – Typical time series acquired on 24/01/2011 at 16:00.

Once it is configured, the acquisition system is capable of continuously measuring the vertical accelerations with no further user interaction. In the present application, the system is programmed to gather the measured data and save it in text files containing one hour length acceleration time series, which corresponds to 72.000 measured samples. Once each of these text files are completed, they are sent to **ViBest/FEUP**, where they are automatically processed and stored in a database previously created for the monitored structure (Magalhães et al.,

2009b; Amador, 2009). A typical acceleration time series obtained with this system is shown in Fig. 6.3.

6.2.1. Automated Tracking of the Dynamic Properties of the Roof Structure

Due to the large amount of data involved in the continuous monitoring of the roof structure, an autonomous monitoring application was developed to automatically process and extract relevant information from the raw data files. The automatic identification of the modal parameters is one of the most important tasks executed by this autonomous application. In the continuous monitoring of the roof structure, the automatic identification of the modal parameters is accomplished by following the approach discussed in Chapter 4.

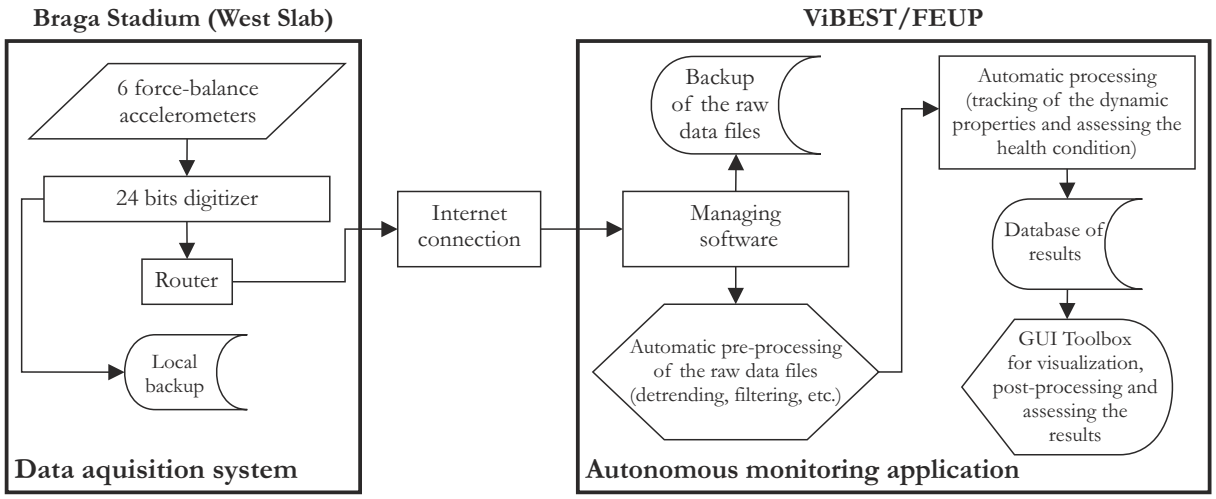

Fig. 6.4 – Data flow of the dynamic monitoring system installed on the West slab of the Braga stadium suspension roof.

The whole process for transformation of the measured responses into relevant information regarding the evolution of the structural condition of the suspension roof is depicted in Fig. 6.4. The autonomous monitoring package is composed by several algorithms that are organized in three main applications: (i) the data managing software, which can be configured to establish a remote connection through the internet with the data acquisition system, transfer the available raw data files, check their validity, store these files in a backup hard disk and pre-process them in order to remove the trends, filter the signals according to a specified cutoff frequency, etc.; (ii) the automatic processing software, which is actually responsible for transforming the acceleration responses acquired by the data acquisition system into relevant information regarding the health condition of the monitored structure; and (iii) the visualization software developed as **GUI**-Toolbox in Matlab® platform to allow the visualization and analysis of the results automatically tracked by the processing software.

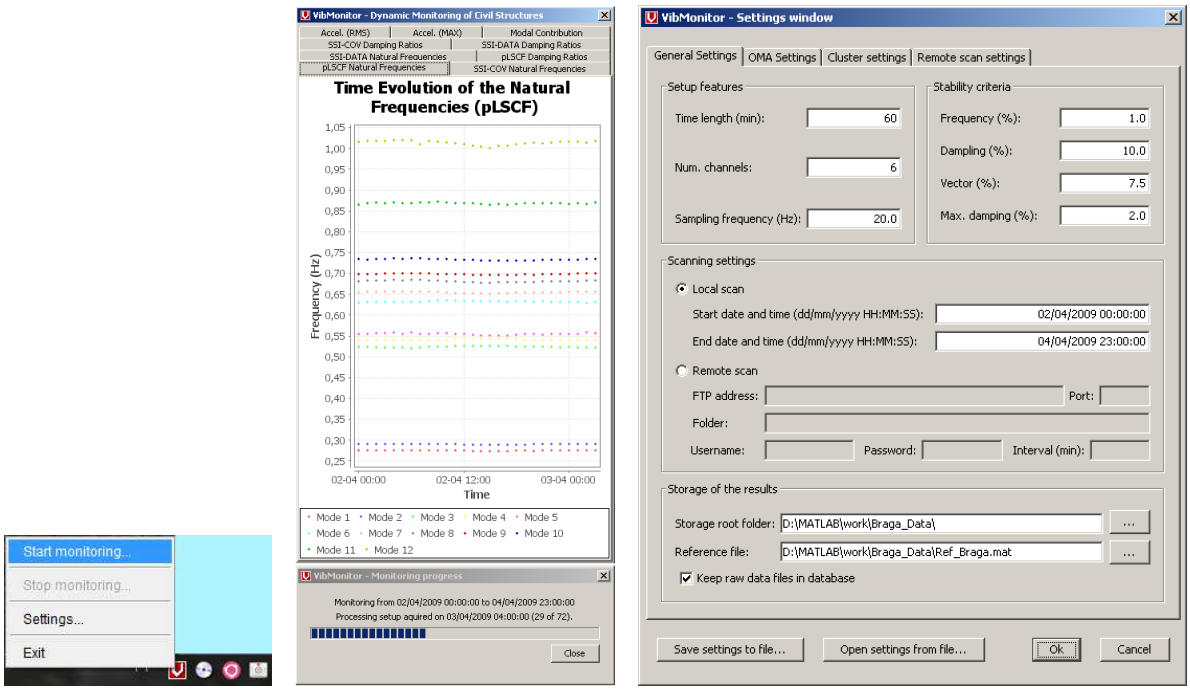

(a) (b) (c)

Fig. 6.5 – Autonomous monitoring application developed in Java® platform: main pop-up menu of the tray application (a); window showing the continuously updated time evolution of the natural frequencies (b); and settings window (c).

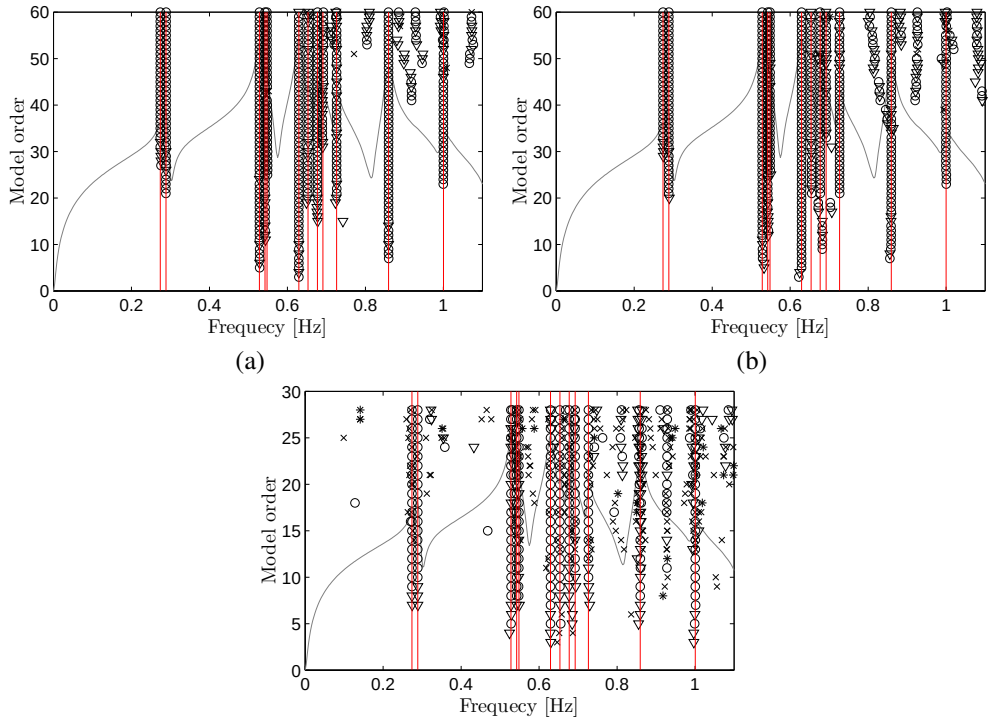

(a) (b)

(c)

Fig. 6.6 – Automated identification of the stabilization diagrams constructed with the **SSI-DATA** (a), **SSI-COV** (b) and **pLSCF** (c) techniques from the time series acquired on 24/06/2011 at 22:00.

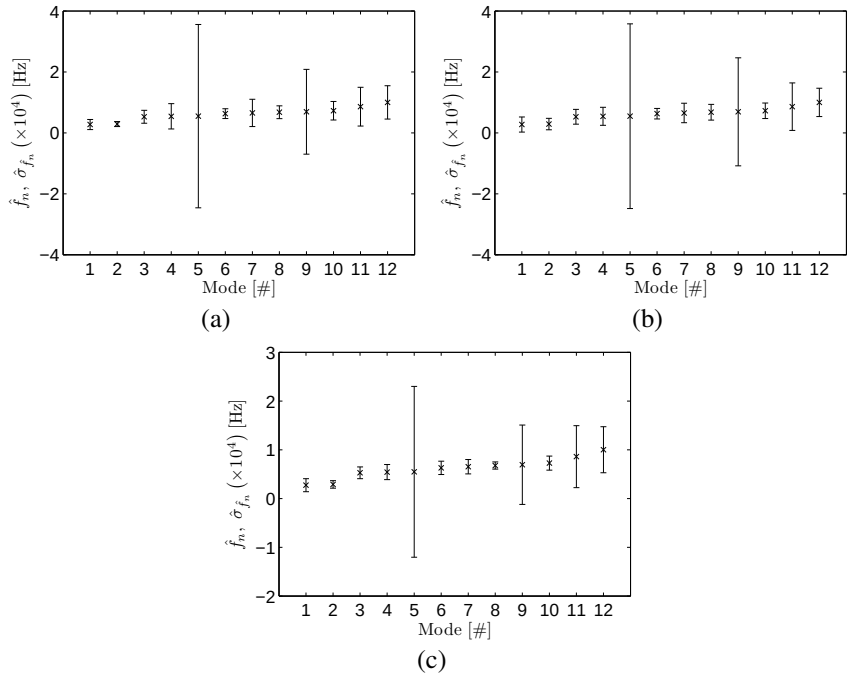

Fig. 6.7 – Automated estimation of the confidence intervals of the natural frequencies identified with the **SSI-DATA** (a), **SSI-COV** (b) and **pLSCF** (c) techniques from the time series acquired on 24/06/2011 at 22:00. The standard deviations are multiplied by factor of 10^4 to improve their visibility within the figure.

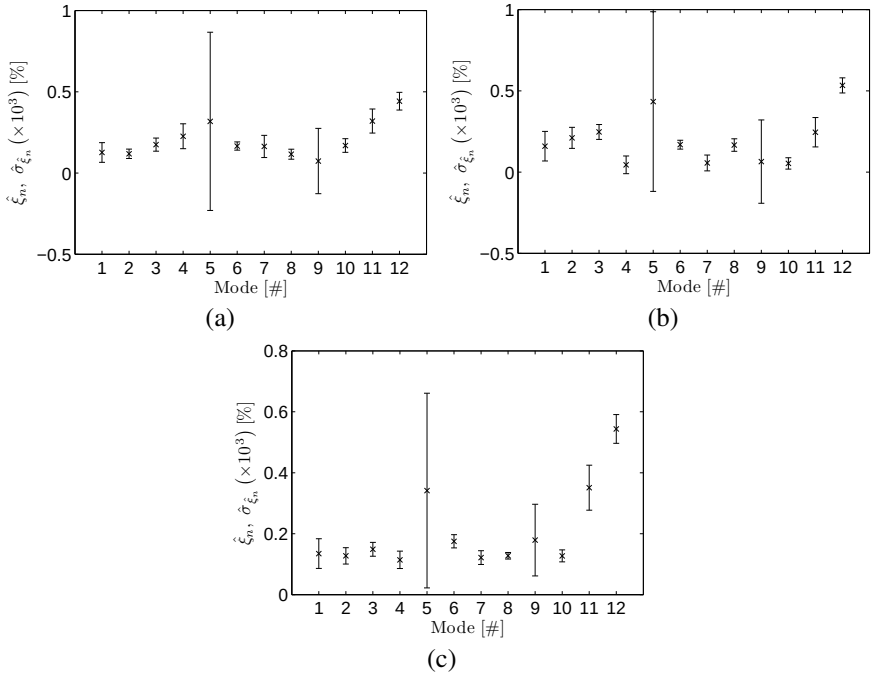

Fig. 6.8 – Automated estimation of the confidence intervals of the damping ratios identified with the **SSI-DATA** (a), **SSI-COV** (b) and **pLSCF** (c) techniques from the time series acquired on 24/06/2011 at 22:00. The standard deviations are multiplied by a factor of 10^3 improve their visibility within the figure.

The acquisition and data processing are executed by the same software in the latest release

of the autonomous monitoring application illustrated in Figure 6.5. This application is called *VibMonitor* and consists of a software that was designed to run as a tray application on the windows operating system and it was developed to consume as minimum processing resources of the hosting computer as possible. One of the main advantages of tray applications like this is that it runs in background, allowing the user of the host computer to perform other tasks while the application runs minimized in the tray. The software is set to automatically identify the modal properties of the monitored structures by means of four state-of-the-art (**MPE**) techniques, namely, the **SSI-COV**, **SSI-DATA** and **pLSCF** methods. These techniques are used in combination with the **pMLE-MM** to yield the confidence intervals of their estimates.

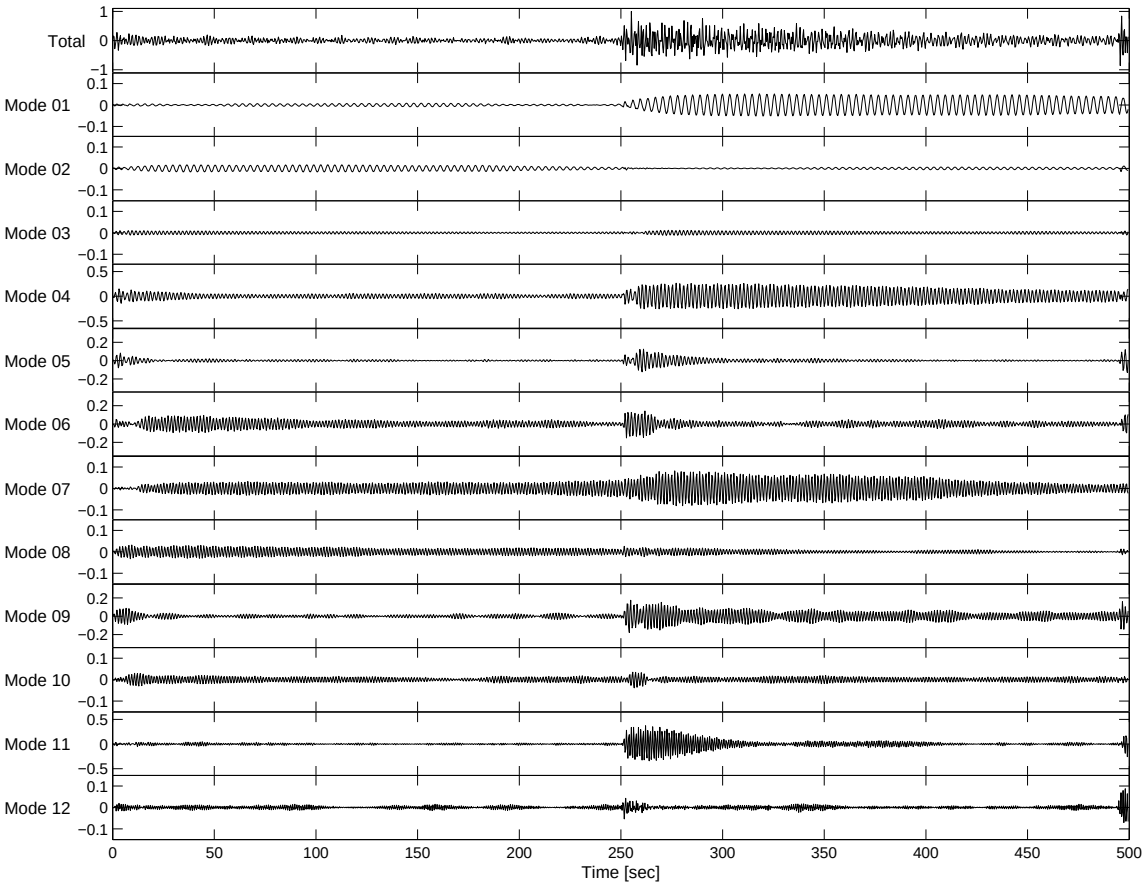

Fig. 6.9 – Automated estimation of the modal responses, $\hat{y}_m$, from the output measured on 24/06/2011 at 22:00 by sensor **A1**.

In the case of the permanent monitoring of the Braga Stadium suspension roof, the autonomous monitoring application can be set to automatically establish a connection every hour with the router available in the data acquisition system, check whether there are new acquired raw data files, transfer and process and extract the modal properties of latest raw data files, and, finally, save the obtained results in the database. Once these properties are stored in the database, they can be visualized by using the **GUI**-Toolbox that will be described in Section 6.2.2. As a result

of the autonomous processing and modal identification of the raw data files, a set of dynamic properties is obtained, i.e., the modal parameters together with their confidence intervals, the maximum and **R**oot **M**ean **S**quare (**RMS**) values of the measured accelerations, and the modal responses and their corresponding contributions to the measured outputs. The identification of the modal parameters is basically performed in three steps. Firstly, stabilisation diagrams are constructed with the **SSI-DATA**, **SSI-COV** and **pLSCF** methods. Next, the poles of these diagrams are used as raw data by the hierarchical cluster algorithm discussed in Chapter 4 which automatically selects the physical poles and compute their mean modal parameters.

Finally, these parameters are used as starting guess by the **pMLE-MM** to estimate their uncertainty intervals, which is performed by using one iteration of the Gauss-Newton algorithm. This three-step automated procedure is illustrated in Fig. 6.6, 6.7 and 6.8. These figures illustrate the automatic identification of the modal properties from the poles of the stabilisation diagrams constructed with the **SSI-DATA**, **SSI-COV** and **pLSCF** methods from the dataset acquired on 24/06/2011 at 22:00. The modal responses estimated for the output measured by sensor **A1** and their contributions are illustrated in Figs. 6.9 and 6.10.

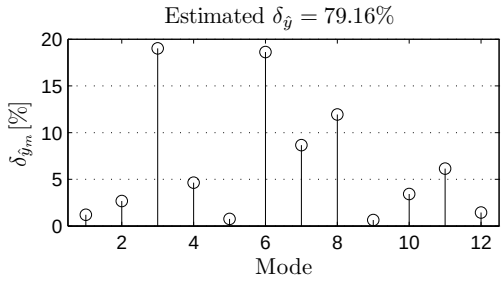

Fig. 6.10 – Automated estimation of the modal contributions to the outputs acquired on 24/06/2011 at 22:00.

6.2.2. Application for Visualization and Analysis of the Results

Since a large amount of data is collected in a long term monitoring, the analysis and management of the results obtained over the time can demand a long time and hard work (Maeck, 2003; Magalhães, 2010), specially if this analysis is carried out using algorithms executed in command line of the Matlab® platform. These difficulties have motivated the development a **GUI**-Toolbox intended to assist the analysts in managing, handling and analysing the large volume of data and results obtained over the course of a continuous dynamic monitoring, allowing them to perform several types of analysis and, therefore, extract as much information as possible regarding the structural and dynamical behaviour of the monitored structures. One of the main advantages of the **GUI**-Toolboxes like this is that the analysis of the monitoring results is performed by basically clicking on the elements of the graphical interface (Amador, 2009).

The **GUI**-Toolbox is basically composed by the main window (main program), shown in Fig. 6.11, and 13 independent auxiliary windows specially designed to manage and allow for the visualization of a specific dynamic property available in the database. Once a time period is selected using the table available in the main window, the data files within the selected period are displayed in the list box located at the right hand side of this window so that the user can access any of the secondary windows by means the tool bar suited in the upper part of the main window and perform the desired analysis. The main available secondary windows in the **GUI**-Toobox are shown in the command flow illustrated in Fig. 6.12.

The functionality of these secondary windows are basically divided in two groups according to type of analysis performed, which can be either a single or a multiple dataset analysis. The analysis carried out in the first group comprises, for instance, the visualization of the modal parameters together with their uncertainty bounds and of the responses of the identified modes and their corresponding contributions to the measured responses. The second group permits, for example, to analyse the time variation of the modal parameters and their uncertainty bounds over the selected period, the variation the of contributions of the identified modes to the measured responses and to analyse the variation of the **RMS** and maxima values of the measured acceleration within the selected period. This second group of analysis also comprises the secondary windows used to assess the correlations among the modal properties and the cross correlations with the results provided by other monitoring systems as, for instance, wind velocity and direction, temperature and cable forces (measured by load cell sensors).

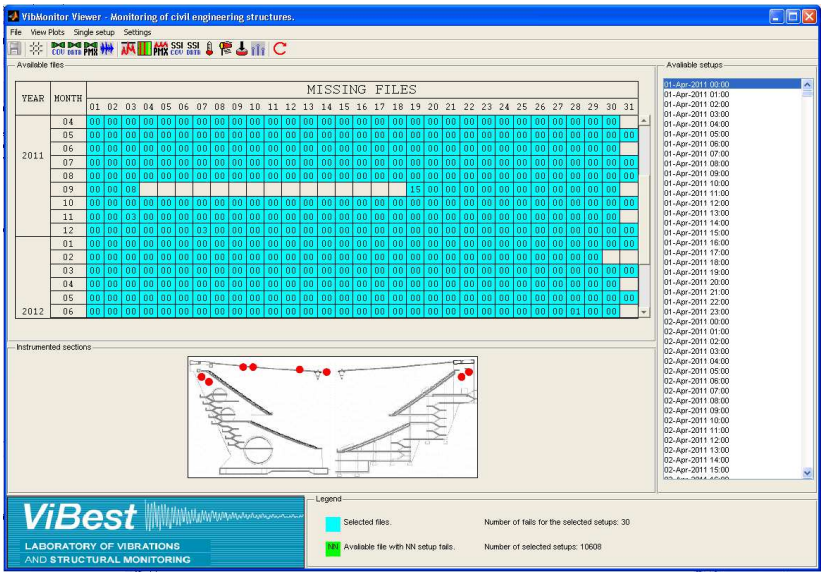

Fig. 6.11 – Overview of the database containing the datasets automatically processed by the autonomous application..

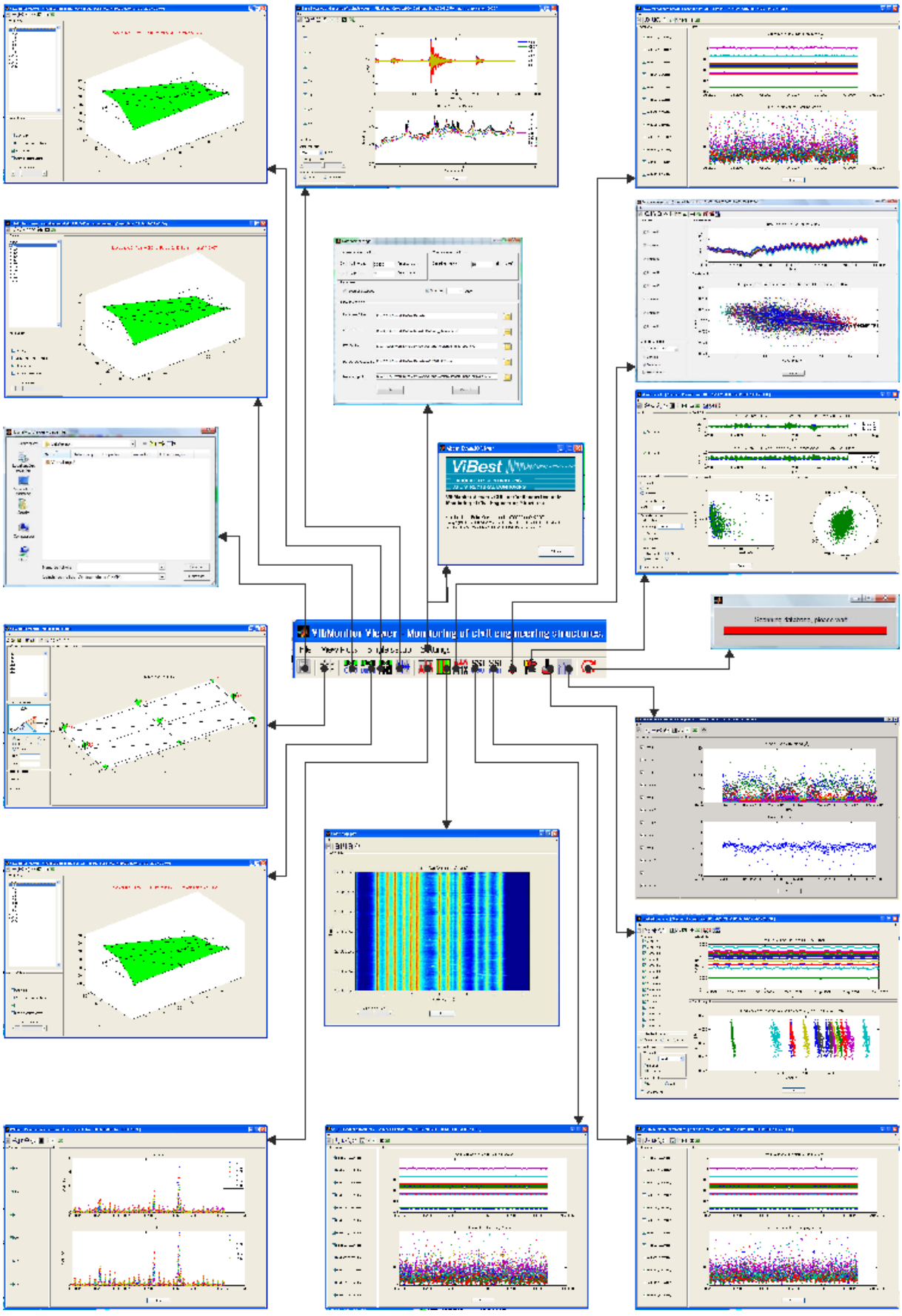

Fig. 6.12 – Command flow of the **GUI**-Toolbox developed to manage, visualize and analyse the results obtained during the permanent dynamic monitoring of civil engineering structures.

6.3. Wind Monitoring System

This system is completely independent of the dynamic monitoring system described in Section 6.2 and was initially installed to characterize a wind model based on the observations collected by the wind monitoring system, and afterwards, it was used to assess the correlations between dynamic responses and the wind actions. It was installed on the West slab of the suspension roof and started to acquire the wind data at the beginning of December, 2011. It comprehends two three-dimensional ultrasonic anemometers which allow for the characterization of the wind through time averaged statistics of speed, direction and incidence angles, spectra and co-spectra of velocity components, and ambient temperature. These quantities were subsequently used to assess the influence of the wind loading on the dynamic behaviour of the roof structure.

According to the scheme and picture presented in Fig. 6.1, the two anemometers, denoted as **W**ind **S**ensor **1** (**WS1**) and **W**ind **S**ensor **2** (**WS2**), were placed on the top of the West slab, both along its longer inner edge (see Fig. 6.1). The anemometer **WS1** was installed in the northernmost point, and **WS2** in the middle of the longer edge of the slab (Martins et al., 2012, 2014), just next to accelerometers **A3** and **A2** of the dynamic monitoring system. Both sensors are supported by masts that are 3 m high in order to reduce the influence of the structure in the flow. As the wind observation is made at just one level, the wind sensors were mounted on top of the masts to avoid direct mast "shadowing" (Kaimal and Finnigan, 1994). In this application, the wind system is set to acquired the wind measurements at a sampling rate of 10 Hz in order to efficiently measure the turbulent component of the wind flow (Kaimal and Finnigan, 1994).

6.4. Monitoring Results

6.4.1. Characterisation of the Wind Measurements

The three-dimensional ultrasonic anemometers were configured to record the wind speed as three wind speed components, each along one the directions of the sonic's coorinate system defined by the orthogonal axes x, y and z. Since these orthogonal axes do not coincide with the directions of interest, a coordinate rotation was applied in order to obtain the mean wind speed, direction and elevation angles, as well as the turbulent component time series in longitudinal, lateral and vertical directions. In this study, a double coordinate rotation scheme was used. This coordinate transformation is detailed described, for instance, in Kaimal and Finnigan (1994) and Wilczak et al. (2001). According to this approach, the block time series are initially averaged in sonic's coordinate system (x, y, z), yielding a vector containing the components of the mean wind speed $\hat{u}_m$, $\hat{v}_m$ and $\hat{w}_m$.

Afterwards this vector is transformed by making use of the double rotation method. The goal of this method is to impose $\bar{v} = \bar{w} = 0$, so that the total velocity vector is expressed in terms of a streamline mean speed plus three orthogonal turbulent speed components $((\bar{U} + u'), v', w')$ of a mean direction angle (γ) and of a mean elevation angle (β). This approach was applied to the wind measurements registered by the two sonic anemometers installed on the suspension roof.

Mean wind speed, direction and elevation angles

The analysis herein presented corresponds to approximately eight months of continuous measurements, between mid-December 2011 and the first days of August 2012. Fig. 6.13 shows the variation of the 10-min mean wind speed measured by the two sonic anemometers since the installation of the wind measurement system. From this representation, one can verify that the evolutions of the mean wind speeds provided by both sensors over the measurement time frame are generally coherent with the values measured by **WS1** being commonly higher. The observed mean wind speed shows maximum values of 9.37 m/s and 7.22 m/s for ultrasonic anemometers **WS1** and **WS2**, respectively.

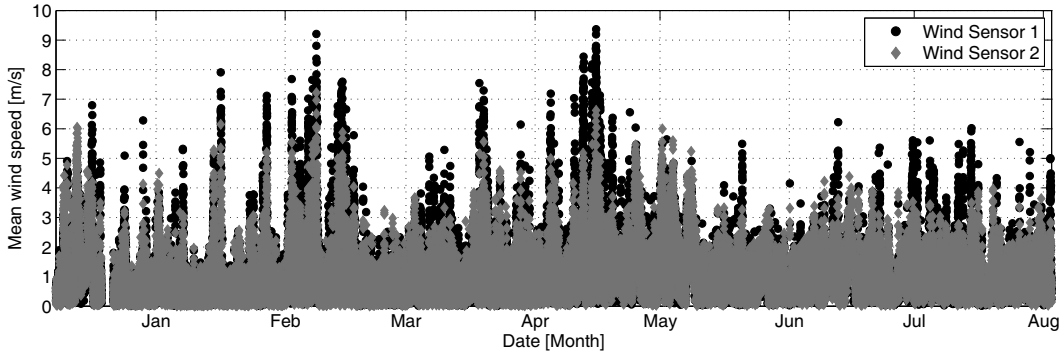

Fig. 6.13 – Time-history of 10-min mean wind speed measured by the two sonic anemometers over the period of 8 months.

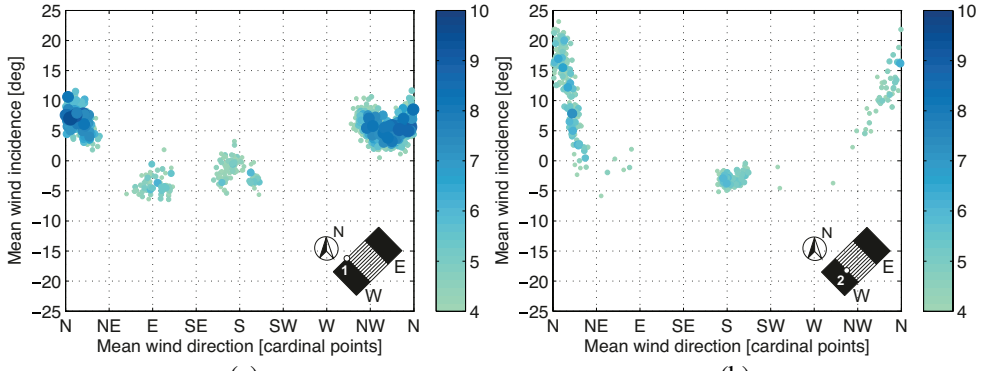

Fig. 6.14 – Distribution of 10-min mean wind speed with direction and incidence angles measured by sonic anemometers **WS1** (a) and **WS2** (b).

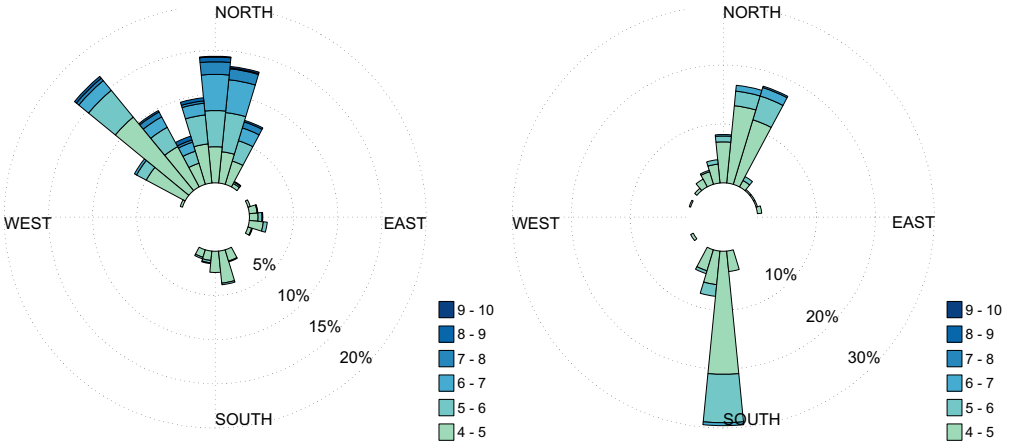

(a) (b)

Fig. 6.15 – Wind rose histograms of 10-min mean speed and corresponding direction for sonic anemometers **WS1** (a) and **WS2** (b).

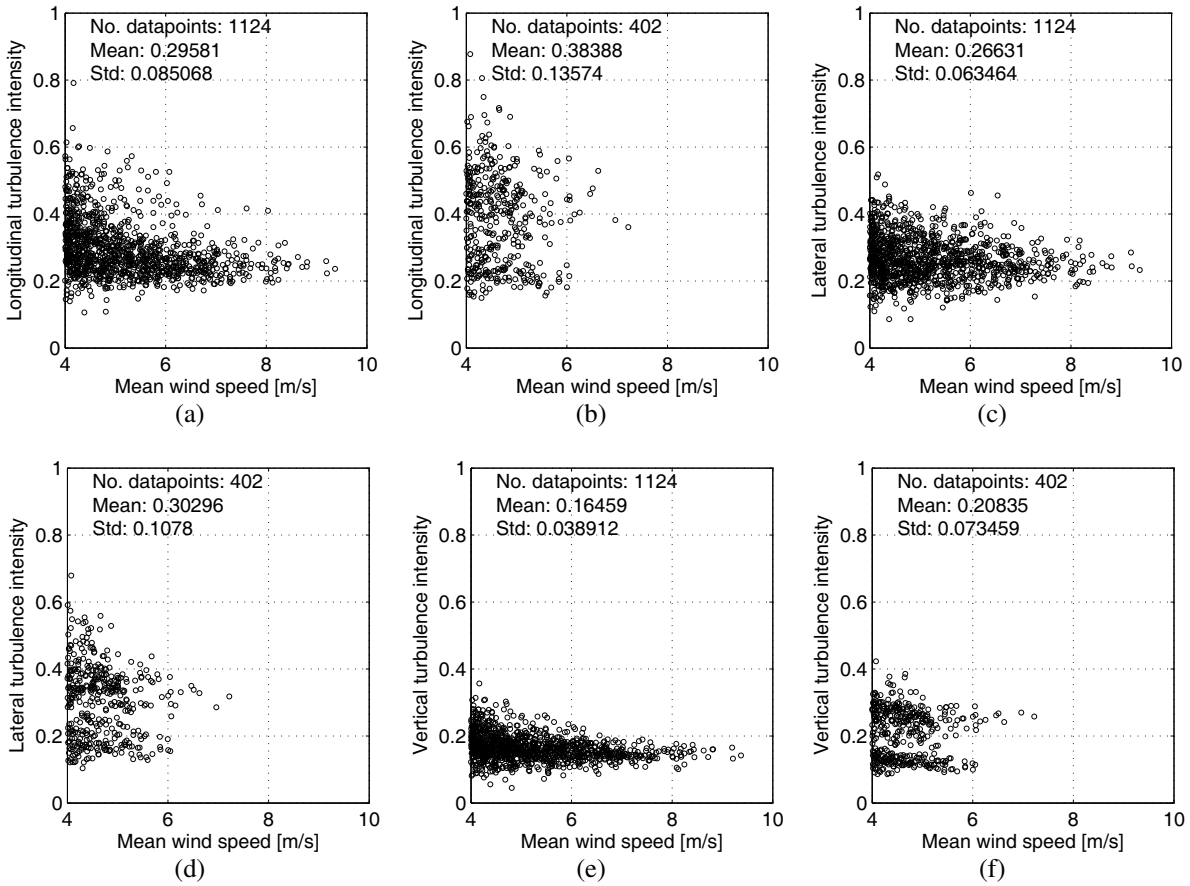

Fig. 6.16 – Variation of the turbulence intensity with the mean wind direction: **WS1** Longitudinal I_u (a); **WS1** Lateral I_v (b); **WS1** Vertical I_w (c); **WS2** Longitudinal I_u (d); **WS2** Lateral I_v (e); and **WS2** Vertical I_w (f).

Nevertheless, it is possible to conclude that the mean wind speed measured is generally low,

with most of the measurements below 4 m/s. Henceforward just the data points with a significant wind speed will be considered and all measurements with 10-min mean wind speed below 4 m/s will be discarded.

Turbulence intensity

Turbulence intensity describes the characteristics of the fluctuating wind speed. The longitudinal, u, lateral, v, and vertical, w, turbulence intensities can be determined by the following equations:

$$I_u = \frac{\sigma_u}{\bar{U}}, \quad I_v = \frac{\sigma_v}{\bar{U}}, \quad I_w = \frac{\sigma_w}{\bar{U}} \tag{6.1}$$

where σ_u, σ_v and σ_w are the standard deviations or the **RMS** values of each fluctuating velocity component and U is the wind mean speed for the same time period. In this study, the same 10-minute period used before was adopted for the calculation of these parameters. Fig. 6.16 shows the variations of the longitudinal, lateral and vertical turbulence intensities as a function of the mean wind speed, calculated independently of directions and incidence angles, for sensors **WS1** and **WS2**. A general trend for $I_u > I_v > I_w$ is noticed across both sensors data. The three components of turbulence intensity measured by sonic anemometer **WS1** represented in Figs. 6.16a-6.16c reveal a standard pattern of variation of the turbulence intensities with wind speed.

In these figures, it is verified a clear trend of the turbulence intensity to decrease and reduce its deviation for higher mean wind speeds. The mean values found for the longitudinal, lateral and vertical turbulence intensities were 0.296, 0.266 and 0.165, respectively, which result in a relative ratio of σ_u:σ_v:σ_w = 1:0.900:0.556. The variation of the turbulence intensities registered by sonic anemometer **WS2**, on the other hand, shows a very scattered distribution, as seen in Figs. 6.16d-6.16f. Despite this scattered behaviour, the same downward trend can be identified for the three turbulence intensities components (σ_u, σ_v, σ_w), although less pronounced.

The ratios between the averaged values of the turbulence intensity in the three directions for this sensor are σ_u:σ_v:σ_w = 1:0.789:0.543. The σ_w/σ_u values are very close to the ratio proposed by Solari and Piccardo (2001) of $\mathbf{E}[\sigma_w/\sigma_u] = 0.5$. The ratio σ_w/σ_u obtained for **WS1** differs from the ration proposed by this author of $\mathbf{E}[\sigma_w/\sigma_u]$ = 0.75, but is well approximated by **WS2**. The turbulence intensity is simply related to the surface roughness (Holmes, 2001), and therefore, to the wind incoming direction. The representation of the turbulence intensities from all incoming directions, in Fig. 6.16, reveals a wide spread distribution of these values, especially in the case of sensor **WS2**. The variation of the longitudinal, lateral and vertical

turbulence intensities as a function of the 10-min mean wind direction, and the respective mean wind speed are represented in Figs. 6.17. From these figures, characteristic turbulence intensities can be identified by direction and a consistent evolution through direction is perceived.

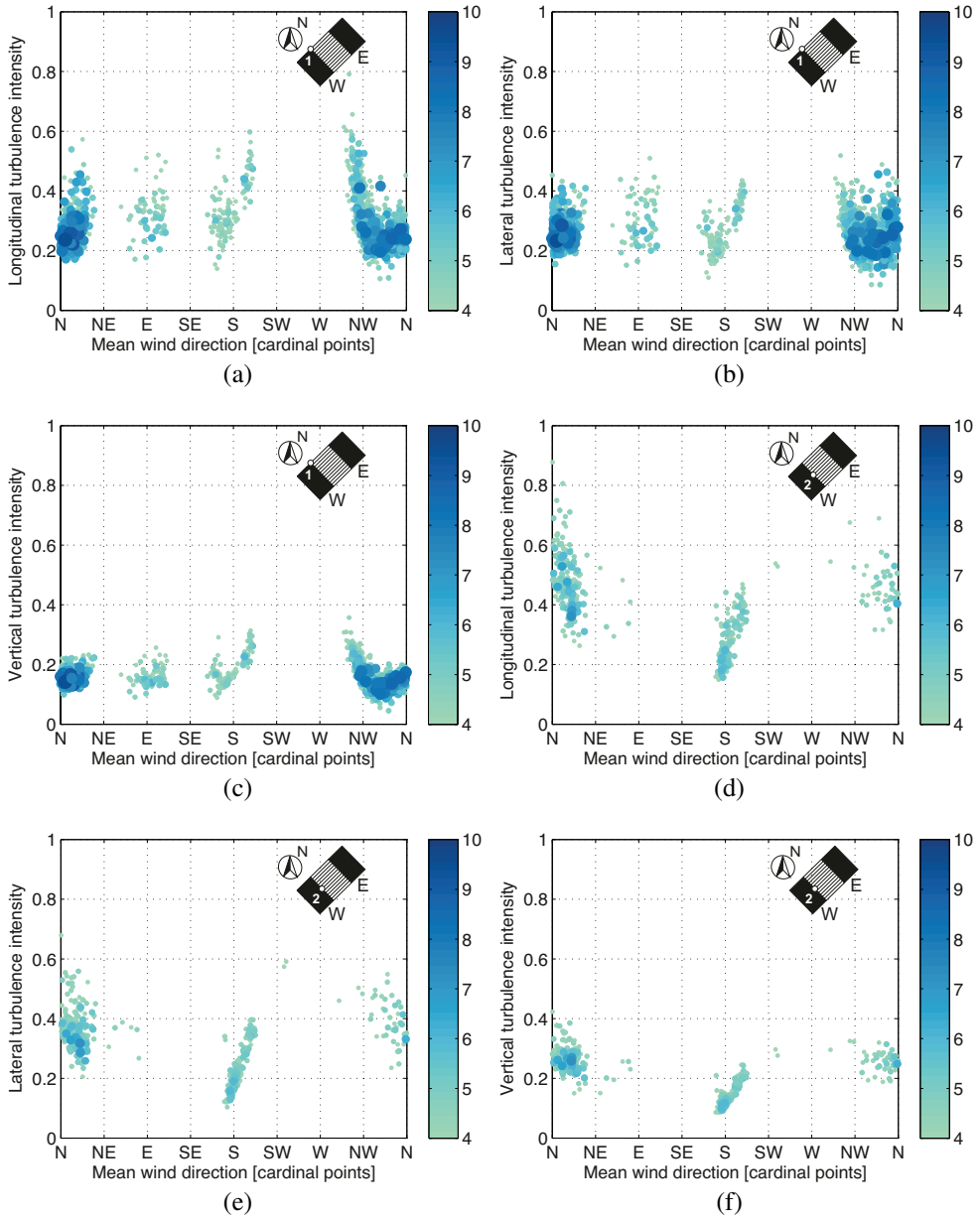

Fig. 6.17 – Variation of the turbulence intensity with the mean wind direction: **WS1** Longitudinal I_u (a); **WS1** Lateral I_v (b); **WS1** Vertical I_w (c);**WS2** Longitudinal I_u (d); **WS2** Lateral I_v (e); and **WS2** Vertical I_w (f).

Fig. 6.18 shows the variation of the averaged longitudinal, lateral and vertical turbulence intensities as a function of the 10-min mean wind direction, categorised in sixteen 22.5° directional sectors. Analysing the result obtained from sensor **WS1** in Fig. 6.18a, it noticed that the three component turbulent intensities are rather homogeneous across all directions, except for the two

upward trends: one between **SE** and **SSW**; and the other between **N** and **WNW**. With regard to the results from sensor **WS2** shown in Fig. 6.18b, it is verified the formation of two rather distinct clusters: the first, centred on the South direction, with an upward trend from **SSE** to **SSW** and a very narrow deviation in direction; and the second, centred on the North direction, with turbulence intensities generally greater than those of the first cluster.

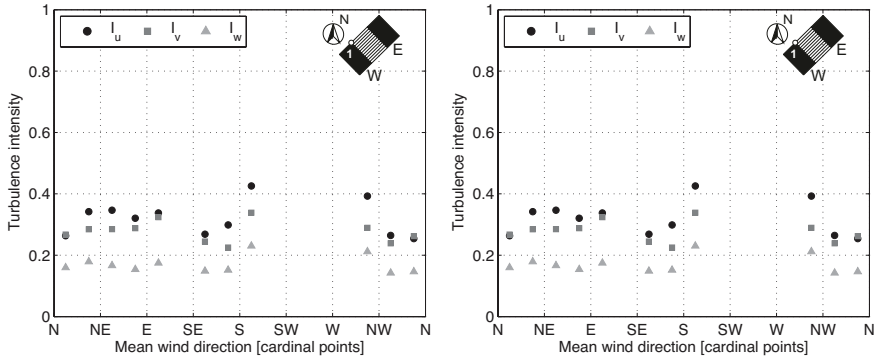

Fig. 6.18 – Variation of averaged longitudinal, lateral and vertical turbulence intensities with 10-min mean wind direction measured by sonic anemometers: **WS1** (a) and **WS2** (b).

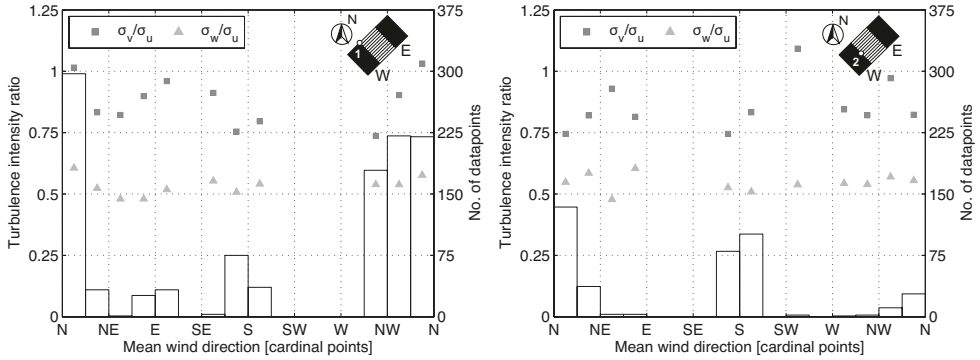

Fig. 6.19 – Variation of averaged turbulence intensities ratios σ_v/σ_u and σ_w/σ_u as a function of 10-min mean wind direction: **WS1** (a) and **WS2** (b).

The variation of the averaged turbulence intensity ratios σ_v/σ_u and σ_w/σ_u as a function of mean direction, categorised in 16 directional sectors, is represented in Fig. 6.19. The overlaid histogram also represented in such figure expresses number of data points measured for each direction sector. Analysing these results, it is noticed that both **WS1** and **WS2** σ_w/σ_u ratios show a rather uniform variation across all analysed sectors, with values close to the ration proposed by Solari and Piccardo (2001) of 0.5. The σ_v/σ_u ratio, on the other hand, shows a fairly distinct variation between the two sonic anemometers measurements and, in most cases, very different values from that proposed by Solari and Piccardo (2001) of 0.75. The highest

ratios found for **WS1** surpass the unit and refer to the two sectors around North. The two sectors around the South direction, on the other hand, present ratios close to 0.75. Furthermore, two peaks can be identified in Fig. 6.19: the higher, around North, and a lower, around **ESE**.

With regard to sensor **WS2**, the maximum average ratio σ_v/σ_u was 1.09 for the **SW-SWW** sector, although just two data points were identified for this direction. Sectors around North and South show values fairly close to 0.75, whereas the other sectors exhibit slightly higher values. Moreover, σ_v/σ_u ratios greater than 1 which indicates a lateral turbulence greater than the longitudinal turbulence, phenomenon rather unusual, but possible in the some circumstances, as discussed in Shiau and Chen (2002).

Power Spectrum of Wind Speed

PSD functions display the energy distribution of the wind speed fluctuating components. Different representations of these functions have been proposed in the literature. The spectrum model proposed by von Kármán (von Kármán, 1948) remains as one of the most widely accepted (Tamura et al., 2005). This model is particularly suitable for conditions where the low-frequency region is of greater importance, which is the case of the Braga stadium suspension roof. The von Kármán reduced auto power spectrum for the along-wind component is defined as:

$$\frac{nS_u(n)}{\sigma_u^2} = \frac{\frac{4nL_u}{\bar{U}}}{\left[1+70.8\left(\frac{nL_u}{\bar{U}}\right)^2\right]^{5/6}} \tag{6.2}$$

where n is the frequency, $S_u(n)$ is the along-wind auto power spectrum, σ_u is the standard deviation of the longitudinal turbulence, u, U is the mean wind speed and L_u is the estimated turbulence integral length scale of the longitudinal wind speed component. For the cross-wind and vertical components, the von Kármán model has the following form:

$$\frac{nS_\varepsilon(n)}{\sigma_\varepsilon^2} = \frac{\frac{4nL_\varepsilon}{\bar{U}}\left[1+755.2\left(\frac{nL_\varepsilon}{\bar{U}}\right)^2\right]}{\left[1+283.2\left(\frac{nL_\varepsilon}{\bar{U}}\right)^2\right]^{11/6}}, \quad \varepsilon = v, w \tag{6.3}$$

where $S_v(n)$ and $S_w(n)$ are the cross-wind and vertical auto power spectra, σ_v and σ_w are the standard deviation of the lateral and vertical turbulences and L_v and L_w are the integral length scales of the cross-wind and vertical turbulence, respectively. Two samples of wind data with very distinct characteristics were selected for spectral analysis, both measured by sonic

anemometer **WS1**. The criterion for this selection was the extraction of two-hour records with relatively high mean wind speed, but with opposite mean direction and incidence angles.

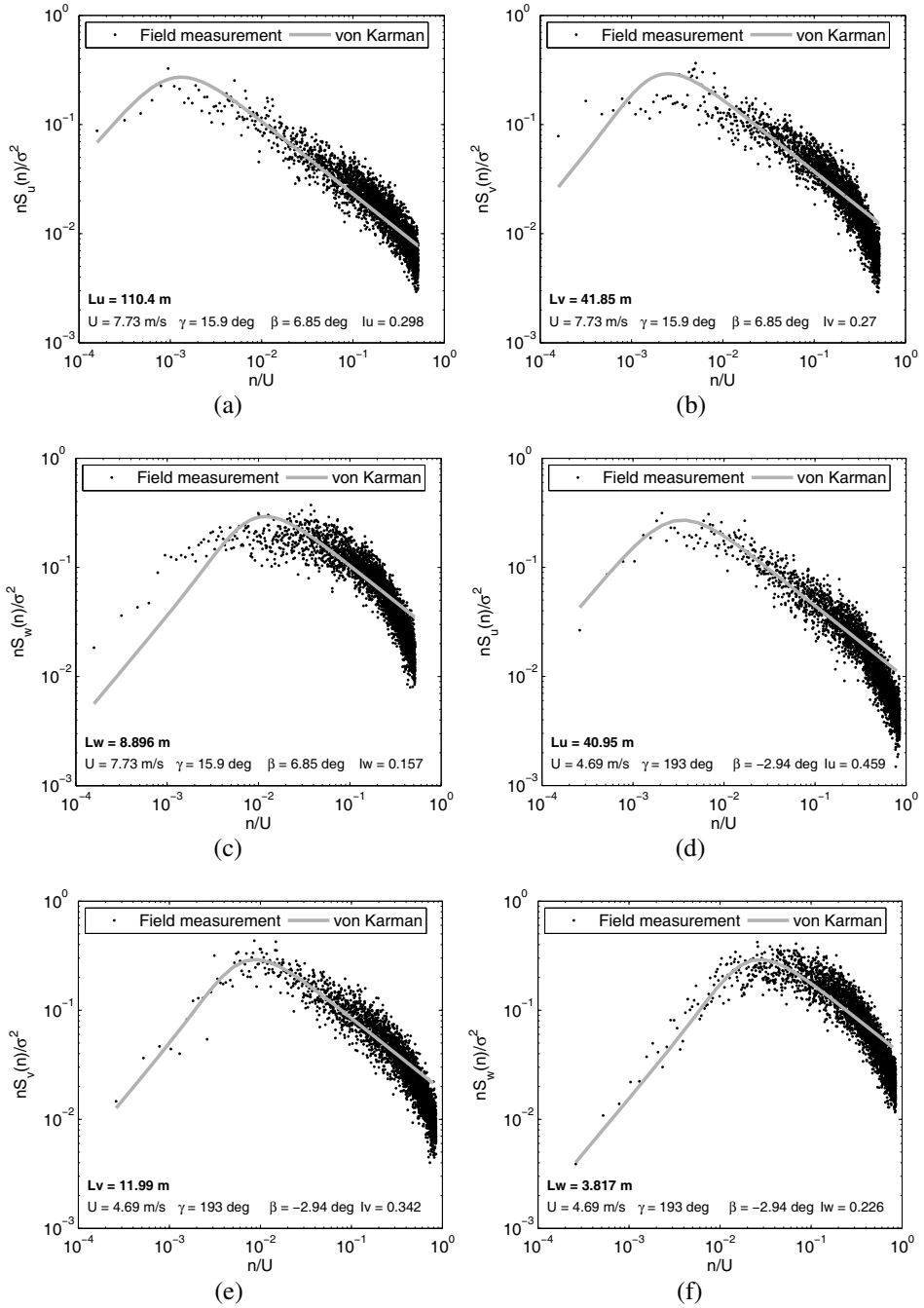

Fig. 6.20 – **PSD** of wind data measured by ultrasonic anemometer **WS1**: North - 8/2/2012: along-wind (a); cross-wind (b); vertical wind (c); South - 25/4/2012 along-wind (d); cross-wind (e); vertical wind (f).

Apart from this criterion, the wind sample should exhibit stationary characteristics, i.e., the mean wind speed from each segment should not differ more than 25% from the mean wind

speed of the full time series and, additionally, the corresponding direction angle must not vary by more than 15° (Cremona and Foucriat, 2002). The first sample chosen, with a North direction (15.9°) and an upward incidence (6.85°), was collected on 8 February 2012 between 11:50 and 13:50, and shows a mean wind speed of 7.73 m/s. The second sample, measured on the 25 April 2012 between 13:30 and 15:30, is characterised by a South direction (193°), a downward incidence (-2.94°) and a mean wind speed of 4.69 m/s.

In order to obtain the **PSD** function for each turbulent component, the time series are divided into data segments with 8192 points and a 50% overlap over the previous and following segments. After applying a Hanning window to all segments, the **FFT** was used to compute individual **PSD**s. Global auto **PSD** function are obtained by averaging all individual **PSD**s previously obtained. The procedure previously described corresponds to the estimation of the **PSD** with the periodogram approach described in Section 2.6. The reduced auto power spectra computed from both wind samples for each turbulent component are depicted in Fig. 6.20.

Turbulent Scales

The turbulence length scales define the average size of the turbulent eddies of the flow. Several criteria can be used to estimate these parameters. In the approach used in this study, the turbulence integral length scales were estimated by fitting the parameters of eqs. (6.1) and (6.2) to the observed velocity spectra. The von Kármán spectra fitted to the **PSD** functions are represented in Fig. 6.20, together with the resulting integral length scale. The von Kármán spectrum appears to fit relatively well the spectra obtained from the field measurements, especially to the points of the spectra of the southern winds suited within the lower frequency range. The values of the turbulence integral length scale obtained for the along-wind, cross-wind and vertical wind directions are, respectively, 110.4 m, 41.85 m and 8.896 m for northern winds and 40.45 m, 11.99 m and 3.817 m for southern winds. A prominent distinction is found between the parameters obtained for the two opposite prevailing directions. Turbulence integral length scales from northern winds present values 2-3.5 times greater than those measured from southern winds. Based on many field measurements, Solari and Piccardo (2001) proposed that the turbulence integral length scales can be estimated by:

$$L_\varepsilon = 300\lambda_\varepsilon (z/200)^\nu, \quad \nu = 0.67 + 0.05\ln(z_0) \quad (\varepsilon = u, v, w) \tag{6.4}$$

where L_ε is the integral length scale for the given direction (u, v or w), z is the height above the ground ($z \leq 200$ m) and z_0 is the roughness length, all in meters. λ_ε is a random variable that assumes values of 1, 0.25 and 0.10 for the three orthogonal directions u, v and w. Taking into account that the ultrasonic anemometer **WS1** is placed at approximately 35 m high and

assuming a terrain roughness of $z_0 = 0.15$ m, value in between categories I and II from Eurocode 1 - Part 1-4 (CEN, 2005), the turbulence integral length scales were assessed based on eq. (6.4). The values obtained with such equation were 110.1 m, 27.52 m and 11.01 m for the along-wind, cross-wind and vertical wind direction, respectively.

While these estimates approximate rather well the along-wind and vertical wind turbulence integral length scales measured for the northern winds, they fail to assess the southern winds values. Considering that the wind from the South direction flows through the West slab and from the terrain behind it at the same level, it is reasonable to consider different height from the ground, z, and terrain roughness, z_0 (see Figs. 5.1 and 5.2). Assuming the ultrasonic anemometer elevation above the West slab at the height $z = 3$ m and a upstream roughness characteristic of smoother terrains $z_0 = 0.02$ m, the following length scales are obtained from eq. (6.4): $L_u = 40.91$ m, $L_v = 10.23$ m and $L_w = 4.09$ m. Comparing these with the measured parameters from the South wind sample, a rather good match is noticed for all three directions.

6.4.2. Time Evolution of the Modal Parameters

The modal parameters (natural frequencies, modal damping ratios, mode shapes and operational factors) of the suspension roof have been continuously tracked from the 60-minute acceleration files acquired by the dynamic acquisition system since March, 2009. The modal parameters together with their confidence intervals and modal contributions are automatically estimated by the autonomous application described in Section 6.2.1. In the case of the continuous monitoring of the Braga stadium suspension roof, this application is configured to automatically identify the first 12 vibration modes suited within the frequency range of 0.0-1.1 Hz. These modes are automatically identified by means of the hierarchical clustering algorithm discussed in Chapter 4.

Fig. 6.21 shows the evolution of the daily mean values of the first 12 identified natural frequencies of the roof structure over four years of monitoring and a detail of the evolution of the natural frequencies of modes 3, 4, 5 and 12 is represented in Fig. 6.22. Analysing the yearly pattern of variation of each identified natural frequencies, it is verified that, whilst no significant variation is noticed over the monitored years for modes 3 and 4, it is clearly seen a slightly decreasing pattern of the other modes over the time, as shown in Fig. 6.22. These results are synthesized in Tab. 6.1, where the mean and standard deviation of the natural frequencies obtained within the first year of monitoring is compared to those from the last year.

Another interesting conclusion drawn from the analysis of the time variation of the natural frequencies is that the underlying environmental conditions affect differently the identified modes of the suspension roof, i.e., the pattern of variation of the natural frequencies of modes 3 and 4

is contrary to that of the other identified modes.

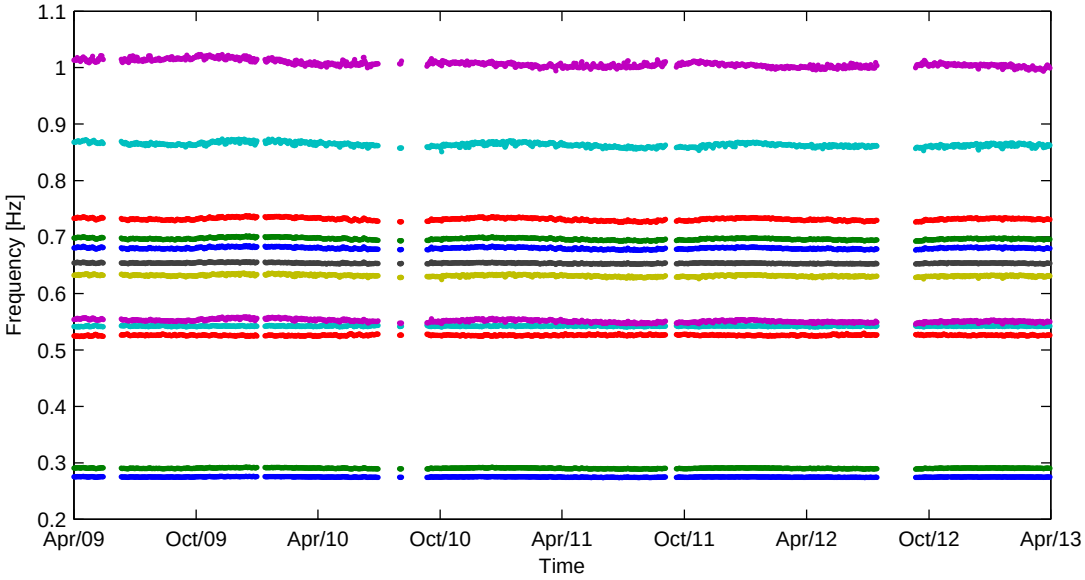

Fig. 6.21 – Time evolution of the daily mean values of first 12 natural frequencies of the suspension roof automatically identified with the **pLSCF** technique in the range of $0-1.1$ Hz along four years of monitoring (from 01/04/2009 to 31/03/2013).

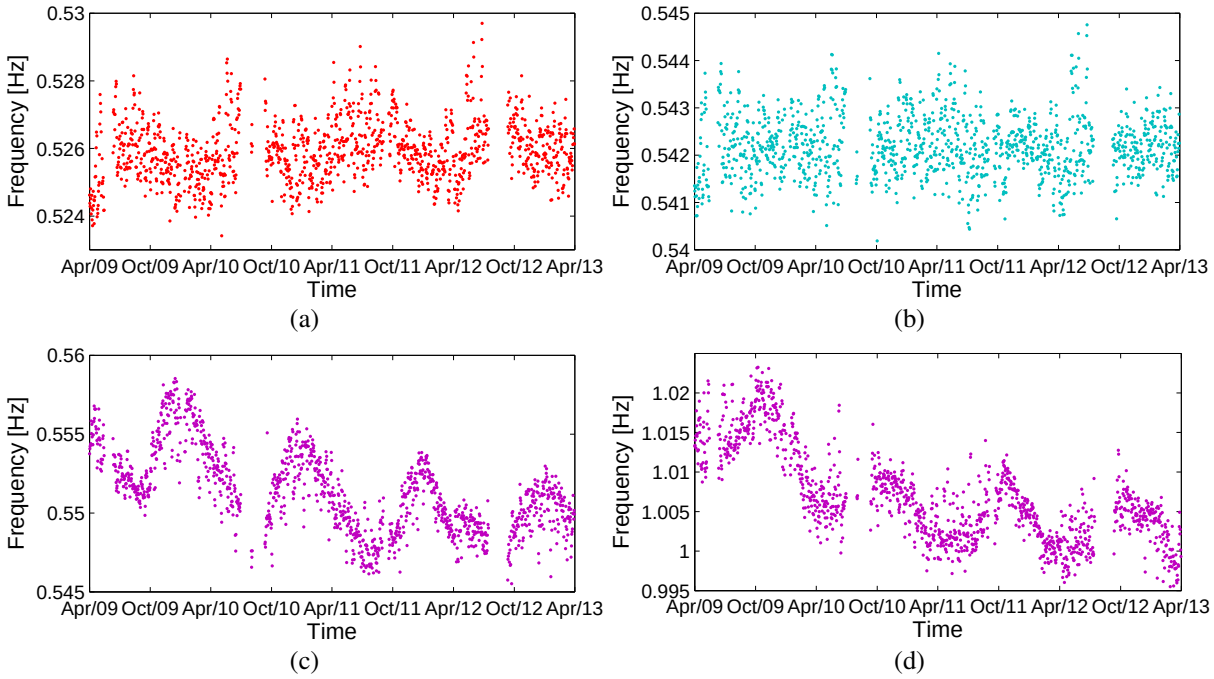

Fig. 6.22 – Time evolution of the daily mean values of the natural frequencies identified with the **pLSCF** technique for modes 3 (a), 4 (b), 5 (c) and 12 (d), along 4 years of monitoring (from 01/04/2009 to 31/03/2013).

This result is illustrated in Fig. 6.23, where the detail of a five-day evolution of the natural frequencies of modes 3, 4, 5 and 12 together with their corresponding confidence intervals is

represented. From these figures, it is observed the daily variation of these natural frequencies and their estimated standard deviations due to the influence of the environmental conditions. Although the environmental and operational conditions affect differently the evolution of the natural frequencies, a well defined cyclic pattern of variation is observed in Figs. 6.23 mostly due to the daily temperature variation. Fig. 6.24 represents the variation of the damping ratios of modes 3, 4, 5 and 12 together with their corresponding standard deviations over the same time frame of five days.

Tab. 6.1 – Mean ($\mu_{\hat{f}_n}$) and standard deviation ($\sigma_{\hat{f}_n}$) values of the natural frequencies estimated from 01/04/2009 to 31/03/2010 and from 01/04/2012 to 31/03/2013 with the **pLSCF** technique.

Mode	From 01/04/2009 to 31/03/2010		From 01/04/2012 to 31/03/2013	
	$\mu_{\hat{f}_n}$ (Hz)	$\sigma_{\hat{f}_n}$ ($\times 10^2$) (Hz)	$\mu_{\hat{f}_n}$ (Hz)	$\sigma_{\hat{f}_n}$ ($\times 10^2$) (Hz)
1	0.2752	0.0664	0.2746	0.0490
2	0.2907	0.0949	0.2902	0.0779
3	0.5256	0.1410	0.5261	0.1368
4	0.5421	0.1259	0.5422	0.1236
5	0.5541	0.2699	0.5496	0.2330
6	0.6329	0.1977	0.6305	0.1662
7	0.6544	0.1428	0.6532	0.1155
8	0.6811	0.2195	0.6798	0.1785
9	0.6983	0.1957	0.6959	0.1574
10	0.7332	0.2572	0.7310	0.2074
11	0.8670	0.4095	0.8616	0.3414
12	1.0145	0.6336	1.0026	0.5157

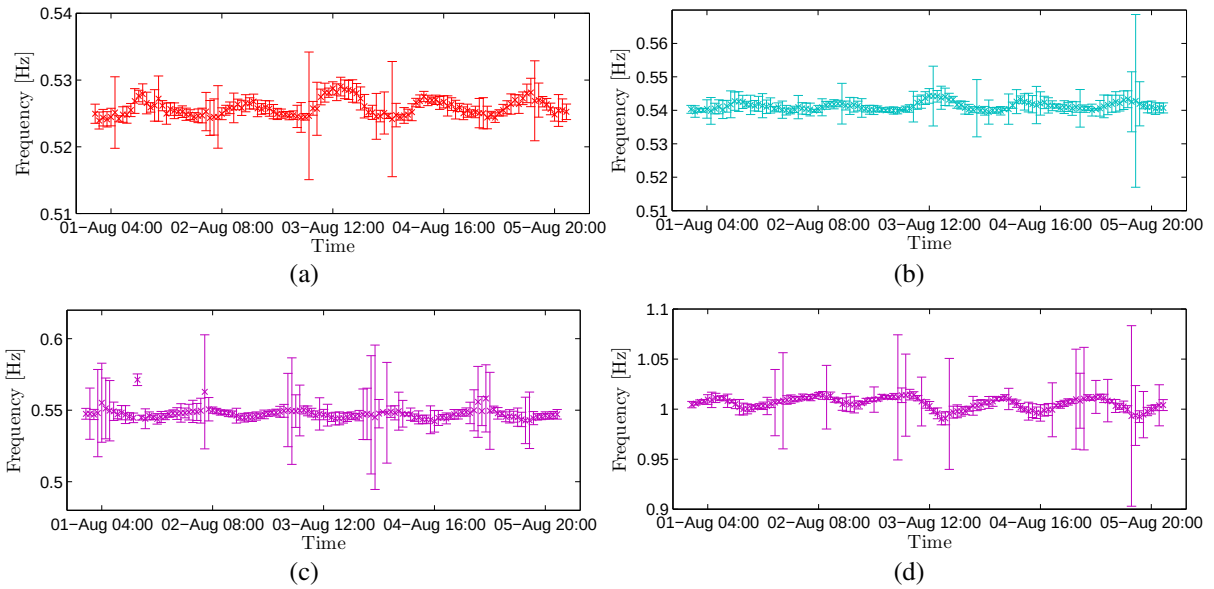

Fig. 6.23 – Time evolution of the natural frequencies together with their standard deviations automatically identified with the **pLSCF** technique for modes 3 (a), 4 (b), 5 (c) and 12 (d), along 5 days of monitoring (from 01 to 5/08/2011). The standard deviations of the natural frequencies in these figures are multiplied by a factor of 10^2 in order to improve their visibility within the figure.

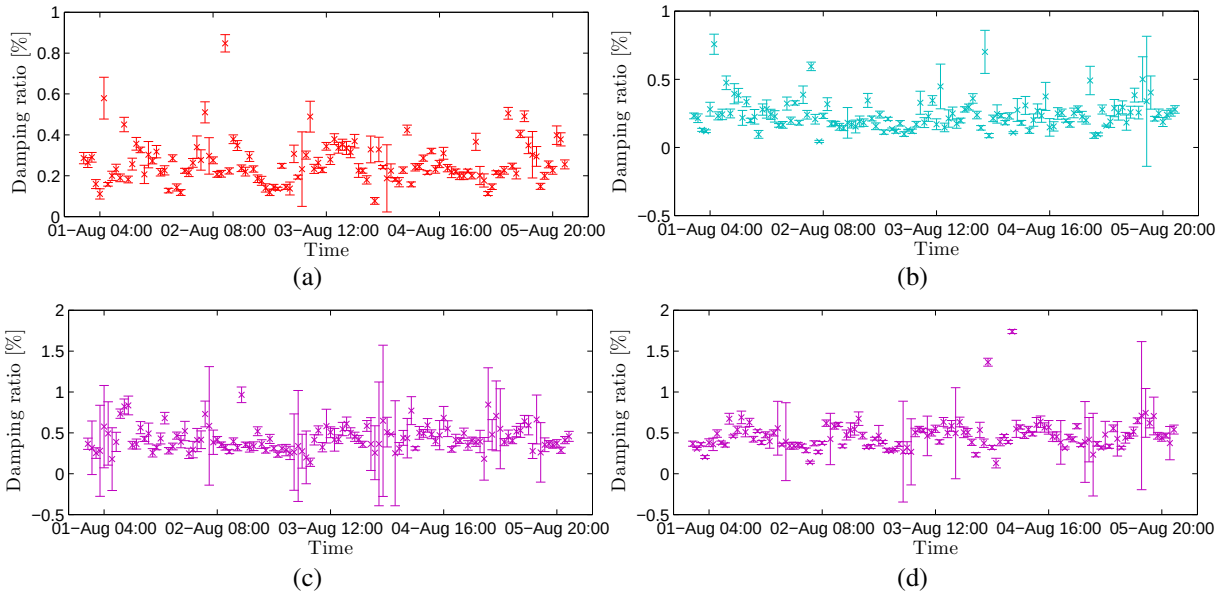

Fig. 6.24 – Time evolution of the modal damping ratios together with their standard deviations automatically identified with the **pLSCF** technique for modes 3 (a), 4 (b), 5 (c) and 12 (12), along 5 days of monitoring from 01 to 05/08/2011. The standard deviations of the modal damping ratios in these figures are multiplied by a factor of 10 in order to improve their visibility within the figure.

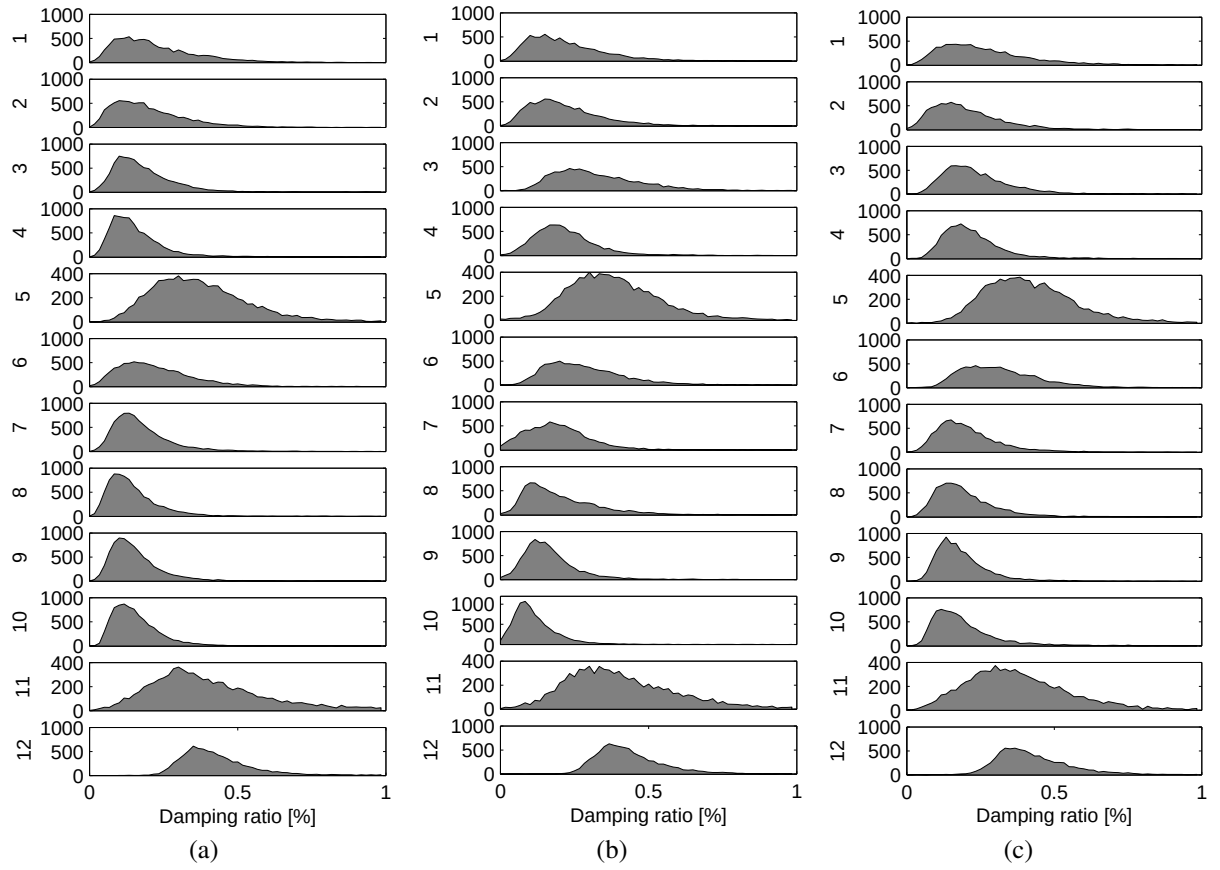

Fig. 6.25 – Dispersion of the damping ratios for the first 12 modes identified over the year of 2011 with the **SSI-DATA** (a), **SSI-COV** (b) and **pLSCF** (c).

Compared to the well defined evolution of the natural frequencies, the modal damping ratios exhibit a significant scatter. This is not only due to the higher uncertainty associated with the estimation of these parameters, but also to the significant dependence on other factors, as, for instance, wind, temperature and vibration amplitude. Nevertheless, a faint daily pattern can be observed, outcome of temperature and wind speed variation. Fig. 6.25 characterises, resorting to histograms, the dominant values and variability of the identified modal damping ratios during the year of 2011 with the **SSI-DATA**, **SSI-COV** and **pLSCF**, showing consistency of the results provided by the three methods.

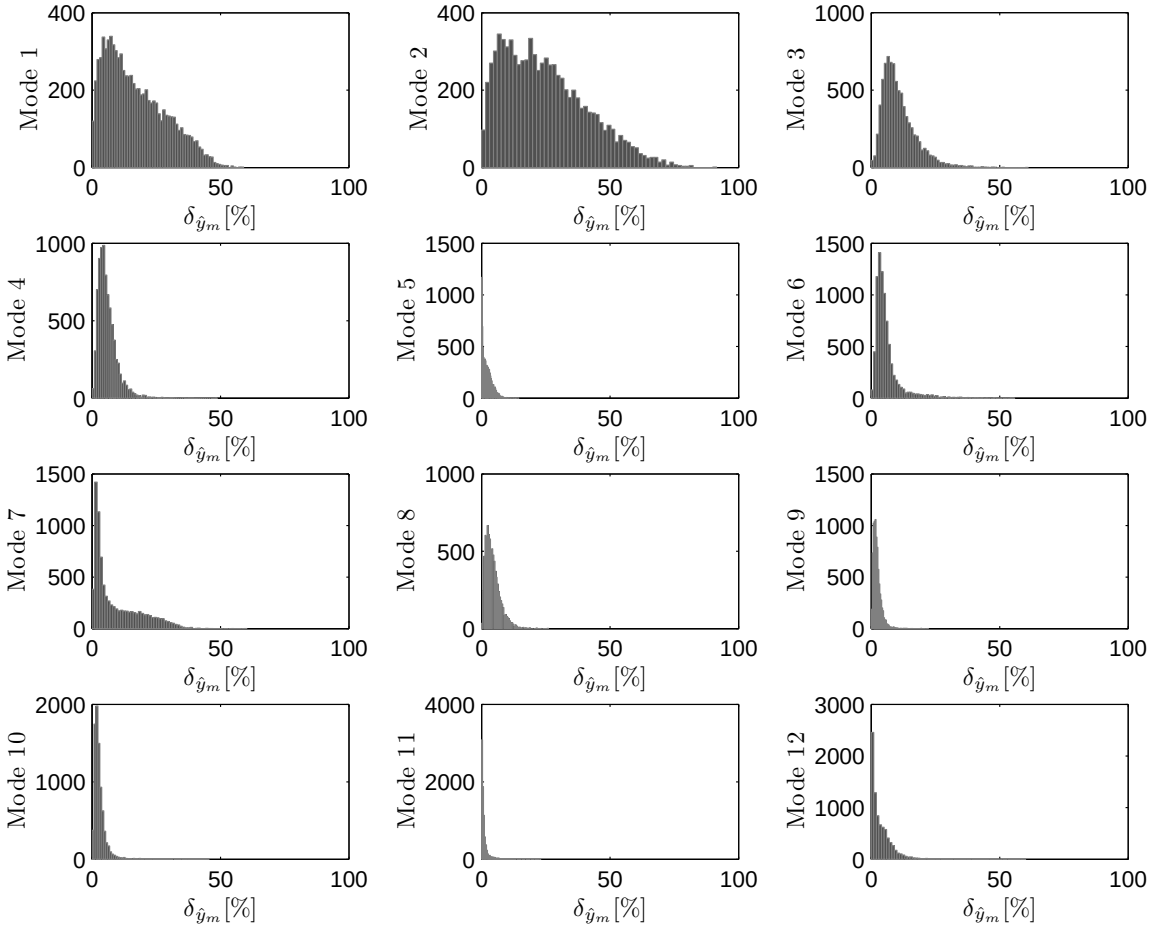

Fig. 6.26 – Dispersion of the modal contributions for the first 12 modes identified with the **SSI-DATA**.

The statistics of the natural frequencies, damping ratios and their respective confidence intervals estimated with the **SSI-DATA**, **SSI-COV**, **pLSCF** and **pMLE-MM** over the course of the aforementioned period are summarized in Tab. C.1 presented in APPENDIX C. The higher variability in the estimation of damping ratios, in contrast with the natural frequencies, is evident in this table. Furthermore, the very low values estimated for the damping ratios, patent in Figs. 6.25, are coherent with results from the **AVT** presented in Chapter 5. In Figs. 6.26, the

histograms of the modal contributions for the 12 identified modes estimated along the year of 2011 are presented.

It is obvious from these results that modes 1 and 2 are those which were more excited by the operational conditions. Moreover, comparing the dispersion of mode 1 to that of 2, one also verifies that the second mode tends to be more sensitive to such conditions, fact that is also corroborated by the results obtained in the **AVT** of the West slab of the suspension roof presented in Chapter 5.

6.5. Influence of Wind and Temperature on Modal Parameters and Structural Response

6.5.1. Wind Induced Response

In order to assess the influence of wind speed on structural response, relationship between the 10-min **RMS** acceleration and the mean wind speed and direction for the same period of time was investigated. The vertical accelerations measured by the six accelerometers of the dynamic monitoring system were analysed for time periods at which the 10-min mean wind speed measured by sensor **WS1** (Fig. 6.1) was greater than 4 m/s.

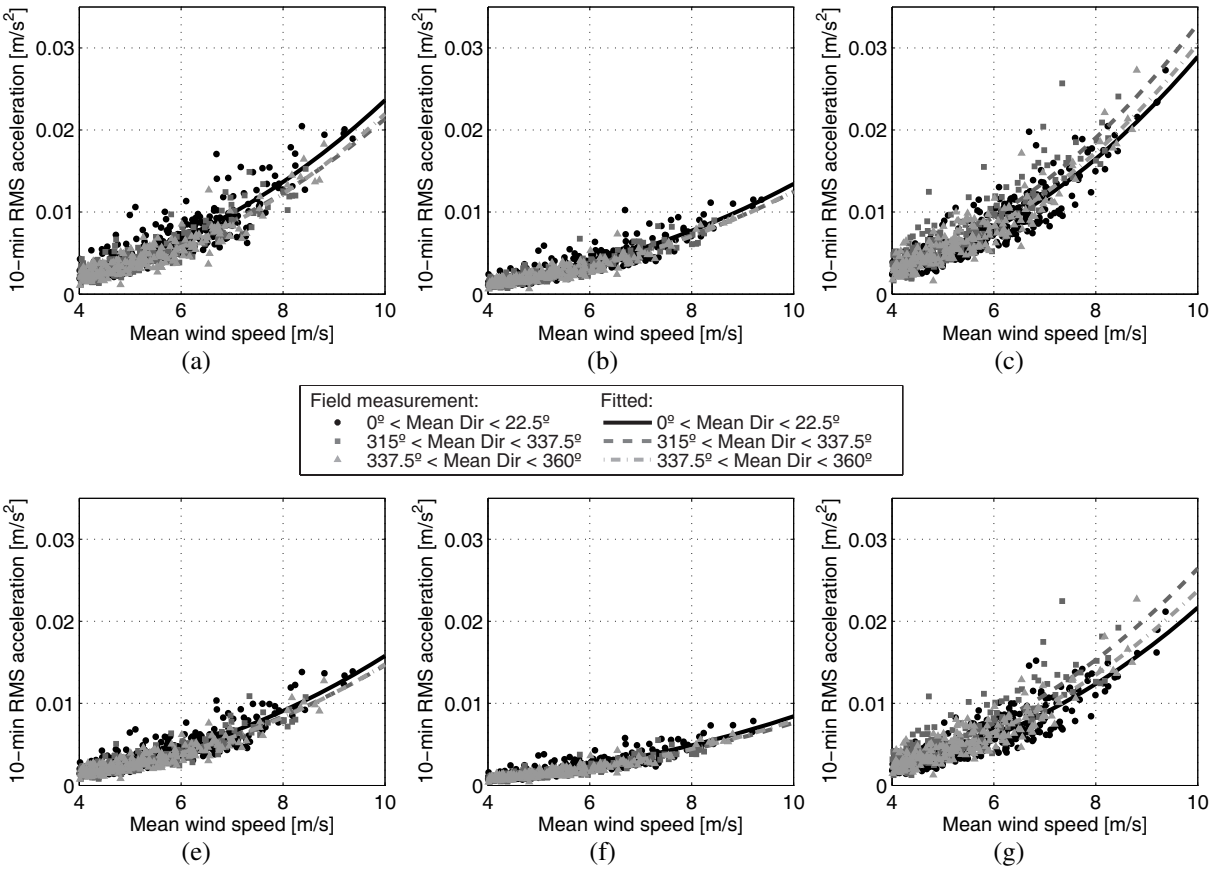

Fig. 6.27 – Relationship between mean wind speed from 3 dominant wind directions and 10-min **RMS** acceleration measured by accelerometers **A1** (a), **A2** (b), **A3** (c), **A4** (c), **A5** (d) and **A6** (f).

Furthermore, the analysis took into account the 10-min mean wind direction, dividing acceleration responses according to sixteen 22.5° directional sectors. Fig. 6.27 shows the relationship between the mean wind speed measured by **WS1** and the **RMS** vertical accelerations measured by each accelerometer according to the three dominant wind directions. From the performed analysis, only the three directional sectors between 315° (**NW**) and 22.5° (**NNE**) showed a reasonable amount of observations.

Tab. 6.2 – Maximum acceleration and regression curves parameters of the acceleration responses by wind direction sector.

Accel.	Direction [°]	Max. **RMS** accel. $[\times 10^{-2}\,\mathrm{m/s^2}]$	Max. accel. $[\times 10^{-2}\,\mathrm{m/s^2}]$	c_1 $[\times 10^{-5}]$	c_2
A1	0 - 22.5	2.05	9.69	8.35	2.45
	315 - 337.5	1.53	8.87	7.41	2.46
	337.5 - 360	1.83	7.87	5.27	2.62
A2	0 - 22.5	1.15	5.43	4.47	2.48
	315 - 337.5	0.9	4.8	4.15	2.48
	337.5 - 360	0.93	5.87	3.33	2.58
A3	0 - 22.5	2.73	13.04	8.69	2.52
	315 - 337.5	2.57	9.86	11.6	2.45
	337.5 - 360	2.73	11.02	8.58	2.55
A4	0 - 22.5	1.39	6.39	5.25	2.48
	315 - 337.5	1.09	5.23	4.73	2.49
	337.5 - 360	1.28	5.43	3.89	2.58
A5	0 - 22.5	0.79	3.31	3.08	2.44
	315 - 337.5	0.55	2.77	2.49	2.49
	337.5 - 360	0.63	2.58	2.05	2.58
A6	0 - 22.5	2.12	9.07	6.64	2.51
	315 - 337.5	2.25	8.63	9.37	2.45
	337.5 - 360	2.27	7.74	7.03	2.52

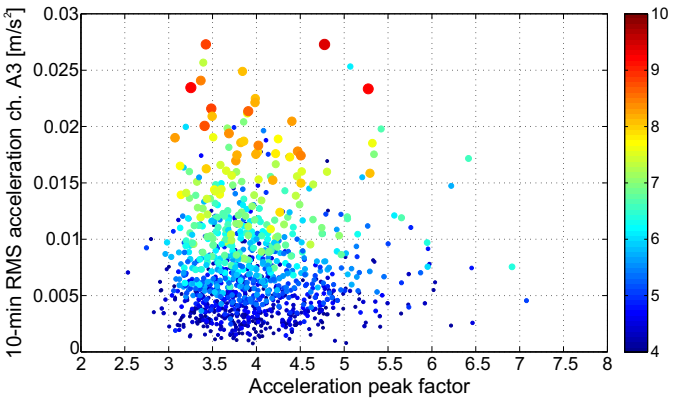

Fig. 6.28 – Variation of peak factor with **RMS** acceleration at channel **A3** and 10-min mean wind speed.

The results presented in Fig. 6.27 clearly shows the similarities in acceleration magnitude between accelerometers in the same suspension roof longitudinal direction (**A1**-**A4**, **A2**-**A5** and

A3-**A6**) (see Fig. 6.1). It is also noticed that sensors placed near the inner edge of the slab (**A1**, **A2** and **A3**) show higher **RMS** accelerations than the correspondent sensors placed along the middle of the slab (**A4**, **A5** and **A6**). The acceleration levels observed for each of the six accelerometers, and the relation between them, reflect the modal shapes of the first vibration modes (see Section 5.6). Tab. 6.2 lists the maximum **RMS** and the maximum acceleration obtained for each direction in each accelerometer.

The accelerometers placed on the Northwest border of the slab (**A3** and **A6**) show the highest magnitudes of acceleration, with nearly 0.03 m/s^2 **RMS** and 0.13 m/s^2 maximum for the higher wind speeds. The accelerometers **A2** and **A5**, set on the middle of the slab, on the other hand, measure the lowest acceleration values. From Fig. 6.27, one can also observe a general trend of increase of the vertical **RMS** acceleration response with the mean wind speed. This trend appears clearer for individual directions. The observed response is characteristic of a turbulence buffeting effect, where the vibration mechanism is controlled by turbulent random pressure fluctuations (Shigehiko et al., 2008). This is further enhanced by the values of the acceleration peak factors at channel **A3** (see Fig. 6.1) represented in Fig. 6.28 as a function of the **RMS** acceleration and the 10-min mean wind speed. According to Li et al. (2007) the regression curves of such response can be expressed by:

$$a_{RMS} = c_1 \bar{U}^{c_2} \tag{6.5}$$

where a_{RMS} is the 10-minute **RMS** acceleration response, $\bar{U}$ is the 10-min mean wind speed, and c_1 and c_2 are the curve fitting parameters. A non-linear least-squares curve fitting was applied to the field measurements of each accelerometer for the three prevalent directions. Tab. 6.2 lists the resulting c_1 and c_2 parameters.

6.5.2. Influence of Temperature and Mean Wind Speed on Natural Frequencies

The modal parameters identified by the dynamic monitoring system reflect the influence of environmental and operational factors. Amongst the various possible factors, temperature and wind have been identified as the those with dominant influence on the variability of these parameters. To understand the corresponding effect, it should be kept in mind the following: rising temperatures causes the elasticity modulus of the concrete of the slabs to decrease and the length of cables to increase. These effects, on their turn, lead to an increment of the sag of the cables and reduction of tension, simultaneously with an increase of the slab bending stiffness. The combination of the two effects may result in increasing or decreasing frequencies for different vibration modes, depending on the relative participation of slab bending and cable deformation.

In order to analyse the dependence between the mean wind speed, the ambient temperature variation and the values of the identified natural frequencies, the Pearson's correlation coefficients (r) were computed. Tab. 6.3 summarises the correlations found between the identified natural frequencies, the mean wind speed and temperature. The analysis of the wind effects, in particular, shows that positive incidence, typical from northern directions, leads to a sag reduction with consequent decrease of the cable tension and, possibly, frequency, whilst negative incidence, typical from Southern directions, has an opposite effect. It is evident from the results presented such table that, apart from mode 3 and 4, the estimated natural frequencies tend to vary inversely with both mean temperature and mean wind speed. The correlations for the natural frequencies of modes 3, 4, 5 and 12 with temperature are shown in Figs. 6.29.

Tab. 6.3 – Pearson correlation coefficients (r) between the natural frequency values and the mean wind speed and mean sonic temperature.

	Mode											
	1	2	3	4	5	6	7	8	9	10	11	12
$\bar{T}$	-0.631	-0.759	0.780	0.646	-0.562	-0.036	-0.447	-0.720	-0.815	-0.820	-0.406	-0.301
$\bar{U}$	-0.304	-0.335	0.067	0.127	-0.501	-0.328	-0.454	-0.408	-0.314	-0.313	-0.390	-0.377

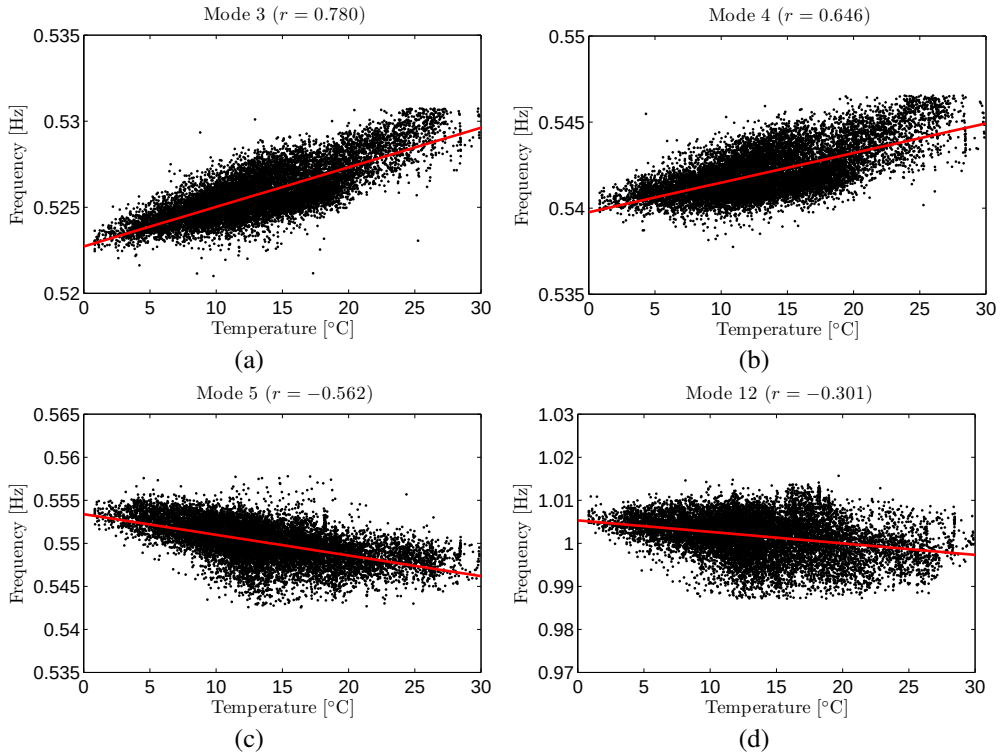

Fig. 6.29 – Correlation between the natural frequencies identified for modes 3 (a), 4 (b), 5 (c) and 12 (d), and the mean sonic temperature.

Analysing these figures, it is noticed that, whist the natural frequencies of modes 5 and 12 tend

to decrease with increasing ambient temperature, an opposite trend is observed for the natural frequencies of modes 3 and 4. These results are believed to be due to the geometrical non-linear behaviour of the suspension roof. In a attempt to interpret these results, the **FE** model of the roof structure described in Section 5.7 was used to simulate the variation of the natural frequencies with temperature. Assuming a reference temperature of 20°C, a temperature variation from -20 to 20°C was applied to the model in order to assess the corresponding influence on the natural frequencies.

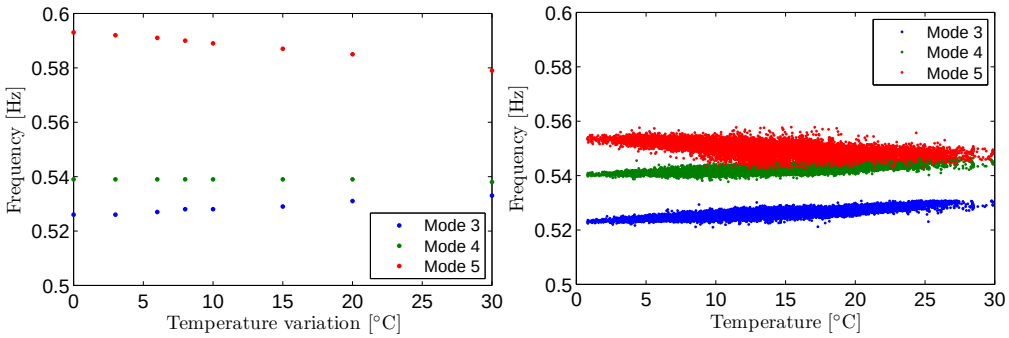

Fig. 6.30 – Variation of the natural frequencies of modes 3, 4 and 5, experimentally identified under varying environmental conditions with the **pLSCF** technique (a) and obtained with a simulated temperature variation using the numerical model (b).

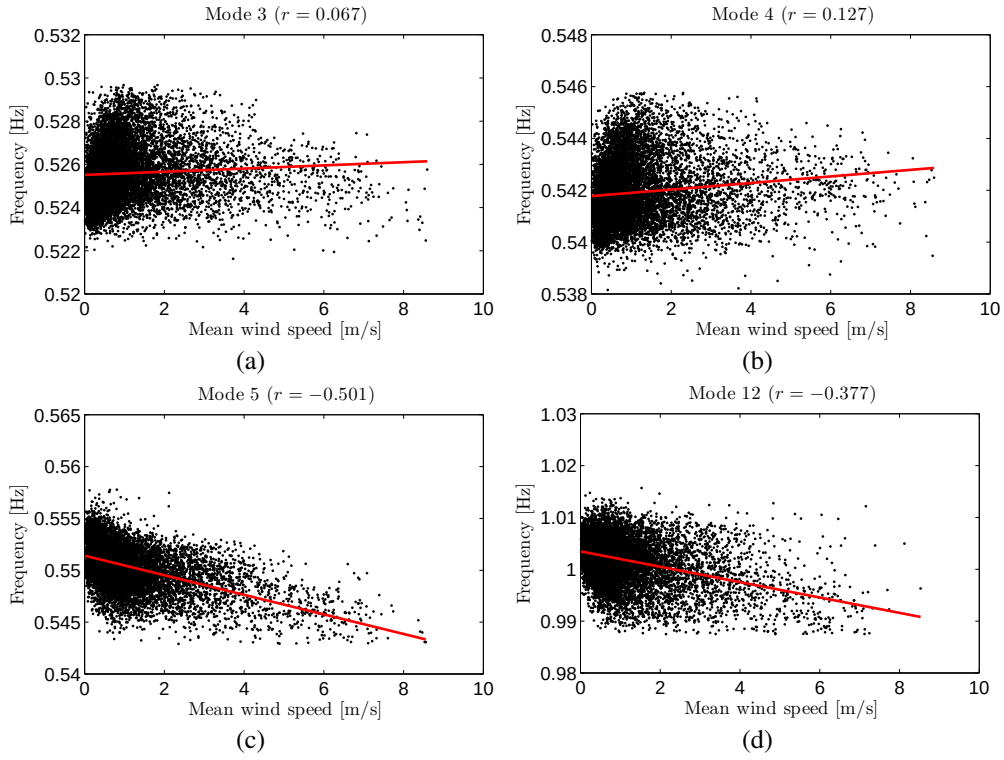

Fig. 6.31 – Correlation between the natural frequencies identified for modes 3 (a), 4 (b), 5 (c) and 12 (d), and the mean sonic temperature.

Comparing the results from the numerical simulation, shown in Fig. 6.30a, to those from the continuous monitoring, represented in Fig. 6.30b, it is verified that a similar pattern of variation was obtained for the natural frequencies of modes 3, 4 and 5, which reveals that, in fact, the temperature has a dominant influence on the variation of these parameters. With regard to the influence of wind, it is verified in Tab. 6.3 that, whist almost no correlation exists between the natural frequency of modes 3 and 4, and the mean wind speed, a noticeable influence of this environmental action on the natural frequencies of the other identified modes is observed.

These results are clearly seen in Figs. 6.31 where the correlations of the natural frequencies of modes 3, 4, 5 and 12 with the 10-min mean wind speed are represented.

6.5.3. Influence of Temperature and Mean Wind Speed on Modal Damping Ratios

As previously discussed, compared to the natural frequencies, the identified damping ratios show a significant scatter. Despite this scattered variation, a slight evidence of a daily pattern variation associated with the wind speed and temperature changes (Fig. 6.24) is perceived. To study the relationship between damping ratios, and the mean temperature and wind speed, Pearson's coefficients (r) between these variables were also calculated. Tab. 6.4 summarises the most important results of the correlation analysis. The coefficients shown in this table reveals a tendency of the identified damping ratios to vary proportionally with both mean wind speed and mean temperature, the only exception being the almost null correlation coefficient obtained between the mean temperature and the damping ratio of mode 11.

Tab. 6.4 – Pearson correlation coefficients (r) between the damping ratios and the mean wind speed and mean sonic temperature.

	Mode											
	1	2	3	4	5	6	7	8	9	10	11	12
$\bar{T}$	0.181	0.153	0.160	0.142	0.190	0.145	0.152	0.204	0.141	0.214	-0.039	0.184
$\bar{U}$	0.370	0.359	0.391	0.306	0.219	0.331	0.327	0.372	0.212	0.355	0.271	0.289

The main conclusion is that, for all investigated modes, the variation of the damping ratio is more associated with the change of mean wind speed than with the mean temperature. For this reason, only the relationship between damping ratios and mean wind speed has been considered in subsequent analyses. Figs. 6.33 present the variation of the damping ratios of modes 3, 4, 5 and 12 with the mean wind speed. The approximate linear relationship observed in the range of measured mean wind speed is common to all identified modes and reflects the wind induced added damping to the total identified damping ratio. The damping estimates corresponding to periods of very low wind speeds (lower than 2 m/s) were averaged for each mode in order to obtain an estimate of the structural damping ($\Delta\xi_{\text{struct}}$).

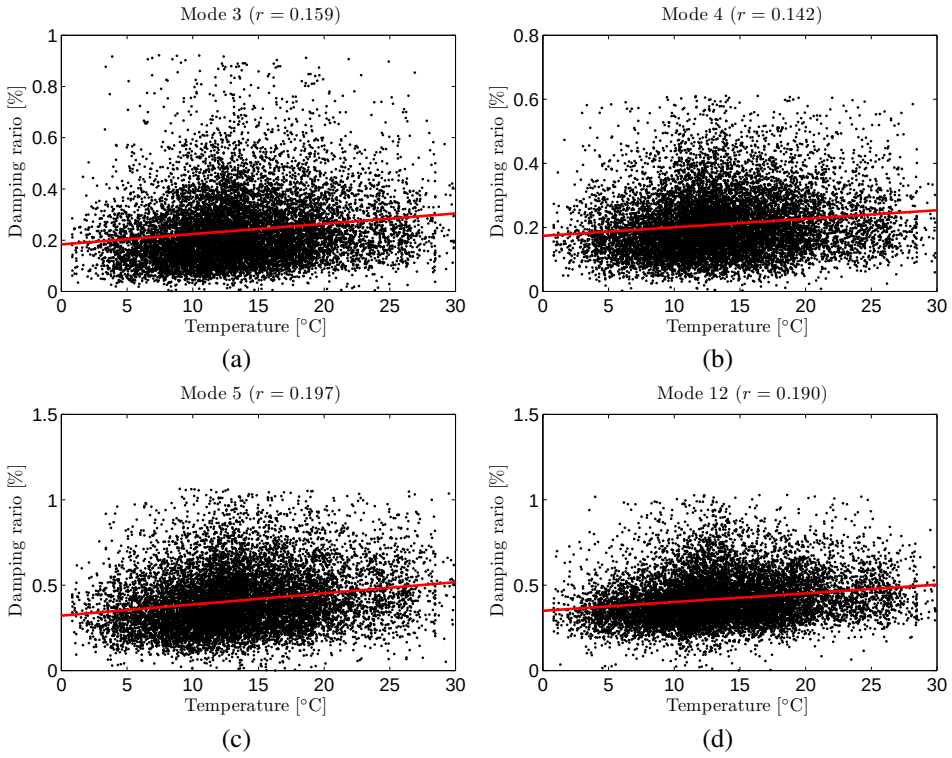

Fig. 6.32 – Correlation between the damping coefficients identified for modes 3(a), 4(b), 5(c) and 12(d), and the mean sonic temperature.

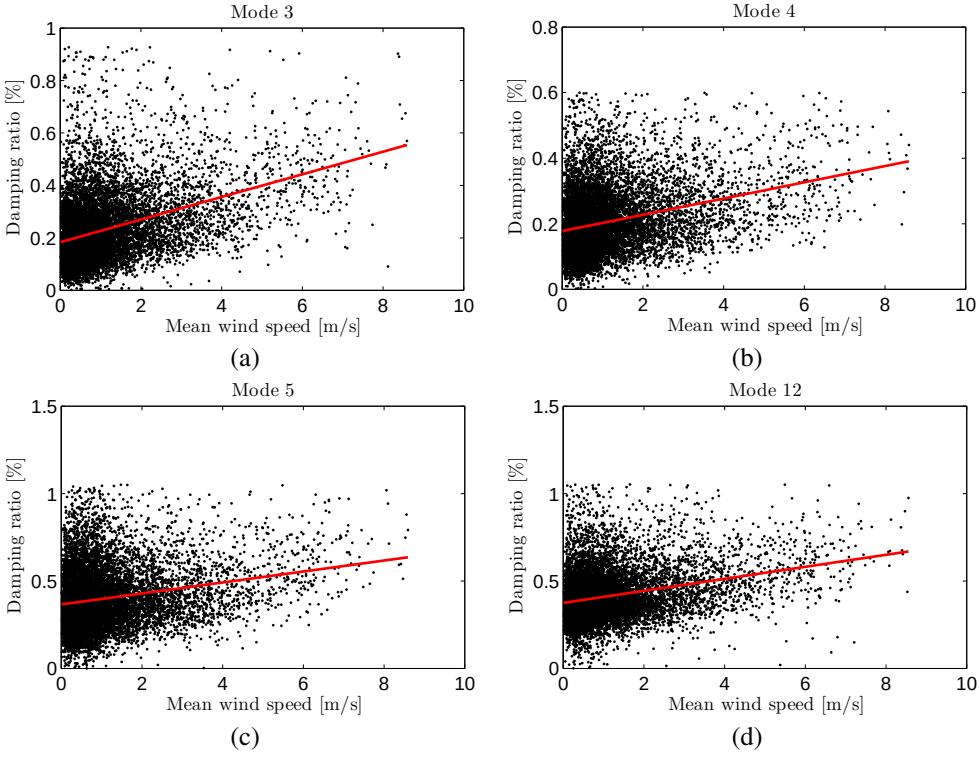

Fig. 6.33 – Correlation between the damping coefficients identified for modes 3(a), 4(b), 5(c) and 12(d), and the mean wind speed.

In a different approach, least-squares linear fit was applied to the damping coefficient associated with mean wind speed higher than 2 m/s. The constant term of the fitted line provides an alternative estimation of the structural damping, while the slope parameter expresses the wind induced added damping gradient $\left(\Delta\xi_{\text{aerodyn}}\right)$ (Macdonald, 2002). Tab. 6.5 summarises the obtained results for all identified modes and the fitted lines shown in Figs. 6.33 were used to estimate the structural and aerodynamic damping coefficients.

A reasonable agreement of the estimated structural damping values is found across all modes, with a general trend for higher values of structural damping $(\Delta\xi_{\text{struct}})$ estimated with the averaging approach. The computed values for wind induced added damping range from 0.02% $(\text{m/s})^{-1}$, for mode 9, to 0.06% $(\text{m/s})^{-1}$, for mode 11, and correspond to an average of 20% of the structural damping per m/s. The quality of the least-square linear fits is generally low, due to the significant scatter of the identified damping ratios. Damping ratios for the Braga suspension roof have been previously estimated based on forced and free vibration tests (Magalhães et al., 2006). The main results of those tests are shown in Tab. 6.5 for comparison with the present estimates.

Tab. 6.5 – Summary of measured damping coefficients.

Mode	ξ_{struct} $(\bar{U} \leq 2\,\text{m/s})$ [%]	Linear regression			Free Vib. Filter [%]	Free Vib. **SSI-COV** [%]	Harmonic Excitation [%]
		ξ_{struct} [%]	ξ_{aerodyn} $[\%\,(m/s)^{-1}]$	r			
1	0.24	0.20	0.05	0.34	-	0.29	0.28
2	0.19	0.14	0.05	0.38	-	0.37	0.27
3	0.24	0.19	0.04	0.36	0.28	0.33	0.22
4	0.20	0.18	0.02	0.26	0.25	0.22	-
5	0.40	0.32	0.04	0.31	-	0.44	-
6	0.30	0.24	0.04	0.37	0.34	0.36	0.43
7	0.28	0.21	0.03	0.31	-	0.29	-
8	0.18	0.15	0.03	0.32	-	0.11	0.2
9	0.18	0.14	0.02	0.28	-	0.18	-
10	0.18	0.16	0.03	0.29	0.2	0.18	-
11	0.35	0.23	0.06	0.44	-	-	-
12	0.42	0.37	0.04	0.30	-	-	-

It is observed that the damping ratios identified from forced and free vibration tests are generally greater than the corresponding values obtained under ambient vibration, fact that can be explained by the larger vibration amplitudes induced during the former tests. Nevertheless, structural damping estimates identified in the present study have the same order of magnitude of previous estimates and should be considered as reasonable approximations.

6.6. Removal of the Environmental Effects and Damage Detection

As shown in previous sections, the variation of the identified natural frequencies is highly influenced by the environmental and operational effects and, therefore, the component of variation due to these effects should be eliminated so that the natural frequencies shifts over the monitoring period can be effectively used as damage indicators. As the temperature of the structure has not been measured over the course of monitoring period, an output-only linear regression based on **PCA** was used to model and remove the effect induced by the environmental and operational conditions on the observed natural frequencies of the suspension roof. As discussed in Section 4.3.1, the first step to stablish such environmental models consists of computing the covariance of the observed features (i.e., the estimated natural frequencies).

In the case of the Braga stadium suspension roof, the computation of such matrix was performed by using the natural frequencies hourly estimated from 01/04/2009 to 31/03/2010 with the **pLSCF** identification technique. This time frame corresponds exactly to one year of monitoring and was taken as a reference period within which the natural frequencies were assumed to be observed in the undamaged condition of the suspension roof. Therefore, these observations are used to compute the reference covariance matrix, which was subsequently employed to remove the environmental and operational effects from future observations. Once the covariance matrix was computed, the next step towards the establishment of an environmental model for the monitored structure consisted of computing the score matrix X. A number of principal components $m = 6$ was chosen to compute this matrix, which corresponds to 99.89% of the 12 available components.

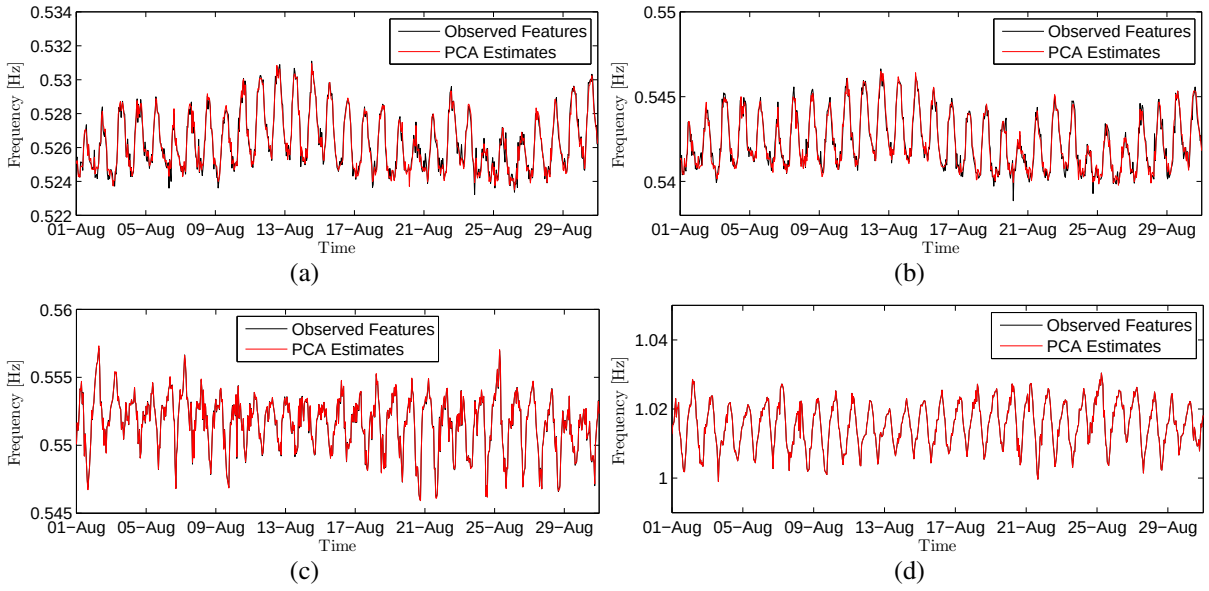

Fig. 6.34 – Time evolution of the natural frequencies of modes 3 (a), 4 (b) 5 (c) and 12 (d) observed (black line) and estimated with the **PCA** approach (red line) from 01/04/2009 to 31/03/2010.

In order to enhance the precision of the **PCA** model, the estimates of the natural frequencies with higher uncertainties (i.e., $\hat{\sigma}_{\hat{f}_n} > 3\sigma_{\hat{\sigma}_{\hat{f}_n}}$, with $\hat{\sigma}_{\hat{f}_n}$ denoting the standard deviations estimated with one iteration of the **pMLE-MM**) were not considered in the computation of the score matrix X. Once this matrix was computed, the natural frequencies were estimated and compared to their observed counterparts identified with the **pLSCF** technique. As shown in Fig. 6.34, the natural frequencies of modes 3, 4, 5 and 12 synthesized with **PCA** model along the month of August, 2009, are in good agreement with those observed within the same period. Afterwards, the **PCA** estimates were used to remove the component of the deviation of the natural frequencies related to environmental and operational factors.

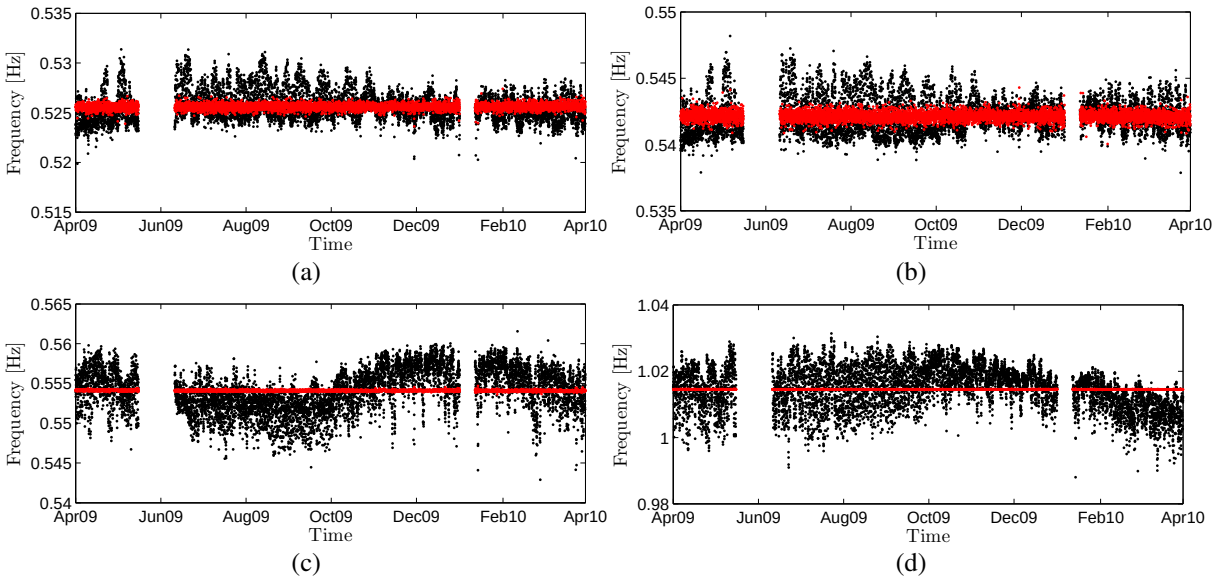

Fig. 6.35 – Time evolution of the natural frequencies of modes 3 (a), 4 (b), 5 (c) and 12 (d) tracked from 01/04/2009 to 31/03/2010 before (black dots) and after (red dots) removal of the environmental and operational effects with the **PCA** approach.

As shown in Figs. 6.35, the deviations of the natural frequencies of these modes after removal of the environmental and operational factors are significantly reduced compared to those of the observed natural frequencies. This is also verified in Tab. 6.6, where the standard deviations of all the 12 identified modes estimated before and after removal of the environmental effects are quantified. As seen in this table, the reduction is more significant for the modes with higher frequency deviations. At this point the effects of environmental and operational conditions were removed from the observed frequencies and, therefore, these features were ready to be used as damage indicators. Aiming at assessing the structural damage of the suspension roof, X-bar and T^2-chart were constructed to control the natural frequency shifts. The idea is that: if the observed frequencies exceed the confidence intervals previously defined and are not characterized as random outliers, these observations are considered to be related to structural change that

may, for instance, be caused by damage events.

Tab. 6.6 – Standard Deviations of the natural frequencies observed from 01/04/2009 to 31/03/2010 before and after removal of the environmental effects with the **PCA** model.

Mode	Before Application of PCA $\sigma_{\hat{f}_n}\left(\times 10^2\right)$ [Hz]	After Application of PCA $\sigma_{\hat{f}_n}\left(\times 10^2\right)$ [Hz]
1	0.664	0.326
2	0.949	0.313
3	1.410	0.261
4	1.259	0.307
5	2.699	0.064
6	1.977	0.063
7	1.428	0.182
8	2.195	0.393
9	1.957	0.379
10	2.572	0.247
11	4.095	0.006
12	6.336	0.019

Tab. 6.7 – Comparison between the outliers rates, I_o, of the observed natural frequencies estimated from 01/04/2009 to 31/03/2010 and from 01/04/2012 to 31/03/2013.

Mode	from 01/04/2009 to 31/03/2010 I_o (%)	from 01/04/2012 to 31/03/2013 I_o (%)
1	1.06	0.68
2	1.14	0.87
3	0.77	0.99
4	0.89	2.10
5	0.72	4.21
6	0.76	2.77
7	0.74	1.32
8	0.89	20.18
9	0.75	11.67
10	0.80	1.14
11	0.79	1.50
12	0.75	15.28

Once these charts were constructed, the main issue was then to distinguish whether a frequency point suited out of the confidence interval corresponds to a random outlier or, in fact, to a structural change. The outlier statistics is an efficient tool that can be used to distinguish random outliers associated to erroneous identification of the natural frequencies from the repeated outliers associated to abnormal events like structural changes. In the present study, the $\bar{X}$-Charts were constructed considering a confidence interval of 95.0% and with the assumption of a normal distribution. These charts were used to control the structural changes by monitoring the frequency shifts of the 12 modes identified over the course of the continuous monitoring of the

Braga stadium suspension roof. In Tab. 6.7 it is summarized the comparison between the outliers rates, I_o, estimated from the frequency samples observed from 01/04/2009 to 31/03/2010 (reference period) and those observed from 01/04/2012 to 31/03/2013.

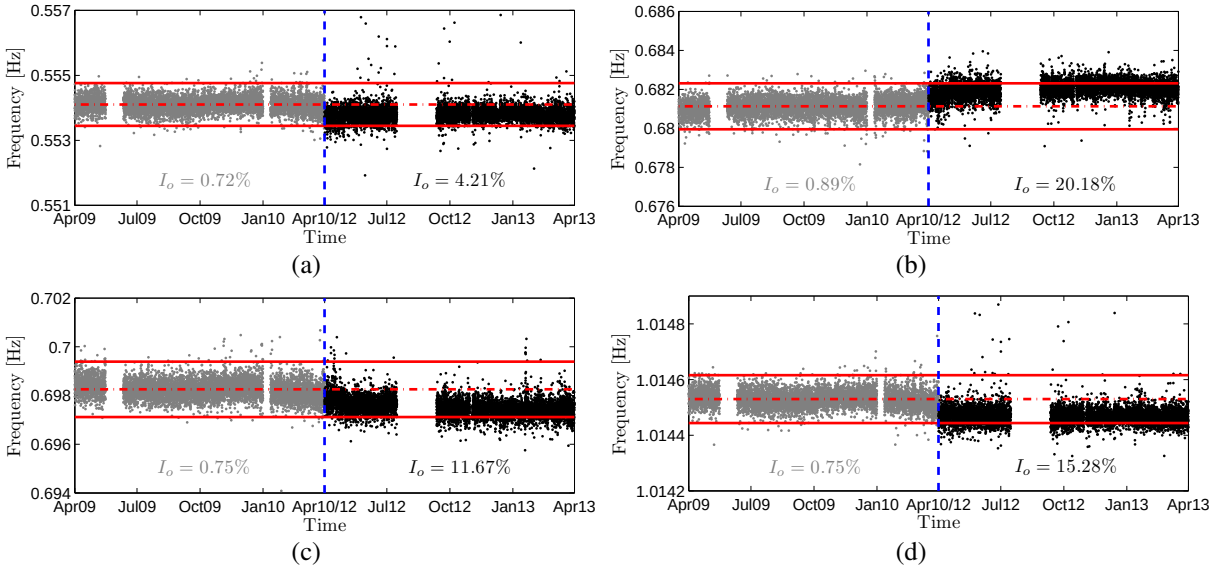

Fig. 6.36 – Time evolution of the observed natural frequencies of modes 5 (a), 8 (b), 9 (c) and 12 (d) tracked from 01/04/2009 to 31/03/2010 (gray dots) and from 01/04/2012 to 31/03/2013 (black dots) after removal of the environmental and operational effects with the **PCA** model.

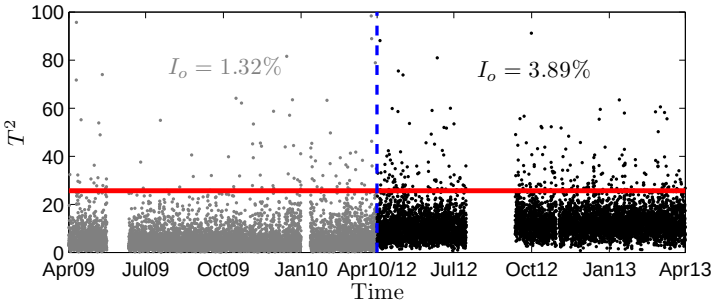

Fig. 6.37 – T^2-Chart constructed with the identified natural frequencies from 01/04/2009 to 31/03/2010 (gray dots) and from 01/04/2012 to 31/03/2013 (black dots) after the removal of the environmental and operational effects with the **PCA** model.

Inspection of this table reveals that significant increments in outliers rate of the latter period took place with regard to those computed for the former (from 01/04/2009 to 31/03/2010). These increments are particularly more significant for modes 5, 8, 9, 12, whose outliers rate climbed from previous 0.72, 0.89, 0.75 and 0.75% to 4.21, 20.18, 11.67 and 15.28%, respectively. The frequency shifts associated to these increments are clearly seen in $\bar{X}$-Charts of Figs. 6.36, which suggests that a structural change may have occurred in the monitored structure. It should be mentioned that, since the **PCA** environmental model is given as a linear transformation based

on the covariance of the observed features, the natural frequency shifts represented in Fig. 6.36 do not necessarily reflect the physical amount of variation on the natural frequencies over the time, but essentially indicate that a change took place. These results are in accordance with T^2-Chart shown in Fig. 6.37.

Differently from the $\bar{X}$ charts, which were built to detect damage from each identified natural frequency, the T^2-Chart illustrated in Fig. 6.37 was constructed to detect damage by means of a novelty index which considers the deviations of all natural frequencies at once and was computed by using the Mahalanobis norm (see Section 4.3.3). In order to control the deviation of such index, the **UCL** was put equal to 25.68. This control limit was computed considering a F-distribution with $m = 6$ and $n_p - m = 6$ degrees of freedom, and a confidence interval of 95%. By comparing the evolution of the T^2 index within 01/04/2012 and 31/03/2013 to that observed within the reference period (from 01/04/2009 and 31/03/2010), one also verifies that a significant variation took place. Such variation is synthesized by the outliers rates, I_o, estimated for both assessed periods presented in Fig. 6.37.

6.7. Conclusions

The modal properties of the Braga stadium suspension roof have been monitored since March, 2009, by an autonomous monitoring application specially designed for this purpose. This application was set to automatically track the modal properties of the suspension roof in the frequency range of 0-1.1 Hz along four years of monitoring by means of 3 different identification techniques. The characterization of the variation of modal properties over the time demonstrates the reliability, robustness and precision of the automated application. The assessment of the time evolution of the modal properties of the suspension roof showed that, differently from other identified modes, the natural frequencies of modes 3 and 4 vary proportionally with the daily and seasonal environmental temperature variations. This unexpected pattern of variation is believed to be due to the complex non-linear structural behaviour of the suspension roof.

Other interesting conclusion drawn from such assessment was obtained from the analysis of the evolution of the modal contributions over the monitored period. The results of this analysis revealed that, although the first and second modes tend to be more excited by the operational actions and, therefore, to contribute more to the measured output responses, no relevant changes on the natural frequencies of these modes were verified over the time. Concerning the analysis of wind measurements, the data registered by two anemometers over the course of 8 months was analysed. The main purposes of the analyses carried out from these measurements were: (1) to obtain a characterisation of the wind action, (2) to establish correlations with the modal parameters and structural responses and (3) to assess the influence of wind and temperature on

the variations of the natural frequencies and modal damping ratios of the suspension roof.

The main conclusions drawn from the analysis of measured wind data are: (1) during the measurement time frame, the mean wind speeds recorded were relatively low; (2) wind sensor **WS1** (located on the slab corner) registered the highest mean wind speeds, with a predominance of the North-Northwest direction, whilst wind sensor **WS2** measured much smaller mean wind speeds with North and South directions; and (3) the wind flows measured by wind sensor **WS2** tend to be more influenced by the stadium structure, fact that can be observed in the very wide spread from the positive wind incidence angle and by the higher turbulence intensities associated to the lower wind speeds. With regard to damage detection based on natural frequency shifts, two periods of analysis were investigated. The first, from 01/04/2009 to 31/03/2010, considered as reference period within which the natural frequencies were assumed to be estimated in the undamaged condition of the roof structure, and the second period, from 01/04/2012 to 31/03/2013, to verify if a permanent structural change has occurred in such structure.

For this purpose, an environmental model based on **PCA** was obtained by using the natural frequencies estimated with the **pLSCF** technique along the reference period as observed features. The precision of this model was then assessed by comparing its estimates with the observed natural frequencies. Aiming at detecting structural changes on the roof structure, this environmental model was applied to the natural frequencies estimated during both periods of analysis to mitigate the influence of the environmental and operational condition on these features. Comparing the results obtained for both periods of analysis, it was concluded that a slight structural change may have occurred in the suspension roof, which suggests that further detailed investigations can be conducted in order to determine the cause of such a change.

Chapter 7

CONCLUSIONS AND FUTURE RESEARCH

7.1. Conclusions

This thesis discussed several practical and theoretical aspects regarding the **MPE** techniques, continuous monitoring and damage detection in civil engineering. One of the most significant aspect of the present work is that it is not restricted to the discussion and application of the existing available theory concerning the input-output and output-only **MPE**, but proposes new theoretical developments in this subject area. The main conclusions of this thesis are highlighted as follows:

- Several models of vibrating structures suited to **EMA** and **OMA** were discussed in the framework of this thesis. An interesting aspect about these models is that, although they address the vibration phenomenon differently, it is verified that they are closely related among themselves.

- From the literature review of the state-of-the-art identification methods it was concluded that **pLSCF** and **SSI**-based techniques are some of the most commonly used identification techniques in **OMA**. The robustness and easiness to be adapted to automated **OMA** verified in the context of this thesis also corroborates this conclusion.

- In Döhler and Mevel (2013) an efficient approach to compute the confidence intervals of the estimates provided by the **SSI-COV** is presented. In context of the present thesis, however, a new strategy was followed to compute the uncertainties on the **SSI-COV** and **SSI-DATA** estimates. This strategy consists of: (1) identifying the poles and the observed mode shapes by means of stabilization diagrams; (2) computing the reference operational factor with the **LSFD** estimator; and, finally, (3) computing the confidence intervals of the estimated modal parameters by making use of the **pMLE-MM**. This strategy was applied to simulated and real-life structures and it was shown that the standard deviations estimated for the **SSI-DATA** and **SSI-COV** modal parameters were in very good agreement with those estimated for the **pLSCF** estimates (see Chapters 3, 5 and 6).

- Concerning the alternative implementation of the **pMLE-MM**, it was shown that the modal parameters and their respective standard deviations provided by such implementation were in very good agreement with the estimates obtained with the implementation proposed by (El-Kafafy, 2013), which demonstrates that it can be used in **EMA** and **OMA** without any loss of efficiency and precision. One of the main advantages of this alternative approach is the possibility to estimate the uncertainties on the identified natural frequencies and modal damping ratios directly from the normal matrices, avoiding the use of explicit linearisation formulas in a final step of the identification process.

- Comparing the poly-reference implementation of the **ML** estimator to its single reference counterpart, it is verified that main advantage of the former is related to the possibility to retain the poly-reference information and improve the estimates provided by the **pLSCF** estimator. The main disadvantage, however, is that it demands a much longer time to compute the normal matrices. The main benefit of the single reference **ML** estimator is that it results in an algorithm significantly faster. The main disadvantages, however, are, in fact, related to the limitations of modal model in pole residue form, as well as to the shortcomings of a single-reference identification technique. These disadvantages include: (1) difficulty of distinguishing between close spaced modes; (2) tendency of overestimating the confidence bounds of close spaced modes; and (3) impossibility to synthesize the spectrum, once the mode shapes and operational factors are estimated from the modal residuals by means of **SVD**.

- When dealing with reasonably separated modes, however, it is observed that the estimates of the uncertainty intervals provided by the single-reference **ML** estimator approximates the uncertainties estimated with its poly-reference counterpart.

- Despite the differences in acquisition of the systems used in the multi-patch operational modal analysis of the Braga stadium suspension roof, a good synchronization of the signals acquired by both systems could be established, thanks to the strategy used to remove the phase between these signals. With regard to the estimation of the modal parameters of the suspension roof, several modes were clearly identified in the frequency range of 0-2 Hz using **PoGER** merging approach combined with **pLSCF** identification technique, but only 30 modes presented well defined configurations. The other modes might be related to the modes of the slab that are poorly excited, to the modes that only involve the slab that was not instrumented or to the individual modes of the cables. Concerning the results of the analysis performed in time-domain, a significant influence of the 1^{st} and 2^{nd} modes on the total responses was verified, which reveals that these modes tend to be more excited by the environmental and operational conditions compared to the other identified modes.

- The autonomous monitoring application developed in the context of this thesis was able to automatically identify the modal parameters of the Braga stadium suspension roof in the frequency range of 0-1 Hz along four years of monitoring by means of 3 different **MPE** techniques with very few identification failures. The robustness and precision of the developed application permitted to characterize the variation the modal properties of the suspension roof and detect changes in its structural condition over the time.

- Concerning the wind measurements, although the results presented in this thesis corresponds to a time frame of only 8 months, some important conclusions were drawn from the analysis of the data collected within this period. It was verified from this analysis, for instance, that: (1) the mean wind speeds recorded during this time frame were relatively low; (2) the wind sensor located on the slab corner registered the highest mean wind speeds, whist the wind sensor located at the middle of longest edge measured much smaller mean wind speeds; and (3) the wind flows at middle of slab tend to be more influenced by the stadium structure.

- The damage assessment of suspension roof based on the variation of natural frequencies revealed that these modal properties are highly influenced by the environmental and operational conditions, fact that was evidenced by the cross correlations between the natural frequencies and modal damping ratios, and the wind measurements. Despite this influence, an output-only environmental model based on **PCA** was efficiently applied to these features to remove the component of deviation due to the environmental and operational conditions, as well as to detect structural changes. The assessment of the variation of these features over the course of four years of monitoring indicates that a slight permanent change has occurred in the roof structure. This conclusion suggests that further detailed investigation can be performed in other to determine and localize the cause of such a change.

7.2. Future Research

This thesis contains useful contributions in the context of **EMA**, **OMA**, automated **MPE** and vibration-based damage detection, particularly in the framework of optimization and uncertainty quantification of the modal parameter estimates. Nevertheless, future research is certainly needed to improve such contributions.

- Although the automated modal analysis application developed in the context of this thesis has proven to be very robust and efficient, new strategies and techniques can be added to improve the performance of this application, particularly when dealing with modes whose natural frequencies cross among themselves over the course of monitoring period. Such improvements can be added, for instance, by taking into account uncertainty intervals of the estimates optimized with the **pMLE-MM**. This can be done by taking advantage of the fact the numerical poles tend to have higher standard deviation compared to the physical ones.

- In this thesis, a new strategy was applied to estimate confidence intervals of the modal

parameters estimated with the **SSI** techniques (e.g. **SSI-DATA** and **SSI-COV**). The efficiency of this strategy was assessed by comparing the estimated uncertainties to those provided by the combined **pLSCF-pMLE-MM** technique. It would be interesting, however, to compare such strategy to the approach described in Döhler and Mevel (2013) in order to assess the efficiency of both strategies in terms of computational performance and precision.

- Following the lines of Vuerinckx et al. (2001), analyse for the (single) reference **ML** estimator, as well as for its poly-reference counterpart discussed in Chapter 3, whether the strongly non-linear relationship between the transfer function coefficients and the modal parameters results in non-ellipsoidal 95% uncertainty bounds, for a number of practical modal analysis problems.

- In context of the high spatial **OMA** of the Braga stadium suspension roof, due to the limited computational resources available, the **pMLE-MM** was only applied to estimate the confidence intervals of the modal parameters provided by the **pLSCF** method. Therefore, it would be interesting to apply the **pMLE-MM** algorithm to fully optimize the modal parameters estimates obtained with **PreGER-pLSCF**, **PoGER-SSI-COV** and **PoGER-pLSCF**, and then assess the gain in precision with respect to the starting estimates.

- In the context of the continuous dynamic monitoring of the Braga Stadium suspension roof discussed in Chapter 6, the **pMLE-MM** was only used to compute the uncertainty bounds on the modal parameters estimated from the continuously collected datasets with the **pLSCF**, **SSI-DATA** and **SSI-COV** identification techniques. Since the **pMLE-MM** algorithm is time consuming and requires a high computational processing load, it was not possible to fully optimize the starting estimates obtained from each measured dataset due to the limited time and computational resources available. Therefore, it would be interesting to assess the gain in precision in terms of monitoring results if the modal parameters are fully optimized with the **pMLE-MM**.

- In this thesis, only a level 1 damage assessment based on natural frequencies was addressed. It would be interesting to extend the assessment capabilities by including mode shape estimates and/or a numerical model of the monitored structure to assess its structural condition, to localize and to quantify the damage in a automated manner.

- In the context of the continuous monitoring of the Braga stadium suspension roof, verify if the variations observed for the natural frequencies are, in fact, associated to a permanent structural change and, with the aid of a refined analytical model of the structure, try

localize and qualify the source of such change.

Appendix A

LSFD WITH ENHANCED UPPER AND LOWER RESIDUALS

A.1. Estimation of the Mode Shapes with LSFD

The **LSFD** estimator is frequently used in conjunction with other frequency-domain identification techniques to estimate either the mode shapes, the operational factors or the modal residuals. If the operational factors, $L \in \mathbb{C}^{N_i \times n}$, the denominator coefficients of the enhanced upper and lower residual model, a,b,$c \in \mathbb{R}$, and the poles, $\lambda_r \in \mathbb{C}$, are known a priori, the modal shapes, $V \in \mathbb{C}^{N_o \times n}$, and the numerator matrix coefficients, AR, BR, $CR \in \mathbb{R}^{N_o \times N_i}$, can be determined in a least-squares sense using the modal model with enhanced residual model (3.131). This is accomplished by minimizing the following equation error with respect to the unknown parameters:

$$E_o(\Theta,\omega) = \sum_{r=1}^{N_m} \frac{v_{or} l_r^T}{j\omega - \lambda_r} + \frac{v_{or}^* l_r^H}{j\omega - \lambda_r^*} + \frac{[AR]_o + j\omega [BR]_o + (j\omega)^2 [CR]_o}{d(\omega)} - H_o(\omega) \tag{A.1}$$

where $E_o(\Theta,\omega) \in \mathbb{C}^{1\times N_i}$ and $H_o(\omega) \in \mathbb{C}^{1\times N_i}$ are row vectors containing the elements of the equation error and of the measured **FRF**s corresponding to output o ($o = 1, 2, \cdots, N_o$), respectively; $[AR]_o$, $[BR]_o$, $[CR]_o \in \mathbb{R}^{1\times N_i}$ stand for the o^{th} row of the numerator residual matrices AR, BR, CR, respectively; and $d(\omega) = a + j\omega b + (j\omega)^2 c$ the denominator of the enhanced residual model. This equation error can be parametrized as:

$$\Theta = \left\langle \mathrm{Re}(V_o) \quad \mathrm{Im}(V_o) \quad [AR]_o \quad [BR]_o \quad [CR]_o \right\rangle \in \mathbb{R}^{1\times(2N_m+3N_i)} \tag{A.2}$$

Writing down eq. (A.1) for each frequency line f ($f = 2, 3, \ldots, N_f$) and reformulating the obtained equations into a single matrix expression, yields:

$$E_o(\Theta) = \Theta J - H_o \tag{A.3}$$

with

$$\begin{aligned} E_o(\Theta) &= \left\langle E_o(\Theta,\omega_2) \quad \cdots \quad E_o(\Theta,\omega_{N_f}) \right\rangle \in \mathbb{C}^{1\times N_i(N_f-1)} \\ H_o &= \left\langle H_o(\omega_2) \quad \cdots \quad H_o(\omega_{N_f}) \right\rangle \in \mathbb{C}^{1\times N_i(N_f-1)} \end{aligned} \tag{A.4}$$

and $J \in \mathbb{C}^{(2N_m+3N_i)\times N_i(N_f-1)}$ denoting the so-called Jacobian matrix. It is straightforward to solve eq. (A.3) for Θ in a linear least squares sense. Yet, in order to guarantee the realness of Θ, J and H_o are replaced in eq. (A.3), respectively, by:

$$(J)_{\text{re}} = \begin{bmatrix} \text{Re}\,(J) & \text{Im}\,(J) \end{bmatrix}, \quad (H_o)_{\text{re}} = \begin{bmatrix} \text{Re}\,(H_o) \\ \text{Im}\,(H_o) \end{bmatrix} \tag{A.5}$$

and, after some manipulations of the resulting expression, the following equation can be derived to compute the mode shapes and residuals:

$$\begin{Bmatrix} \text{Re}\,(V_o)^T \\ \text{Im}\,(V_o)^T \\ [AR]_o^T \\ [BR]_o^T \\ [CR]_o^T \end{Bmatrix} = \left(\text{Re}\left(J^* J^T\right)\right)^{-1} \text{Re}\left(J^* H_o^T\right) \tag{A.6}$$

A.2. Estimation of the Operational Factors with LSFD

If the poles, mode shapes and denominator coefficients of the enhanced residual model are the known parameters, the operational factors, L, and the numerator matrix coefficients AR, BR, CR of the enhanced residual model (3.131) are found in linear least squares sense by following a strategy similar to the one used to estimate the mode shapes in Section A.1. In this case, the following equation error is minimized with respect to the unknown parameters:

$$E_i(\Theta, \omega) = \sum_{r=1}^{N_m} \frac{v_r l_{ri}}{j\omega - \lambda_r} + \frac{v_r^* l_{ri}}{j\omega - \lambda_r^*} + \frac{[AR]_i + j\omega\,[BR]_i + (j\omega)^2\,[CR]_i}{d(\omega)} - H_i(\omega) \tag{A.7}$$

where $E_i(\Theta, \omega) \in \mathbb{C}^{N_o \times 1}$ and $H_i(\omega) \in \mathbb{C}^{N_o \times 1}$ are column vectors containing the elements of the equation error and of the measured **FRF**s corresponding to input i ($i = 1, 2, \cdots, N_i$), respectively; and $[AR]_i$, $[BR]_i$, $[CR]_i \in \mathbb{R}^{N_o \times 1}$ stand for the i^{th} columns of the numerator residual matrices AR, BR, CR, respectively. This equation error can be parametrized as:

$$\Theta = \left\langle \text{Re}\,(L_i) \quad \text{Im}\,(L_i) \quad [AR]_i^T \quad [BR]_i^T \quad [CR]_i^T \right\rangle^T \in \mathbb{R}^{(2N_m + 3N_o) \times 1} \tag{A.8}$$

Reformulating equation error (A.7) for all frequency lines into a single expression, yields:

$$E_i(\Theta) = J\Theta - H_i \tag{A.9}$$

with

$$E_i(\Theta) = \left\{ \begin{array}{c} E_i(\Theta,\omega_2) \\ \vdots \\ E_i(\Theta,\omega_{N_f}) \end{array} \right\} \in \mathbb{C}^{N_o(N_f-1)\times 1}, \quad H_i = \left\{ \begin{array}{c} H_i(\omega_2) \\ \vdots \\ H_i(\omega_{N_f}) \end{array} \right\} \in \mathbb{C}^{N_o(N_f-1)\times 1} \tag{A.10}$$

and $J \in \mathbb{C}^{N_o(N_f-1)\times(2N_m+3N_o)}$ denoting the Jacobian matrix. Once the Jacobian matrix is computed, eq. (A.9) can be solved by making use of the same strategy applied in Section A.1 in order to guarantee the realness of Θ. By applying such strategy to eq. (A.9), the following solution is obtained for Θ:

$$\left\{ \begin{array}{c} \mathrm{Re}\,(L_i) \\ \mathrm{Im}\,(L_i) \\ [AR]_i \\ [BR]_i \\ [CR]_i \end{array} \right\} = \left(\mathrm{Re}\left(J^H J\right)\right)^{-1} \mathrm{Re}\left(J^H H_i\right) \tag{A.11}$$

A.3. Estimation of the Modal Residuals with LSFD

A similar strategy can be applied to estimate the modal residues using the modal model in pole residue form with enhanced upper and lower residual terms as in eq. (2.148). By making of this model, the following equation error is obtained:

$$E_o(\Theta,\omega) = \sum_{r=1}^{N_m} \frac{[Res]_{ro}}{j\omega-\lambda_r} + \frac{[Res]^*_{ro}}{j\omega-\lambda^*_r} + \frac{[AR]_o + j\omega\,[BR]_o + (j\omega)^2\,[CR]_o}{d(\omega)} - H_o(\omega) \tag{A.12}$$

with $[Res]_{ro}$ representing the o^{th} row of the modal residual matrix corresponding to the r^{th} mode and Θ a row vector containing the unknown parameters:

$$\Theta = \left[\mathrm{Re}\,([Res])^T_{1o} \;\; \cdots \;\; \mathrm{Re}\,([Res])^T_{N_m o} \;\; \mathrm{Im}\,([Res])^T_{1o} \;\; \cdots \;\; \mathrm{Im}\,([Res])^T_{N_m o} \;\; [AR]^T_o \;\; [BR]^T_o \;\; [CR]^T_o\right]^T \in \mathbb{R}^{(2N_m+3)\times N_i} \tag{A.13}$$

writing down eq. (A.12) for each frequency line f, yields:

$$E_o(\Theta) = J\Theta - H_o = 0 \tag{A.14}$$

with $E_o(\Theta)$ and H_o given now by:

$$E_o(\Theta) = \begin{bmatrix} E_o(\Theta, \omega_2) \\ \vdots \\ E_o(\Theta, \omega_{N_f}) \end{bmatrix} \in \mathbb{C}^{(N_f-1)\times N_i}, \quad H_o = \begin{bmatrix} H_o(\omega_2) \\ \vdots \\ H_o(\omega_{N_f}) \end{bmatrix} \in \mathbb{C}^{(N_f-1)\times N_i} \tag{A.15}$$

and $J \in \mathbb{C}^{(N_f-1)\times(2N_m+3)}$ representing the Jacobian matrix. Since the parameters Θ are assumed to be real coefficients, they are found by following the same strategy used to derive eq. (A.6), yielding:

$$\begin{Bmatrix} \mathrm{Re}\left([Res]\right)_{1o} \\ \vdots \\ \mathrm{Re}\left([Res]\right)_{N_m o} \\ \mathrm{Im}\left([Res]\right)_{1o} \\ \vdots \\ \mathrm{Im}\left([Res]\right)_{N_m o} \\ [AR]_o \\ [BR]_o \\ [CR]_o \end{Bmatrix} = \left(\mathrm{Re}\left(J^H J\right)\right)^{-1} \mathrm{Re}\left(J^H H_o\right) \tag{A.16}$$

Appendix B

HIGH SPATIAL RESOLUTION **OMA** OF THE BRAGA STADIUM SUSPENSION ROOF

B.1. Identification Results Obtained with PreGER and pLSCF

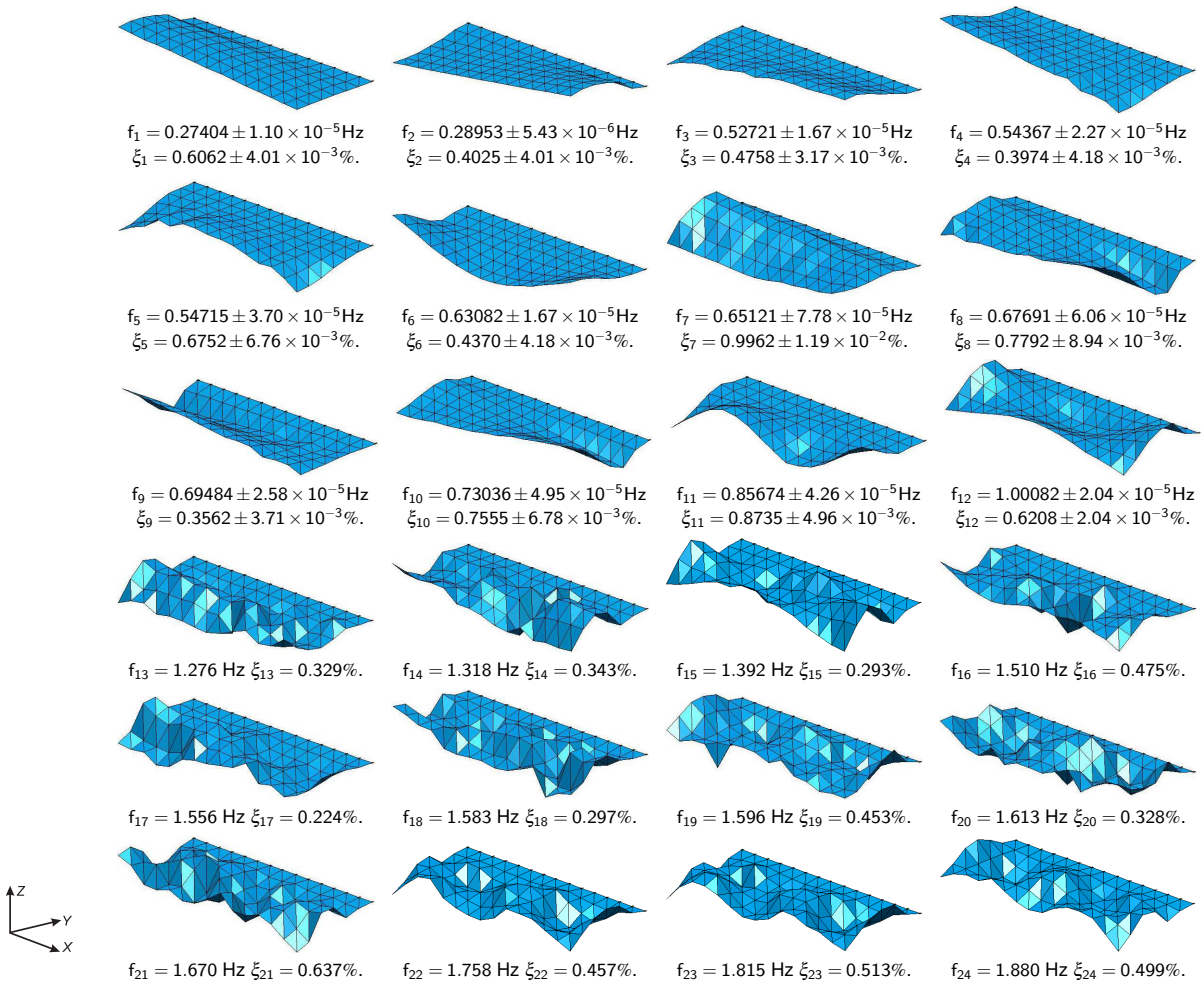

Fig. B.1 – Natural frequencies, damping coefficients and the corresponding mode shapes of vibration of the West slab experimentally identified in the range of 0-2 Hz using **PreGER** merging strategy and the **pLSCF** technique.

B.2. Identification Results Obtained with PoGER and SSI-COV

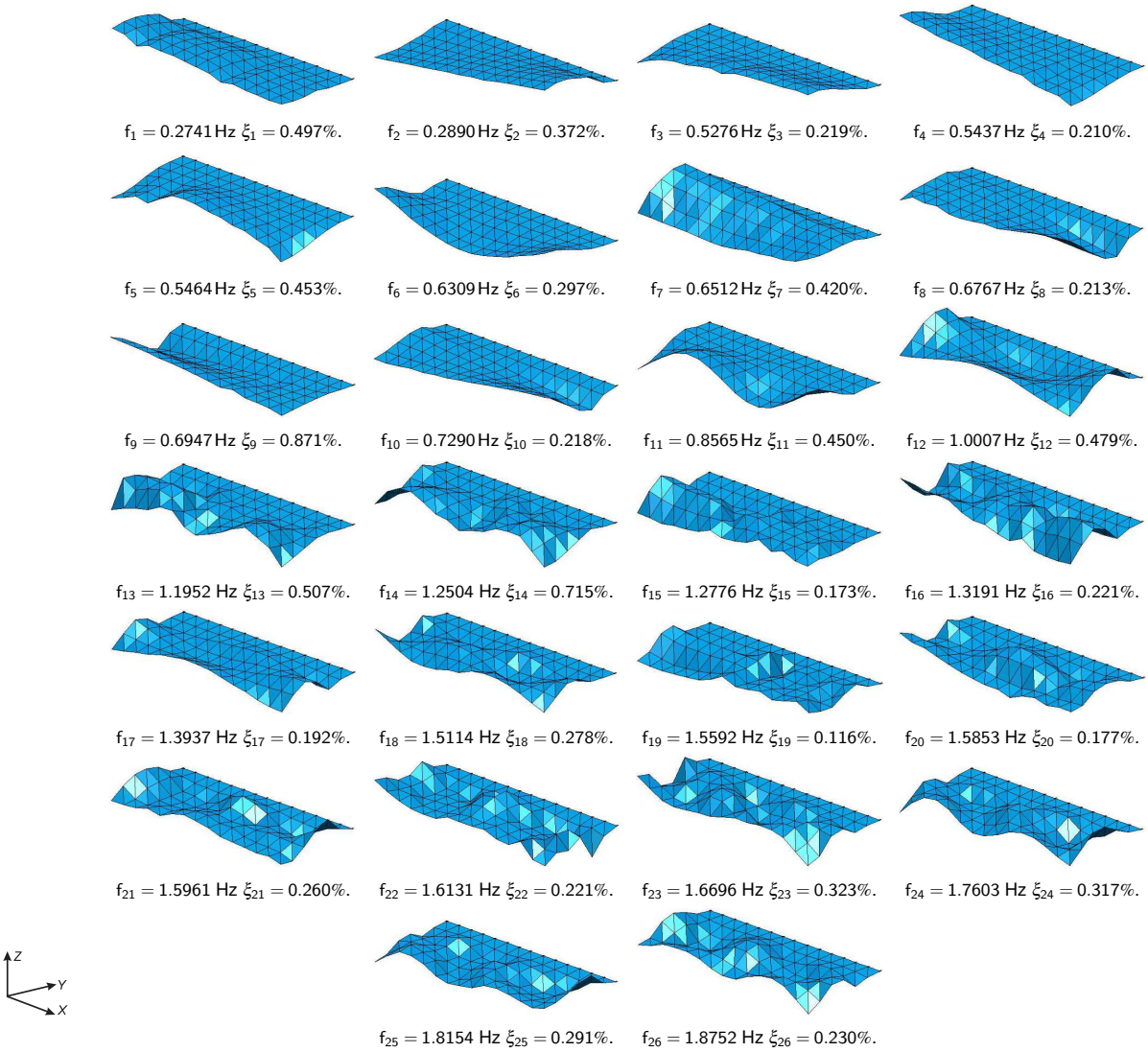

Fig. B.2 – Natural frequencies, damping coefficients and the corresponding mode shapes of the West slab experimentally identified in the range of 0-2 Hz using the **PoGER** approach and the **SSI-COV** technique.

B.3. Identification Results Obtained with PoGER and pLSCF

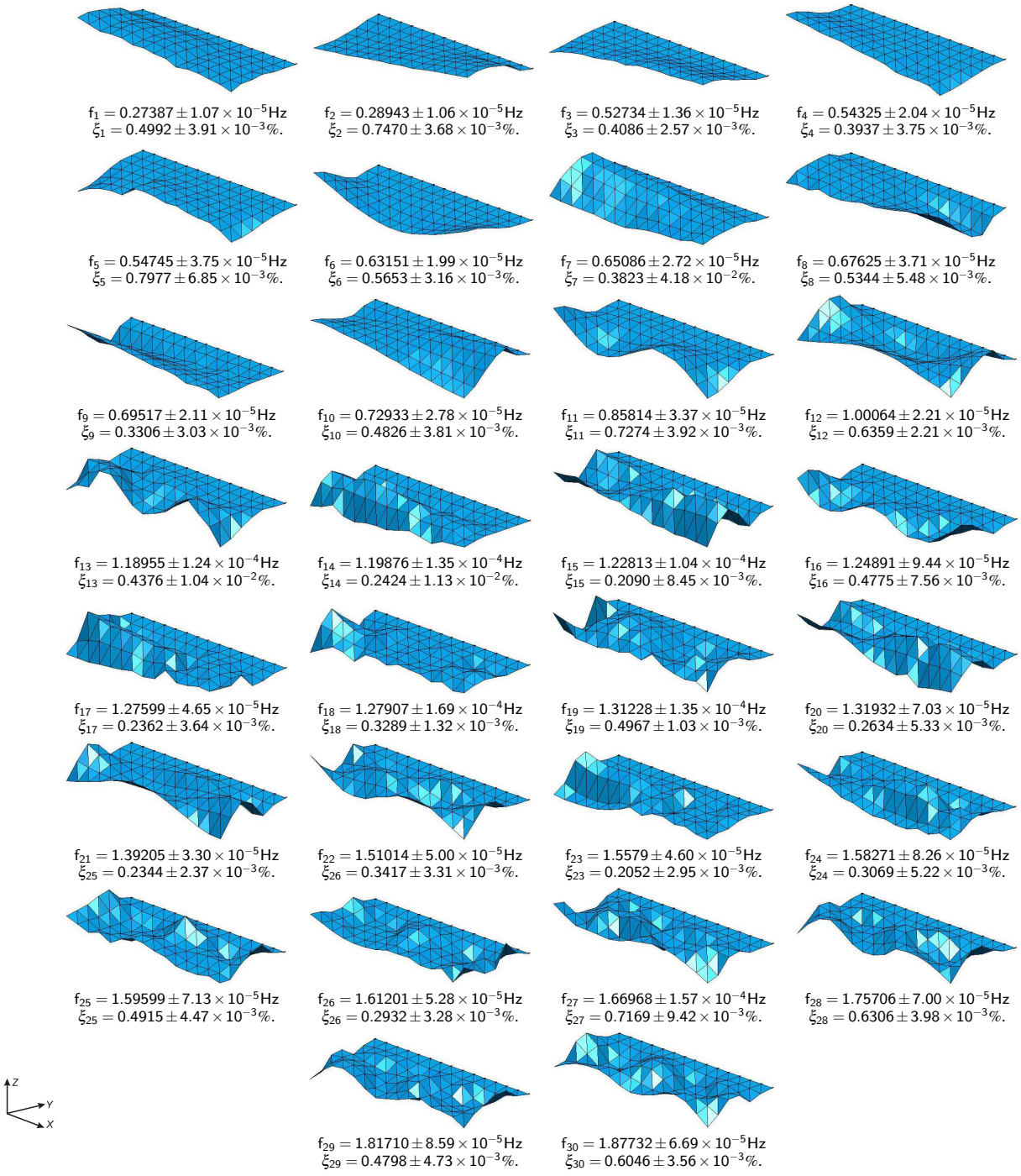

Fig. B.3 – Natural frequencies and damping coefficients with their respective confidence bounds, and the corresponding mode shapes of vibration of the West slab experimentally identified in the range of 0-2 Hz using the **PoGER** approach and the **pLSCF** technique.

Appendix C

STATISTICS OF THE NATURAL FREQUENCIES AND DAMPING RATIOS MONITORED OVER THE YEAR OF 2001

Tab. C.1 – Mean and standard deviation values of the natural frequencies and damping ratios estimated with **SSI-DATA**, **SSI-COV** and **pLSCF**, and standard deviations of their uncertainties intervals estimated with the **pMLE-MM** over the year of 2011.

MPE Technique	Mode	Estimated Parameters				Estimated Standard Deviations			
		$\mu_{\hat{f}_n}$ (Hz)	$\sigma_{\hat{f}_n}$ (Hz) $(\times 10^3)$	$\mu_{\hat{\xi}_n}$ (%)	$\sigma_{\hat{\xi}_n}$ (%) $(\times 10)$	$\mu_{\hat{\sigma}_{\hat{f}_n}}$ (Hz) $(\times 10^4)$	$\sigma_{\hat{\sigma}_{\hat{f}_n}}$ (Hz) $(\times 10^4)$	$\mu_{\hat{\sigma}_{\hat{\xi}_n}}$ (%) $(\times 10^2)$	$\sigma_{\hat{\sigma}_{\hat{\xi}_n}}$ (%) $(\times 10^2)$
SSI-DATA	1	0.27455	0.58	0.24518	1.57	0.18	0.26	0.65	0.96
	2	0.29008	0.92	0.21625	1.49	0.09	0.13	0.31	0.45
	3	0.52602	1.49	0.22809	1.32	0.29	0.47	0.55	0.89
	4	0.54213	1.35	0.19270	1.06	0.35	0.37	0.64	0.68
	5	0.55009	2.80	0.44480	1.88	2.25	2.96	4.07	5.35
	6	0.63090	2.10	0.30324	1.49	0.36	0.41	0.57	0.65
	7	0.65304	1.25	0.23983	1.17	0.49	0.60	0.75	0.92
	8	0.67942	2.12	0.18420	1.20	0.37	0.46	0.54	0.68
	9	0.69584	1.99	0.18314	1.04	0.68	0.82	0.98	1.18
	10	0.73064	2.75	0.18119	1.35	0.33	0.38	0.45	0.52
	11	0.86303	4.09	0.51886	3.17	1.59	1.25	1.84	1.44
	12	1.00482	5.37	0.50148	2.71	0.54	0.60	0.54	0.60
SSI-COV	1	0.27456	0.58	0.23383	1.48	0.14	0.20	0.52	0.73
	2	0.29007	0.93	0.23602	1.52	0.10	0.14	0.35	0.49
	3	0.52605	1.51	0.34848	2.00	0.41	0.42	0.77	0.80
	4	0.54216	1.35	0.23470	1.22	0.35	0.36	0.65	0.66
	5	0.55019	2.92	0.40550	1.86	2.06	2.54	3.73	4.59
	6	0.63088	2.11	0.31958	1.88	0.34	0.39	0.54	0.61
	7	0.65299	1.23	0.21128	1.69	0.39	0.43	0.60	0.66
	8	0.67938	2.14	0.20906	1.46	0.36	0.38	0.53	0.56
	9	0.69581	2.00	0.17431	1.07	0.62	0.63	0.89	0.90
	10	0.73059	2.76	0.12610	0.96	0.25	0.24	0.34	0.33
	11	0.86222	4.36	0.43810	2.29	1.45	1.10	1.68	1.27
	12	1.00445	5.49	0.45461	1.50	0.45	0.46	0.45	0.46
pLSCF	1	0.27457	0.59	0.28523	1.85	0.10	0.17	0.36	0.61
	2	0.29007	0.93	0.21662	1.46	0.06	0.09	0.20	0.31
	3	0.52614	1.51	0.27273	2.03	0.14	0.25	0.27	0.48
	4	0.54222	1.35	0.22994	1.24	0.20	0.26	0.36	0.49
	5	0.55029	2.96	0.43288	1.85	1.14	1.65	2.06	2.99
	6	0.63084	2.11	0.33461	1.86	0.21	0.26	0.33	0.41
	7	0.65323	1.31	0.27934	2.03	0.26	0.33	0.40	0.50
	8	0.67954	2.15	0.20243	1.24	0.22	0.36	0.33	0.53
	9	0.69585	2.02	0.18938	0.97	0.39	0.52	0.57	0.75
	10	0.73061	2.75	0.20029	1.34	0.20	0.37	0.28	0.50
	11	0.86217	4.36	0.40029	2.17	1.62	1.62	1.87	1.87
	12	1.00437	5.41	0.45799	1.81	0.61	0.96	0.61	0.95

Appendix D

MODAL PROPERTIES OF THE LATTICE TOWER STRUCTURE USED IN SIMULATION EXAMPLES

In this appendix, the modal properties of the lattice tower structure used in Chapters 2, 3 and 4 is presented. The exact natural frequencies, damping ratios and modal masses are presented in Tab. D.1, whist the real modes are shown in Tab. D.2. The purpose of this appendix is to allow for reproducibility of the identification results obtained throughout this thesis by other researchers.

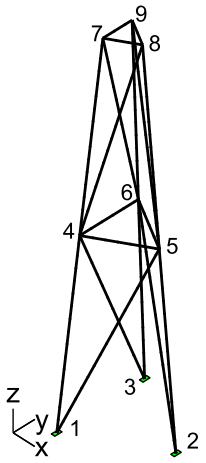

Tab. D.1 – Natural frequencies, damping ratios and modal masses of the lattice tower structure used in simulation examples.

Mode	f_n [Hz]	ξ_n [%]	m_i [Kg]
1	1.2869	1.0	2608.8271
2	1.2937	1.0	2592.8286
3	2.2250	1.0	281.0965
4	3.8712	1.0	1431.1279
5	3.8932	1.0	1410.8619
6	6.1745	1.0	54.2551
7	14.3476	1.0	14.2185
8	14.4828	1.0	19.2943
9	16.1054	1.0	48.3293
10	16.1452	1.0	48.2533
11	20.2652	1.0	11.7349
12	21.9314	1.0	1620.9371
13	26.4391	1.0	5.0991
14	26.6597	1.0	5.1761
15	38.5221	1.0	5.2109
16	38.7803	1.0	6.0801
17	45.6078	1.0	341.6011
18	46.0007	1.0	4.1369

Tab. D.2 – Real modes of the lattice tower structure used in simulation examples.

DOF/Mode	1	2	3	4	5	6
1	0.4468	-0.6874	0.3127	0.3392	0.6939	0.1024
2	-0.6972	-0.4527	-0.1825	-0.6996	0.3094	-0.0583
3	-0.1535	0.0972	0.6919	0.1836	0.1287	-0.0468
4	0.4489	-0.6965	0.0014	0.3186	0.6843	0.0022
5	-0.7059	-0.4370	0.3573	-0.7115	0.3235	0.1151
6	0.1269	0.1106	0.6946	-0.1849	0.0980	-0.0492
7	0.4530	-0.7100	-0.3104	0.3150	0.7140	-0.0984
8	-0.6964	-0.4554	-0.1829	-0.6918	0.3326	-0.0586
9	-0.0022	-0.1295	0.7165	0.0280	-0.1924	-0.0271
10	0.6378	-0.9859	0.1808	-0.4521	-0.9673	-0.1968
11	-0.9953	-0.6416	-0.1021	0.9861	-0.4612	0.1132
12	-0.0783	0.0693	0.9832	0.2200	0.2015	-0.9721
13	0.6400	-0.9925	0.0078	-0.4557	-0.9801	-0.0036
14	-1.0000	-0.6303	0.1976	1.0000	-0.4387	-0.2217
15	0.0457	0.0748	0.9851	-0.1705	0.1656	-0.9768
16	0.6426	-1.0000	-0.1654	-0.4619	-1.0000	0.1901
17	-0.9952	-0.6422	-0.1022	0.9853	-0.4654	0.1135
18	-0.0115	-0.0249	1.0000	0.0530	-0.1247	-1.0000

REFERENCES

Akaike, H. (1974). Stochastic Theory of Minimal Realization. *IEEE Transactions on Automatic Control*, 19(6):667–674.

Amador, S. (2007). Programa Computacional com Interface Grafica para Identificacao Estocastica de Parametros Modais de Estruturas Civis - Aplicacao em Pontes e Torres de Linha de Transmissao. Master's thesis, Federal University of State of Pará, Brazil. In portuguese.

Amador, S. (2009). Dynamo Viewer Uses's Guide: A Graphical User Interface for Long Term Dynamic Monitoring of Civil Engineering Structures.

Amador, S. (2010). Operational Modal Analysis Studio 2010 - User's Guide. Manual rev. 1, FEUP.

Amador, S., Magalhães, F., Caetano, E., and Cunha, A. (2011). Analysis of the Influence of Environmental Factors on Modal Properties of the Braga Stadium Suspension Roof. In *Proceedings of the International Conference on Experimental Vibration Analysis for Civil Engineering Structures (EVACES) 2011*, Varenna, Italy.

Amador, S., Martins, N., Magalhães, F., Caetano, E., and Cunha, A. (2012). One Year of Continuous Dynamic Monitoring of a Football Stadium Suspension Roof: Analysis of Data Provided by an Autonomous Monitoring Application. In *Proceedings of the International Conference on Noise and Vibration Engineering (ISMA) 2012*, Leuven, Belgium.

Andersen, P. (1997). *Identification of Civil Engineering Structures Using Vector ARMA Models*. PhD thesis, Aalborg Universisty, Department of Building Technology and Structural Engineering, Danmark.

Arnold, W.F., I. and Laub, A. (1984). Generalized Eigenproblem Algorithms and Software for Algebraic Riccati Equations. *Boundary-Layer Meteorology*, 72(12):1746–1754.

Arruda, J. R. F. (1992). Objective Functions for the Nonlinear Curve Fit of Frequency-response Functions. *AIAA Journal*, 30(3):855–857.

Battista, R. C. and Pfeil, M. S. (2000). Reduction of Vortex-induced Oscillations of Rio- Niteroi Bridge by Dynamic Control Devices. *Journal of Wind Engineering and Industrial Aerodynamics*, 84(3):273–288.

Bendat, J. S. and Piersol, A. G. (1993). *Engineering Applications of Correlation and Spectral Analysis*, volume 1. John Wiley and Sons, New York, USA, second edition.

Bezdek, J. C. (1981). *Pattern Recognition with Fuzzy Objective Function*, volume 1. Plenum Press, New York, USA, first edition.

Brincker, R., Ventura, C. E., and Andersen, P. (2001). Damping Estimation by Frequency Domain Decomposition. In *Proceedings of the 19th International Modal Analysis Conference (IMACXIX)*, volume 1, Orlando, Florida, USA. Society for Experimental Mechanics.

Brincker, R., Zhang, L., and Andersen, P. (2000). Modal Identification from Ambient Responses Using Frequency Domain Decomposition. In *Proceedings of the 18th International Modal Analysis Conference (IMACXVIII)*, San Antonio, Texas, USA. Society for Experimental Mechanics.

Böswald, M., Göge, D., Füllekrug, U., and Govers, Y. (2006). A Review of Experimental Modal Analysis Methods with Respect to their Applicability to Test Data of Large Aircraft. In *Proceedings of the International Conference on Noise and Vibration Engineering (ISMA) 2006*, pages 2461–2481, Leuven, Belgium.

Caetano, E. and Cunha, A. (2001). Numerical Modeling of the Structural Behaviour of the New Braga Stadium Roof. Technical report, FEUP/VIBEST.

Caetano, E., Cunha, A., and Magalhães, F. (2010). Numerical and Experimental Studies of Braga Sports Stadium Suspended Roof. *Journal of Structure and Infrastructure Engineering*, 6(6):715–724.

Cara, F. R., Juar, J., Reynders, E., and De Roeck, G. (2013). Modal Contribution and State-space Order Selection in Operational Modal Analysis. *Mechanical Systems and Signal Processing*, 38(2):276–298.

Carden, E. P. and Brownjoh, J. M. W. (2008). Fuzzy Clustering of Stability Diagrams for Vibration-based Structural Health Monitoring. *Computer-Aided Civil and Infrastructure Engineering*, 23(5):360–372.

Cauberghe, B. (2004). *Applied Frequency-domain System Identification in the Field of Experimental and Operational Modal Analysis*. PhD thesis, Faculteit Toegepaste Wetenschappen Pleinlaan Vrije, Universiteit Brussel (Belgium).

Cauberghe, B., Guillaume, Verboven, P., Parloo, E., and Vanlanduit, S. (2004). A Poly-reference Implementation of the Maximum Likelihood Complex Frequency-domain Estimator and Some Industrial Applications. In *Proceedings of the 22nd International Modal Analysis Conference (IMACXXII)*, Dearborn, Michighan, USA. Society for Experimental Mechanics.

CEN (2005). *Eurocode 1: Actions on structures - General actions - Part 1-4: Wind actions*.

Chopra, A. K. (1995). *Dynamics of Structures - Theory and Applications to Earthquake Engineering*, volume 1. Prentice Hall, New Jersey, USA.

Chou, J.-H. and Ghabouss, J. (2001). Genetic Algorithm in Structural Damage Detection. *Computers & Structures*, 79(14):1335–1353.

Cremona, C. and Foucriat, J.-C. (2002). *Comportement au Vent des Ponts*, volume 1. Presses de l'École Nationale des Ponts et Chaussées, France, first edition. In french.

Cunha, A., Caetano, E., Magalhães, F., and Moutinho, C. (2013). Recent Perspectives in Dynamic Testing and Monitoring of Bridges. *Journal of Structural Control and Health Monitoring*, 20(6):853–877.

De Boe, P. and Golinval, J.-C. (2003). Principal Component Analysis of Piezo-sensor Array for Damage Localization. *Structural Health Monitoring*, 2(2):137–144.

De Troyer, T., Guillaume, P., Pintelon, R., and Vanlanduit, S. (2009a). Fast Calculation of Confidence Intervals on Parameter Estimates of Least-squares Frequency-domain Estimators. *Mechanical Systems and Signal Processing*, 23(2):261–273.

De Troyer, T., Guillaume, P., and Steenackers, G. (2009b). Fast Variance Calculation of Polyreference Least-squares Frequency-domain Estimates. *Mechanical Systems and Signal Processing*, 23(5):1423–1433.

Deraemaekera, A., E. Reynders, E., G. De Roeck, G., and Kullaac, J. (2008). Vibration-based Structural Health Monitoring Using Output-only Measurements Under Changing Environment. *Mechanical Systems and Signal Processing*, 22(1):34–56.

Döhler, M., Hille, F., Mevel, L., and Rücker, W. (2014). Structural Health Monitoring with Statistical Methods During Progressive Damage Test of S101 Bridge. *Engineering Structures*, 69(15):183–193.

Döhler, M. and Mevel, L. (2013). Efficient Multi-order Uncertainty Computation for Stochastic Subspace Identification. *Mechanical Systems and Signal Processing*, 38(2):346–366.

Döhler, M., Reynders, E., Magalhães, F., Mevel, L. De Roeck, G., and Cunha, A. (2010). Pre- and Post-identification Merging for Multi-Setup OMA with Covariance-Driven SSI. In *Proceedings of the 28th International Modal Analysis Conference (IMACXXVIII)*, Jacksonville, Florida, USA. Society for Experimental Mechanics.

Doebling, S., Farrar, C., Prime, M., and Shevitz, D. (1996). Damage Identification and Health Monitoring of Structural and Mechanical Systems from Changes in their Vibration Characteristics: A Literature Review. Report LA-13070-MS. Los Alamos National Laboratory. Los Alamos, USA.

Doebling, S., Farrar, C., Prime, M., and Shevitz, D. (1998). A Review of Damage Identification Methods that Examine Changes in Dynamic Properties. *Shock and Vibration Digest*, 30(2):91–105.

El-Kafafy, M. (2013). *Design and Validation of Improved Modal Parameter Estimators*. PhD thesis, Faculty of Engineering, Department of Mechanical Engineering, Vrije Universiteit Brussels, Brussels, Belgium.

El-Kafafy, M., De Troyer, T., Peeters, B., and Guillaume, P. (2013). Fast Maximum-likelihood Identification of Modal Parameters with Uncertainty Intervals: A Modal Model-based Formulation. *Mechanical Systems and Signal Processing*, 37(1-2):422–439.

El-Kafafy, M., Guillaume, P., De Troyer, T., and Peeters, B. (2012a). A Frequency-domain Maximum Likelihood Implementation Using the Modal Model Formulation. In *Proceedings of the 16th IFAC Symposium on System Identification*, Brussels, Belgium. International Federation of Automatic Control.

El-Kafafy, M., Guillaume, P., Peeters, B., Marra, F., and Coppotelli, G. (2012b). Advanced Frequency-domain Modal Analysis for Dealing with Measurement Noise and Parameter Uncertainty. In *Proceedings of the 30th International Modal Analysis Conference (IMACXXX)*, Jacksonville, Florida, USA. Society for Experimental Mechanics.

Ewins, D. J. (1984). *Modal Testing: Theory and Practice*. Research Study Press LTD.

Farrar, C. R., Doebling, S. W., and Duffey, T. A. (1999). Vibration-based Damage Detection. In *Proceedings of SD2000, the Structural Dynamics Forum*, Los Alamos, NM, USA.

Fladung, W. (2012). Implementation of an SDOF Parameter Estimation Method with Generalized Residuals. In *Proceedings of the 30th International Modal Analysis Conference (IMACXXX)*, Jacksonville, Florida, USA. Society for Experimental Mechanics.

Furtado, R., Quinaz, C., and Bastos, R. (2005). The new Braga Municipal Stadium, Braga, Portugal. *Structural Engineering International*, 15(2):72–76.

Glad, T. and Ljung, L. (2000). *Control Theory - Multivariate and Nolinear Methods*, volume 1. Taylor and Francis, New York, NY.

Gomes, H. M. and Silva, N. (2008). Some Comparisons for Damage Detection on Structures Using Genetic Algorithms and Modal Sensitivity Method. *Applied Mathematical Modelling*, 32(11):2216–2232.

Guillaume, P. (1992). *Identication of Multi-input Multi-output Systems Using Frequency-domain Models*. PhD thesis, Vrije Universiteit Brussel, Belgium.

Guillaume, P., De Troyer, C., and C., D. S. (2006). OMAX - A Combined Experimental-operational Modal Analysis Approach. In *Proceedings of the International Conference on Noise and Vibration Engineering (ISMA) 2006*, pages 2985–2996, Leuven, Belgium.

Guillaume, P., Hermans, L., and Van-der Auweraer, H. (1999). Maximum Likehood Identification of modal parameters from Operational Data. In *Proceedings of the 17th International Modal Analysis Conference (IMACXVII)*, Kissimmee, Florida, USA. Society for Experimental Mechanics.

Guillaume, P. and Schoukens, J. (1998). A Weighted Total Least Squares Estimator for Multivariable Systems with Nearly Maximum Likelihood Properties. *IEEE Transactions on Instrumentation and Measurement*, 47(4):818–822.

Guillaume, P., Schoukens, J., and Pintelon, R. (1989). Sensitivity of Roots to Errors in the Coefficient of Polynomials Obtained by Frequency-domain Estimation Methods. *IEEE Transactions on Instrumentation and Measurements*, 38(6):1050–1056.

Guillaume, P., Verboven, P., Vanlanduit, S., Van-der Auweraer, H., and Peeters, B. (2003). A Poly-reference Implementation of the Least-squares Complex Frequency-domain Estimator. In *Proceedings of the 21st International Modal Analysis Conference (IMACXXI)*, Kissimmee, Florida, USA. Society for Experimental Mechanics.

Hermans, L., Guillaume, P., and Van-der Auweraer, H. (1998). A Frequency-domain Maximum Likelihood Approach for the Extraction of Modal Parameters from Output-only Data. In *Proceedings of the Conference on Noise and Vibration Engineering (ISMA) 23*, K.U. Leuven, Leuven, Belgium.

Hermans, L. and Van-Der-Auweraer, H. (1999). Stochastic Theory of Minimal Realization. *Mechanical Systems and Signal Processing*, 13(2):193–216.

Holmes, J. (2001). *Wind Loading of Structures*, volume 1. Taylor and Francis, New York, USA, second edition.

Hu, W.-H. (2011). *Operational Modal Analysis and Continuous Dynamic Monitoring of Footbridges*. PhD thesis, Faculty of Engineering of the University of Porto, Porto, Portugal.

Hu, W.-H., Caetano, E., and Cunha, A. (2012). Comparison of Different Methods for Removal of Environmental and Operational Effects on Modal Properties and Damage Detection. In *Proceedings of the 5th European Conference on Structural Control (EACS) 2012, Genoa, Italy*, number 164.

Juang, J.-N. (1996). *Applied System Identification*, volume 1. Prentice Hall, Englewood Cliffs, NJ, USA.

Kailath, T. (1980). *Linear Systems*. Prentice-Hall, UpperSaddleRiver.

Kaimal, J. C. and Finnigan, J. J. (1994). *Atmospheric Boundary Layer Flows: Their Structure and Measurement*. Oxford University Press, New York, USA.

Krzanowski, W. (2000). *Principles of Multivariate Analysis: A User's Perspective*, volume 1. Oxford University Press, Oxford, revised edition.

Kullaa, J. (2003). Damage Detection of the Z24 Bridge Using Control Charts. *Mechanical Systems and Signal Processing*, 17(1):163–170.

Kung, S. (1978). A New Identification and Model Reduction Algorithm via Singular Value Decomposition. In *Proceedings of the 12th Asilomar Conference on Circuits, Systems and Computers*, pages 705–714, CA, USA. Asilomar.

Li, Q. S., Xiao, Y. Q., Fu, J. Y., and Li, Z. N. (2007). Full-scale Measurements of Wind Effects on the Jin Mao Building. *Journal of Wind Engineering and Industrial Aerodynamics*, 95(6):445–466.

Ljung, L. (1999). *System Idetification - Theory for the User*, volume 1. Prentice Hall, Eaglewood Cliffs, New Jersey.

Macdonald, J. H. G. (2002). Separation of the Contributions of Aerodynamic and Structural Damping in Vibrations of Inclined Cables. *Journal of Wind Engineering and Industrial Aerodynamics*, 90(1):19–39.

Maeck, J. (2003). *Damage Assessment of Civil Engineering Structures by Vibration Monitoring*. PhD thesis, Katholieke Universiteit Leuven, Leuven, Belgium.

Magalhães, F. (2010). *Operational Modal Analysis for Testing and Monitoring of Bridges and Special Structures*. PhD thesis, Faculty of Engineering of the University of Porto, Porto, Portugal.

Magalhães, F., Caetano, E., and Cunha, A. (2006). Operational Modal Analysis of the Braga Sports Stadium Suspended Roof. In *Proceedings of the 24th International Modal Analysis Conference (IMACXXIV)*, St. Louis, MO, USA. Society for Experimental Mechanics.

Magalhães, F., Caetano, E., and Cunha, A. (2008). Operational Modal Analysis and Finite Element Model Correlation of the Braga Sport Stadium Suspended Roof. *Engineering Structures*, 30(6):1688–1698.

Magalhães, F., Caetano, E., and Cunha, A. (2009a). Online Automatic Identification of the Modal Parameters of a Long Span Arch Bridge. *Mechanical Systems and Signal Processing*, 23(2):316–329.

Magalhães, F., Cunha, A., and Caetano, E. (2009b). Installation of a Continuous Dynamic Monitoring System at Braga Stadium Suspended Roof: Initial Results from Automated Modal Analysis. In *Proceedings of the International Operational Modal Analysis Conference (IOMAC) 2009*, volume 1, Ancona, Italy.

Maia, S., He, L., Lin, S., and To, U. (1998). *Theoretical and Experimental Modal Analysis*, volume 1. Research Studies Press LTD.

Manson, G. (2002). Identifying Damage Sensitive, Environment Insensitive Features for Damage Detection. In *Proceedings of the 3rd International Conference on Identification in Engineering Systems*, pages 187–197, Swansea. Institute of Physics Publishing.

Manson, G., Lee, B., and Staszewski, W. (2004). Eliminating Environmental Effects from Lamb Wave-based Structural Health Monitoring. In *Proccedings of the International Conference on Noise and Vibration Engineering (ISMA) 2004*, Leuven, Belgium.

Martins, N., Caetano, E., Diord, S., Magalhães, F., and Cunha, A. (2014). Dynamic Monitoring of a Stadium Suspension Roof: Wind and Temperature Influence on Modal Parameters and Structural Response. *Engineering Structures*, 59:80–94.

Martins, N., Cardoso, A., and Caetano, E. (2012). Development of an Observation System Based on Anemometry to Characterize the Wind Action Over a Suspension Roof. In *Proceedings of 1st ECCOMAS Young Investigators Conference, Aveiro, Portugal*, Aveiro, Portugal.

MathWorks, T. (2010). *Using Matlab Version V7.11 (R2010b)*. The MathWorks.

Mevels, L., Benveniste, A., and Goursat, M. (2002). Mergin Sensor Data from Multiple Measurement Set-ups from Non-stationary Subspace-based Modal Analysis. *Journal of Sound and Vibration*, 249(4):719–741.

Mitra, S. K. (1998). *Digital Signal Processing - A Computer-based Approach*, volume 1. McGraw-Hill, New York, USA.

Montgomery, D. (2005). *Introduction to Statistical Quality Control*, volume 1. John Wiley & Sons, River Street, Hoboken, NJ, 6th edition.

Ni, Y. O., Hua, X. G., Fan, K. Q., and Ko, J. M. (2005). Correlating Modal Properties with Temperature using Long-term Monitoring Data and Support Vector Machine Technique. *Engineering Structures*, 27(12):1762–1773.

NTSB (2008). Collapse of I-35W Highway Bridge, Minneapolis, Minnesota, August 1, 2007 - Accident Report. Technical report, National Transportation Safaty Board, USA.

Olson, C. F. (1995). Parallel Algorithm for Hierarchical Clustering. *Parallel Computing*, 21(8):1313–1325.

Oracle (2012). *The Java EE 6 Tutorial*. Oracle.

Overchee, P. V. and De-Moor, B. (1996). *Subspace Identification for Linear Systems: Theory, Implementation and Applications*, volume 1. Kluwer Academic Publishers, Katholieke Universiteit Leuven, Belgium.

Parloo, E. (2003). *Application of Frequency-domain System Identification Techniques in the Field of Operational Modal Analysis*. PhD thesis, Faculteit Toegepaste Wetenschappen Pleinlaan Vrije, Universiteit Brussels, Belgium.

Parloo, E., Verboven, P., Guillaume, P., and Van Overmeire, M. (2001). Maximum Likelihood Identification of Modal Parameters from Non-stationary Operational Data. In *Proceedings of the 19th International Modal Analysis Conference (IMACXIX)*, Kissimmee, Florida, USA. Society for Experimental Mechanics.

Peeters, B. (2000). *System Identification and Damage Detection in Civil Engineering*. PhD thesis, Katholieke Universiteit Leuven, Leuven, Belgium.

Peeters, B. and De Roeck, G. (1999a). Reference-based Stochastic Subspace Identification for Output-only Modal Analysis. *Mechanical Systems and Signal Processing*, 13(6):855–878.

Peeters, B. and De Roeck, G. (1999b). Reference Based Stochastic Subspace Identification in Civil Engineering. In *Proceedings of the 2nd International Conference on Identification in Engineering Systems*, pages 639–648, Swansea, UK.

Peeters, B., El-Kafafy, M., and Guillaume, P. (2012). The New PolyMAX Plus Method: Confident Modal Parameter Estimation Even in Very Noisy Cases. In *Proceedings of the International Conference on Noise and Vibration Engineering (ISMA) 2012*, Leuven, Belgium.

Peeters, B., Guillaume, P., Van-der Auweraer, H., Cauberghe, B., and Leuridan, J. (2004a). Automotive and Aerospace Applications of the PolyMAX Modal Parameter Estimation Method. In *Proceedings of 22nd International Modal Analysis Conference (IMACXXII)*, Dearborn, Michigan, USA. Society for Experimental Mechanics.

Peeters, B., Lowet, J., Van-der Auweraer, H., and Leuridan, J. (2004b). A New Procedure for Modal Parameter Estimation. *Sound and Vibration*, 38(1):24–29.

Peeters, B., Van-der Auweraer, H., Guillaume, P., and Leuridan, J. (2004c). The PolyMAX Frequency-domain Method: A New Standard for Modal Parameter Estimation ? *Shock and Vibration*, 11(3-4):395–409.

Peeters, B., Van-Der-Auweraer, H., Vanhollebeck, F., and Guillaume, P. (2007). Operational Modal Analysis for Estimating the Dynamic Properties of a Stadium Structure During a Football Game. *Shock and Vibration*, 14(4):283–303.

Pintelon, R., Guillaume, P., and Schoukens, J. (2007). Uncertainty Calculation in (Operational) Modal Analysis. *Mechanical Systems and Signal Processing*, 21(6):2359–2373.

Pintelon, R. and Schoukens, J. (2001). *System Identification: A Frequency Domain Approach*, volume 1. IEEE Press, Piscataway.

Reynders, E. (2009). *System Identification and Modal Analysis in Strutural Mechanics*. PhD thesis, Katholieke Universiteit Leuven, Leuven, Belgium.

Reynders, E., Houbrechts, J., and De Roeck, G. (2012). Fully Automated (Operational) Modal Analysis. *Mechanical Systems and Signal Processing*, 29:228–250.

Reynders, E., Magalhães, F., Roeck, G., and Cunha, A. (2009). Merging Strategies for Multi-setup Operational Modal Analysis: Application to the Luiz I Steel Arch Bridge. In *Proceedings of the 27th International Modal Analysis Conference (IMACXXVII)*, Orlando, Florida, USA. Society for Experimental Mechanics.

Rocklin, G., C. J. and Vold, H. (1985). A Comparison of H1, H2, and Hv Frequency Response Functions. In *Proceedings of the 3rd International Modal Analysis Conference (IMACIII)*, Orlando, Florida, USA. Society for Experimental Mechanics.

Ross, R. M. and Matthews, S. L. (1995). In-service Structural Monitoring - A State of the Art Review. *Structural Engineering*, 73(2):23–31.

Rytter, A. (1993). Vibration Based Inspection of Civil Engineering Structures.

Schoukens, J. and Pintelon, R. (1991). *Identification of Linear Systems: A Practical Guide to Accurate Modeling*, volume 1. Pergamon Press, London, UK.

Scionti, M. and Lanslots, J. P. (2005). Stabilisation Diagrams: Pole Identification Using Fuzzy Clustering Techniques, Advances in Engineering Software. *Computer-Aided Civil and Infrastructure Engineering*, 36(11-12):768–779.

Shiau, B.-S. and Chen, Y.-B. (2002). Observation on Wind Turbulence Characteristics and Velocity Spectra Near the Ground at the Coastal Region. *Journal of Wind Engineering and Industrial Aerodynamics*, 90(12-15):73–86.

Shigehiko, S., Nakamura, T., Inada, F., and Kato, M. (2008). *Flow-induced Vibrations: Classifications and Lessons from Practical Experiences*, volume 1. Elsevier Science, River Street, Hoboken, NJ, new edition.

Sohn, H., Farrar, R., Hemez, M., Czarnecki, J., Shunk, D., Stinemates, W., and Nadler, R. (2004). A Review of Structural Health Monitoring Literature: 1996-2001. Los Alamos National Laboratory. Los Alamos, USA.

Solari, G. and Piccardo, G. (2001). Probabilistic 3-D Turbulence Modeling for Gust Buffeting of Structures. *Probabilistic Engineering Mechanics*, 16(1):73–86.

Sontag, E. (1998). *Mathematical Control Theory - Deterministic Finite Dimensional Systems*, volume 1. Springer-Verlag, New Jersey, USA.

Steenackers, G. and Guillaume, P. (2005). Structural Health Monitoring of the Z24 Bridge in the Presence of Environmental Changes using Modal Analysis. In *Proceedings of 23rd International Modal Analysis Conference (IMACXXIII)*, Orlando, Florida, USA.

Tamura, Y., Kareem, A., Solari, G., Kwok, K. C. S., Holmes, J. D., and Melbourne, W. (2005). Aspects of the Dynamic Wind-induced Response of Structures and Codification. *Wind and Structures*, 8(4):251–268.

Van-der Auweraer, H., Guillaume, P., Verboven, P., and Valanduit, S. (2001). Application of a Fast-stabilization Frequency Domain Parameter Estimation Method. *Journal of Dynamic System, Measurment and Control*, 123(4):651–658.

Van Overschee, P. and De Moor, B. (1991). Subspace Algorithm for the Stochastic Identification Problem. In *Proceedings of the 30th IEEE Conference on Decision and Control*, pages 1321–1326, Brighton, UK.

Van Overschee, P. and De Moor, B. (1993). Subspace Algorithm for the Stochastic Identification Problem. *Automatica*, 29(3):649–660.

Vapnik, V. N. (1999). An overview of Statistical Learning Theory. *IEEE Transaction on Neural Networks*, 10(5):988–999.

Verboven, P. (2002). *Frequency-domain System Identification for Modal Analysis*. PhD thesis, Vrije Universiteit Brussel, Mechanical Engineering Department, Brussels, Belgium.

Verboven, P., Guillaume, P., Cauberghe, B., Vanlanduit, S., and Parloo, E. (2005). A comparison of Frequency-domain Transfer Function Model Estimator Formulations for Structural Dynamics Modelling. *Journal of Sound and Vibration*, 279(3-5):775–798.

von Kármán, T. (1948). Progress in the Statistical Theory of Turbulence. In *Proceedings of the National Academy of Sciences of the United States of America*, volume 34, pages 530–539, Los Angeles, California, USA.

Vuerinckx, R., Pintelon, R., Schoukens, J., and Rolain, Y. (2001). Obtaining Accurate Confidence Regions for the Estimated Zeros and Poles in System Identification Problems. *IEEE Transactions on Automatic Control*, 46(4):656–659.

Wilczak, J. M., Oncley, S. P., and Stage, S. A. (2001). Sonic Anemometer Tilt Correction Algorithms. *Boundary-Layer Meteorology*, 99(1):127–150.

Yan, A.-M., Kerschen, G., De Boe, P., and Goninval, J.-C. (2005a). Structural Damage Diagnosis Under Varying Enviromental Conditions - Part I - A Linear Analysis. *Mechanical Systems and Signal Processing*, 1(19):847–864.

Yan, A.-M., Kerschen, G., De Boe, P., and Goninval, J.-C. (2005b). Structural Damage Diagnosis Under Varying Enviromental Conditions - Part II - Local PCA for Non-linear Cases. *Mechanical Systems and Signal Processing*, 19(4):865–880.

Zhang, Q. W. (2007). Statistical Damage Identification for Bridges Using Ambient Vibration Data. *Computers and Structures*, 85(7-8):476–485.